Accelerator Design for a Super B Factory at KEK *

edited by J. W. Flanagan and Y. Ohnishi

March 9, 2004

*Letter of Intent for KEK Super B Factory (Part III)

Contents

Chapter 1

Executive Summary

The target luminosity of SuperKEKB is 1-5$\times 10^{35}$ cm^{-2}s^{-1}, a goal which comes from physics requirements [1, 2]. The SuperKEKB collider will be constructed by re-using most of the components of KEKB, especially the ring magnets (outside of the interaction region) and the klystrons used to supply RF power to the cavities. However, there are also many components that need to be modified or newly developed. In order to achieve the primary luminosity target of 10^{35} cm^{-2}s^{-1}, which is ten times as high as the present luminosity, the beam current of the low energy ring (LER) needs to be increased to approximately 10 A. A higher beam current implies a large power loss to synchrotron radiation and higher order modes (HOM). This makes the design of the RF system and the vacuum system quite challenging. We plan to use two types of RF cavities: the Accelerator Resonantly coupled with Energy Storage (ARES) and Single-Cell superconducting Cavities (SCC). The number of RF stations must be increased by a factor of 2 in order to stably store large beam currents. The development of a HOM damper is one of the most important issues, since the present RF system was designed for a beam current of 2.6 A for the positron beam and 1.1 A for the electron beam. Unlike in KEKB, a longitudinal feedback system will become necessary. Issues of electron cloud instability and ion instabilities also arise from the higher beam currents. We have found that ante-chambers and solenoid coils are very effective in suppressing the electron cloud instability; an ante-chamber is being considered in the vacuum system to suppress the generation of photo-electrons, while, solenoid coils will be mounted on the beam chambers prior to installation to prevent the build-up of an electron cloud. The bunch-by-bunch feedback system will be improved to handle the increasingly severe coupled-bunch instabilities in both rings.

Improvements to the injector linac will be necessary because of the shorter beam lifetime and injection to a larger beam current. The exchange of electrons and positrons between the LER and the HER may reduce the electron-cloud instability. We plan to use C-band accelerating structures, which realize approximately double the energy gain of the S-band structures, for the energy upgrade of the positron injector within the restricted length of the beam line.

A damping ring for the positron beam will be constructed in order to reduce the emittance of the injected beam. The lower emittance of the injected beam provides two benefits: the aperture of the ring can be small, and the detector background can be reduced during injection. The design of the interaction region is very restricted by aperture issues.

Beta functions at the interaction point (I.P) will be squeezed to 3 mm, as well as the

bunch length. Final focusing quadrupole magnets and special magnets are to be located nearer to the I.P than those of the present KEKB. The crossing angle is 30 mrad to keep the beams separated in the special magnets.

It has been confirmed that a beam-beam parameter of up to ∼0.05 can be achieved in a collision with a finite crossing angle, both theoretically and experimentally. However, a head-on collision greatly improves the luminosity, according to beam-beam simulations. For instance, the beam-beam parameter of 0.14 is expected from strong-strong simulations and 0.28 from weak-strong simulations. This improvement provides the luminosity of 2.5-5×10^{35} $cm^{-2}s^{-1}$. Therefore, a crab crossing scheme, which effectively creates a head-on collision, is to be applied to SuperKEKB. In order to implement the crab crossing, crab cavities will be installed in both rings. We have designed and developed new crab cavities that can be utilized at a large beam current. The crab crossing has the potential to achieve a beam-beam parameter greater than 0.05, which needs to be confirmed experimentally. We have a plan to test the crab crossing at KEKB in 2005.

The KEKB collider has achieved a luminosity of 10^{34} $cm^{-2}s^{-1}$ in 2003. The design of SuperKEKB has evolved from the experience of KEKB. The luminosity of 10^{35} $cm^{-2}s^{-1}$ is a new frontier for the next generation of B factories.

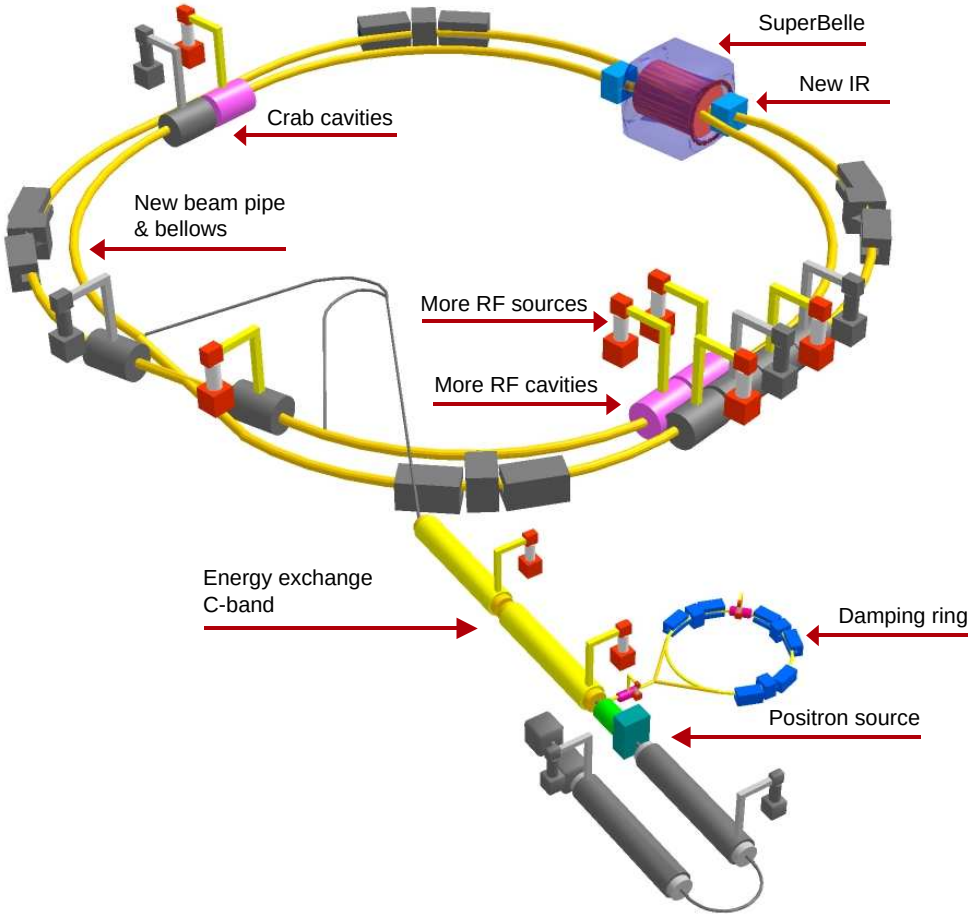

Figure 1.1: Schematic layout of accelerator upgrade for SuperKEKB.

Bibliography

[1] "The third Workshop on Higher Luminosity B Factories", Shonan Village Center, Hayama, Japan, August 6-7, 2002, KEK Proceedings 2002-17, January 2003 A/H.

[2] "Expression of Interest in A High Luminosity Upgrade of the KEKB Collider and the Belle Detector", January 10, 2002, http://belle.kek.jp/superb/eoi.

Chapter 2

Machine Parameters

2.1 Luminosity

Luminosity is defined as the interaction rate per unit cross section,

$$L = \frac{N_{e+} N_{e-} f}{4\pi \sigma_x^* \sigma_y^*} R_L, \tag{2.1}$$

where e^+ and e^- denote a positron and an electron, N is the number of particles per bunch, f is the collision frequency, R_L is the luminosity reduction factor, and σ_x^* and σ_y^* are the horizontal and vertical beam size at I.P, respectively. The luminosity can alternatively be expressed as

$$L = \frac{\gamma_{e\pm}}{2er_e} \left(1 + \frac{\sigma_y^*}{\sigma_x^*}\right) \left(\frac{I_{e\pm} \cdot \xi_{y,e\pm}}{\beta_y^*}\right) \left(\frac{R_L}{R_{\xi_y}}\right), \tag{2.2}$$

where the beam-beam parameters are

$$\xi_{x,y,e\pm} = \frac{r_e}{2\pi\gamma_{e\pm}} \frac{N_{e\mp} \cdot \beta_{x,y}^*}{\sigma_{x,y}^* \left(\sigma_x^* + \sigma_y^*\right)} R_{\xi_{x,y}}, \tag{2.3}$$

and we assume the following transparency conditions:

$$\varepsilon_{e+} = \varepsilon_{e-},\ \beta_{y,e+}^* = \beta_{y,e-}^*,\ \xi_{y,e+} = \xi_{y,e-},\ \gamma_{e+} I_{e+} = \gamma_{e-} I_{e-}. \tag{2.4}$$

In the above expressions, r_e is the classical electron radius, I the beam current, β_y^* the vertical beta function at I.P, R_ξ the reduction factor for the beam-beam parameter, γ the Lorentz factor, and ε the emittance.

SuperKEKB is, like KEKB, a double-ring asymmetric energy collider. The beam energy is 8 GeV for the high energy ring (HER), and 3.5 GeV for the low energy ring (LER). The luminosity formula (Eq. (2.2)) tells us that the luminosity is proportional to the beam current, beam-beam parameter, and the inverse of the vertical beta function at the I.P. However, the transparency condition is not satisfied in the present KEKB, with the maximum luminosity found at an increased HER beam current. We have found that the luminosity is degraded by an LER vertical beam size blow-up caused by photoelectron clouds. We will install solenoid coils and ante-chambers in the arc section to minimize this effect in SuperKEKB. Beam energy exchange, with electrons injected into the LER

instead of the HER, and positrons injected into the HER, is also under consideration to reduce the effect of the photoelectron cloud and to minimize the injection times; in general, the positron injection rate is lower than the electron injection rate. Thus, the machine design is based on Eq. (2.2) to determine the fundamental parameters. We consider a flat beam ($\sigma_y^*/\sigma_x^* \ll 1$) in the present design. The other parameters, except for the ratio of the reduction factors, are constant. Part of the luminosity reduction comes from geometrical effects, significant for Gaussian beams where the bunch length is larger than β_y^*. Another luminosity reduction factor comes from the finite crossing angle [1]. The luminosity reduction factor is expressed by

$$R_L(\theta_x, \varepsilon_x, \varepsilon_y, \beta_x^*, \beta_y^*, \sigma_z) = \frac{a}{\sqrt{\pi}} e^b K_0(b), \tag{2.5}$$

where K_0 is the Bessel function and

$$a = \frac{\beta_y^*}{\sigma_z} \tag{2.6}$$

$$b = \frac{a^2}{2}\left[1 + \left(\frac{\sigma_z}{\sigma_x^*}\tan\frac{\theta_x}{2}\right)^2\right]. \tag{2.7}$$

The crossing angle is denoted by θ_x and σ_z is the bunch length. On the other hand, the beam-beam reduction can be written by

$$R_{\xi_y}(\theta_x, \varepsilon_x, \varepsilon_y, \beta_x^*, \beta_y^*, \sigma_z) = \int dz' \rho(z') \sqrt{1 + \left(\frac{S}{\beta_y^*}\right)^2} f_y\left(z' \tan\frac{\theta_x}{2}, \sigma_x^*(S), \sigma_y^*(S)\right), \tag{2.8}$$

where $S = (z^* - z')/2$, z^* is a coordinate after Lorentz transformation to the head-on collision, ρ is the longitudinal beam distribution, and f_y is the Montague's function. The ratio of the reduction factors, R_L/R_{ξ_y}, is around 0.8, although it depends on the emittances, beta functions at the I.P and crossing angle, as shown in Fig. 2.1.

In summary, a small vertical beta function at the I.P, large beam-beam parameters, and large beam currents are necessary to obtain a higher luminosity. In order to achieve the primary luminosity target of 10^{35} cm^{-2}s^{-1}, we propose that β_y^* be reduced to 3 mm, the bunch length, σ_z, also be reduced to 3 mm to minimize the hour-glass effect [2], and the beam currents be raised to 9.4 A for the LER and 4.1 A for the HER. The number of bunches is 5018, resulting from a 2% abort gap, since we adopt the same RF frequency as that of KEKB, 509 MHz. Consequently, the bunch spacing, s_b, is 0.6 m at minimum. Once the total beam current, I, is given, the number of particles per bunch, N, is expressed as

$$N = \frac{I s_b}{e\beta c}. \tag{2.9}$$

The beam-beam parameter is assumed to be 0.05 in the case of a finite horizontal crossing angle of 30 mrad without crab cavities. The choice of β_x^* affects the luminosity and dynamic aperture, as well as the detector backgrounds. The beam-beam parameter, given by Eq. (2.3), also determines the horizontal emittance,

$$\varepsilon_x = \frac{r_e}{2\pi\gamma_{e\pm}} \frac{I_{e\mp} s_b}{e\beta c} \frac{R_{\xi_y}}{(1+\kappa)\xi_{y,e\pm}}, \tag{2.10}$$

where we choose the optimal coupling [3, 4]: $\kappa = \sigma_y^*/\sigma_x^* = \varepsilon_y/\varepsilon_x = \beta_y^*/\beta_x^*$. On the other hand, the lattice design permits a choice of horizontal emittances in the range from 10 nm to 36 nm. The emittance is controlled via the dispersion at noninterleaved 2.5 π cells in the arc section. Wigglers are used in the LER to control the emittance.

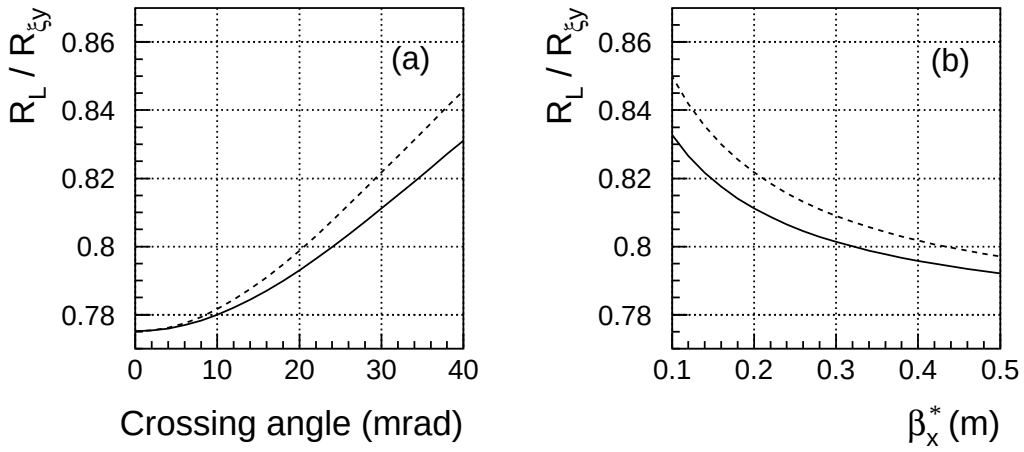

Figure 2.1: Ratio of the reduction factors as a function of (a) crossing angle at β_x^*=20 cm and (b) horizontal beta at I.P for 30 mrad crossing angle. The solid line shows ε_x=30 nm (κ=6 %) and the dashed line shows ε_x=24 nm (κ=1 %).

2.2 Crab crossing

Recently, we have studied the effect of a finite crossing angle at large beam-beam parameters. KEKB has achieved a beam-beam parameter of 0.05 with a crossing angle of 22 mrad. The beam-beam performance up to 0.05 seems to be independent of the crossing angle. However, we need higher beam-beam parameters to achieve a target luminosity several times larger than 10^{35} cm^{-2}s^{-1}. The beam-beam effects have been investigated using weak-strong and strong-strong beam-beam simulations. We use a Gaussian approximation model and a particle in cell (PIC) model in the strong-strong simulation. According to the Gaussian model, the beam-beam parameter, ξ_y, increases linearly with the beam current up to $\sim$0.38 for case of a head-on collision, while it saturates at around 0.05$\sim$0.06 for the case of a finite crossing angle. However, the beam-beam parameter for a head-on collision in the PIC model is limited to 0.14; there is a discrepancy over the achievable beam-beam parameter between the Gaussian model and the PIC model. If the colliding beam can maintain a Gaussian distribution during beam-beam interactions, a higher beam-beam parameter is feasible. The beam-beam halo also limits the beam-beam parameter. We find that a head-on collision is better than a finite crossing angle when considering the beam-beam halo in the weak-strong simulations. The finite crossing angle induces a z-dependent dispersion at the I.P. However, there are many benefits from the finite crossing in simplifying the IR design and avoiding undesired collisions due to multi-bunch operation. To cancel the z-dependent dispersion, we introduce crab cavities. When a head-on collision with crab crossing is employed, the beam-beam parameter is expected to be at least 0.14 at β_x^*=20 cm for the design beam current.

The main parameters are listed in Table 2.1. The machine parameters are determined by the lattice parameters, beam currents, and RF parameters of the ring in the case without beam-beam interactions. The *nominal* beam-beam parameters and *nominal* reduction factors can be calculated by using lattice parameters without beam-beam interactions. In the existence of the beam-beam interaction, the beam sizes at I.P can change dynamically. When we extract beam-beam parameters from the simulation results, we use luminosity obtained from the beam-beam simulation and Eq. (2.2) with nominal emittances and beta functions instead of Eq. (2.3) with dynamical quantities. The nominal beam-beam parameters and the beam-beam parameters obtained from the simulations are also shown in Table 2.1.

Parameters		LER / HER			Unit
Beam energy	E	3.5 / 8.0			GeV
Beam current	I	9.4 / 4.1			A
Particles/bunch	N	1.18×10^{11} / 5.13×10^{10}			
Number of bunches	n_b	5018			
Circumference	C	3016.26			m
Bunch spacing	s_b	0.6			m
Horizontal β at I.P	β_x	0.2			m
Vertical β at I.P	β_y	0.003			m
Bunch length	σ_z	0.003			m
Radiation loss	U_0	1.23 / 3.48			MeV/turn
Synchrotron tune	ν_s	0.031 / 0.019			
Horizontal betatron tune	ν_x	45.506 / 44.515			
Vertical betatron tune	ν_y	43.545 / 41.580			
Crab cavities		No	Yes		
Horizontal emittance	ε_x	30	24		nm
Coupling parameter	κ	6	1		%
Crossing angle	θ_x	30	0 (crab)		mrad
Luminosity reduction*	R_L	0.76	0.86		
ξ_x reduction*	R_{ξ_x}	0.73	0.99		
ξ_y reduction*	R_{ξ_y}	0.94	1.11		
Horizontal beam-beam*	ξ_x	0.079	0.137		
Vertical beam-beam*	ξ_y	0.051	0.218		
Beam-beam simulation		S-S	W-S	S-S	W-S
Vertical beam-beam (simulation)	ξ_y	0.051	0.14	0.28	
Luminosity	L	1	2.5	5	$\times 10^{35}$ cm^{-2}s^{-1}

* nominal value
S-S : Strong-Strong simulation
W-S : Weak-Strong simulation

Table 2.1: Machine parameters of SuperKEKB.

Bibliography

[1] K. Hirata, Phys. Rev. Lett. 74, 2228 (1995).

[2] G. E. Fischer, SLAC Report SPEAR-154 (1972).
SPEAR Ring Group, IEEE Trans. Nucl. Sci. NS-20, 3, 838 (1973).
M. Furman, Proc. 1991 IEEE Particle Accelerator Conference, 422 (1991).

[3] M. A. Furman, LBL-PUB-5379, SLAC-418 (1993).

[4] A. A. Garren et al., Proc. 1989 IEEE Particle Accelerator Conference, 1847 (1989).

Chapter 3

Beam-Beam Interactions

3.1 Introduction

In this chapter, we discuss how large a beam-beam parameter can be achieved. If we assume the design parameters listed in Table 2.1, the beam-beam parameter is expected to be 0.05∼0.28. The beam-beam parameter increases linearly with the number of particles per bunch, according to Eq. (2.3), in the region of low beam current. Once the bunch current exceeds a certain threshold, the beam-beam parameter increases at a slower rate, or saturates. This phenomenon is called the beam-beam limit. The beam size is increased by the beam-beam interaction over this threshold. Therefore, the beam-beam parameter and the luminosity are reduced to be lower than the simple geometrical value.

Numerical simulations help us to understand, and can predict, the beam-beam limit. There is no analytic method to predict the precise limit because of a strong nonlinear phenomenon. Two types of simulation methods are used. One type is a weak-strong simulation in which one beam is assumed to be a fixed charge distribution (the strong beam) and the other beam is represented by a collection of macro-particles (weak beam). The other type of simulation is a strong-strong simulation* in which both beams are represented by macro-particles. The weak-strong simulation has generally been used to design colliders for high-energy physics experiments because the strong-strong simulation can be affected by numerical noise. However, it is not clear whether the weak-strong simulation can predict the beam-beam limit precisely or not. The strong-strong simulation includes all of the possible mechanisms that cause the beam-beam limit. We compare the results from the strong-strong simulation with those from the weak-strong simulation in order to evaluate the beam-beam parameter.

As described in the previous chapter, when we discuss results from beam-beam simulations, we define the beam-beam parameter as follows:

$$\xi_{y,e\pm} = \frac{2er_e}{\gamma_{e\pm}} \left(\frac{\sigma_x^*}{\sigma_x^* + \sigma_y^*} \right) \left(\frac{L\beta_y^*}{I_{e\pm}} \right) \left(\frac{R_{\xi_y}}{R_L} \right), \tag{3.1}$$

where σ_x^*, σ_y^*, β_y^*, R_L, and R_{ξ_y} are nominal values.

*The meaning of "strong beam" in the weak-strong simulation is different from that in the strong-strong simulation.

3.2 Simulation methods

The one-turn map for macro-particles in an $e^{\pm}$ beam, $\boldsymbol{x} = (\boldsymbol{x}_+, \boldsymbol{x}_-)$, is expressed by [1]

$$\begin{aligned} \boldsymbol{x}(C) &= S\exp\left[-:\int_0^C (H_0 + H_{bb})ds:\right]\boldsymbol{x}(0) \\ &= V_0(C)S\exp\left[-:\int_{-\Delta}^{\Delta} V_0^{-1}(s)\phi_{bb}(s)V_0(s)ds:\right]\boldsymbol{x}(0), \end{aligned} \tag{3.2}$$

where

$$\phi_{bb}(s) = \phi_+(\boldsymbol{x}_-) + \phi_-(\boldsymbol{x}_+). \tag{3.3}$$

$\phi_\pm(\boldsymbol{x}_\mp, s_\mp)$ is the potential of the $e^{\pm}$ beam at the coordinates of the macro-particles in the $e^{\mp}$ beam. $V_0(C)$, which is the transfer map of the lattice, is given by

$$V_0(C) = S\exp\left[-:\int_0^C (H_{0,+} + H_{0,-}(s))ds:\right]. \tag{3.4}$$

$V_0(s)$ is the transfer map from the collision point ($s = 0$) to the interaction point of a longitudinal slice of the bunch, $H_{0,\pm} = (p_{x,\pm}^2 + p_{y,\pm}^2)s/2$.

The one-turn map for a macro-particle consists of the product of two maps due to the beam-beam interaction and transfer at the arc section. The transfer map of the arc section is expressed by a linear transfer matrix, with tracking done element by element. The beam-beam map is determined by the tracking of macro-particles in one beam including encounters with the electromagnetic force of the other beam. The electromagnetic field, which is formed in the transverse plane of the beam, can be represented by a two-dimensional potential. The potential is evaluated by solving a Poisson equation for the macro-particle distribution of the other beam. For a collision with a finite crossing angle, the plane in which the electromagnetic field is induced is different from the transverse plane for the other beam. In this case, a Lorentz transformation is applied to the two beams to make them collide along a common axis. The details of this approach are discussed in Section 3.4.

The potential, ϕ, is determined by the two-dimensional Poisson equation,

$$\triangle_\perp \phi_\pm(x, y; z, s) = \frac{r_e}{\gamma_\mp}\rho_\pm(x, y; z, s), \tag{3.5}$$

where ρ is the density of the beam population at a given (z, s); it is the transverse distribution of a longitudinal slice of the bunch that collides with a particle with longitudinal coordinate z at s. In this connection, the longitudinal coordinate of the slice is $z' = z - 2s$. The potential is a function of z of the macro-particle in the $e^{\mp}$ beam. The distribution of the longitudinal slice at $z' = z - 2s$ gives the potential. Thus, the distribution of the $e^{\pm}$ beam at s depends on the beam-beam interaction with that part of the $e^{\mp}$ beam with $z' > z$. We use two methods to evaluate the beam-beam interaction (ϕ). One is a Gaussian model and the other is the particle-in-cell method (PIC). In the Gaussian model, particles in a beam interact with the other beam, which is approximated to be Gaussian in distribution. In the PIC method, particles interact with the other beam, which can have an arbitrary distribution.

Equilibrium distributions of the two beams are obtained by iterating the map, including the damping and excitation due to synchrotron radiation. The luminosity is

determined by the equilibrium distributions. In the simulation, particles are initialized as a Gaussian distribution derived from the design emittance and beta functions. Radiation damping and excitation are applied to the normal mode. The bunch beam is represented by 10^5 macro-particles and is divided into 5 longitudinal slices. The simulation gives the distributions $\rho_+(x, y, z; s)$ and $\rho_-(x, y, z'; s)$ at the interaction point $s = 0$ after tracking the macro-particles through several damping times. The luminosity is estimated by the equilibrium beam distributions, as follows:

$$L = \sum^{f_{rep}} \int \rho_+(x, y, z; s)\rho_-(x, y, z'; -s)dxdydzdz', \tag{3.6}$$

where f_{rep} is the repetition frequency, and the integration is performed while keeping $s = (z - z')/2$.

3.2.1 Gaussian model

A simple way to calculate the electromagnetic field is to assume that the transverse distribution of the beam is a Gaussian distribution. In the weak-strong simulation, the beam size is given by the design emittances and the beta functions. The beam size is kept constant during the simulation. In the strong-strong simulation, the beam size is given by the rms values of the macro-particles. The rms values are evaluated for both beams at every integration step of Eq. (3.2).

The potential, ϕ, is given by

$$\phi_\pm(x, y, z; s) = \frac{r_e N}{4\pi\gamma_\mp\sigma_x\sigma_y} \int dx'dy' \ln|(x - x')^2 + (y - y')^2| \exp\left(\frac{x'^2}{\sigma_x(s)^2} + \frac{y'^2}{\sigma_y(s)^2}\right). \tag{3.7}$$

The derivatives for x and y are given by the complex error function [2]. The macro-particles in the other beam are tracked in the electro-magnetic field given by Eq. (3.7) along the integration step given by Eq. (3.2). The integration step along s is replaced by the z of the beam which induces the field. This process corresponds to slicing of the beam. The kick affecting a tracked particle depends on the particle's z coordinate. A longitudinal kick occurs at each step of integration [3, 4].

3.2.2 Particle-in-cell method

The particle-in-cell method deals with a collision between beams with arbitrary distributions. The potential, ϕ, is determined by the two-dimensional Poisson equation,

$$\triangle_\perp \phi_{\pm,i}(x, y; z, s) = \frac{r_e}{\gamma_\mp}\rho_\pm(x, y; z, s), \tag{3.8}$$

where ρ is the density of the beam at a given (z, s). The potential is solved by the particle-in-cell (PIC) method. Macro-particles are mapped onto a two-dimensional grid space [5].

An extension to three-dimensional space is performed by slicing a bunch along the z direction. Interactions between pairs of slices are evaluated in two-dimensional space. Particles in a bunch move across the longitudinal slices due to synchrotron oscillations. When the vertical beta function is comparable to the bunch length, the transverse kick of a

particle encounters a discontinuity at the crossing point between two slices. Consequently, a large amount of numerical noise arises and the symplecticity is broken. In order to reduce the longitudinal discontinuity, an interpolation of the potential [6] is applied. The PIC method is better than the Gaussian model, because the beam distribution may be arbitrary. The PIC model gives a precise Yokoya factor for the spectra of coherent beam-beam modes, while the Gauss model gives a smaller factor than the correct Yokoya factor.

3.3 Beam-beam limit for luminosity

We here discuss the beam-beam limit on the luminosity. A different beam-beam limit beam lifetime is discussed later. In this section, the beam-beam limit for a zero crossing angle is considered. However, the finite crossing angle scheme has been adopted in the present KEKB. A discussion of the finite crossing angle is given in the next section.

3.3.1 Two-dimensional model

The bunch length is neglected in the two-dimensional model, that is, $\Delta \to 0$ is assumed in Eq. (3.2). Figure 3.1 shows the beam-beam parameters obtained by the Gaussian and the PIC models. The nominal beam-beam parameter is calculated from Eq. (2.3). The beam-beam parameter increases to over 0.2 in the Gaussian model, while the PIC method gives a beam-beam limit of around 0.05. Figure 3.2 shows the vertical beam size and dipole amplitude given by the PIC and the Gaussian models. In the PIC model, the dipole amplitude grows to about the design beam size, ~ 1 μm, and the rms beam size also grows as shown in Fig. 3.2 (a). A coherent instability, which is observed for beam-beam parameters larger than 0.05, causes the beam-beam limit. A coherent instability has been found in several strong-strong codes using the PIC model [7]. The Gaussian model does not show this remarkable coherent motion, as shown in Fig. 3.2 (b). Figures 3.2 (c) and (d) show detailed structures of the dipole motion for the PIC and the Gaussian model. The PIC model gives motion in the coherent π mode, while the Gaussian model gives the σ mode motion.

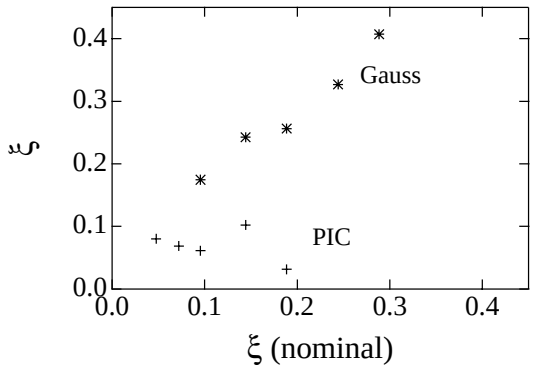

Figure 3.1: Beam-beam parameter estimated from the luminosity as a function of the nominal value. The crosses and diamonds denote the beam-beam parameters given by the PIC and the Gaussian models, respectively.

Figures 3.3 and 3.4 show the Fourier amplitudes of the dipole motion in the Gaussian and PIC models. Although σ- and π-mode peaks are found in both models, their behaviors

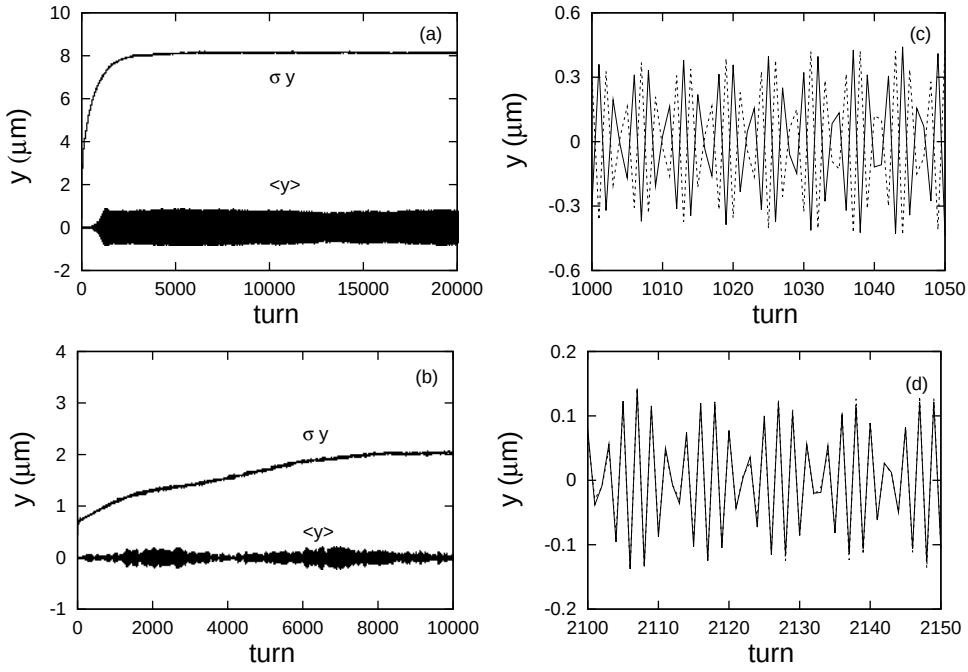

Figure 3.2: Evolution of the vertical beam size and dipole amplitude. (a), (b) The beam size and dipole amplitude given by the PIC and Gaussian models, respectively. (c), (d) Dipole motions during short periods indicate coherent modes.

are different. The σ mode is always enhanced relative to the π mode, but does not grow significantly in the Gaussian model. Therefore, the beam-beam system remains stable. On the other hand, the π mode is enhanced relative to the σ mode in the PIC model and grows strongly at high beam currents. Though this behavior might depend on the tune operating point, such a remarkable difference is interesting. Enhancement of the σ mode might be a particular feature of the Gaussian model.

The coherent motion is expected to be smeared during operation with different tunes. Figure 3.5 shows the turn-by-turn evolution of the beam-beam parameter for operation with different tunes. The tune operating points are (0.506,0.545) for the LER and (0.515,0.58) for the HER, respectively. The operating point is similar to that of the present KEKB. The figure shows that the luminosity is improved by having a tune difference. There has been much discussion about whether the PIC model is reliable or not in terms of the stability over several thousand turns. There is a possibility that numerical noise enhances coherent motions or particle diffusion. The behavior of the coherent motion is confirmed by several codes [7] and the result does not depend on the statistics and the choice of mesh in the PIC model. Numerical diffusion can be examined by using weak-strong simulations [8]. Simulations using the exact formula [2] and the PIC method are compared for a given Gaussian strong beam. Figure 3.6 shows the turn-by-turn evolution of the luminosity for an exact formula and for the PIC method. There is no influence of the numerical diffusion in the PIC model.

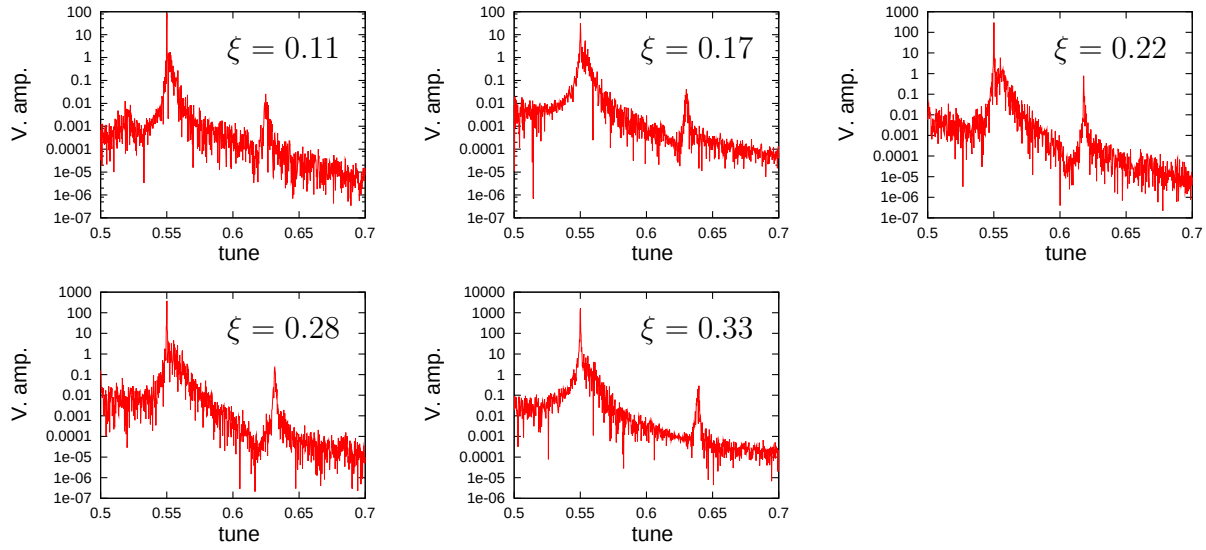

Figure 3.3: Fourier spectra for the vertical dipole motion obtained by the Gaussian model. The nominal beam-beam parameter is $\xi = 0.11$, 0.17, 0.22, 0.28, and 0.33.

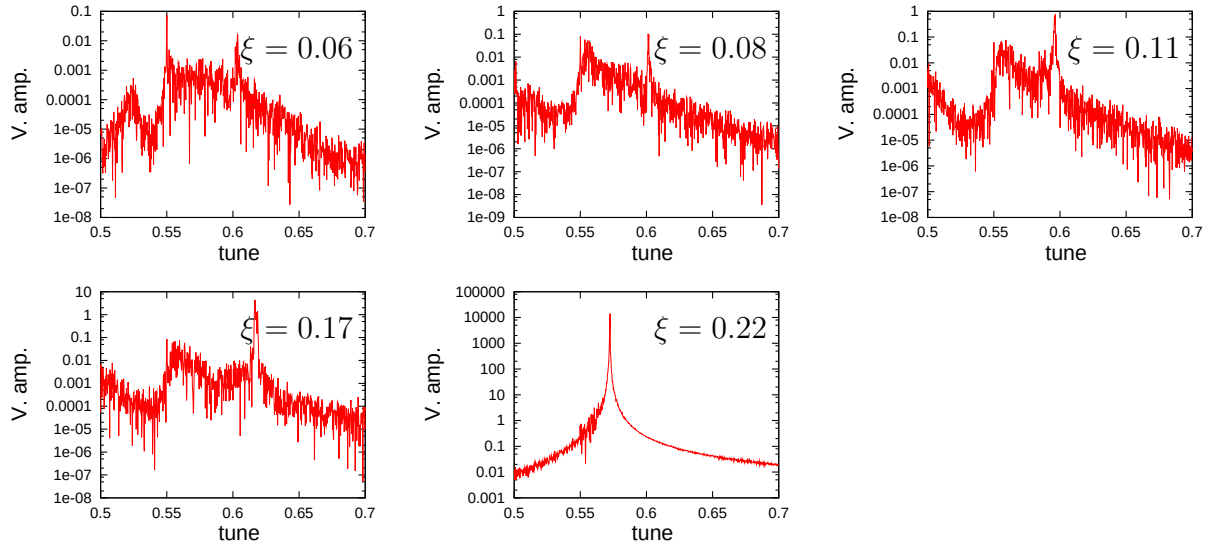

Figure 3.4: Fourier spectra for the vertical dipole motion obtained by the PIC model. The nominal beam-beam parameter is $\xi = 0.06$, 0.08, 0.11, 0.17 and 0.22.

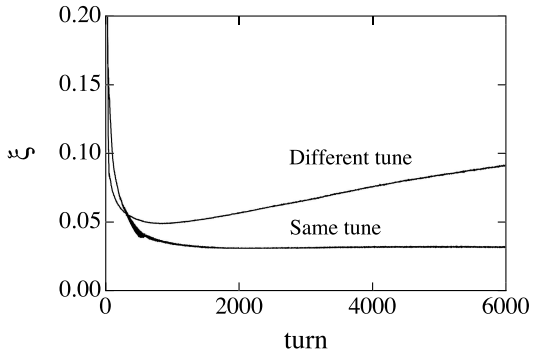

Figure 3.5: Evolution of the beam-beam parameter for different tunes. The LER and the HER are operated at tunes of (0.506,0.545) and (0.515,0.58), respectively.

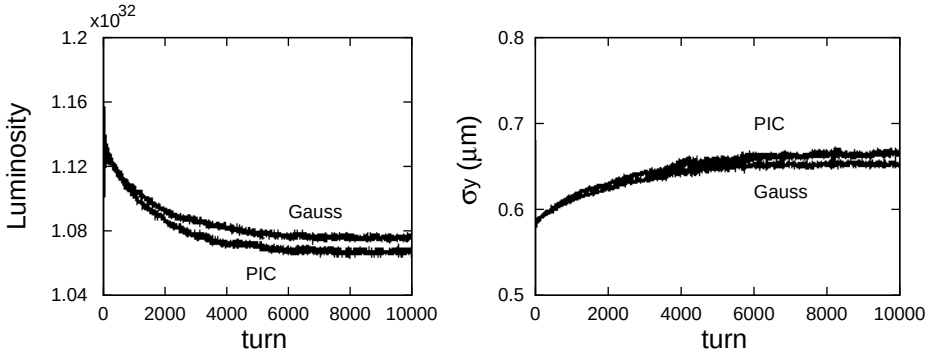

Figure 3.6: Evolution of the luminosity and vertical beam size given by the weak-strong simulation using the PIC method and by the exact solution for a Gaussian strong-beam distribution.

3.3.2 Three-dimensional model

We consider here the bunch length in the beam-beam effect. When integration along s in Eq. (3.2) is performed, the integration is replaced with that along z of the colliding bunch. We discuss a three-dimensional simulation for the case of a zero crossing angle in this section. The integration is replaced by the product of discrete maps. The discretization corresponds to the slicing of a bunch.

$$\prod_{i=1}^{N_{sl,-}} \exp\left[- : V_{0,+}^{-1}(s_{-,i})\phi_{-,i}(\boldsymbol{x}_+, s_{-,i})V_{0,+}(s_{-,i})\Delta s : \right] \times \prod_{j=1}^{N_{sl,+}} \exp\left[- : V_{0,-}^{-1}(s_{+,j})\phi_{+,j}(\boldsymbol{x}_-, s_{+,j})V_{0,-}(s_{+,j})\Delta s : \right], \tag{3.9}$$

where $s_{\mp,i} = (z_\pm - z_{\mp,i})/2$ is the interaction point of a positron/electron that collides with the i-th electron/positron slice. $\phi_{\pm,i}$ is the two-dimensional potential of the i-th positron/electron slice that arrives at $s_{\pm,i}$. The Gaussian and PIC models are used to obtain ϕ in a similar way as in the two-dimensional model.

Figure 3.7 shows the beam-beam parameter and beam sizes for various beam currents obtained by the Gaussian and PIC models. The horizontal axis in the figure represents the nominal beam-beam parameter calculated from Eq. (2.3). The results given by the Gaussian approximation and the PIC method are very different. No remarkable increase can be found in the horizontal beam size, but one is found in the vertical beam size for both models. However, the enlargement given by the PIC method is stronger than that in the Gaussian approximation. The Gaussian approximation gives a beam-beam parameter larger than 0.2, while a saturation of the beam-beam parameter at around 0.1 is found in the PIC method. There is no coherent motion in the first and second moments, $\langle x_i \rangle$ and $\langle x_i x_j \rangle$, in both methods. A weak-strong simulation with a Gaussian fixed beam [9] provides similar results to those from the Gaussian strong-strong simulation. Figure 3.8 shows the evolution of the luminosity for various nominal beam-beam parameters obtained by the PIC simulation. The behavior of the luminosity is smooth for $\xi = 0.04$ and 0.09, while sudden changes are sometimes found for $\xi \geq 0.13$.

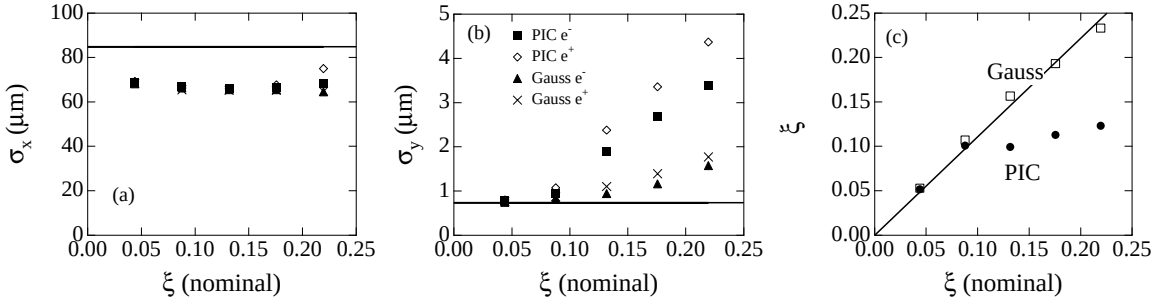

Figure 3.7: Beam sizes and the beam-beam parameter as functions of the nominal beam-beam parameter obtained by the strong-strong simulations with the particle-in-cell method and Gaussian approximation. (a), (b) Horizontal and vertical beam size. (c) Effective beam-beam parameter.

Figure 3.9 shows the vertical particle distributions during an abrupt change in the luminosity. Both the electron and positron distributions are shown in the figure. The

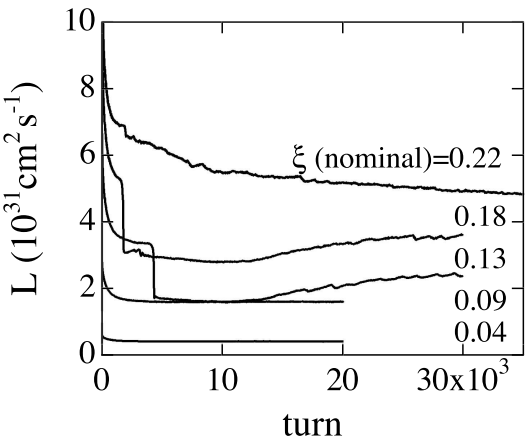

Figure 3.8: Evolution of luminosity for various nominal beam-beam parameters in the three-dimensional model.

widths of both distributions are enlarged and the shapes are distorted from a Gaussian shape, while both beams are overlapping each other. The final distributions after 25,000 turns are shown in Fig. 3.9(d). The distribution of the positrons is slightly broader than that of the electrons because of the difference in the radiation damping time. Both distributions, which are distorted from a Gaussian one, especially in the tail part, are considered to be an equilibrium distribution of the two colliding beams.

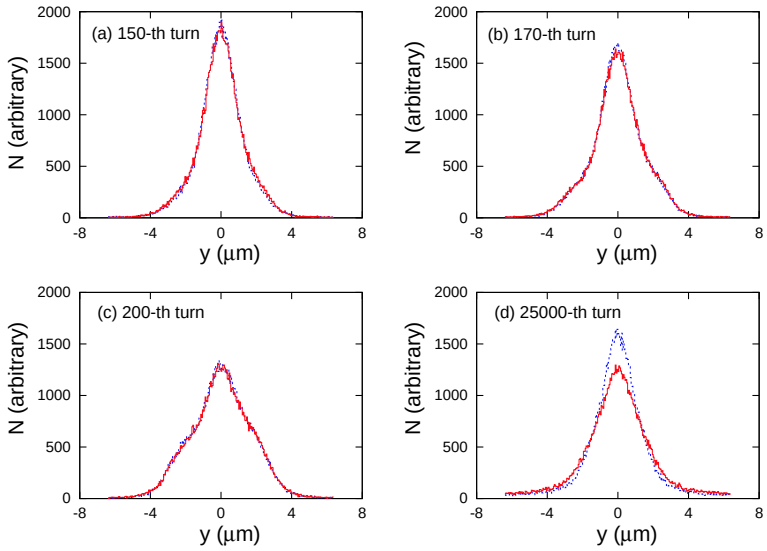

Figure 3.9: Evolution of the vertical distribution of electron and positron beams. The distributions after (a) 150, (b) 170, (c) 200 and (d) 30,000 turns.

We believe that the beam-beam limit is determined by the equilibrium distribution of the two beams, but that it is not caused by coherent motion. In order to confirm this assumption, we performed a modified weak-strong simulation involving the particle distribution obtained from the strong-strong simulation. If the beam-size enlargement is due to an incoherent phenomenon, the same luminosity and size should be obtained in the final state. The strong beam, which is the electron beam in this analysis, is given the same

distribution as the final distribution obtained from the strong-strong simulation with the PIC code, while the weak positron beam is initialized with the designed Gaussian distribution at the initial state. In this approach, any coherent motion is suppressed. Figure 3.10 shows the transition of the beam-beam parameter obtained from the strong-strong and the weak-strong simulations. The beam-beam parameter is at a similar level after 40,000 turns in either of the two models. The evolutions of the beam size in the strong-strong and the weak-strong simulations are shown in Fig. 3.11 (a) and (b), respectively. The size of the positron beam in the two simulations grows to a similar value. The luminosity from the weak-strong simulation is in agreement with that of the strong-strong simulation to within 15%. Figure 3.11 (c) shows the evolution of the beam size obtained from the weak-strong simulation in which the weak positron beam interacts with a fixed Gaussian electron beam. The beam size is much less than that for the distorted beam that is utilized in the modified weak-strong and the strong-strong simulations. This means that the distortions are propagated between the two beams. Thus, if one beam is distorted from a Gaussian, the other beam is also distorted automatically.

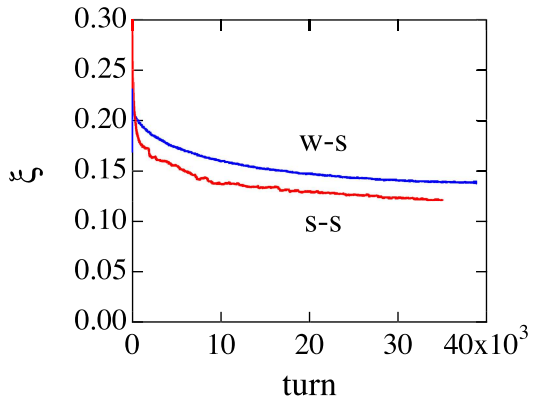

Figure 3.10: Evolution of the beam-beam parameter as a function of turn number. The beam-beam parameter is obtained from weak-strong and strong-strong simulations.

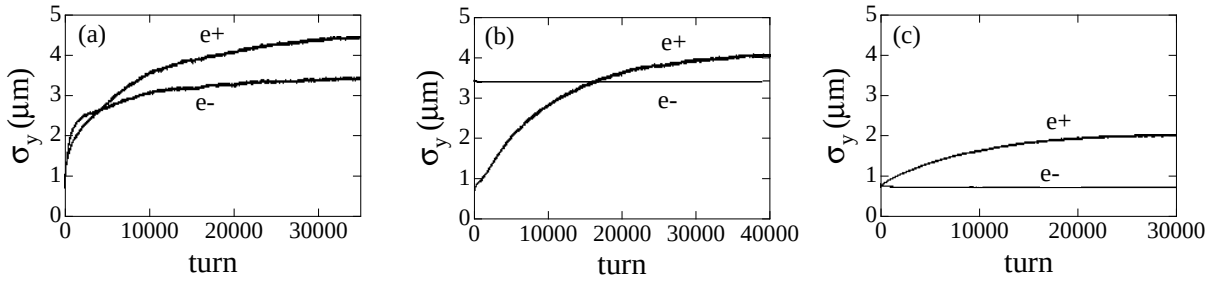

Figure 3.11: Evolution of vertical beam size as a function of turn number. The beam sizes for (a) a strong-strong simulation, (b) a modified weak-strong simulation, and (c) a weak-strong simulation in which a weak positron beam interacts with a fixed Gaussian electron beam are shown.

It is interesting to see a Poincaré plot for the distorted and Gaussian distribution in the weak-strong simulation. Figure 3.12 shows a Poincaré plot in $y - p_y$ phase space. The results are obtained from the two-dimensional simulation for simplicity. Ten particles with

zero initial x and z amplitudes are tracked while interacting with three types of beams: a distorted distribution obtained by the strong-strong simulation; a Gaussian distribution whose force is calculated by the PIC method; also, a Gaussian whose force is calculated exactly using the complex error function, where the radiation damping and excitation are omitted. Figures 3.12 (b) and (c) are given by the PIC method and an exact formula for the Gaussian distribution. The trajectories in Fig. 3.12 (a), obtained by the strong-strong simulation, are different from Figs. 3.12 (b) and (c) for the Gaussian case, but no clear information on the mechanism of the beam-beam limit is given.

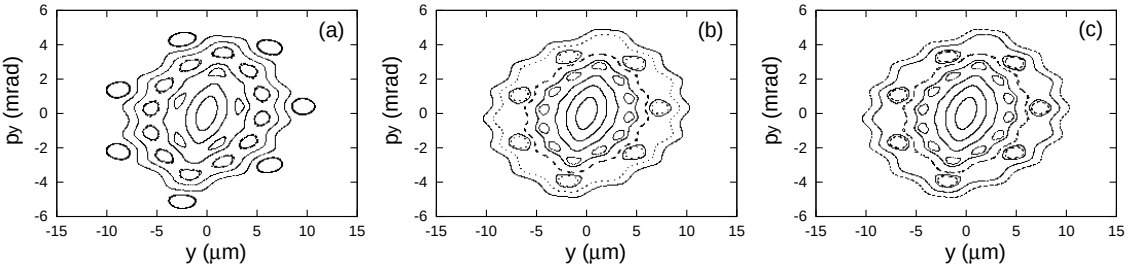

Figure 3.12: Poincaré plot for the distorted and Gaussian distributions given by a two-dimensional simulation. (a) PIC method for the distorted distribution. (b) PIC method for Gaussian distribution. (c) Exact error function formula for Gaussian distribution.

We now discuss the diffusion of the beam-beam system. Figure 3.13 shows the evolution of the beam-beam parameter and the vertical beam size, respectively. The evolution with damping and excitation of synchrotron radiation and the evolution in the Hamiltonian system without radiation are also shown in Fig. 3.13. The beam-beam parameter and the vertical beam size are calculated from the distorted distribution obtained by a strong-strong simulation, a Gaussian distribution whose force is calculated by the PIC method, and from a Gaussian whose force is calculated by the exact formula using the complex error function. For the beam-beam system without synchrotron radiation, the beam-beam parameter and the beam size remain at their initial values; that is, diffusion due to nonlinearity is weak. The above behaviors, when including radiation, are different from each other. Synchrotron radiation plays an important role in the beam-beam limit.

Coherent motion, which restricts the luminosity in the two-dimensional simulation, disappears in the three-dimensional simulation. In order to investigate the reason, three-dimensional simulations are performed using a short bunch length. Figure 3.14 shows the evolution of the beam-beam parameter for various bunch lengths. Two kinds of beam-beam parameter are found in the figure: one is 0.1 for $\sigma_z = 1.5$ mm and the other is 0.03 for $\sigma_z = 0.3$, 0.6, and 1 mm. The beam-beam parameter for a short bunch length, $\sigma_z \leq 1$ mm, is similar to that obtained by a two-dimensional simulation. The beam-beam parameter for $\sigma_z = 1.5$ mm is also similar to that of the design value, $\sigma_z = 3$ mm. Coherent motion is observed for a bunch length of 1 mm or less, but not observed for longer bunch lengths. The threshold of the bunch length seems to be about $\beta_y/2$, since the vertical beta function is 3 mm. This result might be due to a spread of the beam-beam tune shift along the longitudinal direction. In the case of SuperKEKB, the bunch length, $\sigma_z = 3$ mm, is comparable to that of the vertical beta function. The incoherent effect dominates over the coherent instability.

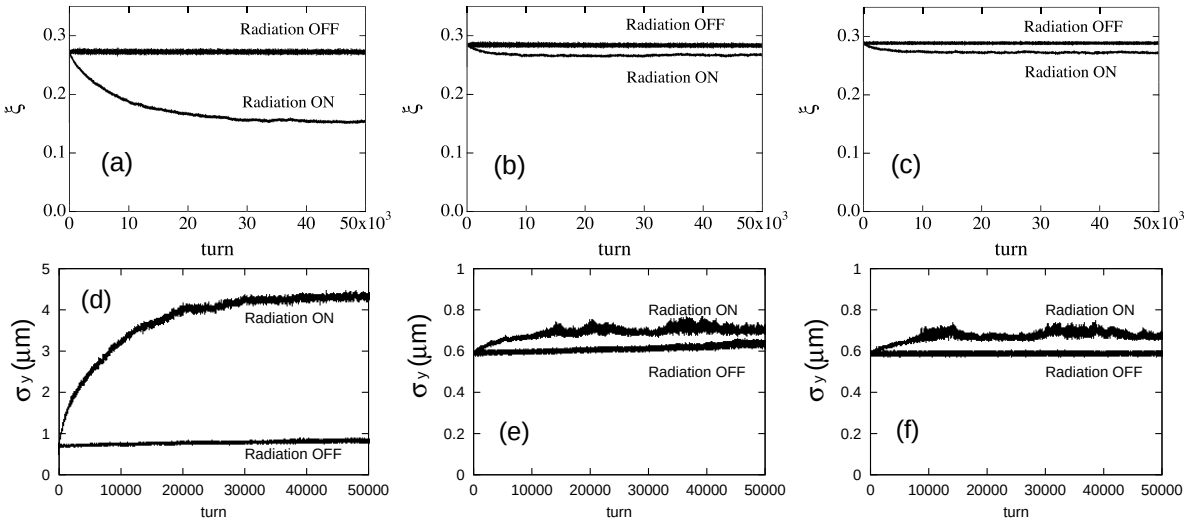

Figure 3.13: Evolution of the beam-beam parameter and the vertical beam size given by two-dimensional simulations. The two lines correspond to turning the synchrotron radiation on and off. (a), (d) PIC method for distorted distribution. (b), (e) PIC method for Gaussian distribution. (c), (f) Exact error function formula for Gaussian distribution.

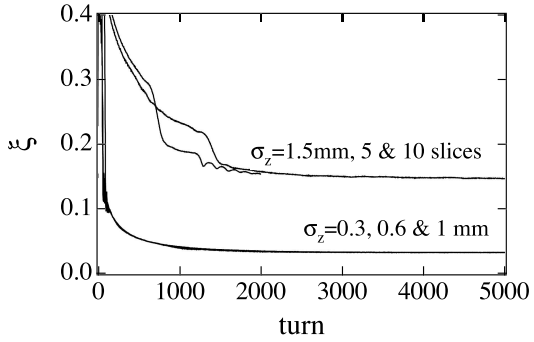

Figure 3.14: Evolution of the beam-beam parameter for various bunch lengths. For $\sigma_z = 1.5$ mm, the simulations were performed for 5 and 10 slices.

3.4 Crossing angle

A finite crossing-angle scheme has been adopted in the present KEKB. Achievement of the design luminosity, 10^{34} cm^{-2}s^{-1}, at KEKB indicates that the finite crossing-angle scheme has no problem to achieve a beam-beam parameter of up to 0.05. As shown in the previous section, the beam-beam limit without a crossing angle is about 0.1 in the three-dimensional simulation. The collision scheme with a crossing angle should be reviewed with a view to progressing towards higher luminosity. Crab cavities effectively make a collision with a finite crossing angle into a head-on collision. The feasibility of crab cavities is described here.

The collision with crossing angle is treated by a Lorenz boost to a head-on frame from the laboratory frame [10, 11]; i.e., particles in the beam are transferred to the head-on frame, then collide, and are transferred to the laboratory frame by the inverse of the Lorenz boost. In the laboratory frame, the s axes of two beams are chosen to be their directions of motion, and the electromagnetic field of a beam is formed in the plane perpendicular to its s axis. The beam-beam force that the other beam encounters is not in the transverse direction. The time when the beam encounters the force depends on the positions of the two beams. In the head-on frame, the s axes of the two beams coincide, except that the direction is opposite. Beam particles in the two beams basically move along the s direction and the beam-beam force is perpendicular to the s axis. The principle axis of the beam ellipsoid does not coincide with the s direction. Thus, $\langle xz \rangle$ is not zero for the case of a horizontal crossing angle.

The Lorentz transformation from the laboratory frame to the head-on frame is given for a half crossing angle (θ) as follows:

$$\begin{aligned}
x^* &= \tan\theta z + \left(1 + \frac{p_x^*}{p_s^*}\sin\theta\right) x, \\
y^* &= y + \sin\theta \frac{p_y^*}{p_s^*} x, \\
z^* &= \frac{z}{\cos\theta} - \frac{H^*}{p_s^*}\sin\theta x, \\
p_x^* &= \frac{p_x - \tan\theta H}{\cos\theta}, \\
p_y^* &= \frac{p_y}{\cos\theta}, \\
p_z^* &= p_z - \tan\theta p_x + \tan^2\theta H,
\end{aligned} \tag{3.10}$$

where

$$H = (1+p_z) - \sqrt{(1+p_z)^2 - p_x^2 - p_y^2}, \tag{3.11}$$

$$p_s = \sqrt{(1+p_z)^2 - p_x^2 - p_y^2}. \tag{3.12}$$

A star designates a dynamical variable in the head-on frame. H^* and p_s^* are $H(\boldsymbol{p}^*)$ and $p_s(\boldsymbol{p}^*)$, respectively. Note that the x^* and y^* axes are defined in the same direction for both beams. The s^* axes are defined in opposite directions, since the two beams travel in opposite directions.

The linear part of the transformation is expressed by a matrix:

$$M_{crs} = \begin{pmatrix} 1 & 0 & 0 & 0 & \tan\theta & 0 \\ 0 & 1/\cos\theta & 0 & 0 & 0 & 0 \\ 0 & 0 & 1 & 0 & 0 & 0 \\ 0 & 0 & 0 & 1/\cos\theta & 0 & 0 \\ 0 & 0 & 0 & 0 & 1/\cos\theta & 0 \\ 0 & -\tan\theta & 0 & 0 & 0 & 1 \end{pmatrix}. \tag{3.13}$$

This transformation is not symplectic: the determinant of the transfer matrix M_{crs} is $\cos^{-3}\theta$ instead of 1. This is due to the fact that the Lorenz transformation is not symplectic for the accelerator coordinates, because the Hamiltonian is divided by a reference momentum. This is not a problem, because the inverse factor of $\cos^3\theta$ is applied by an inverse transformation. By including this transformation into V_0 of Eq. (3.2), a simulation can be performed without any change, except that the beam shape has a gradient in the $x-z$ plane. The gradient is considered automatically in the three-dimensional simulation. Figure 3.15 shows the relation between the beam-beam parameter (ξ) and the bunch population for collisions with and without a crossing angle of 22 mrad. Figure 3.15 (a) and (b) were obtained by weak-strong and strong-strong simulations, respectively. The beam-beam limit is > 0.35 or 0.14 for collisions without a crossing angle, as is discussed in the previous section. The ξ in the crossing collision shows a similar behavior for both of the two simulations; that is, ξ is saturated at around 0.06.

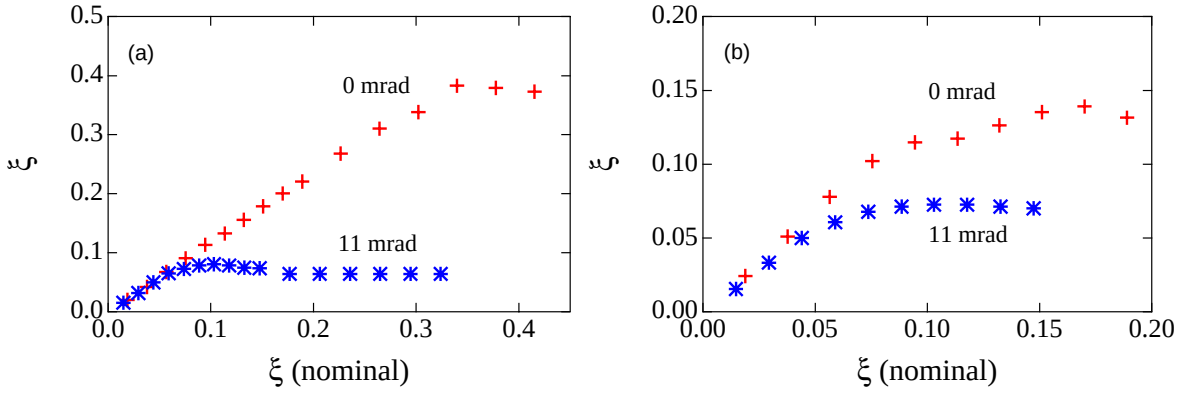

Figure 3.15: Beam-beam parameters for a zero and finite crossing angle. (a) Weak-strong. (b) Strong-strong simulations.

Figure 3.16 shows the beam-beam parameter as a function of the half crossing angle. The geometrical luminosity, which is also plotted in the figure, is less dependent on the crossing angle. The simulated luminosity has a peak near the zero-crossing angle in the simulations. The peak structure of the strong-strong simulation is narrower than that of the weak-strong simulation.

The beam-beam parameters in the weak-strong simulation are similar to those of the strong-strong simulation at a half crossing angle of 11 mrad. However, this agreement might be accidental. These results indicate that the collision performance for a zero crossing angle is much better than that for the finite crossing angle. The crab cavity creates a generalized time dispersion, $x = \zeta_x z$, with respect to z. The dispersion corresponds to

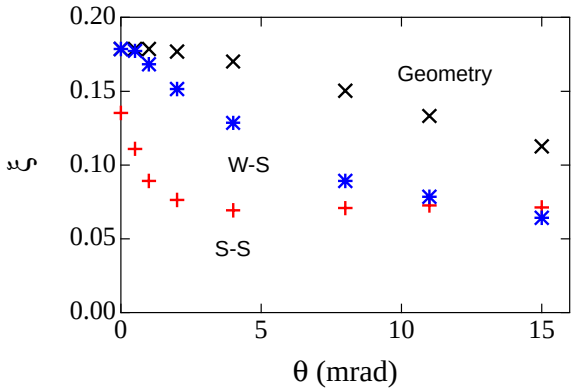

Figure 3.16: Beam-beam parameters for various crossing angles. Beam-beam parameter from geometrical luminosity, the weak-strong, and strong-strong simulations.

(1,5) and (6,2) components of the transfer matrix that has the same structure as that between the laboratory and the head-on frame for collision of the finite crossing angle. This means that a collision with a finite crossing angle can effectively be converted into one with a zero crossing angle using crab cavities. Therefore, the crab cavities are expected to improve the luminosity significantly.

There is a reason why the crossing angle makes the luminosity worse. We focus on nonlinear diffusion, as in the previous section. The weak-strong simulation with the Gaussian model is used here. Figure 3.17 shows the evolution of the luminosity for zero and finite crossing angles. Pictures (a) and (b) depict the luminosity evolutions with/without synchrotron radiation damping, respectively, for a tune operating point of (0.508,0.55). This operating point is close to that of the LER in the present KEKB. For a zero crossing angle, diffusion due to nonlinearity is not seen, as is discussed in the previous section. For a finite crossing angle, diffusion is clearly seen. Including synchrotron radiation causes the diffusion to be emphasized even more. Pictures (c) and (d) are depicted for the tune operating point of (0.518,0.58). This operating point is close to that of the HER in the present KEKB. The diffusion rate due to nonlinearity, which depends on the operating point, is worse than that at the previous operating point. The beam-beam limit or total diffusion when including synchrotron radiation is also worse than at the previous point.

The crossing angle induces nonlinear diffusion in both the vertical and horizontal beam directions. Figure 3.18 shows the spreading of the horizontal and vertical beam sizes due to the crossing angle. The crossing angle which causes linear $x - z$ coupling also affects the vertical diffusion. A small diffusion is found for a zero crossing angle. It is not found at all in the two-dimensional simulation, as shown in Figure 3.18 (c).

Similar diffusion is also induced by the $x - y$ coupling. Figure 3.19 shows that the diffusion is found in the beam-beam parameter with the $x-y$ coupling, $r_4 = 0$. Nonlinear diffusion in Fig. 3.19 (a) shows an interesting feature. The strength of the diffusion is different between the two- and three-dimensional simulations: i.e., it is weaker for the two-dimensional simulation than it is for the three-dimensional simulation. Therefore, the extra dimension contributes to the diffusion.

The nonlinear diffusion due to the crossing angle is not found in the collision with zero crossing angle. There is no diffusion for not only the Gaussian strong beam but also the distorted beam as is shown in Figure 3.17. The diffusion at zero crossing angle is related

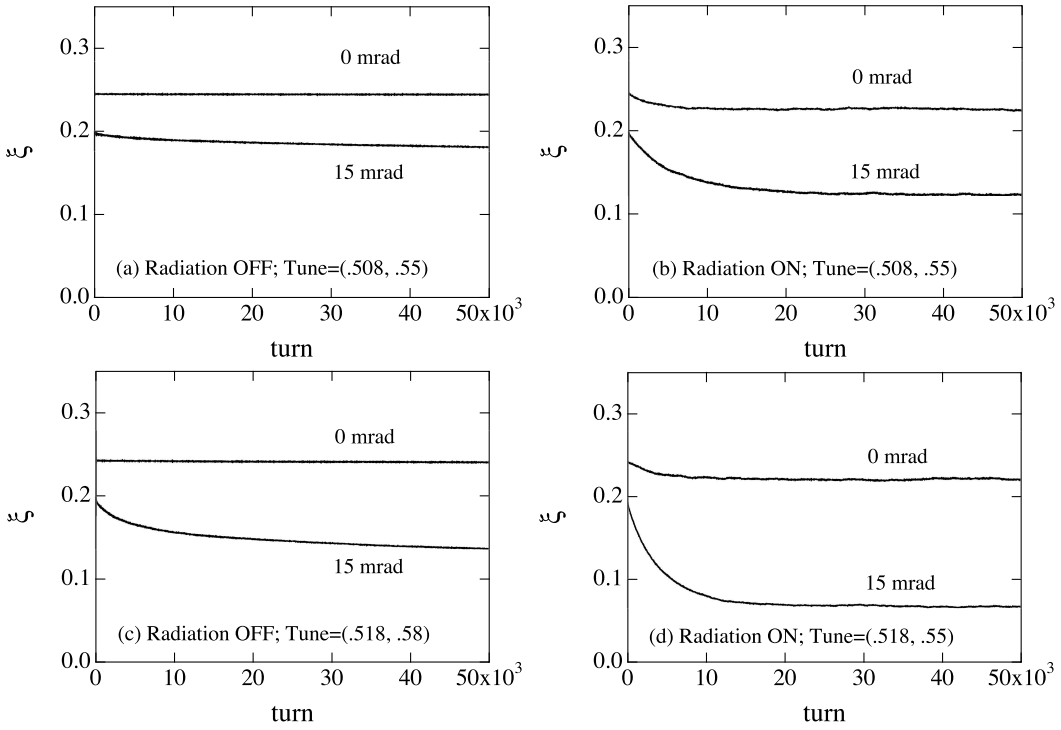

Figure 3.17: Diffusion due to crossing angle. (a) and (b) show the evolution of the beam-beam parameter with/without synchrotron radiation damping for the tune operating point (0.508,0.55). (c) and (d) show the evolution of the beam-beam parameter with/without synchrotron radiation damping for the tune operating point (0.518,0.58).

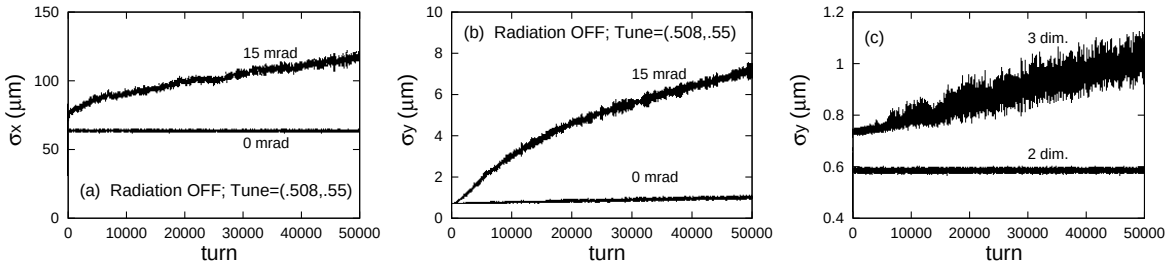

Figure 3.18: Spreading of horizontal and vertical beam size due to crossing angle. Figures (a) and (b) depict the evolutions of the horizontal and vertical beam sizes, respectively. Fugure (c) depicts the diffusion seen in two and three dimensional simulations for zero-crossing angle and no synchrotron radiation.

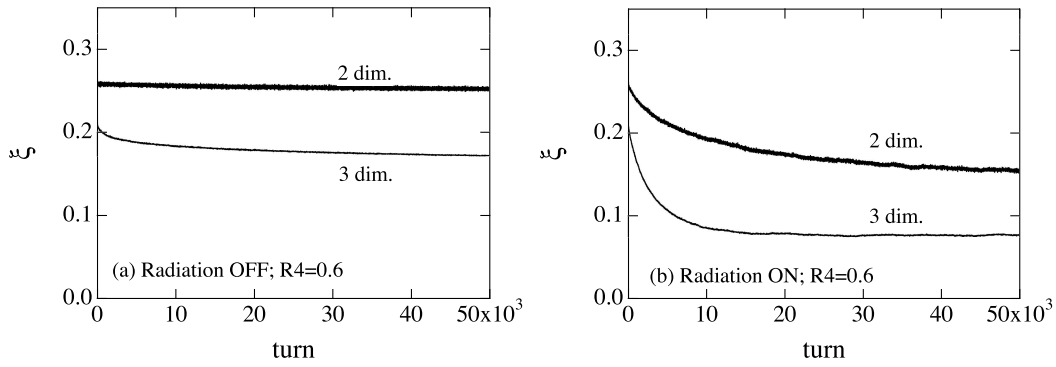

Figure 3.19: Diffusion as seen in the beam-beam parameter with $x-y$ coupling, $r_4 = 0.6$. (a) and (b) show the evolution of the beam-beam parameter with and without synchrotron radiation, respectively. In each case, both two- and three-dimensional simulations are shown.

to synchrotron radiation. The simulation is based on the two-dimensional PIC model. It would be interesting to see nonlinear diffusion for the three-dimensional PIC model.

So far, we have neglected the difference between a true head-on collision without a crossing angle and a crab collision with a finite crossing angle. The nonlinear term of the transformation in Eq. (3.11) should be considered to confirm the validity of the crab crossing. Figure 3.20 shows the evolution of the luminosity for a head-on collision without a crossing angle and a crab collision with a finite crossing angle of 22 mrad. The two cases completely agree with each other: that is, the crab collision achieves the same performance as the head-on collision. If a single crab cavity is installed in a ring, ζ_x and ζ_x' are not controlled simultaneously. In this case, ζ_x' might have a finite value, even if $\zeta = 0$ is satisfied. Figure 3.20 shows the luminosity evolution for $\zeta_x' = 0.1$ m^{-1}.

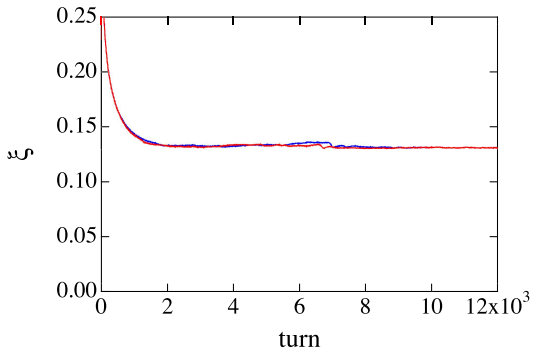

Figure 3.20: Evolution of the luminosity for a head-on collision without a crossing angle and for a crab collision with a finite crossing angle of 11 mrad.

3.5 Beam-beam tail

The beam-beam tail that affects the beam lifetime limits the luminosity of colliders [12, 13]. The weak-strong simulation is used to estimate the halo. Figure 3.21 shows the

particle distribution of the beam. An aperture of more than $30\sigma_y$ is required. This value is the same level as in the present KEKB with a finite crossing angle.

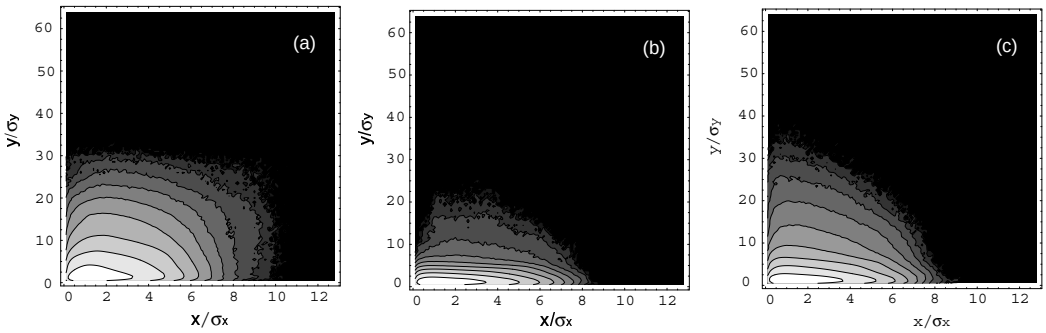

Figure 3.21: Contour plot of the transverse particle density in a bunch obtained by the weak-strong simulation. Present KEKB parameters with (a) and without crossing angle (b). SuperKEKB without crossing angle (c).

As discussed in the previous section, the deviation from the Gaussian distribution is critical in determining the beam-beam limit for the luminosity. The mechanism of the luminosity limit is due to the diffusion of the particle distribution. Therefore, the same mechanism should affect the halo formation.

3.6 Toward a higher beam-beam parameter

At the present stage, the achievable beam-beam parameter is considered to be about 0.1. This implies a maximum luminosity of $2 \sim 3\times10^{35}$ cm^{-2}s^{-1} with the design parameters. If the target luminosity is 5×10^{35} cm^{-2}s^{-1} or more, some special techniques will be required. Within the scope of conventional methods, one possibility is to adjust β_x. Figure 3.22 (a) shows the beam-beam parameter for various emittances and horizontal beta functions at the collision point. A lower beta function makes the beam-beam parameter larger, but lower emittance does not contribute to an improvement of the luminosity.

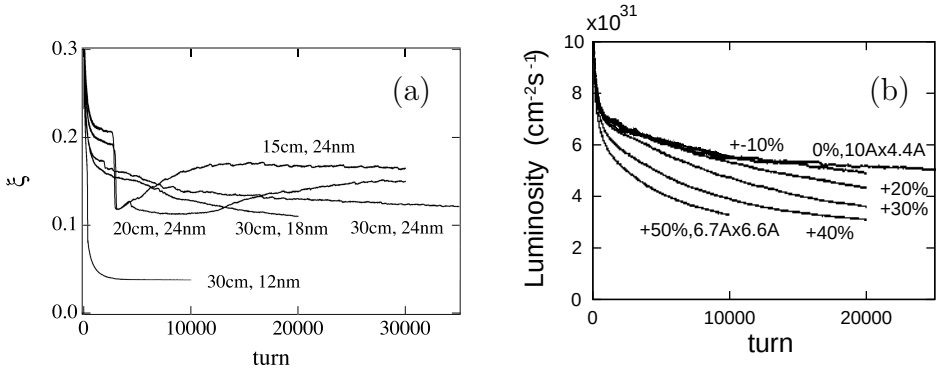

Figure 3.22: (a) Beam-beam parameter for various emittances and horizontal beta functions. (b) Luminosity for various current ratios.

Another possibility is to adjust the beam current ratio between the positron beam and the electron beam. Figure 3.22 (b) shows the luminosities for various beam-current ratios. The ratio is varied from -10% to +50%, where 0% corresponds to the ratio satisfying the transparency condition, $N_+\gamma_+ = N\gamma_-$. Thus, +(-)10% means 10% more (less) current for the high-energy beam. A deviation of more than ±10% deviation from the transparency condition caused the luminosity to degrade.

3.7 Summary

The beam-beam limit has been studied for SuperKEKB using various types of computer simulations. The simulation methods are as follows:

A) Weak-strong simulation using a Gaussian strong beam in two-dimensional space ($x - y$).

B) Weak-strong simulation using a Gaussian strong beam in three-dimensional space ($x - y - z$).

C) Weak-strong simulation with the strong beam having an arbitrary distribution using the PIC algorithm in two-dimensional space ($x - y$).

D) Weak-strong simulation with the strong beam having an arbitrary distribution using the PIC algorithm in three-dimensional space ($x - y - z$) (under construction).

E) Strong-strong simulation using a Gaussian approximation in two-dimensional space ($x - y$).

F) Strong-strong simulation using a Gaussian approximation in three-dimensional space ($x - y - z$).

G) Strong-strong simulation with each beam having an arbitrary distribution using the PIC algorithm in two-dimensional space ($x - y$).

H) Strong-strong simulation with each beam having an arbitrary distribution using the PIC algorithm in three-dimensional space ($x - y - z$).

The results are summarized as follows.

- Simulations with the Gaussian approximation, (A,B,E,F), give unlimited beam-beam parameters greater than 0.2.
- Two-dimensional strong-strong simulation with the PIC code (G) gives a beam-beam limit of around 0.05 due to a coherent π mode instability. This instability disappears when using different tunes between two rings.
- Three-dimensional strong-strong simulation with the PIC code (H) gives a beam-beam limit of around 0.1 due to an incoherent distortion of the distribution. The coherent motion found in the two-dimensional simulation (G) is not observed.
- Weak-strong simulation (C,D) with the distorted beam distribution gives a beam-beam limit of around 0.1, which is consistent with the strong-strong simulation (H).

- Nonlinear diffusion without synchrotron radiation is weak for the Gaussian and the distorted beams in the two-dimensional weak-strong simulation.
- The crossing angle degrades the beam-beam performance; therefore, crab cavities are required for SuperKEKB.
- The crossing angle and $x - y$ coupling enhance nonlinear diffusion.

We have a discrepancy in the beam-beam limit between the Gaussian model and the PIC method. The PIC method is more accurate. Therefore, the achievable beam-beam limit is around 0.1, because the cause of the beam-beam limit is a distortion of the beam distribution, which is out of the scope of the Gaussian model. The beam-beam parameter is increased up to about 0.12 for a smaller β_x. A crab cavity is necessary to achieve a beam-beam parameter larger than 0.1.

We have some issues to study in the near future:

- Develop a weak-strong simulation with the three-dimensional PIC algorithm.
- Halo estimation using the PIC weak-strong simulation.
- Beam-beam compensation scheme to obtain a higher beam-beam parameter.

The beam-beam limit in the case without synchrotron radiation is better than that with radiation. This might be considered strange given the lower beam-beam limit of proton storage rings. A discussion of the beam-beam limit for proton beams can be found elsewhere.

Bibliography

[1] A. J. Dragt, Lectures on nonlinear orbit dynamics, In 1981 Fermilab Summer School, AIP Conference Proceedings Vol. 87, 1982.

[2] M. Bassetti and G. Erskine, CERN-ISR TH/80-06 (1980).

[3] K. Hirata, H. Moshammer and F. Ruggiero, Particle Accelerators, **40**, 205 (1993).

[4] K. Ohmi and A.W. Chao, Proceedings of ECLOUD'02, CERN-2002-001, 227-234 (2002).

[5] K. Ohmi, Phys. Rev. Ebf 62, 7287 (2000).

[6] K. Ohmi, Proceedings of PAC03 (2003).

[7] M. Tawada, Y. Cai, K. Ohmi and J. Qiang, KEK-Preprint 2003-82 (2003).

[8] J. Qiang, private communications (2003). (KEK-preprint 2003-95)

[9] K. Ohmi, Proceedings of PAC03 (2003).

[10] K. Oide and K. Yokoya, Phys. Rev. A**40**, 315 (1989).

[11] K. Hirata, Phys. Rev. Letters, **74**, 2228 (1995).

[12] T. Chen, J. Irwin and R. Siemann, Phys. Rev. E**49**, 2323 (1994).

[13] D. Shatilov, Part. Accel., **52**, 65 (1996).

Chapter 4

Lattice Design

4.1 Beam-optical parameters

The lattices of the KEKB colliding rings have wide ranges of tunability for the horizontal emittance, ε_x, and the momentum compaction factor α_p:

$$1.0 \times 10^{-8} \text{ m} \leq \varepsilon_{\text{x}} \leq 3.6 \times 10^{-8} \text{ m}, \tag{4.1}$$

$$-4 \times 10^{-4} \leq \alpha_p \leq 4 \times 10^{-4}. \tag{4.2}$$

These flexibilities come from the unit-cell structure of KEKB, the 2.5π cell. Without changing the lattice in the arcs, the beam-optical parameters can be adjusted to the required values for SuperKEKB, as listed in Table 4.1. Only the interaction region (IR) in the Tsukuba straight section must be reconstructed to achieve $\beta_y^* = 3$ mm.

The design values of ε_x and β_x^* have been determined by luminosity considerations based on beam-beam simulations and the feasibility of the IR design. The design value of α_p is selected so as to satisfy the condition for the bunch length, $\sigma_z = 3$ mm, at a given value of the RF voltage, V_c. The synchrotron tune, ν_s, is given as

$$\nu_s = \frac{C\alpha_p\sigma_\delta}{2\pi\sigma_z}, \tag{4.3}$$

where C is the circumference and σ_δ is the relative momentum spread.

		LER	HER	Unit
Horizontal emittance	ε_x	2.4×10^{-8}	2.4×10^{-8}	m
Beta function at IP	β_x^*/β_y^*	200/3	200/3	mm
Momentum compaction	α_p	2.7×10^{-4}	1.8×10^{-4}	
Momentum spread	σ_δ	7.2×10^{-4}	6.8×10^{-4}	
RF voltage	V_c	15	20	MV
Bunch length	σ_z	3	3	mm
Synchrotron tune	ν_s	0.031	0.019	

Table 4.1: Beam-optical parameters of SuperKEKB

4.2 2.5π cell and noninterleaved chromaticity correction scheme

The arcs of the KEKB rings consist of 2.5π unit cells that have been developed to meet the following requirements: (1) Include noninterleaved sextupole pairs for chromaticity correction; and (2) Maintain a reasonable range of tunability for both ε_x and α_p.

Two noninterleaved pairs of sextupole magnets are placed in a cell, as shown in Fig. 4.1, and the number of the sextupole pairs in the whole ring amounts to 52. In the LER, two more pairs are installed in the IR to locally correct the chromaticities of the final quadrupole magnets. Two sextupole magnets in a pair are connected with a pseudo $-I$ transformer,

$$\begin{pmatrix} -1 & 0 & 0 & 0 \\ m_{21} & -1 & 0 & 0 \\ 0 & 0 & -1 & 0 \\ 0 & 0 & m_{43} & -1 \end{pmatrix}. \tag{4.4}$$

By this arrangement, the principle nonlinearities of the sextupoles are cancelled in each pair, which creates a large transverse dynamic aperture.

There are 7 families of quadrupole magnets in a cell with 6 constraints: 4 for the pseudo $-I$ conditions of two sextupole pairs, and 2 for adjusting of ε_x and α_p by tuning the horizontal dispersions at the dipole magnets. All of the constrains are reasonably satisfied with a sufficient number of quadrupole families. Although the present cells have been optimized at $\varepsilon_x = 1.8 \times 10^{-8}$ m, both rings still reserve sufficient tuning ranges of ε_x and α_p around the design values.

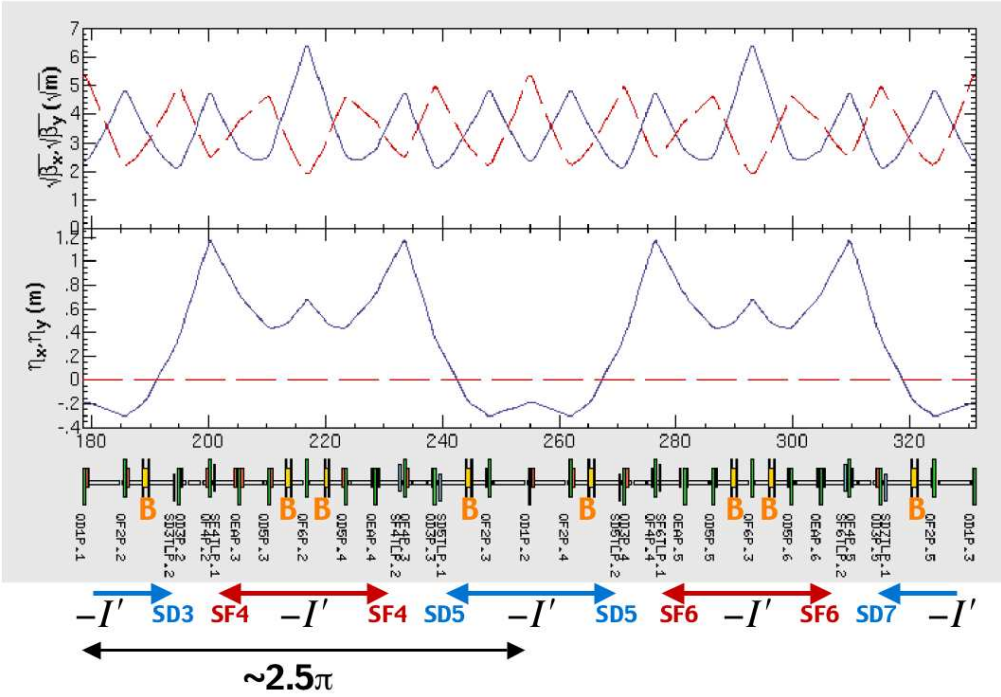

Figure 4.1: Noninterleaved 2.5π cell structure in LER.

4.3 Interaction region

The final-focus quadrupole magnets are placed as close as possible to the interaction point (IP) in order to minimize the chromaticities. The solenoid field of SuperBelle is fully compensated with compensation solenoids on each side of IP,

$$\int B_z dz = 0. \tag{4.5}$$

The remaining $x - y$ coupling components, and the horizontal and vertical dispersions are all corrected to be zero at the IP, and are localized in the IR on each side of the IP with 4 or 6 skew quadrupole magnets, as well as horizontal and vertical dipole magnets. In order to reduce the synchrotron-light background, the bending angles of the dipole magnets must be limited to be as small as possible on the upstream side of the HER, and then the crossing angle between the axis of the SuperBelle solenoid and the HER orbit is selected to be 22 mrad, which is the same as in the present lattice. Other geometrical conditions for the beam crossing angle of 30 mrad are also matched, as well as the beam-optical parameters. A local chromaticity correction scheme is adopted only in the LER at present. There is a tuning section in each ring at each end of the IR, where 6 quadrupole magnets are placed in the region of $\eta_{x,y} = 0$ to adjust $\beta^*_{x,y}$, keeping unchanged the coupling and dispersive region around the IP.

The IR lattice of both rings is shown in Figs. 4.2 and 4.3. The design principles for the IR discussed above are almost the same as in the present lattice. The main difference is a greater overlapping of the solenoid field on the final vertical-focusing quadrupole magnets (QCSs); no serious problem has been discovered so far concerning this matter.

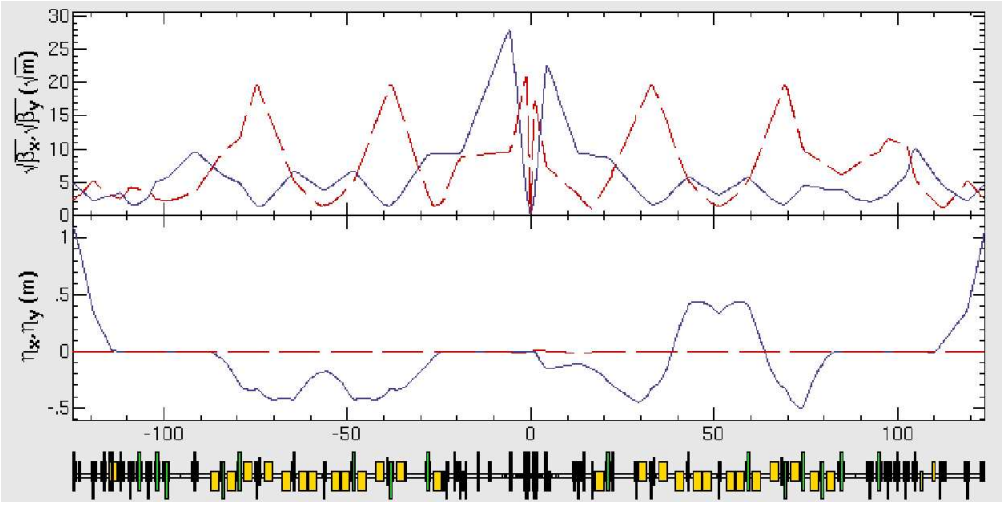

Figure 4.2: Lattice design (LER) in the interaction region.

4.4 Dynamic apertures

The dynamic apertures have been estimated with particle tracking in 6-dimensional phase space. Figure 4.4 shows the dynamic aperture in the LER. The beta functions at the IP are 20 cm in the horizontal and 3 mm in the vertical direction. The required values of

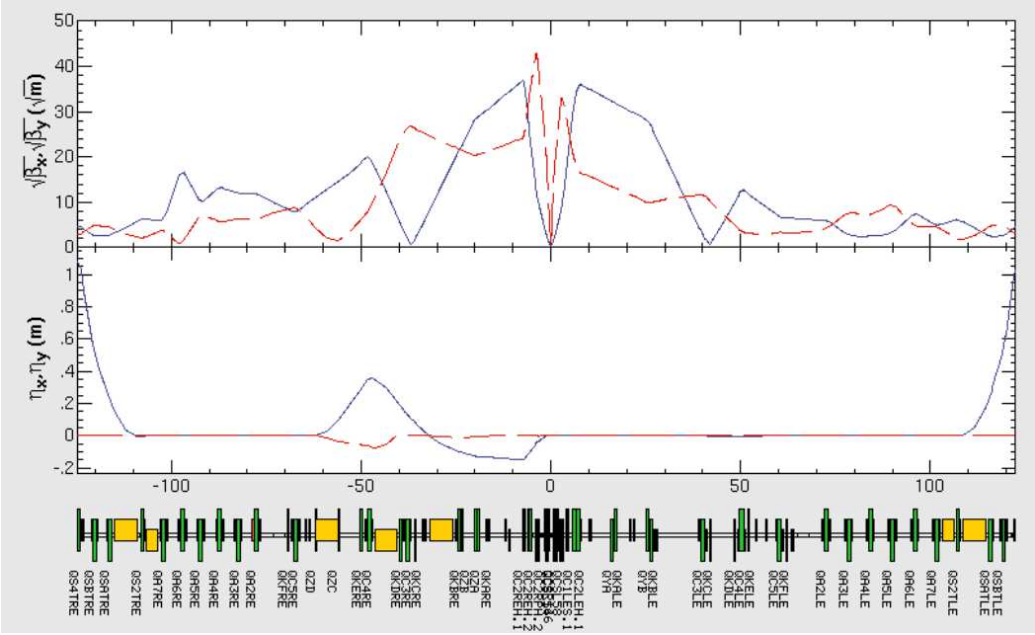

Figure 4.3: Lattice design (HER) in the interaction region.

the transverse dynamic apertures: $A_x/A_y = 7.5 \times 10^{-6}/1.2 \times 10^{-6}$ m for the LER and $A_x/A_y = 4.5 \times 10^{-6}/5.2 \times 10^{-7}$ m for the HER. The transverse dynamic aperture in the LER is acceptable and that in the HER is being investigated. In the present IR model, the field distribution around the IP, that is, that of SuperBelle and the compensation solenoids and QCSs along the longitudinal direction on the solenoid axis, is given by 4-cm-thick slices of constant B_z, or $K1 = B'/B\rho$. The multipole components of the final quadrupole magnets have not yet been included. From experience at KEKB, the dynamic apertures are not affected by the multipole components within the region where the requirement for the field quality is satisfied, $\delta K1/K1 \leq 1 \times 10^{-3}$. However, further improvements of the IR lattice are now in progress using more realistic models with multipole components.

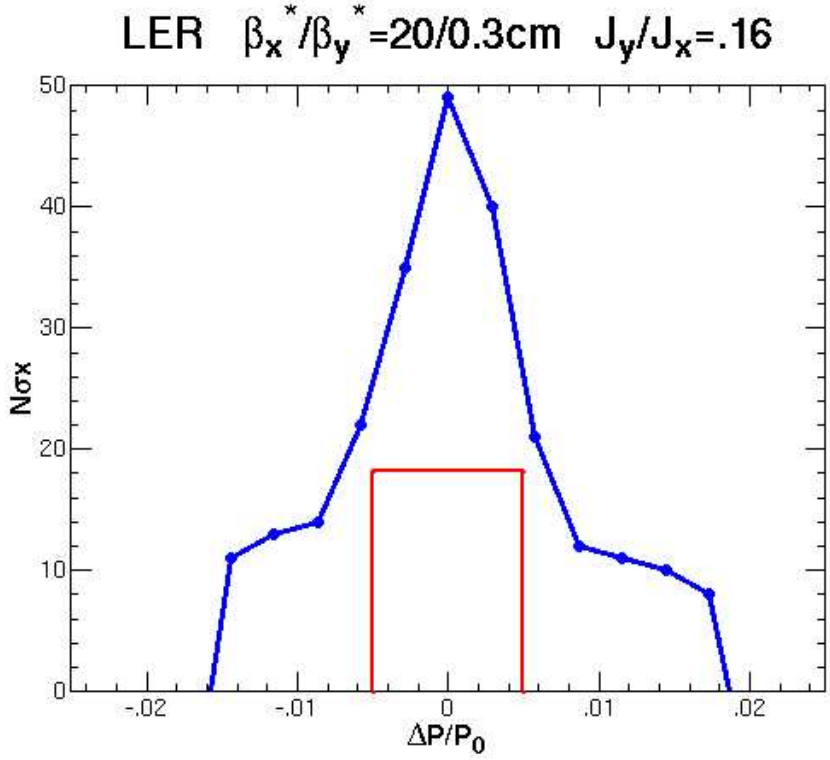

Figure 4.4: Dynamic aperture in the LER. The square region shows the aperture of the injected beam.

Chapter 5

Interaction Region

5.1 Introduction

5.1.1 Choice of basic design parameters

Prior to starting the IR design of SuperKEKB, some basic parameters were assumed, to achieve the target luminosity. In Table 5.1, we summarize the design parameters of SuperKEKB relevant to the IR design together with the achieved and design parameters [1] in the present KEKB.

		Achieved	KEKB design	SuperKEKB	Unit
Vertical beta at I.P	β_y^*	5.8∼7	10	3	mm
LER current	I_{LER}	∼1.8	2.6	9.4	A
HER current	I_{HER}	∼1.2	1.1	4.1	A
Bunch length	σ_l	∼7	5	3	mm
Half crossing angle	ϕ_{cross}	±11	±11	±15	mrad
Horizontal beta at I.P	β_x^*	∼60	33	20	cm
Emittance	ε_x^*	18∼24	18	24	nm

Table 5.1: Design parameters for SuperKEKB together with the design parameters of the present KEKB and the parameters actually achieved.

Of the parameters listed in the table, the vertical beta function at the IP, the beam currents and the bunch length are the most basic ones for SuperKEKB. We will need to make every kind of effort to realize these parameters. The crossing angle of ±15 mrad is an assumption for the IR design, which we might change during the course of the IR design. The horizontal beta function at the IP and the horizontal emittance were chosen based on beam-beam simulations to maximize the expected luminosity.

5.1.2 Issues

The assumed parameters of SuperKEKB listed above immediately lead to the issues listed in Table 5.2. Most of the design work will center around struggles with these issues, in particular the requirement of the lower beta functions at the IP, the physical aperture around the IP and the dynamic aperture. The physical aperture issue is discussed in this section. The dynamic aperture issue is described in another chapter of this report.

Through experience at the present KEKB, we expect that the detector beam background and heating of the IR components will be severe problems in designing the IR. The beam background issue is discussed elsewhere in this report. Studies on heating of the IR components have just begun.

Issues	Causes
Physical aperture around IR	Lower beta at IP
Dynamic aperture	Lower beta at IP
Detector beam background	Higher beam current
Heating of IR components	Higher beam current and short bunch length

Table 5.2: Issues in the SuperKEKB IR design and their causes.

5.1.3 IR design goals

The first task of the IR design is to work out a magnet layout and IR optics with sufficient dynamic aperture at the design values of the beta functions at the IP. The physical aperture issue is closely connected with the IR optics design. The physical aperture also has close connections with the IR magnet design and the quality of the injecting beams. Therefore, we have to concurrently pursue designs of the IR optics, the IR magnets and the injector beam quality until we find a consistent set of solutions for all of these issues.

The next step of the IR design is to do more detailed work based on this basic design, which includes more detailed IR magnet designs, estimations of the detector beam background, and work on the heating of the IR components. In this stage, the design of the vacuum system including a cooling method for the vacuum chambers will be carried out. This work also includes an estimation of HOM power and its counter-measure. More detailed engineering, such as on the mechanical supports for the magnets, solutions of spatial conflicts among components and radiation shields, etc., will also be done at this stage. Another important job at this stage is to design beam monitor systems in the IR, such as a special BPM system and a luminosity monitor.

We are now at the end of the first stage and have just started on the second stage. In this report, we describe the results of design work on the first stage.

5.2 Design fundamentals

5.2.1 Layout of IR magnets and basic optics design

A common technique for realizing lower beta functions at the IP is to put the final focus quadrupoles closer to the IP. At SuperKEKB, we will make use of this technique, as is shown below. In the present design, we tried to design the IR as a natural extension of the present KEKB as much as possible. As for the physical space between the physics detector and the accelerator components, we assume the same border as in the present KEKB. One small difference from the present KEKB case is that the crossing angle is changed from $\pm$ 11 mrad to $\pm$ 15 mrad. Due to this difference, we have to change the relationship between Belle and the accelerator, as shown in Fig. 5.1. As can be seen in the figure, the HER axis will not change and the Belle solenoid axis will not be rotated in

the SuperKEKB case. On the other hand, the LER axis will be rotated by 8 mrad. The beam pipe and SVD have a finite angle of 7 mrad with respect to the Belle solenoid axis. Of course, the QCS magnets will be placed parallel to the Belle solenoid.

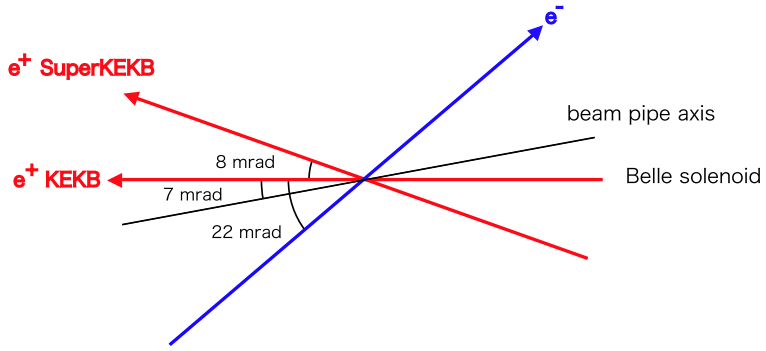

Figure 5.1: Geometrical relationship between SuperKEKB and SuperBelle.

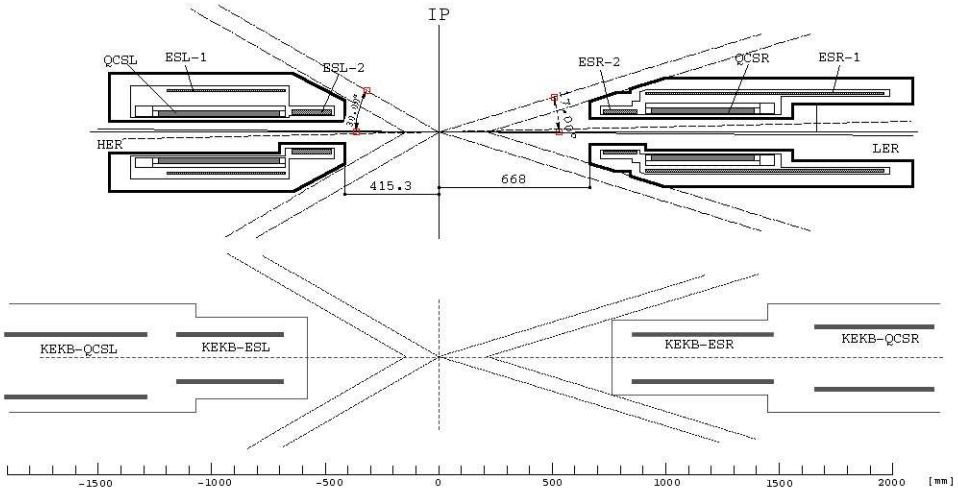

Figure 5.2: Layout of the QCS and ES magnets together with the present KEKB case.

With these restrictions, we tried to place the final-focus quadruple (QCS) magnets as close to the IP as possible. The basic method for achieving this is that the compensation solenoid (ES) magnets, which are located closer to the IP than the QCS magnets in the present KEKB, will overlap with the QCS magnets. Figure 5.2 shows a layout of the QCS and ES magnets in SuperKEKB. Also shown in the figure is that of the present KEKB. As is seen in the figure, the ES magnets are divided into two parts. While the longer parts overlap with the QCS magnets, the shorter parts are placed on the IP side of the QCS magnets. The reason why the ES magnets are divided is to reduce the electro-magnetic force acting on the ES magnets, as is discussed in the next section. Other details of the QCS design are also described in the next section. In Table 5.3, we summarize some characteristic parameters of the QCS magnets to make a comparison between SuperKEKB and the present KEKB.

Figure 5.3 shows the layout of the IR magnets. The IR optics are shown in Fig. 5.4. Details of the IR optics design are described elsewhere in this report. In the design of the

Parameters	SuperKEKB	Present KEKB	Unit
Distance from IP to QCSL	0.969	1.60	m
Distance from IP to QCSR	1.163	1.92	m
Effective length of QCSL	0.3982	0.483	m
Effective length of QCSR	0.333	0.385	m
Field Gradient of QCSL	35.4	21.66	T/m
Field Gradient of QCSR	37.2	21.73	T/m

Table 5.3: Characteristic parameters of the QCS magnets.

IR described in the following, we took this magnet layout and IR optics as given.

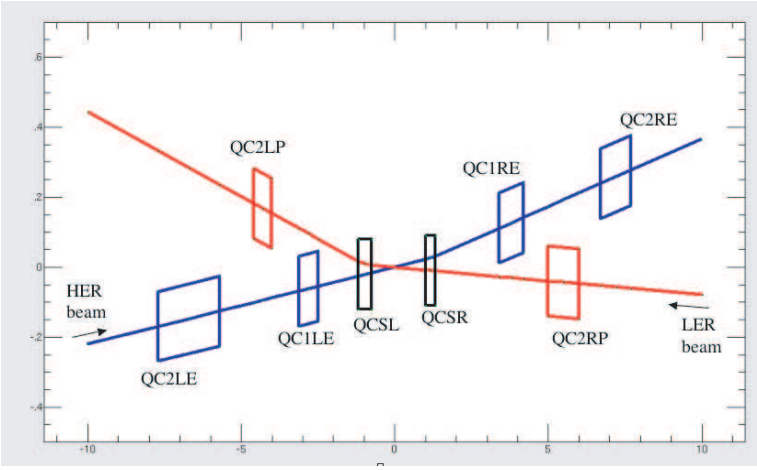

Figure 5.3: Layout of the IR magnets.

5.2.2 Issues related to physical aperture

Since the beta functions at the IP in SuperKEKB are smaller than those in the present KEKB, the physical aperture in the IR will potentially be a serious issue. To design the IR magnets (and other components), we need to know the values of the physical aperture at each component, which is needed for stable beam operation. They are determined by the beta functions at the components, and the necessary beam acceptance that is needed for beam injection. Since we can not choose the beta functions at the components freely due to several strict requirements, such as pre-determined values of the beta functions at the IP, the requirements on the physical aperture reduce to requirements on the beam acceptance. As shown below, there is some room to reduce the beam acceptance with effort. One important thing to notice is that the LER and the HER will exchange electron and positron beams after upgrade of the IR in our present strategy. This means that both rings will have to accept both beams, and that the required beam acceptance is determined by the beam which requires wider acceptance.

The linac beam emittance and the injection error are two main sources of the required acceptance. More precisely, the required acceptance is mainly determined by the linac beam emittance, Twiss parameters at the injection points, optics matching conditions between the beam transport line and the ring and also the septum thickness. Of these

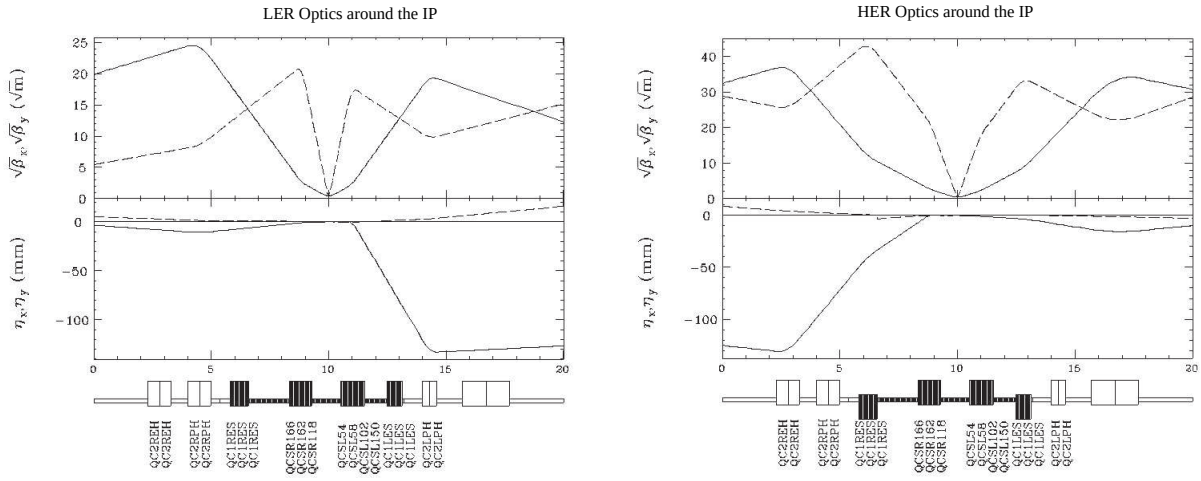

Figure 5.4: Optical functions around the I.P. The solid and dashed lines show the horizontal and vertical parameter, respectively.

parameters, the ring beta functions at the injection point can be changed relatively freely, and the linac beam emittance can be reduced if we take certain measures. We have estimated the required acceptance as a function of these parameters. The estimation method was the same as that used in the design phase of the present KEKB [2]. In this calculation, we used the parameters given in Table 5.4.

		unit
Septum thickness	6	mm
Ring emittance (ε_x)	24	nm
Linac beam emittance (ε_{xi})	150 (or free)	nm
Ring β_x	90.4 (or free)	m
N_i	2	σ_{xi}
N_s	2	σ_{xi}
N_r	3	σ_x

Table 5.4: Parameters used for the horizontal acceptance calculation. N_i denotes the number of sigmas required of injection acceptance. N_s denotes the distance from the center of the injecting beam to the septum chamber in units of σ_{xi}. N_r denotes the distance from the center of the stored beam to the chamber wall at the injection point in units of σ_x when the kicker magnets are excited.

The results of the calculations on horizontal acceptance are shown in Fig. 5.5 and 5.6. Figure 5.5 shows the required acceptance as a function of the ring beta function at the injection point. In this case, the beta function of the beam-transport line is chosen at the optimum values, such that the required acceptance is minimized. As shown in the figure, the required acceptance does not decrease very much with a higher ring beta function than about 100m. Therefore, we assumed a β_x^* of 90.4 m, which is the same value as that in the KEKB design. We have found that the required acceptance is not very sensitive to the septum thickness. It is the linac beam emittance that is most critical to the required acceptance. Figure 5.6 shows the required acceptance as a function of the linac beam emittance. In the calculation shown in Fig. 5.5, the linac beam emittance is assumed to

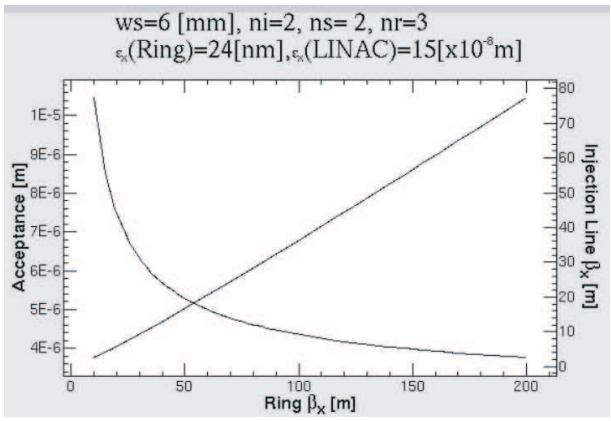

Figure 5.5: Required horizontal acceptance as a function of the ring beta function.

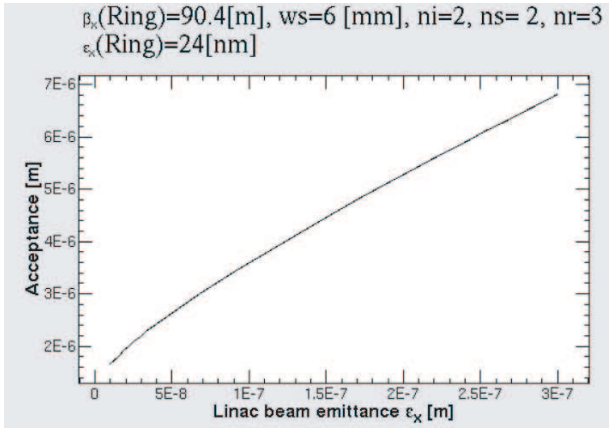

Figure 5.6: Required horizontal acceptance as a function of the injector beam emittance.

be 150 nm. This value is based on experience in the present KEKB, as explained below.

Assuming that there is no effective improvement in the linac beam emittance, the expected emittance in SuperKEKB is estimated based on experience with the present linac. In usual beam operation, typical values of the positron and electron beam emittances are 350 nm at 3.5 GeV and 20 nm at 8.0 GeV, respectively. In this case, the positron beam has a higher emittance and determines the requirements of the beam acceptance in both rings of SuperKEKB. Considering adiabatic damping, the expected emittance of the positron beam at 8 GeV is about 150 nm, which we used in the above calculation. With these emittance values, the required beam acceptances at SuperKEKB were estimated. The results are listed in Table 5.5. In this table, we break out separately the contribution of the (horizontal) injection error, which means the area of the ellipse in the phase space depicted by the center of the injected beam, while the required acceptance contains both the contributions from the injection error and the linac beam emittance. Table 5.5 includes calculations of the vertical acceptance. The calculation method for the vertical direction is similar to that in the horizontal direction, except that there is no injection error in the vertical direction.

Based on the required beam acceptance given in Table 5.5, the design of the IR magnets was carried out. However, we could not find a realistic solution, particularly for the IR special magnets, such as the QC1 magnets. This has motivated us to construct a damping

	LER	HER	Unit
Linac beam emittance (Horizontal)	3.5	1.5	10^{-7} m
Linac beam emittance (Vertical)	3.0	1.3	10^{-7} m
Required acceptance (Horizontal)	7.5	4.5	10^{-6} m
Injection Error (Horizontal)	3.4	2.4	10^{-6} m
Required acceptance (Vertical)	1.2	0.52	10^{-6} m

Table 5.5: Required ring acceptance without effective improvements to the linac beam emittance.

ring for the positron beam. Such a damping ring is also useful to transport the positron beam through the C-band structures in the linac. Based on the assumption that we will construct a damping ring for the positron beam, the required beam acceptance of the rings in SuperKEKB is now determined by the electron beam. The calculation of the required beam acceptance in this case is given in Table 5.6. One should note that the contribution from the injection error is not very small compared with the (total) required acceptance. This means that we do not have a strong motivation to construct a damping ring for the electron beam from the viewpoint of reducing the required acceptance. The IR magnet design described in the next section has been carried out based on the parameters given in Table 5.6.

	LER	HER	Unit
Linac beam emittance (Horizontal)	4.6	2.0	10^{-8} m
Linac beam emittance (Vertical)	4.6	2.0	10^{-8} m
Required acceptance (Horizontal)	2.6	1.9	10^{-6} m
Injection Error (Horizontal)	1.8	1.5	10^{-6} m
Required acceptance (Vertical)	1.8	0.80	10^{-7} m

Table 5.6: Required ring acceptance determined by the electron beam (assuming a damping ring is constructed for the positron beam).

5.2.3 Issues related to SR from QCS magnets

In designing the IR magnets, one of the critical points is how to avoid heating due to synchrotron radiation (SR) from the QCS magnets. To study this issue, we have to know the path of the SR. Basically this can be done by using an assumed layout of the IR magnets and beam trajectories calculated while assuming the beam optics. In addition to this estimation, we have to take the effects of closed orbit distortions (COD) and the divergence of the SR arising from the beam emittance into consideration. When we study the latter contribution, it is critically important to consider the effects of the dynamic beta and the dynamic emittance effect from the beam-beam effects. In this subsection, we describe some details of these effects.

Regarding the effects of COD, we estimated them based on experiences in the present KEKB. There are three major sources of COD change: drifts of the orbits for various reasons; iBump tuning; and other artificial bumps for machine tuning or for machine study. Of the 3 sources, the third one (artificial change of orbits) gives the largest contributions in the present KEKB. Taking into consideration experiences at KEKB, we assume that

the ranges of COD change at the IP in SuperKEKB are ± 0.71 mrad and ± 430 μm for the horizontal angle and the horizontal offset, respectively. Also, we assume vertical angle variations of ± 0.5 mrad and a vertical offset of ± 200 μm at the IP.

As for the effects of the beam emittance, we used 3 σ in the beam sizes. To take both of the effects of the beam size and the angular divergence into account, we considered the particle distribution in phase space. The particle distribution in phase space at the source point (QCS), transformed with a transfer matrix of the drift space (from the source point to the observation point), gives the distribution of synchrotron light at the observation point. To estimate the effects of the dynamic beta, we used a well-known analytical formula based on a simple one-turn map. As for the efects of the dynamic emittance, we used an analytical formula developed by K. Hirata et al. [3]. In case of the horizontal direction, both β_x^*/β_{x0}^* and $\varepsilon_x/\varepsilon_{x0}$ are functions of the horizontal tune (ν_x) and the nominal beam-beam parameter (ξ_{x0}). Here, β_{x0}^* and ε_{x0} are the unperturbed beta function at the IP and the horizontal emittance. In this calculation, we assumed that the fractional part of the horizontal tune is 0.51. Figure 5.7 shows the result of these calculations. As shown in the figure, the horizontal emittance increases and the horizontal beta function at the IP decreases with a higher beam-beam parameter. Assuming that ξ_{x0} amounts to 0.1 also in SuperKEKB, the horizontal emittance (ε_x) changes from 24 nm to 58 nm due to the beam-beam effect. Also the horizontal beta function at the IP shrinks from 20 cm to 4.44 cm. Due to these changes, the horizontal beam size at the IP changes but the amount of the change is relatively small, since these two effects cancel out each other to some extent. On the other hand, the angular divergence at the IP increases greatly, since these two effects additively work to enlarge it. Therefore, at the entrance of the QCS magnets, we see a large enhancement of the horizontal angular divergence (one should remember that the angular divergence is conserved in a drift space). With this large angular divergence of the beams, the divergence of the SR also becomes large. The calculation in the vertical direction can be done similarly. One should note that the analytical formula for the dynamic emittance effect is not applicable in the vertical direction, since the greatest part of the vertical emittance is created by machine errors. However, we applied the formula to the vertical direction for our present purposes, since there is no other way to estimate the effect for the time being. In any event, the effect is not as large in the vertical direction as it is in the horizontal, since the vertical tune is not as close to the half integer resonance as it is in the horizontal case. The formula gives a change of the vertical emittance from 0.18 nm to 0.23 nm, assuming that the fractional part of the vertical tune is 0.57 and ξ_{y0} is 0.1. As for the dynamic beta effect, we can use the analytical formula also in the vertical direction. Due to the beam-beam effect, the vertical beta function shrinks from 3 mm to 1.7 mm with the tune and the nominal beam-beam parameters mentioned above.

With the parameters estimated above, the divergence of the SR from the QCS magnets was calculated at each IR magnet (QC1 and QC2). Table 5.7 gives the spread of SR in the horizontal direction at the exit of the QC1 magnets. As can be seen in the table, the contributions from the emittance effect are larger than those from the COD effects. Table 5.8 shows the spread of SR in the vertical direction at the exit of the QC1 magnets.

The design of the IR magnets discussed in the next section was made while considering the SR spread calculated above. The other parameters that we need to know about the SR from the QCS magnets are the critical energy and its power. Table 5.9 shows a

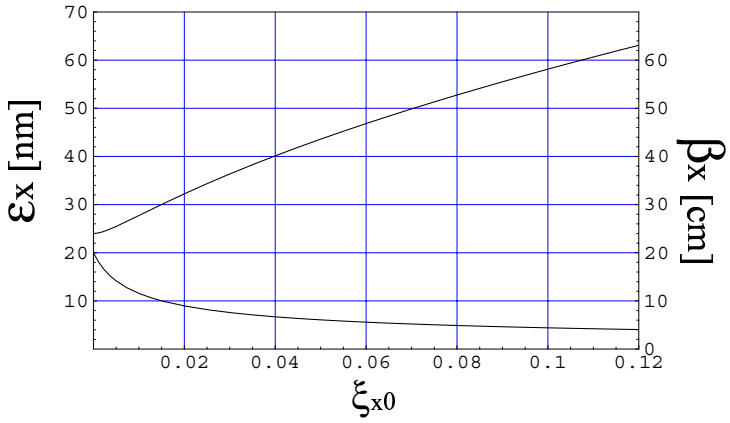

Figure 5.7: Effects of the dynamic beta and the dynamic emittance.

Source Observation	QCSRE(IP) QC1RE(Arc)	QCSRE(Arc) QC1RE(Arc)	QCSLE(IP) QC1LE(Arc)	QCSLE(Arc) QC1LE(Arc)	Unit
ε_x		58			nm
Distance	3.20	2.87	2.36	1.94	m
Δx(COD)	3.5	5.2	2.6	5.5	mm
$\Delta x(3\sigma)$	12.9	17.7	9.9	18.3	mm
Δx(total)	16.4	22.9	12.5	23.8	mm

Table 5.7: Spread of SR from the QCS magnets in the horizontal direction observed at the exit of the QC1 magnets. "IP" and "Arc" in the parentheses indicate the IP side and on the Arc side of the magnets, respectively. The horizontal emittance of 58 nm includes the dynamic emittance effect.

Source Observation	QCSRE(IP) QC1RE(Arc)	QCSRE(Arc) QC1RE(Arc)	QCSLE(IP) QC1LE(Arc)	QCSLE(Arc) QC1LE(Arc)	Unit
ε_y		0.93			nm
Distance	3.20	2.87	2.36	1.94	m
Δy(COD)	2.2	1.4	1.5	1.1	mm
$\Delta y(3\sigma)$	13.2	8.1	9.9	3.3	mm
Δy(total)	15.4	9.5	11.4	4.4	mm

Table 5.8: Spread of SR from the QCS magnets in the vertical direction observed at the exit of the QC1 magnets. "IP" and "Arc" in the parentheses mean on the IP side and on the Arc side of the magnets, respectively. As for the vertical emittance, we used the value of 0.23 nm, which includes the dynamic emittance effect, multiplied by a factor of 4, to take some beam blowup into consideration.

calculation of the critical energy of the SR. This data is needed to calculate the detector beam background. In Table 5.10, we show calculations of the power of SR. Compared with the case of KEKB, the power in SuperKEKB will increase by nearly one order of magnitude due to the higher beam currents and the higher magnetic field of the QCS magnets. How to deal with this high SR power is one of the key engineering issues in the next stage.

		QCSR	QCSL	Unit
Distance from IP to magnet center		1163.3	969.4	mm
Orbit offset at QCS magnets	Δx	34.5	29.1	mm
Field Gradient	G	37.2	35.4	T/m
Magnetic Field	B	1.28	1.03	T
Beam Energy	E_b	8.0	3.5	GeV
Critical Energy	u_c	54.7	8.40	keV

Table 5.9: Calculation of the critical energy of SR from the QCS magnets.

		QCSR	QCSL	Unit
Magnet Length		0.33	0.42	m
Orbit offset at QCS magnets	Δx	34.5	29.1	mm
Field Gradient	G	37.2	35.4	T/m
Magnetic Field	B	1.28	1.03	T
Beam Energy	E_b	8.0	3.5	GeV
Beam Current	I	4.1	9.4	A
Power	P	179	64.6	kW

Table 5.10: Calculation of the power of SR from the QCS magnets.

5.3 IR magnet design

5.3.1 Strategy of IR magnet design

With the several assumptions described in the previous section, design of the IR magnets has been achieved. For the time being, we have still several options for the magnet design. Here, we lay them out. For the QC1 magnets, there are two options: a conventional normal conducting type and a superconducting type. At present, we think that the normal conducting type has a higher priority than the superconducting, which means that we will adopt the normal conducting type if we do not find any insurmountable problems with it. As for the crossing angle, our present assumption is $\pm$15 mrad. This value is larger than that of the present machine, where we have $\pm$11 mrad. The motivation for this increase lies in mitigating the difficulties with the IR magnet design, particularly of the QC1 magnets. On the other hand, reducing the crossing angle also has some merits. For example, with a smaller crossing angle, we can reduce the SR power emitted from the QCS magnets, and also decrease the RF voltage of the crab cavity. Considering these merits, we are trying to design the IR magnets with a smaller crossing angle of $\pm$11 mrad as a backup option.

5.3.2 Superconducting magnets in the interaction region

Guidelines for the magnet design

Superconducting magnets in the interaction region are considered for the detector-solenoid field compensation magnets (ESL and ESR), the final-focus quadrupoles (QCSL and QCSR) and the special magnets (QC1L and QC1R). These magnets are designed under the following constraints:

- The boundaries between the Belle detector and the accelerator components are kept the same as that in the present KEKB.
- The final focus quadrupoles, QCS, are located as close to the interaction point, IP, as possible.
- The synchrotron light from the QCS magnets passes through the bores of the QCS and QC1 cryostats.
- The beam envelopes and orbits are defined in case of $\beta_x^* = 20$ cm, $\beta_y^* = 3$ mm. The crossing angle is 30 mrad ($\pm$ 15mrad). As a backup option, we also considered the case where the crossing angle is 22 mrad. For a crossing angle of 30 mrad, the LER beam axis at the IP has an angle of 8 mrad with respect to the Belle axis. For an angle of 22 mrad, the LER beam is on the same axis as the Belle axis.
- The QCS magnetic centers are coincident with the incoming beam centers. The magnetic axes of the ES magnets are the same as the Belle axis.

30-mrad crossing angle

The horizontal envelopes of the beams and the synchrotron light are shown in Fig. 5.8. It is calculated that the heat loads due to the synchrotron fans emitted from the QCSL and QCSR are 65 kW and 179 kW, respectively. The magnets and cryostats are designed to avoid any interference with the beam pipes, beams and synchrotron fans. The bores of the cryostats for the QCSs and QC1s are shown in Fig. 5.8. The design of the magnets and the cryostats started with these space constraints.

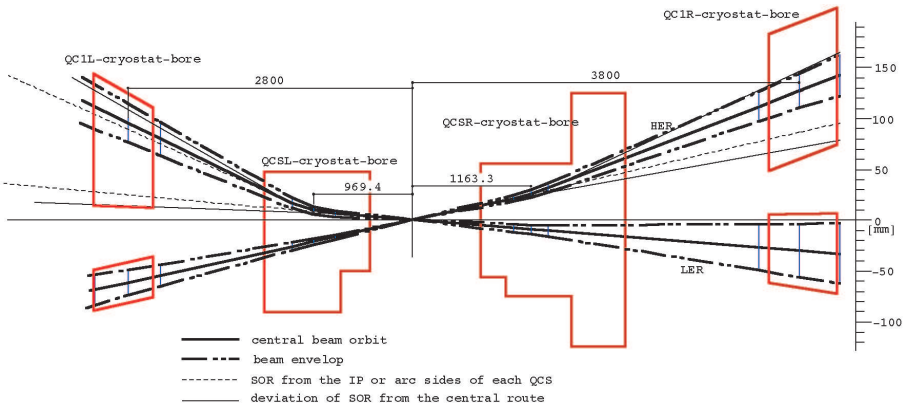

Figure 5.8: Horizontal beam envelopes and synchrotron fans for $\beta_x^* = 20$ cm and $\beta_y^* = 3$ mm.

	ESL-1	ESL-2	ESR-1	ESR-2	Unit
Central field w.o. Belle field	2.23	3.72	2.98	2.11	T
Max. field in the coil w.o. Belle field	2.59	4.14	3.00	2.45	T
I_{op}	615	615	619	619	A
I_{op}/I_c	48	63	51	47	%
Coil					
Inner radius	185	77	155	77	mm
Outer radius	194	93.9	165.2	87.2	mm
Length	519	175	1050	150	mm

Table 5.11: Design parameters of ESR and ESL

Each pair of QCS and ES magnets on the left and right sides is contained in a single cryostat. In order to locate the QCS magnet at the closest position to the IP, the ES magnet is divided into two parts. One is overlaid with the QCS magnet, and the other is placed in front of the QCS magnet as shown in Fig. 5.9.

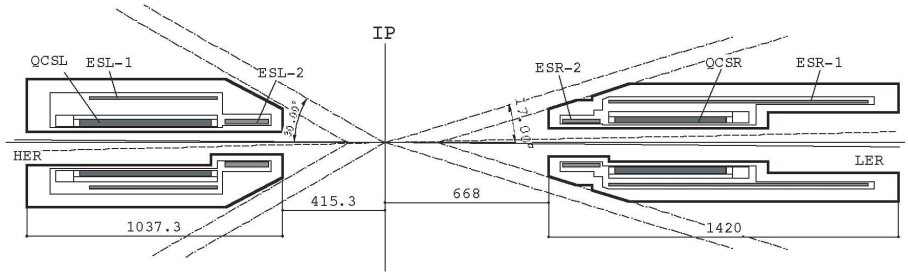

Figure 5.9: Longitudinal cross-sectional view of the magnet-cryostats.

The compensation solenoid, ES, has the function of canceling out the influence of the solenoid field of the Belle detector on both beams. For this purpose, on each side of the IP, the integrated solenoid field of the ES magnets along the Belle axis is designed to be the same absolute value as that of the Belle solenoid, but with the opposite sign. Here, one should note that cancellation is required on each side of the IP. This is because the x-y coupling at the IP may induce unwanted beam-beam blowup. The design parameters of the ES are listed in Table 5.11. The solenoid field of the ES magnets, which overlap with the QCS magnets, reduces the operating margin of each QCS magnet. Therefore, the solenoid field strength is determined to be less than 3T. According to this field configuration, the electro-magnetic forces on the ESL and the ESR are calculated to be 48 kN and 22 kN, respectively. The directions of these forces are outward from the IP. Figure 5.10 shows the solenoid field profiles on the Belle axis compared with the profile at KEKB.

The cross sections of the QCS magnet cryostats are shown in Fig. 5.11. Figure 5.11 also shows the beam envelopes at the center and the ends of the QCS effective magnetic length. The QCS magnets consist of 6 layer coils with an innermost radius of 90.0 mm. The QCS magnets on both sides have a similar cross section as shown in Fig. 5.11. Since the LER beam has an angle of 8 mrad with respect to the Belle axis and the HER beam has an angle of 22 mrad, the magnetic centers of QCSL and QCSR have horizontal offsets of 21.2 mm and 9.2 mm from the Belle axis, respectively. The design parameters of the

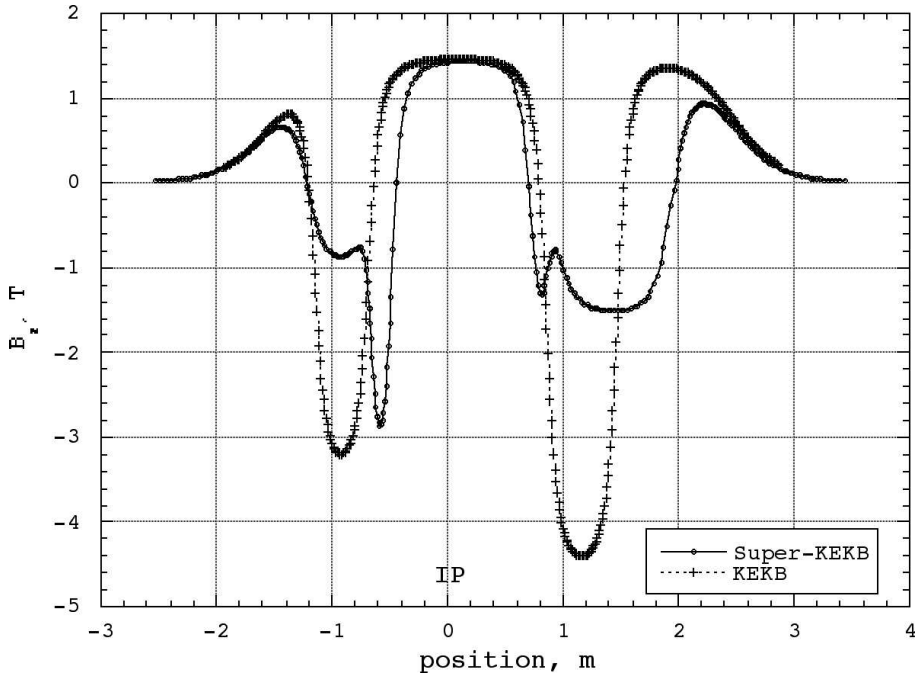

Figure 5.10: Bz profiles along the Belle axis.

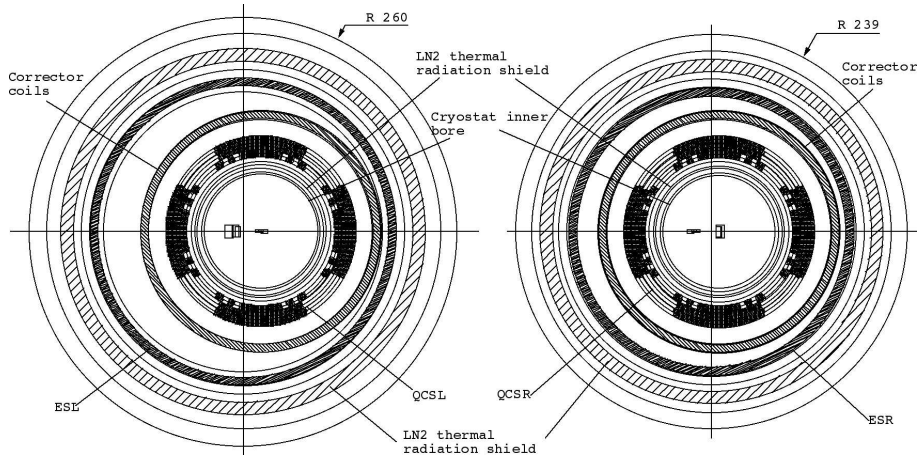

Figure 5.11: Cross sectional views of magnet-cryostats for QCS and ES magnets.

QCS are listed in Table 5.12. The QCS magnets are required to generate a field gradient of 36.0 T/m. The effective magnetic length of the QCS is 0.333 m and 0.398 m for the right and left side, respectively. The size of the superconducting cable is 1.09 mm wide by 4.08 mm high, and the conductor current at operation is 1133.7 A. The ratio of the operating current, I_{op}, to the critical current, I_c, under the Belle and ES solenoid fields is less than 70 %. This ratio is almost same as that of the KEKB-QCS magnets. Reduction of the magnet current provides an additional margin of 20 W at 4.5 K for the helium refrigerator. The multipole coefficients of this cross section are less than 1×10^{-4} at a radius of 55 mm.

		Unit	
Field Gradient	36.0	T/m	
Effective magnetic length	0.333	m	QCS-R
	0.398	m	QCS-L
I_{op}	1133.7	A	
I_{op}/I_c with Belle and ES field	< 70	%	
Max. field in the coil without Belle and ES field	3.74	T	
Coil			
Inner radius	90.0	mm	
Outer radius	116.08	mm	
Superconducting cable			
Size without electrical insulation	1.09×4.08	mm	
Strand diameter	0.59	mm	
Number of strand	24		
Field quality in the 2 dim. cross sec. @ r=55mm			
b_6	1.6×10^{-5}		
b_{10}	6.1×10^{-5}		
b_{14}	4.3×10^{-5}		

Table 5.12: Design parameters of the QCS magnet

The QC1 magnets for KEKB are of conventional type, but have some unusual characteristics: a high current density of 85A/mm^2 for QC1L and a half-quadrupole magnet for QC1R. In order to improve the field quality and to reduce the risk of burnout of the normal-conducting cable, superconducting full quadrupole QC1 magnets have been proposed for SuperKEKB. The cross sections of these magnets are shown in Fig. 5.12. Since the spatial constraints from the iron yoke and the superconducting coils between the two beam pipes are very stringent, the beam pipes serve the function of being the inner bores of the cryostat. The design parameters of the QC1 are listed in Table 5.13. The QC1L magnet consists of a single layer of superconducting coil, whose inner radius is 31 mm. The designed QC1L generates field gradients of 42.9 T/m at a current of 1319 A. The effective magnetic length of QC1L is 0.232 m. The maximum field in the magnet is 1.62 T and the leakage field at the LER beam is less than 1.5 Gauss. The superconducting cable is a solid composite of rectangular cross-section, which is the same as the cable for the ES magnets; the design current is 59% of the critical value of this cable. As shown in Fig. 5.12, additional rectangular openings are added at azimuthal positions of 90, 180 and 270 degrees in the iron yoke to maintain the quadrupole symmetry. The QC1R magnet

has a larger bore than the QC1L because the synchrotron light from QCSL must pass through this bore. Therefore, the QC1R magnet consists of two layer coils to generate a field gradient of 34 T/m with a sufficient operating margin. The required effective magnetic length from the beam optics is 0.266 m. The maximum field in the magnet is 3.28 T at the current of 1319 A. This current corresponds to 73% of the conductor critical value. The maximum leakage field at the LER beam during operation reaches 20 Gauss. This leakage field can be reduced to the same level as that from the QC1L magnet by putting a magnetic shield on the LER beam pipe.

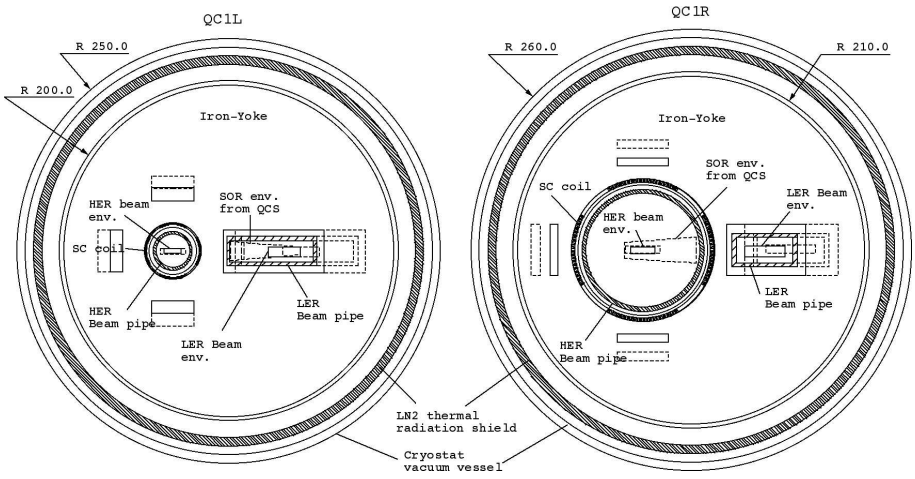

Figure 5.12: Cross-sectional views of the QC1L and QC1R magnets. The solid and broken lines show the cross sections on the IP side and the arc side, respectively.

	QC1L	QC1R	Unit
Field Gradient	42.9	34.0	T/m
Effective magnetic length	0.232	0.266	m
I_{op}	1319	1319	A
I_{op}/I_c	59	73	%
Max. field in the magnet	1.62	3.28	T
Coil	1 layer	2 layers	
Inner radius	31.0	80.0	mm
Outer radius	33.0	84.0	mm
Iron yoke			
Outer radius	200	210	mm
Leak field on LER beam	< 1.5	< 20	Gauss

Table 5.13: Design parameters of the QC1 magnets

22-mrad crossing angle (backup option)

Since these heat loads due to synchrotron light from the QCS are quite high, we investigate the possibility of a smaller crossing angle to reduce this load. Figure 5.13 shows the horizontal beam envelopes and the aperture for the synchrotron light in the case of a

crossing angle of 22 mrad. As the crossing angle decreases from 30 mrad to 22 mrad, the cryostat bores of the QCSR and the QCSL have a greater spatial margin for the beam pipes. However, since the distance between the two beams at the centers of the both QC1 magnets is reduced from 157 mm to 115 mm, designing the magnets becomes more difficult. In the following, the design of the QC1 magnets is described.

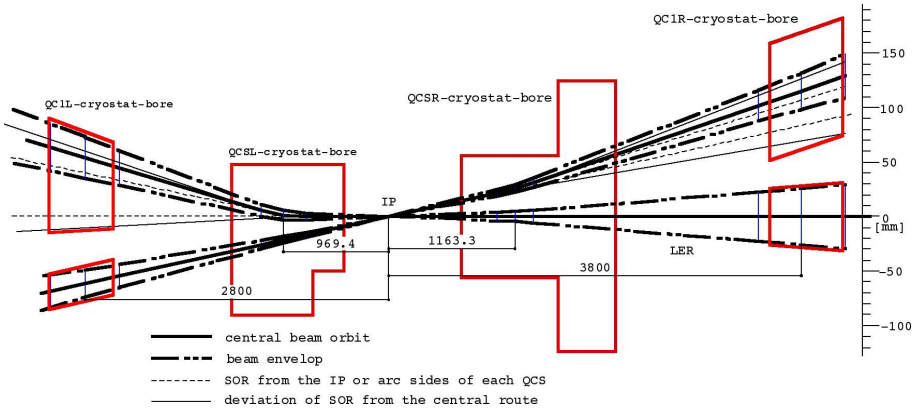

Figure 5.13: Horizontal beam envelops and synchrotron light for a crossing angle of 22 mrad.

Figure 5.14 shows the cross sections of the QC1 magnets designed for a crossing angle of 22 mrad. The parameters of the superconducting coils are the same as those designed for a 30 mrad crossing angle. By changing the crossing angle from 30 mrad to 22 mrad, the thickness of the iron yoke between the coil and the LER beam pipe at the magnet center is reduced from 25.4 mm to 9.8 mm for the QC1R and from 32.3 mm to 10.5 mm for the QC1L, respectively. The reduction of the thickness increases the leak field at the LER beam position. In particular, for the QC1R magnet at a field gradient of 34 T/m, it is calculated that the leak field becomes 30 Gauss at the magnet center. This leak field would disturb the beam optics in the interaction region. In order to reduce the leak field, we have considered using iron as the beam-pipe material. In that case, it is estimated that the maximum leak field would be less than 2.5 Gauss. However, in order to use iron, we need to employ the vapour deposition of copper inside the beam pipe. This method has already been used for the ARES cavities of KEKB. Thus, the superconducting QC1 magnets for the crossing angle of 22 mrad are practical. Further R&D is necessary on the cryostat components and 3-dimensional field calculations.

5.3.3 IR Special quadrupole magnets

A schematic view of the beam line near the IP is shown in Fig. 5.15. Normal conducting, specially shaped quadrupole magnets are required in the region where the beam separation is very small. Four magnets (QC1LE, QC1RE, QC2LE, QC2RE) are for the HER and two (QC2LP, QC2RP) are for the LER. The vertical focusing strength is tuned to the 3.5 GeV LER beam. An extra focusing field for the 8 GeV HER beam is provided by a pair of QC1LE and QC1RE magnets. The QC2LE and QC2RE magnets provide the horizontal focusing of the HER beam and QC2LP and QC2RP provide that of LER beam.

These magnets are designed to meet the following criteria:

- Due to the limited separation space the conductor thickness must be minimized.

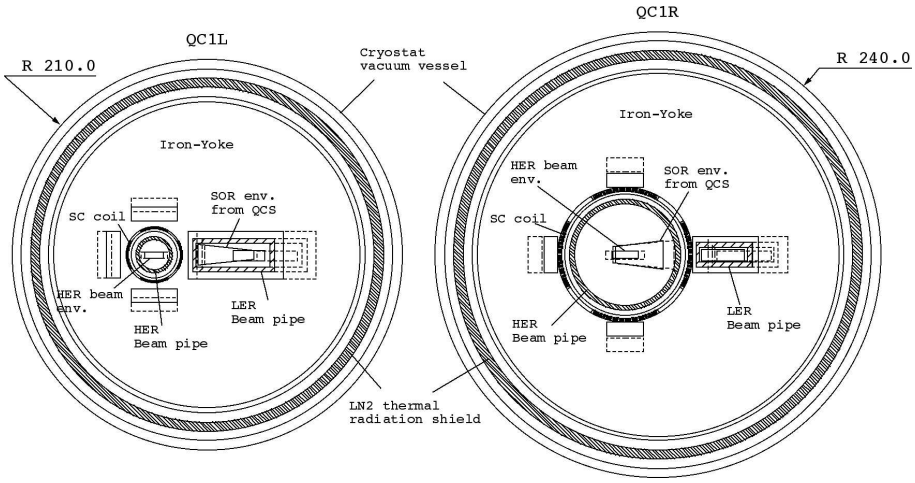

Figure 5.14: Cross-sectional views of the QC1L and QC1R magnets for a crossing angle of 22 mrad. The solid and broken lines show the cross sections on the IP side and the arc side, respectively.

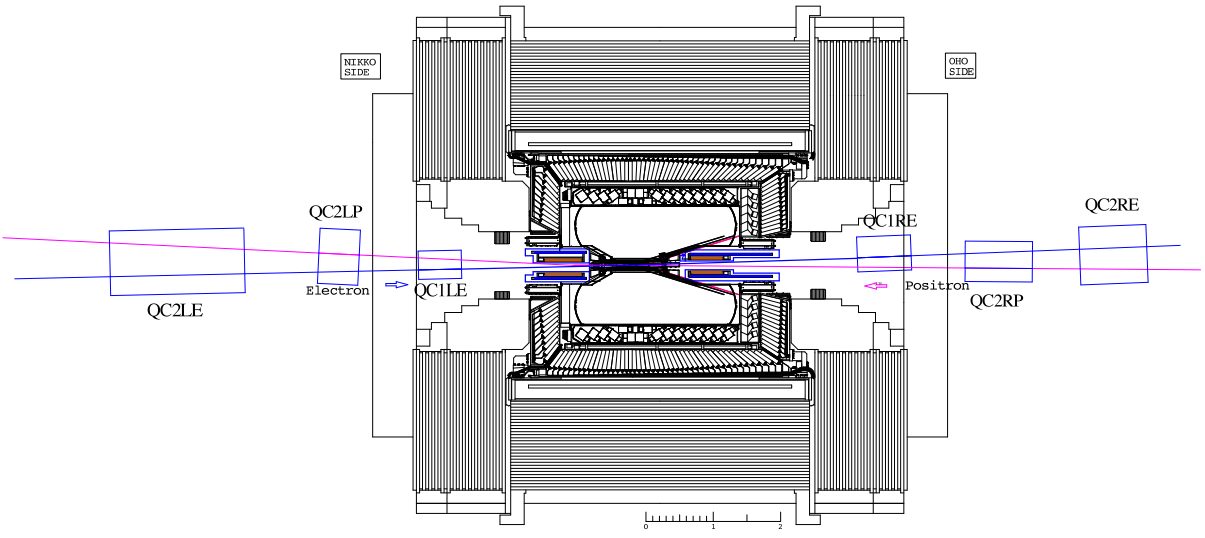

Figure 5.15: Schematic side view of the SuperKEKB IR region

- A large aperture with good field quality is required for the large beta functions. The required field quality is $\Delta(GL)/GL < \pm 1 \times 10{-}3$ in the maximum amplitudes of the injected beam for each magnet.
- The magnet must have a field-free space for the other ring's beam.

The specifications for these quadrupole magnets are listed in 5.14 and 5.15. A crossing angle of 30 mrad and a damping ring for the positron beam are assumed in the design of these magnets. The beam emittance envelopes of $\epsilon_x = 1.9 \times 10^{-6}$ and $\epsilon_y = 8.0 \times 10^{-8}$ m for the HER and $\epsilon_x = 2.6 \times 10^{-6}$ m and $\epsilon_y = 1.8 \times 10^{-7}$ m for the LER are assumed during injection.

The synchrotron radiation power of SuperKEKB would be much larger than that of KEKB. The SR from QCSR and QCSL would be 179 (27)and 65 (10) kW, respectively for SuperKEKB (KEKB). (The values in parentheses are the KEKB design parameters.) These magnets are designed to avoid direct exposure of their vacuum chambers by SR. In designing, we used the estimates for the path of SR described in the previous section.

		QC1LE	QC2LE	QC1RE	QC2RE	Unit
Field gradient		15.5	3.4	12.0	8.8	T/m
Pole length		0.64	2.0	0.75	0.8	m
Focusing		V	H	V	H	
β_x		77.5	1098	148	1329	m
β_y		1085	494	1824	674	m
Entrance aperture	H	14.7	46.7	14.3	46.6	mm
(HER)	V	9.3	6.5	11.5	7.9	mm
Exit aperture	H	10.3	38.9	20.3	50.6	mm
(HER)	V	9.1	6.8	11.9	7.3	mm
Entrance aperture	H	21.6	24.6	22.8	38.1	mm
(LER)	V	5.3	5.5	6.2	3.2	mm
Exit aperture	H	16.2	28.8	24.5	36.3	mm
(LER)	V	6.0	4.7	5.2	3.0	mm
Beam separation	Entrance	222.2	501.0	138.5	291.5	mm
Beam separation	Exit	160.4	360.7	175.6	337.8	mm
SR* size	H	25.0	63.8	32.8	62.0	mm
	V	22.8	58.2	30.8	58.2	mm
separation from SR*	Entrance	117.0	177.5	34.6	85.9	mm
separation from SR*	Exit	102.5	240.2	47.0	101.4	mm

Table 5.14: Specification of the IR special quadrupole magnets for HER. H and V denote the horizontal and vertical direction, respectively. *Size of the synchrotron radiation emitted at the IP side edge of QCSR.

All of these magnets are designed as asymmetrical full quadrupole magnets, like those of KEKB. The conductor shape of these magnets resembles that of a septum magnet. The cross-sections of these magnets are shown in Fig. 5.16. One beam passes through the quadrupole field center and the other beam goes through the field-free channel in the yoke, which is surrounded by an iron frame. This iron frame works as a mechanical support for the coil, on which various forces, such as thermal expansion and electromagnetic bursting, work during excitation. The parameters of these magnets are listed in 5.16.

		QC2LP	QC2RP	Unit
Field gradient		6.7	3.4	T/m
Pole length		0.6	1.0	m
Focusing		H	H	
β_x		366	585	m
β_y		98	75	m
Entrance aperture	H	23.0	39.2	mm
(HER)	V	8.5	9.0	mm
Exit aperture	H	28.6	28.7	mm
(HER)	V	7.9	10.6	mm
Entrance aperture	H	29.1	39.4	mm
(LER)	V	4.4	3.4	mm
Exit aperture	H	31.0	30.0	mm
(LER)	V	4.2	4.2	mm
Beam separation	Entrance	153.6	259.1	mm
Beam separation	Exit	182.6	212.8	mm
SR size *	H	37.5	47.8	mm
	V	34.2	44.9	mm
separation from SR*	Entrance	140.3	186.0	mm
separation from SR*	Exit	117.0	155.2	mm

Table 5.15: Specification of the IR special quadrupole magnets for LER. H and V denote the horizontal and vertical direction, respectively. *Size of the synchrotron radiation emitted at the IP side's edge of QCSL.

	QC1LE	QC2LE	QC1RE	QC2RE	QC2LP	QC2RP	Unit
Field gradient	15.5	3.4	12.0	8.8	6.7	3.4	T/m
Pole length	0.64	2.0	0.75	0.8	0.6	1.0	m
Bore radius	25	50	48	90	80	40	mm
Current	3920	3400	11050	28400	17100	1980	AT
Coil turns	3	8	3	16	15	3	/pole
Current density of septum conductor	30	10	70	24	31	15	A/mm^2
Leakage field	-0.65∼0	-0.4∼0	-1.1∼0	-0.35∼0	-0.85∼0	-0.35∼0	Gauss

Table 5.16: Parameters of special quadrupole magnets.

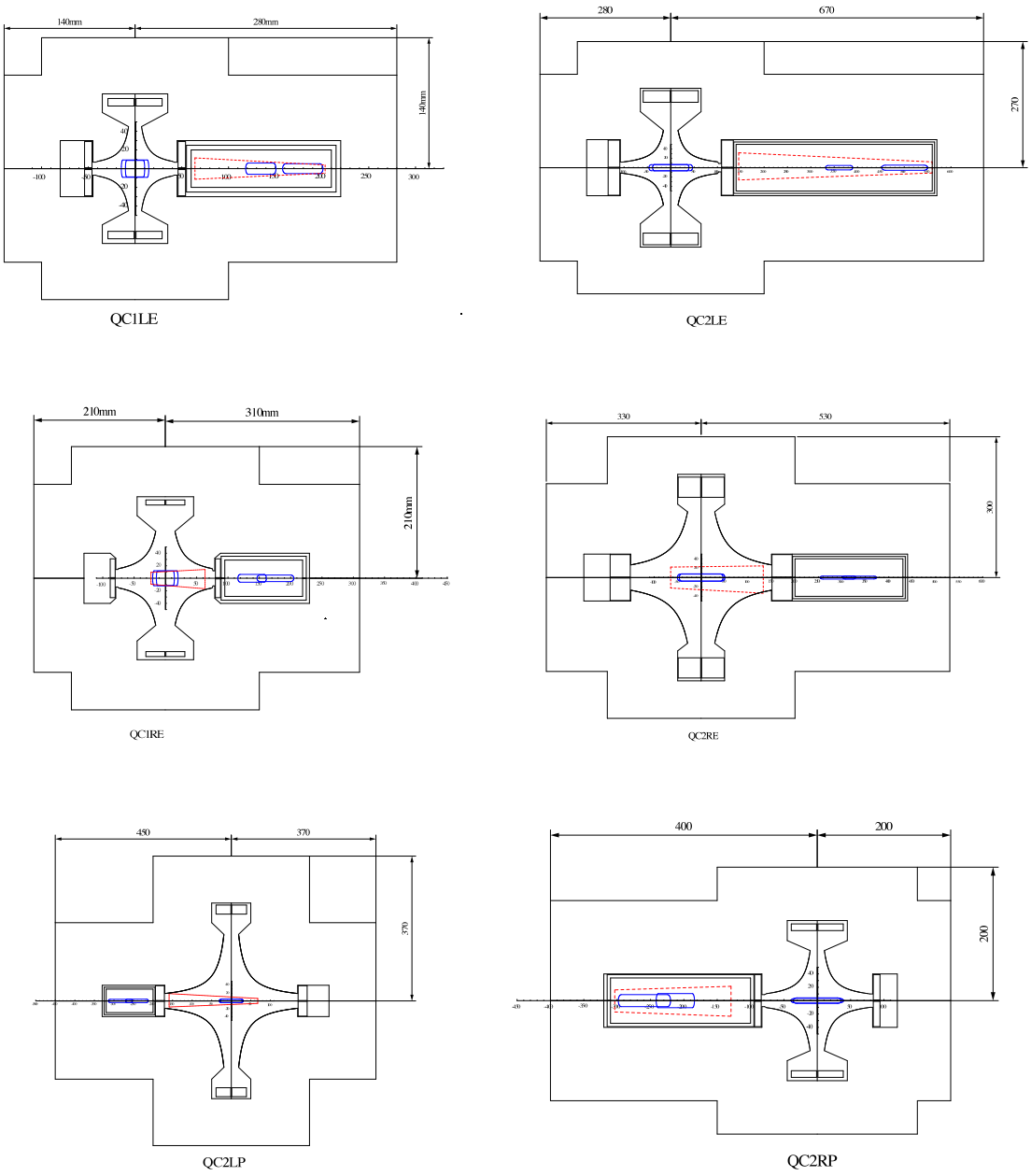

Figure 5.16: Cross-section view of the IR special quadrupole magnets and the beam positions and beam envelop during the injection time at the edge of each magnets. The SR size is also indicated by the red dashed line.

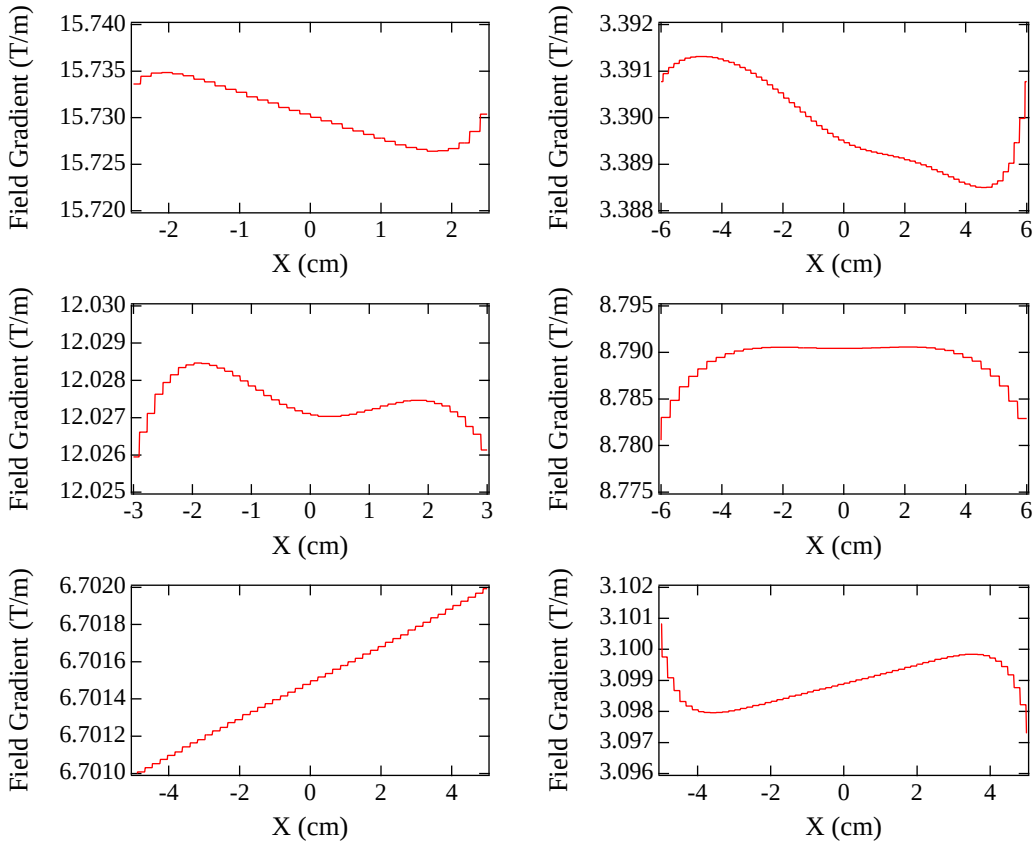

Figure 5.17: Calculated distribution of the field gradient of the special quadrupole magnets.

Because of the lack of quadrupole symmetry of the iron yoke and the truncation of the hyperbolic contour of the poles, the magnetic fields of these magnets are likely to have unnecessary multipole components, which may reduce the dynamic aperture. To reduce these multipole components, the shape of the pole face shim was optimized using the computer code OPERA-2d [4]. Figure 5.17 shows the calculated distributions of the field gradient of the special quadrupole magnets. In two-dimensional calculations, the requirements for these magnets were satisfied.

These magnets have very high current densities and a high water flow rate. An interlock system for the magnet's hollow conductor to prevent the magnets from burning out and an oxygen removal system for the cooling water will be necessary. Since the longitudinal position of QC1 will be about 50 cm closer to the IP, the space between QC1 and the Belle end yoke will be very tight as shown in Fig. 5.18. In addition, the magnetic leakage field from the Belle solenoid will increase to about 600 Gauss. The leakage fields create an undesired skew octupole field component at the fringe of these magnets, which may degrade the dynamic aperture. This issue should be studied further in the future.

5.4 Summary and future prospects

As mentioned at the beginning of this chapter, we are at the end of the first stage of the IR design. We now have a consistent design of the IR magnet layout, the IR optics and

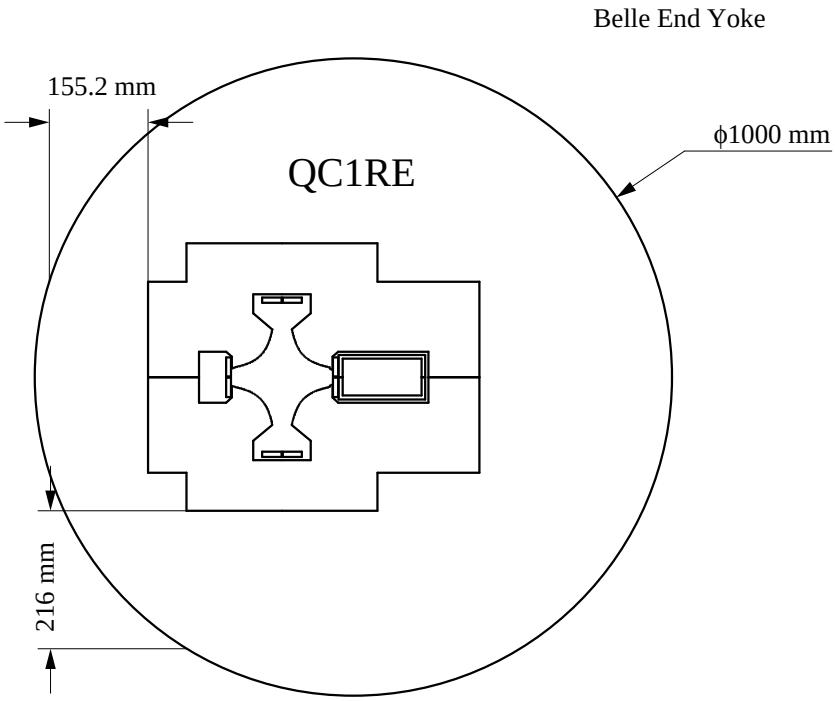

Figure 5.18: Schematic cross-section views of the QC1RE magnet and Belle End Yoke

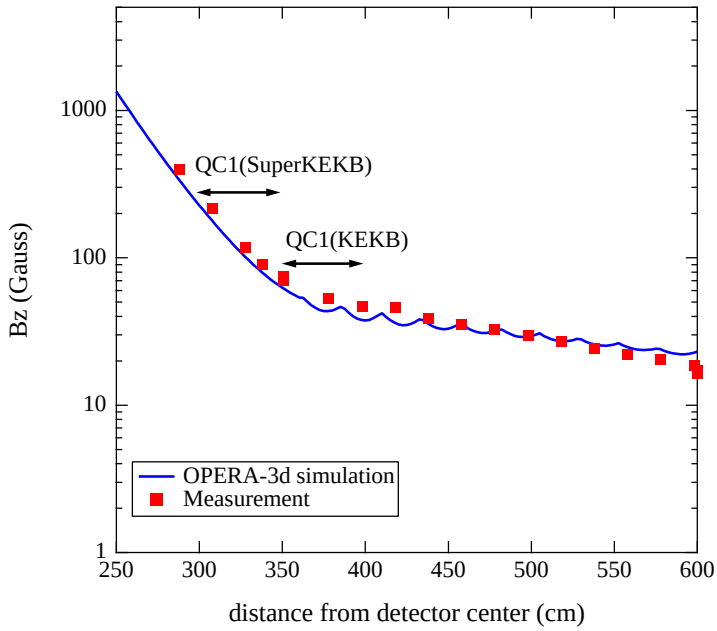

Figure 5.19: Distribution of the axial magnetic field, Bz, along the axis of the belle solenoid field.

realistic IR magnet designs, which provide sufficient physical and dynamic aperture. One important note is that we need to construct a positron damping ring to ensure a sufficient physical aperture. Issues of dynamic aperture are described elsewhere in this document. We feel that the feasibility of the SuperKEKB IR has been confirmed through the designs described in this chapter. During the course of the design work, we found some possible problems, such as how to handle a very high power of SR from the QCS magnets and the issue of a leakage field from the Belle solenoid to the QC1 magnets. These issues will be considered shortly.

After that, we will undertake design work at the second stage where we have to study the detector beam background and the design of the IP beam pipe with the present IR design, 3D designs of the IR magnets, heating of the IR components, the design of the vacuum system including a cooling method for the vacuum chambers, an estimation of the HOM power and its counter-measures, more detailed engineering work, such as on the mechanical supports for the magnets, solutions of spatial conflicts among components and the design of beam monitor systems in the IR, such as a special BPM system and a luminosity monitor.

Bibliography

[1] KEKB B-Factory Design Report, KEK Report 95-7, June 1995.

[2] M. Kikuchi, in private communications.

[3] K. Hirata and F. Ruggiero, LEP Note 611, August 1988.

[4] OPERA-2d, Vector Fields Limited, Oxford, England.

Chapter 6

Magnet System

The magnets from KEKB will be re-used, with some slight modifications, for the upgrade to SuperKEKB. The current specifications and performance of the conventional magnets can be found in the KEKB construction report [1]; however, some modifications and additional magnets are needed due the upgrade of the vacuum system and installation of crab cavities. The upgrades of the final-focusing quadrupole magnets and the special quadrupole magnets are described in the section on the interaction region. A summary of new magnets to be fabricated is given in Table 6.1.

Magnet	Number	Location
HER-Qscc (quads with big bore radius)	19+1(spare)	Nikko
LER-Qrf	2	Oho
Stronger HER-SxD mag.	49	Arc section
Wide gap vertical steering magnets	∼450	Arc and Tsukuba

Table 6.1: Fabrication of new magnets

6.1 Installation of crab cavities

To accommodate the installation of crab cavities in the Nikko straight section, four horizontal steering magnets will be added in the LER weak bend regions in that area. The weak bend regions are located at the edge of the arc sections where they meet the Nikko straight section. Two of the additional steering magnets will be installed in the upstream (right-hand side) weak bend region, and the other two in the downstream (left-hand side) region.

In the HER, six new magnet power supplies need to be installed and two power supplies require modifications. Five of the six new supplies are 30-kW, single-magnet supplies, while the sixth one powers two magnets with up to 60 kW. Two power supplies, that are currently supplying power to five or six magnets each, will be reassigned to power only two magnets each.

6.2 Replacement of beam-pipe chamber

In order to replace the beam-pipe chambers, the upper halves of the quadrupole, skew-quadrupole (skew-Q), and sextupole magnets are first removed. The horizontal steering magnets are also removed. The positions of the coil support spacers for the bending magnets must be adjusted to accommodate the new beam-pipe chambers, which have wider width than the present chambers. In the case of the wiggler magnets, the spacers that are installed between the upper and lower magnetic poles are to be replaced with smaller width spacers. Then the beam chambers are to be replaced with the new design incorporating an ante-chamber, and the magnets are to be re-assembled.

6.3 Installation of ARES RF cavities

ARES RF cavities are installed in the Oho straight section to handle the design beam current in the LER. In order to accommodate these RF cavities, six quadrupole magnets will be replaced by Qrf-magnets with a larger bore radius. Four Qrf-magnets, which we have already kept as spares at KEKB, can be installed in the Oho section. However, two Qrf-magnets need to be fabricated.

6.4 Replacement of beam-pipe chamber in Nikko section

Replacement of beam-pipe chambers with chambers of larger diameter is planned in the Nikko straight section in the HER to reduce the HOM wake fields induced by the beam, because the superconducting RF cavities (SCC) are sensitive to HOM wake fields. To enable this, 19 quadrupole magnets have to be replaced by quadrupole magnets (Qscc) with a larger bore diameter of 240 mm. These Qscc-magnets are to be newly fabricated.

6.5 Rearrangement of magnet positions in the Tsukuba section

A rearrangement of magnet positions in the Tsukuba straight section is planned. There are 29 dipole magnets, 50 quadrupole magnets, 4 sextupole magnets, and 20 skew-Q magnets. Besides these main magnets, there are 50 vertical and 55 horizontal steering magnets. Those magnets will be rearranged as follows:

1. Upper parts of quadrupole, sextupole and skew-Q magnets removed.
2. Beam chambers removed.
3. Upper parts of quadrupole, sextupole and skew-Q magnets re-installed.
4. Magnets removed from their current locations.
5. New position monuments installed on the tunnel floor.

6. Positions for these new monuments surveyed, and their coordinates established.
7. Base plates for the magnets removed.
8. New base plates installed to new positions.
9. Magnets installed on the new base plates.
10. Alignment of the magnets performed.
11. Upper parts of quadrupole, sextupole and skew-Q magnets again removed.
12. New beam chambers installed.
13. Upper parts of the quadrupole, sextupole and skew-Q magnets again re-installed.

6.6 Replacement of HER sextupole magnets

In order to extend the tuning range for HER chromaticity correction, HER D-type sextupole magnets are planned to be replaced by new sextupole magnets that have stronger magnetic fields. The 53 HER-SxD sextupole magnets (including one spare) will be newly fabricated. The magnetic fields will be measured before the magnets are installed in the arc section.

6.7 Energy exchange

"Energy exchange" means that the electron energy changes to 3.5 GeV from 8 GeV and the positron energy changes to 8 GeV from 3.5 GeV. The polarities of the magnets in the LER and the HER have to be reversed as part of the energy exchange. Changing the polarities will be done by exchanging the cable connections at the power supplies. In the case of the superconducting final quadrupole magnets at the IR, the polarity will be changed by exchanging cable connections to the current lead at the local sub-cooler located on the basement floor in the Tsukuba experimental hall.

6.8 Additional equipment

Installation of dipole magnets for HER local chromaticity correction

Installation of dipole magnets in the Tsukuba straight section in the HER is under consideration in order to enable local chromaticity correction, as is performed in the LER. For this purpose, 26 dipole magnets have to be newly fabricated and installed.

Remote control of chicane magnet positions

Four sets of dipole magnets (chicane magnets) are to be placed in the Oho and Nikko straight sections in order to adjust the orbit length in the LER. Each set consists of four dipole magnets. When the excitations of the wiggler magnets are changed, the positions of these magnets have to be changed manually. It currently takes about three

days. If the movement of the magnets can be done remotely, this time can be saved and this procedure should improve beam operation. Magnet movers and movable vacuum chambers are needed to make this possible.

Bibliography

[1] K. Egawa et al., "Magnet system for the KEKB main ring", Nucl. Inst. & Meth. in Phys. Research A 499 (2003).
"KEKB Accelerator Papers", KEK Preprint 2001-157, December 2001.

Chapter 7

Impedance and Collective Effects

7.1 Resistive wall instability

The growth rate of the resistive wall instability is given as

$$g = \frac{cI}{4\pi\nu_\beta E}\sum_{p=-\infty}^{\infty} ReZ((pM+\mu+N_\beta)\omega_0+\delta\nu_\beta\omega_0), \tag{7.1}$$

where E is the beam energy, ν_β is the betatron tune, N_β is the integer part of the betatron tune, I is the total beam current, $\delta\nu_\beta$ is the fractional part of the betatron tune, ω_0 is the angular revolution frequency, μ is the mode number of the instability, M is the number of bunches and c is the speed of light. ReZ is the real part of the resistive wall impedance, written as

$$ReZ = sign(\omega)\frac{Z_0\cdot R}{b^3}\cdot\delta, \tag{7.2}$$

$$\delta = \sqrt{\frac{2c}{Z_0\sigma \mid \omega \mid}}, \tag{7.3}$$

where Z_0 is the impedance of the vacuum (=377 Ω), R is the average radius of the ring and σ is the conductivity of the wall material. In Eq. (7.1) a round beam pipe and a uniform beam fill with equally spaced bunches are assumed. For $M = 5120$ and the design beam current, the calculated growth rates are given in Table 7.1. For the HER, where the cross section of the chamber is 98(H)×50(V) mm, a chamber radius of 25 mm was used. Since all growth rates given in Table 7.1 are smaller than the damping rate of the bunch-by-bunch feedback system, which is expected to be 5000 s^{-1}, the instability can be suppressed by the bunch-by-bunch feedback system.

	LER	HER	Unit
Horizontal	843	959	s^{-1}
Vertical	919	1096	s^{-1}

Table 7.1: Growth rate of the resistive wall instability.

7.2 Closed orbit instability

Recently, it has been pointed out that a closed orbit may experience an unstable drift due to a long-range resistive wake [1]. The threshold intensity of the closed-orbit instability is given as

$$N_{th} = \frac{2\pi^2 b^2 \gamma \nu_\beta \delta\nu_\beta}{r_e \Pi g}, \tag{7.4}$$

where γ is the Lorentz factor, r_e is the classical electron radius, Π is the circumference of the ring, g is the material factor, which is 1 for an ideal magnetic material outside. From Eq. (7.4) the threshold currents are calculated to be 12.3 A and 12.2 A for the LER and the HER, respectively. The threshold currents are both above the design currents.

7.3 Electron-cloud instability in the positron ring

Electron clouds produced by synchrotron light and/or beam-induced multipacting causes single-bunch and coupled-bunch instabilities. This electron-cloud effect, especially a beam blowup caused by the single-bunch instability, is one of the most important issues faced at existing B factories. Beam blowup is suppressed to some extent by a weak solenoid field of several tens of Gauss, which is applied along the vacuum chamber. In SuperKEKB, ante-chambers will be employed to alleviate heat load from the beam. Ante-chambers will also be effective to reduce the creation of primary photo-electrons. Since the buildup of an electron cloud is a very complicated process, it has been studied mainly by numerical simulations. To evaluate the electron cloud at SuperKEKB, we performed a simulation of the cloud buildup by a program named CLOUDLAND, developed by L. F. Wang [2]. Table 7.2 gives the parameters used in the simulation. We assumed that a positron beam is stored in the HER, and that the primary electrons are generated uniformly around the chamber wall, assuming that the ante-chambers work well to absorb photons. Since we have no reliable way to estimate how many electrons are produced on the chamber wall, we provisionally assumed that the number of primary electrons is 1% of the number of photons that are emitted by synchrotron radiation. Table 7.3 gives the simulated average electron density and the electron density at the center of the chamber at various locations in the ring. Figure 7.1 shows the electron distribution in various magnets. The results are summarized as follows:

1. A solenoid field of 60 G is very effective for reducing the electron density at the center of a chamber,

2. A substantial electron cloud remains inside bending and quadrupole magnets.

One theory [3] shows that the condition for a strong head-tail instability to occur is

$$\int \rho \cdot ds > \frac{2\gamma\nu_s}{\pi r_e \beta_y}, \tag{7.5}$$

where ρ is the cloud density near the beam, s is the obit length, ν_s is the synchrotron tune, and β_y is the average vertical beta function. The right-hand side of Eq. (7.5) is 4.5×10^{15} m^{-2} in the case of SuperKEKB. Using ρ's from Table 7.3, $\int \rho \cdot ds$ was calculated to be

0.6×10^{15} m^{-2}, which is below the threshold value of the instability. In the simulation, several uncertain assumptions about the distribution of the electrons on the chamber wall and the amount of primary electrons were used. Also, the behavior of the electron cloud inside the magnets has not been studied experimentally. Further experimental and simulation studies are necessary to obtain a more reliable estimation. Because the simulation shows that solenoids are very effective at sweeping electrons out of the beam path, the vacuum chambers in the drift spaces of SuperKEKB will be covered by solenoid windings. Table 7.4 gives tentative parameters of the solenoid system. The solenoids will be installed both in the LER and in the HER, because the positron beam will be stored in the LER in the early stages of operation, and then stored in the HER after the LINAC upgrade.

		Unit
Beam energy	8	GeV
Bunch spacing	2	ns
Number of particles in a bunch	5.2×10^{10}	
Chamber radius	37	mm
Maximum secondary emission yield	1.5	
Energy of maximum secondary yield	250	eV
Number of bunches	200	
Number of train	1	
Primary electron yield	0.01	
rms bunch length	3	mm
Horizontal emittance	2.4×10^{-8}	m
Vertical emittance	4.8×10^{-10}	m
Average horizontal beta function	10	m
Average vertical beta function	10	m

Table 7.2: Parameters used in the simulation of the electron-cloud buildup.

	Field strength	average (10^{12} m^{-3})	at pipe center (10^{12} m^{-3})
Drift space		1.0	-
Bending magnet	0.25 (T)	20.0	0.6
Quadrupole magnet	10.3 (T/m)	8.4	0.46
Solenoid	60 (G)	0.61	0.0

Table 7.3: Average electron volume density and electron volume density at a pipe center in various magnetic fields.

7.4 Ion instability in the electron ring

In SuperKEKB the electron beam will be stored in the LER, after a LINAC upgrade. Compared with KEKB, where the electron beam is stored in the HER, the beam energy

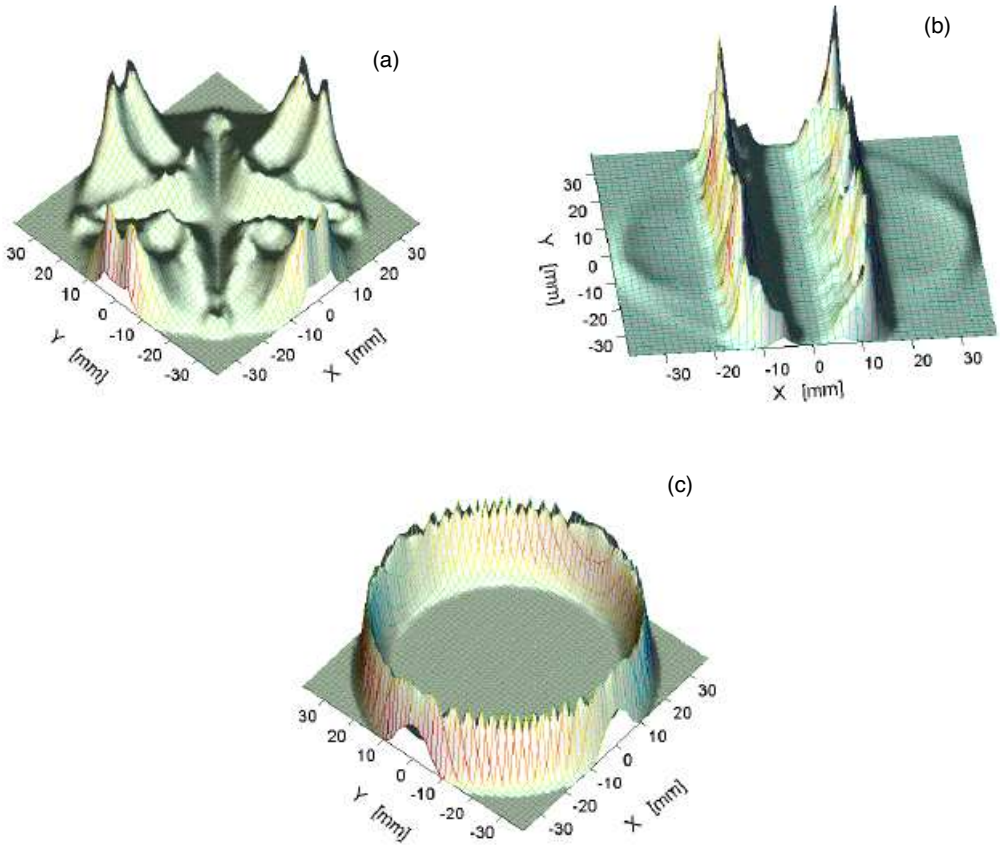

Figure 7.1: Distribution of electrons inside magnets: a) qadrupole; b) dipole; and c) solenoid.

	LER	HER	Unit
Field strength	60		G
Current	3.8		A
Diameter of wire	1.6		mm
Layers of winding	2		
Total length of solenoid	2470	1850	m
Total turns of winding	309	231	10^4
Resistance of wire	13.1	9.1	kΩ
Dissipated power	189	131	kW

Table 7.4: Main parameters of the solenoid system.

is reduced from 8 to 3.5 GeV and a large beam current of 9.4 A is stored in the LER at SuperKEKB. The ion instability would be strong enough to degrade the luminosity. Fig. 7.2 shows the result of a simulation [4] of this instability. In this simulation, the bunch was assumed to be Gaussian and the ions are treated as macro-particles. The parameters for the simulation are listed in Table 7.5. The result shows that the amplitude grows rapidly up to about the vertical beam size, then almost saturates. In the region of rapid growth, the growth time is less than 10 turns for a vacuum pressure of 10^{-7} Pa, which is five-times smaller than the design value of the vacuum system. The growth time is much larger than the damping time of the bunch-by-bunch feedback system, which is expected to be 20 turns. In the saturation region, the growth time is 560 turns, which is well above the damping time of the feedback system. The ion instability may not cause a beam loss because the growth time in the saturation region is smaller than the damping time of the feedback system. However, this may cause a dipole oscillation whose amplitude is on the order of the beam size, and may lead to a loss of luminosity. Thus, the ion instability would be an issue for SuperKEKB. As shown in Fig. 7.2, if the electron beam is stored in the HER, the growth time is 50 turns in the rapid-growth region, which is larger than the damping time of the feedback system. Electron storage in the HER is preferable to that in the LER from the viewpoint of ion instability.

	LER	HER	Unit
Beam energy	3.5	8	GeV
Bunch spacing	2		ns
Number of particles in a bunch	11.7×10^{10}	5.1×10^{10}	
Number of bunches	5000		
Number of train	1		
Vacuum pressure	1×10^{-7}		Pa
rms bunch length	3		mm
Horizontal emittance	2.4×10^{-8}		m
Vertical emittance(m)	4.8×10^{-10}		m
Ion	CO^+		

Table 7.5: Parameters used in the simulation of the ion instability.

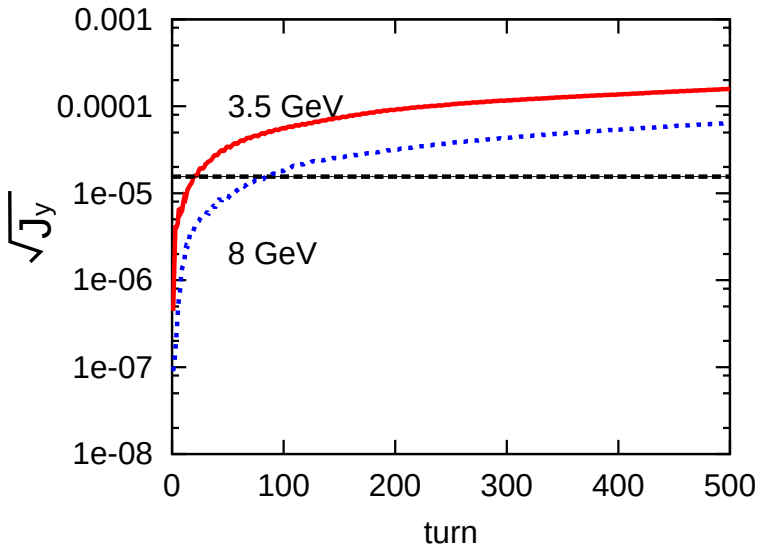

Figure 7.2: Vertical growth of the ion instability. The blue dotted line and red solid line show the evolution of $\sqrt{J_y}$ ($\sqrt{m}$) for 8 and 3.5 GeV, respectively. The green dotted line shows (vertical emittance)$^{1/2}$.

7.5 Coherent synchrotron radiation

7.5.1 Introduction

Electrons traveling along curved trajectories emit synchrotron radiation. This radiation is emitted coherently when the wavelength is longer than the electron bunch length. This component is called coherent synchrotron radiation (CSR). Transverse and longitudinal forces have serious effects on the particles, such as emittance growth and an increase in the energy spread [5, 6, 7]. Recently, short bunch lengths are sought to satisfy various requirements. For example, FELs require a high peak current for a given bunch charge, ERLs often require a short duration of radiation, and B-factories and linear colliders require a short bunch to achieve higher luminosities. CSR is an important issue in the design of these accelerators.

A number of analytic and numerical studies on CSR have been performed. Analytic solutions have been found under some conditions: steady states in a vacuum [9]; steady states between parallel plates [8]; and transient states in a vacuum [10]. These analytic formulas can describe the fundamental properties of CSR. However, if transient effects become substantial and suppression by the vacuum chamber is not negligible, these analytic formulas can not be applied. Furthermore, the transverse beam size is neglected and the bunch shape has to be rigid in these formalisms. Consequently, one has to rely on numerical approaches for practical research. We present a numerical method based on a mesh calculation of the electromagnetic field in the frequency domain. We assume ultra-relativistic electron bunches as source charges, $\gamma = \infty$, where γ is the Lorentz factor. We also assume, as in [15], that the size of the chamber cross section, a, is much smaller than the radius of curvature. In general, in order to perform a proper simulation, the mesh size should be much smaller than the wavelength of the field. However, the mesh size is allowed to be larger than the radiation wavelength in our formalism because the

radiation propagating in the direction opposite that of the beam is ignored.

We begin with Maxwell's equations in a vacuum and Fourier transform them into the frequency domain. We then approximate these equations based on the assumptions described above, and solve them numerically by finite difference. The reference orbit, which gives the coordinates, is arbitrary in the vacuum chamber. The source bunch can be set to any 3D distribution around the reference orbit. The evolution term in the basic equation enables us to simulate the CSR in transient states. The cross section of the vacuum chamber can be any shape and vary along the reference orbit. With this method, we solve Maxwell's equations by using meshes with boundary conditions.

7.5.2 Theory

To derive the fundamental equations, we adopt following approximations:

(a) The size of the chamber cross section, a, is much smaller than the bending radius, ρ, i.e., $\epsilon \equiv \sqrt{a/\rho} \ll 1$.

(b) A bunch consists of ultra-relativistic electrons, $\gamma = \infty$. Under this assumption, the longitudinal component of the electric field is much smaller than the transverse one.

(c) The radiation components propagating at large angles with respect to the beam are ignored (paraxial approximation). In particular, this assumption excludes the vacuum chamber having a projection from the wall, which would cause a wave propagating in the opposite direction.

(d) The chamber is perfectly conducting.

(e) The bunch shape does not change. This assumption can be relaxed so as to include 'predictable' changes (those approximated by a simple optics calculation). A dynamic change of the bunch shape due to the CSR, itself, cannot be included.

We employ a coordinate system, (x, y, s), which is often used in accelerator physics, where s is the distance along the reference orbit, and x and y are perpendicular to s. For simplicity, we assume a planar orbit in the (x, s) plane with curvature radius $\rho(s)$, though it is easy to extend to the case of a general 3D orbit. Thus, the unit vectors $(\boldsymbol{e}_x, \boldsymbol{e}_y, \boldsymbol{e}_s)$ satisfy

$$\frac{d\boldsymbol{e}_x}{ds} = \frac{\boldsymbol{e}_s}{\rho(s)}, \qquad \frac{d\boldsymbol{e}_s}{ds} = -\frac{\boldsymbol{e}_x}{\rho(s)}. \tag{7.6}$$

The variables in the time domain have the symbol $^{(t)}$, while the others are variables in the frequency domain. We define the Fourier transformation of the function f as follows:

$$f^{(t)}(\tau) = \frac{1}{2\pi} \int_{-\infty}^{\infty} dk\, f(k)\, e^{-ik\tau}, \tag{7.7}$$

where $\tau \equiv t - s$ and k is the wave number. This means that $f(k)$ is a normal Fourier transform of $f^{(t)}$ with respect to t, but the factor e^{iks} taken off. We put $c = 1$ (velocity of light) in this analysis.

We reduce the Maxwell equations to a simpler form for numerical calculations. We denote the electric and magnetic fields by $\boldsymbol{E}$ and $\boldsymbol{B}$; the charge density and current density are denoted by J_0 and $\boldsymbol{J}$.

Maxwell's equations in the accelerator coordinates are

$$\frac{1}{g}\left(\frac{\partial(gE_s^{(t)})}{\partial y} - \frac{\partial E_y^{(t)}}{\partial s}\right) + \frac{\partial B_x^{(t)}}{\partial t} = 0, \tag{7.8}$$

$$\frac{1}{g}\left(\frac{\partial(gB_s^{(t)})}{\partial y} - \frac{\partial B_y^{(t)}}{\partial s}\right) - \frac{\partial E_x^{(t)}}{\partial t} = \mu_0 J_x^{(t)}, \tag{7.9}$$

$$\left(\frac{\partial B_y^{(t)}}{\partial x} - \frac{\partial B_x^{(t)}}{\partial y}\right) - \frac{\partial E_s^{(t)}}{\partial t} = \mu_0 J_s^{(t)}, \tag{7.10}$$

where $g = 1 + x/\rho(s)$. We assume that the current flows along the reference orbit, $\boldsymbol{J}^{(t)} = J_s^{(t)}\,\boldsymbol{e}_s$.

When we consider the frequency domain, the field variables are functions not only of (x, y), but also of s. Fourier transformations of Eqs. (7.8) and (7.9) without higher order terms, $O(\epsilon^2)$, gives

$$B_x = -E_y, \qquad B_y = E_x. \tag{7.11}$$

Neglecting higher order terms, $O(\epsilon^3)$, Eq. (7.10) can be expressed in terms of the electric field,

$$E_s = \frac{i}{k}\left(\frac{\partial E_x}{\partial x} + \frac{\partial E_y}{\partial y} - \mu_0 J_s\right). \tag{7.12}$$

B_s can be obtained from $E_x and E_y$ as follows:

$$B_s = \frac{i}{k}\left(\frac{\partial E_x}{\partial y} - \frac{\partial E_y}{\partial x}\right). \tag{7.13}$$

Thus, the longitudinal components can be expressed in terms of the transverse components.

We now derive an equation that describes the evolution of the transverse fields. From Maxwell's equations, we obtain

$$\boldsymbol{\nabla}(\boldsymbol{\nabla}\cdot\boldsymbol{E}^{(t)}) - \boldsymbol{\nabla}\times(\boldsymbol{\nabla}\times\boldsymbol{E}^{(t)}) - \frac{\partial^2\boldsymbol{E}^{(t)}}{\partial t^2} = \left(\boldsymbol{\nabla}J_0^{(t)} + \frac{\partial\boldsymbol{J}^{(t)}}{\partial t}\right). \tag{7.14}$$

We Fourier transform Eq. (7.14) into the frequency domain and neglect the higher order terms, $O(\epsilon^2)$:

$$\hat{D}E_x - \frac{\partial J_0}{\partial x} = -\frac{\partial^2 E_x}{\partial s^2} + C_x, \tag{7.15}$$

$$\hat{D}E_y - \frac{\partial J_0}{\partial y} = -\frac{\partial^2 E_y}{\partial s^2} + C_y, \tag{7.16}$$

where

$$\hat{\mathcal{D}} = 2ik\frac{\partial}{\partial s} + \frac{\partial^2}{\partial x^2} + \frac{\partial^2}{\partial y^2} + \frac{2k^2 x}{\rho}, \tag{7.17}$$

$$C_x = x\left(\frac{\partial}{\partial s}\frac{1}{\rho}\right)\left[ikE_x + \frac{\partial E_x}{\partial s}\right] + \left(\frac{\partial}{\partial s}\frac{1}{\rho}\right)E_s, \tag{7.18}$$

$$C_y = x\left(\frac{\partial}{\partial s}\frac{1}{\rho}\right)\left[ikE_y + \frac{\partial E_y}{\partial s}\right]. \tag{7.19}$$

The last term in Eq. (7.18) might be large where the curvature changes rapidly, particularly at the edge of a bending magnet. Integrating the term over the edge, we can roughly estimate the jump of E_x, approximately, as

$$\delta E_x \sim \pm \frac{1}{2i} \frac{E_s}{k\rho} = O(\epsilon^3). \tag{7.20}$$

We can neglect the last term in Eq. (7.18).

Similarly, the first terms in the square brackets in Eq. (7.18) and (7.19) might be large. Integration of the term over the edge gives a rough estimation of the jump of E_x and E_y as

$$\delta E_{x,y} \sim \pm \frac{x}{2\rho} E_{x,y} = O(\epsilon^2). \tag{7.21}$$

Thus, the first terms in Eqs. (7.18) and (7.19) are negligible.

In the case of a hard-edge magnet, the second terms in the square brackets in Eqs. (7.18) and (7.19) can be the square of a δ-function, because $E_{x,y}$ can be step-function-like. The jump in E_x at the edge is

$$\delta E_{x,y} \sim \frac{x/\rho}{2i} \frac{E_{x,y}}{k\, l_{\mathrm{edge}}}, \tag{7.22}$$

where l_{edge} is the edge length. If the bunch length is comparable to, or shorter than, the edge length of the magnet, $\sigma_s \sim 1/k \lesssim l_{\mathrm{edge}}$, the jump δE_x is $O(\epsilon^2)$, so we can neglect the term. Thus, the terms C_x and C_y are negligible.

Finally, we perform the most important approximation. We define the Fourier transform with the factor e^{iks} taken out. If the wave propagates nearly parallel to the beam (paraxial approximation), the remaining s-dependence of $\boldsymbol{E}(x, y, s)$ will be weak. Thus, we neglect the terms of the second derivative with respect to s in Eqs. (7.15) and (7.16). This approximation means that we neglect waves with a phase of $k(s+t)$. We ignore the radiation that propagates in the opposite direction to the beam. If the vacuum chamber has projections on the wall, we can not use this approximation because of the reflected waves. As a result, all terms on the RHS of Eqs. (7.15) and (7.16) are small. Thus, we obtain

$$\frac{\partial}{\partial s}\begin{pmatrix} E_x \\ E_y \end{pmatrix} = \frac{i}{2k}\left[\left(\boldsymbol{\nabla}_\perp^2 + \frac{2k^2 x}{\rho}\right)\begin{pmatrix} E_x \\ E_y \end{pmatrix} - \boldsymbol{\nabla}_\perp J_0\right], \tag{7.23}$$

where $\boldsymbol{\nabla}_\perp = (\partial_x, \partial_y)$ and $\boldsymbol{\nabla}_\perp^2 = \partial_x^2 + \partial_y^2$. The RHS of this equation is identical to the fundamental equation in [15], except that we have included the source term and have assumed $\gamma = \infty$. Our equation describes the evolution of the field, whereas the equation in [15] describes only the steady state.

If we remove the source term from Eq. (7.23), it is identical to the equation of laser propagation in a non-uniform medium in terms of Cartesian coordinates(x, y, z):

$$\frac{\partial \boldsymbol{E}_L}{\partial z} = \frac{i}{2k}\left[\boldsymbol{\nabla}_\perp^2 + \left(\frac{1}{n^2} - 1\right)k^2\right]\boldsymbol{E}_L, \tag{7.24}$$

where n is the refraction index of the medium. It is a function of the coordinates in the case of a non-uniform medium. The laser beam is bent due to the non-uniform medium. Comparing Eq. (7.23) with Eq. (7.24), we find that the term $2k^2 x/\rho$ in Eq. (7.23) plays the role of a refraction index, $n(x) = 1 - x/\rho$, varying as x. This means that the radiation

follows a bent path in a vacuum. The reason is that we use curvilinear coordinates, so that the radiation propagating in a straight line deviates from the curved axis.

We also note that Eq. (7.23) is a Schrödinger-like equation. We can, in fact, obtain the Schrödinger equation from the Klein-Gordon equation by using the same mathematical procedure, i.e., take out the time dependence, e^{-imt} (m = rest mass), from the wave function, and ignore the remaining second derivative with respect to t.

Eq. (7.23) can be solved as an initial-value problem with respect to s under the boundary condition of a vanishing tangential electric field on the wall. The Maxwell equation is basically elliptic with respect to the spatial coordinate. Nevertheless, our equation can be solved step by step with s. The reason is that there is no backward wave in our case.

In Section **7.5.4**, we compare our simulation results with existing analytic theories. Since the theories are given for special cases of the charge distribution, we need to modify Eq. (7.23) slightly.

We introduce a line charge distribution in Eq. (7.23),

$$J_0(x, y, k) = \lambda(k)\delta(x - x_c)\delta(y - y_c), \tag{7.25}$$

where $\lambda(k)$ is the line-charge density in the frequency domain and (x_c, y_c) is the offset from the reference orbit. We adopt a Gaussian distribution for $\lambda^{(t)}(\tau)$. The line-charge distribution in the frequency domain, $\lambda(k)$, is also Gaussian:

$$\lambda^{(t)}(\tau) = \frac{1}{\sqrt{2\pi}\sigma_s} e^{-\tau^2/2\sigma_s^2}, \tag{7.26}$$

$$\lambda(k) = e^{-(\sigma_s k)^2/2}, \tag{7.27}$$

where σ_s is the rms bunch length. Since the field from a line charge is extremely singular, we separate the radiation field from the beam field to avoid dealing with the δ-function in the simulation code,

$$\boldsymbol{E} = \boldsymbol{E}^{(r)} + \boldsymbol{E}^{(b)}, \tag{7.28}$$

where $\boldsymbol{E}^{(r)}$ is the radiation field, and $\boldsymbol{E}^{(b)}$ is the beam field, which is defined as the electric field in the (straight) drift space. An explicit expression for the beam field can be obtained by Gauss's law:

$$\begin{pmatrix} E_x^{(b)} \\ E_y^{(b)} \end{pmatrix} = \frac{Ne\lambda(k)}{2\pi(x^2 + y^2)} \begin{pmatrix} x \\ y \end{pmatrix}, \quad E_s^{(b)} = 0, \tag{7.29}$$

where N is the number of electrons in a bunch and e is the charge element. Since we assume $\gamma = \infty$, the longitudinal component of the beam field is zero.

Substitution of Eq. (7.29) into Eq. (7.23) eliminates the source term,

$$\frac{\partial}{\partial s}\begin{pmatrix} E_x^{(r)} \\ E_y^{(r)} \end{pmatrix} = \frac{i}{2k}\left[\left(\boldsymbol{\nabla}_\perp^2 + \frac{2k^2 x}{\rho}\right)\begin{pmatrix} E_x^{(r)} \\ E_y^{(r)} \end{pmatrix} + \frac{2k^2 x}{\rho}\begin{pmatrix} E_x^{(b)} \\ E_y^{(b)} \end{pmatrix}\right]. \tag{7.30}$$

Similarly, Eq. (7.12) becomes

$$E_s^{(r)} = \frac{i}{k}\left(\frac{\partial E_x^{(r)}}{\partial x} + \frac{\partial E_y^{(r)}}{\partial y}\right). \tag{7.31}$$

Obviously, we have to use $\boldsymbol{E}^{(r)} + \boldsymbol{E}^{(b)}$ when imposing the boundary condition.

7.5.3 Algorithm

We here assume, for simplicity, that the chamber is rectangular with a constant size. We introduce a finite difference to Eqs. (7.30) and (7.31). $x_i = i\Delta x, (i = 0 \sim m)$, $y_j = j\Delta y, (j = 0 \sim n)$ and $s_\ell = \ell\Delta s, (\ell = 0 \sim u)$, where i, j, ℓ are the indices of x, y, z, respectively. For convenience in using the central difference, we define the field components at $s = s_\ell$ as follows:

$$\begin{array}{ll} E_{x,(i,j)} & = E_x(x_{i-1/2}, y_j), \quad (1 \le i \le m,\ 0 \le j \le n), \\ E_{y,(i,j)} & = E_y(x_i, y_{j-1/2}), \quad (0 \le i \le m,\ 1 \le j \le n), \\ E_{s,(i,j)} & = E_s(x_i, y_j), \qquad (0 \le i \le m,\ 0 \le j \le n), \end{array} \tag{7.32}$$

where $x_{i-1/2} \equiv (x_{i-1} + x_i)/2$, etc.

We apply the central difference for the second derivative with respect to x, y:

$$f''(x) \approx \frac{f(x + \Delta x) - 2f(x) + f(x - \Delta x)}{(\Delta x)^2}. \tag{7.33}$$

As for the derivative with respect to s, we employ the leap-frog difference,

$$f(s + \Delta s) \approx f(s - \Delta s) + 2\Delta x f'(s). \tag{7.34}$$

Euler's difference,

$$f(s + \Delta s) \approx f(s) + \Delta x f'(s), \tag{7.35}$$

is always unstable under a step-by-step iteration with s.

From now on, we omit the radiation symbol $^{(r)}$ and substitute the index (ℓ) for s. The finite-difference equation of (7.30) is then given by

$$E^{(\ell+1)}_{x,y(i,j)} = E^{(\ell-1)}_{x,y(i,j)} + i\frac{\Delta s}{k}\Big(G^{(\ell)}_{x,y(i,j)} + H^{(\ell)}_{x,y(i,j)} + I^{(\ell)}_{x,y(i,j)}\Big), \tag{7.36}$$

where

$$G^{(\ell)}_{x,y(i,j)} = \frac{E^{(\ell)}_{x,y(i+1,j)} - 2E^{(\ell)}_{x,y(i,j)} + E^{(\ell)}_{x,y(i-1,j)}}{\Delta x^2}, \tag{7.37}$$

$$H^{(\ell)}_{x,y(i,j)} = \frac{E^{(\ell)}_{x,y(i,j+1)} - 2E^{(\ell)}_{x,y(i,j)} + E^{(\ell)}_{x,y(i,j-1)}}{\Delta y^2}, \tag{7.38}$$

$$I^{(\ell)}_{x(i,j)} = \frac{2k^2}{\rho} x_{i-1/2}\Big(E^{(\ell)}_{x(i,j)} + E^{(b)}_{x(i,j)}\Big), \tag{7.39}$$

$$I^{(\ell)}_{y(i,j)} = \frac{2k^2}{\rho} x_i\Big(E^{(\ell)}_{y(i,j)} + E^{(b)}_{y(i,j)}\Big). \tag{7.40}$$

Similarly, Eq. (7.31) becomes

$$E^{(\ell)}_{s(i,j)} = \frac{i}{k}\left(\frac{E^{(\ell)}_{x(i+1,j)} - E^{(\ell)}_{x(i,j)}}{\Delta x} + \frac{E^{(\ell)}_{y(i,j+1)} - E^{(\ell)}_{y(i,j)}}{\Delta y}\right). \tag{7.41}$$

Assuming perfectly conducting walls, the tangent components of the field are zero on the walls. The x component on the horizontal walls and the y component on the vertical walls are zero. Thus they are given by

$$E^{(\ell)}_{x(i,j)} = -E^{(b)}_{x(i,j)} \quad \text{for} \quad j = 0, n, \quad 1 \le i \le m, \tag{7.42}$$

$$E^{(\ell)}_{y(i,j)} = -E^{(b)}_{y(i,j)} \quad \text{for} \quad i = 0, m, \quad 1 \le j \le n, \tag{7.43}$$

where E_x and E_y are decoupled because of the rectangular cross section. Another boundary condition, valid for constant cross section, is $E_s = 0$ on the wall.

Let us give the initial condition at the entrance of a magnet. It is reasonable to assume that the field is in a steady state in the chamber with $\rho = \infty$. We put $\partial_s E_{x,y(i,j)} = 0$ in Eq. (7.30). Then, we solve

$$G_{x,y(i,j)} + H_{x,y(i,j)} + I_{x,y(i,j)} = 0 \tag{7.44}$$

with the boundary condition. The leap-frog method requires two initial conditions at $s = s_0$ and at s_{-1}, but they are the same. After the initial conditions are given, we repeat the following procedure from 1 to 4 in each step of s_ℓ ($\ell = 1, 2, \ldots, n$):

1. Calculate $E_{x,y}$ inside the chamber using Eq. (7.36)
2. Calculate E_x, E_y on the boundary using Eq. (7.43)
3. Calculate E_s inside the chamber using Eq. (7.41)
4. Give boundary values to E_s.

The whole procedure, including initial conditions, is repeated for different wave numbers, $k_{(p)}$, for the Fourier transformation. The mesh size depends on the wave number, $k_{(p)}$. Hence, we have to interpolate the field to obtain the fields on a common mesh for the Fourier transformation using Eq. (7.7).

In order to perform the simulation, the most important factor is the mesh size. The mesh size should be determined while considering two aspects. One is the accuracy, and the other is the stability of iterations. The typical scale of the field in the (x, y, s) direction is obtained by a dimensional analysis of Eq. (7.30). The mesh size must be considerably smaller than the corresponding scale length:

$$\Delta x, \Delta y \ \ll \ x_{\rm typ},\ y_{\rm typ} \sim (\rho/k^2)^{1/3}, \tag{7.45}$$

$$\Delta s \ \ll \ s_{\rm typ} \sim (\rho^2/k)^{1/3}. \tag{7.46}$$

Note that these scale lengths are much larger than the wavelength, $1/k$.

On the other hand, the mesh size must satisfy another condition for stable iteration. For an analysis of stability, ignoring the curvature term in Eq. (7.23),

$$\frac{\partial E_{x,y}}{\partial s} = \frac{i}{2k} \boldsymbol{\nabla}_\perp^2 E_{x,y}, \tag{7.47}$$

and considering a solution of the form

$$E^{(\ell)}_{x,y(i,j)} \propto e^{i(i\xi + j\eta + \ell\zeta)}, \tag{7.48}$$

the dispersion relation of the leap-frog iteration is given by

$$\sin\zeta = \frac{2\Delta s}{k}\left(\frac{\sin^2(\xi/2)}{\Delta x^2} + \frac{\sin^2(\eta/2)}{\Delta y^2}\right). \tag{7.49}$$

To keep the iteration stable, ζ must be real for any real numbers ξ and η. Accordingly, the mesh size must satisfy

$$\frac{2\Delta s}{k}\left(\frac{1}{\Delta x^2} + \frac{1}{\Delta y^2}\right) < 1. \tag{7.50}$$

In numerical calculations, the mesh size must satisfy Eqs. (7.45), (7.46), and (7.50). Since we repeat the tracking for different wave numbers, $k_{(p)}$ ($p = 1, 2, \ldots$), these conditions, assigned on the mesh size, change with $k_{(p)}$. One can easily show that Euler's difference (7.35) is always unstable for any mesh size.

7.5.4 Comparison with analytic theories

In order to check the justification of the simulation using the mesh algorithm, we compared the results with analytic solutions derived by (A) Derbenev *et.al*[9], (B) Warnock[8], and (C) Saldin *et.al*[10]. They were obtained from different conditions, as listed here:

	(A)	(B)	(C)
state	steady	steady	transient
shield	free	parallel plates	free

We assumed that the line charge density has a Gaussian longitudinal distribution given by Eq. (7.26). We compared the longitudinal electric field, E_s, obtained by our simulation with the analytic expressions. In order to compare the numerical results with cases (A) and (C), the cross section of the chamber has to be large enough to avoid shielding effects. In the case of (B), only the side walls must be sufficiently distant. We simulate infinite space by choosing a chamber size as large as possible within the limitation $\sqrt{w/\rho}, \sqrt{h/\rho} \ll 1$, where w is the full width, and h is the full height of the chamber cross section. Since the analytic formulas (A) and (B) describe the field of the CSR in the steady state, we have to track the particles over a long distance, $L_m \gg 2(3\rho^2\sigma_s)^{1/3}$. If the tracking length is too large, however, the radiation reflected by the wall can reach the observation points and invalidate the comparison. Therefore, we have to choose an appropriate tracking distance.

In Fig. 7.3 the horizontal axis is the position in the bunch in units of the rms bunch length (bunch head to the right). The vertical axis is the longitudinal electric field, E_s, normalized by the factor $E_0 = 2Nr_emc^2/\sqrt{2\pi}(3\rho^2{\sigma_s}^4)^{1/3}$. We used an rms bunch length of $\sigma_s = 0.3$ mm, and the curvature radius of $\rho = 10$m, in all simulations. The unshielded CSR in the steady state (A) is also shown in Fig. 7.3. The larger cross section gives similar results to the analytic formula. In comparison, the tiny differences behind the bunch between them is due to reflection on the wall.

The shielded CSR in the steady state (B) is shown in Fig. 7.4 for various sizes of the chamber height. In all cases, the simulation results agree with the analytic formula.

The unshielded CSR in transient states (C) is shown in Fig. 7.5 for various distances, s, from the entrance of the magnets with a chamber size of $w \times h = 34\text{cm} \times 28$ cm. The results again agree well with the analytic formula, though the case of $s = 100$ cm shows a small difference. To check the effects of the finite distance to the wall, we simulate the case of a smaller chamber, 10×10 cm. The results are shown in Fig. 7.6. Comparing the two cases, we can see that the residual difference from the analytic formula comes from the finite distance to the wall.

7.5.5 Application to the KEKB LER

We applied this method to the KEKB LER and calculated the change in the particle's energy due to CSR. Though the actual shape of the chamber cross section is round, we

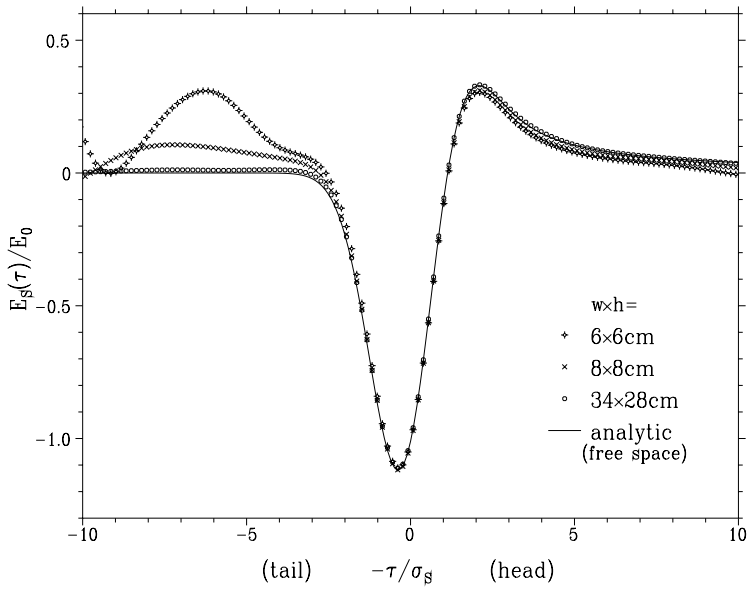

Figure 7.3: Longitudinal electric field, E_s, in the steady state without shielding. Derbenev's formula is plotted with a solid line. The dots are the simulation results for various sizes of vacuum chamber, corresponding to $w \times h = 6 \times 6$ cm, 8×8 cm, and 34×28 cm, respectively. The length of the magnet is 2.1 m. E_s is calculated at the center $x = y = 0$ of the chamber.

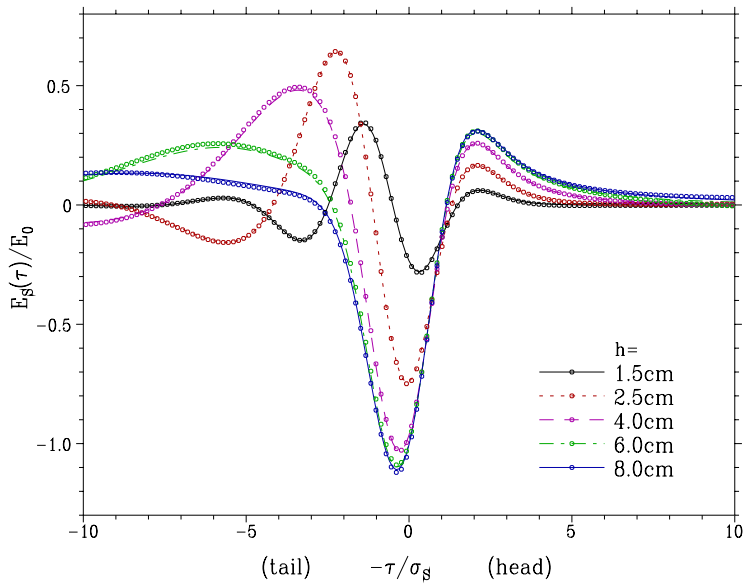

Figure 7.4: Longitudinal electric field, E_s, in the steady state at $x = y = 0$ between infinite parallel plates. Warnock's formula is plotted with solid lines. The dots are simulation results. The different symbols show the gap between the two horizontal parallel plates: $h = 1.5$ cm, 2.5 cm, 4 cm, 6 cm, and 8 cm, respectively. The width of the chamber is $w = 50$ cm and the length of the magnet is 3 m.

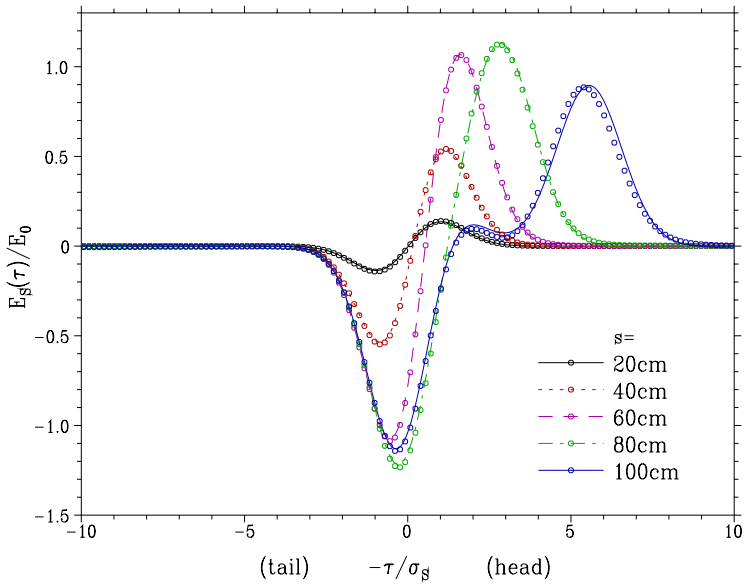

Figure 7.5: Longitudinal electric field, E_s, at $x = y = 0$ in the transient state without shielding. Saldin's formula is plotted with solid lines, and the dots are simulation results. The different symbols indicate the tracking length from the entrance of the magnet: $s = 20$ cm, 40 cm, 60 cm, 80 cm, and 100 cm, respectively. The size of the chamber cross section is $w \times h = 34$ cm $\times$ 28 cm.

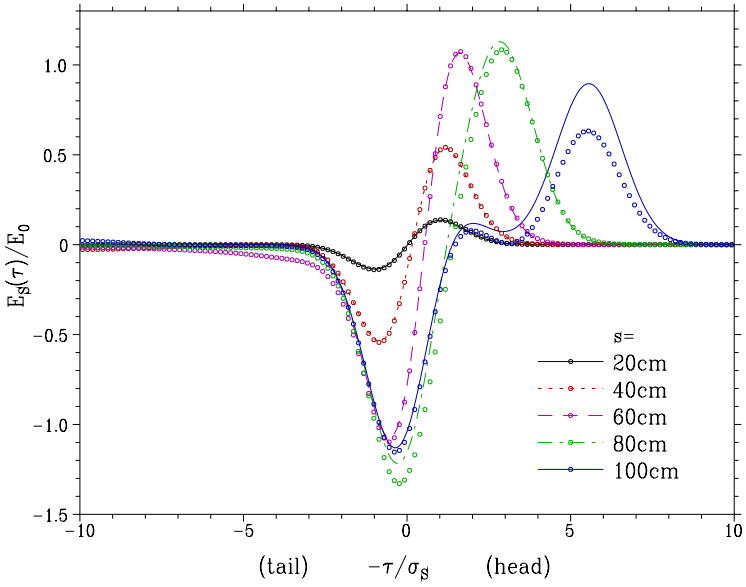

Figure 7.6: Longitudinal electric field, E_s, in the transient state with shielding. The chamber size is $w \times h = 10$ cm$\times$10 cm. The other parameters are the same as in Fig. 7.5.

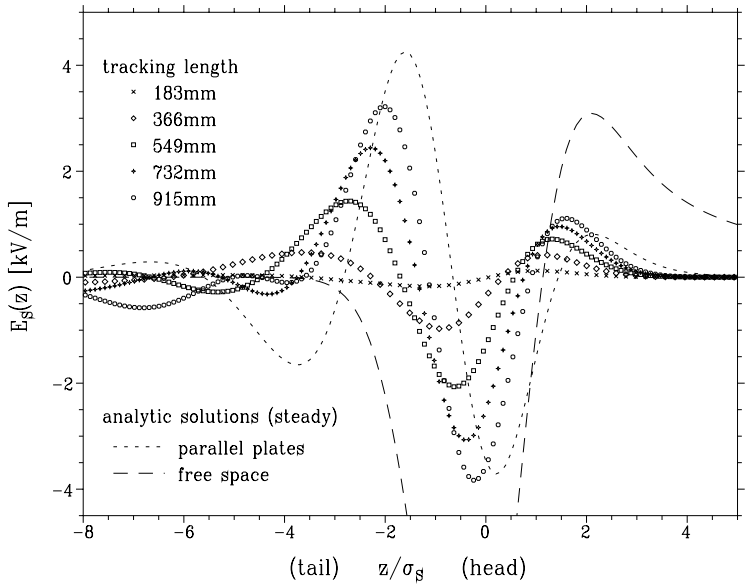

Figure 7.7: Longitudinal electric field E_s in a bending magnet of the KEKB LER. The different symbols denote the tracking length from the entrance of the magnet: 183 mm ($\times$), 366 mm ($\diamond$), 549 mm ($\Box$), 732 mm(+), 915 mm ($\circ$). The dashed line is the analytic solution of the steady state in free space. The analytic solution of the infinite parallel plates is plotted with the dotted line. The half gap between the parallel plates is 47 mm, which is the same as the full height of the chamber.

substituted a square cross section; the half height, r, is equal to the radius of the round cross section. The longitudinal electric field of the CSR in the KEKB LER is shown in Fig. 7.7. The horizontal axis is the position in the bunch, $z = s - t$, in units of rms. The bunch length was $\sigma_s = 3$ mm, and the transverse beam size was zero in the simulations. The number of particles was $N = 3.3 \times 10^{10}$, the half-height of the chamber was $r = 47$ mm, the length of the magnet was 915 mm, and the bending radius was $\rho = 16.3$ m. The different symbols show the tracking distance from the entrance of the magnet. In order to confirm the shielding and transient effects, the analytic solutions are also plotted in Fig. 7.7: the steady state in free space is represented by a dashed line, and the steady state among infinite horizontal parallel plates is represented by a dotted line. One finds that the CSR evolves as the particles travel through the magnet. This shows that the CSR is transient in the magnets of the KEKB LER. Compared with the solution in free space (dashed line), the longitudinal electric field is fairly reduced. The difference between them implies that the CSR is strongly shielded by the chamber.

We compared this result with another analytic solution, which describes the unshielded CSR in the transient state. The solution and the simulation result are shown in Fig. 7.8. The electric field around the head of the bunch is suppressed due to the shielding. On the other hand, the reflected waves reach the tail of the bunch.

Fig. 7.9 shows the energy change due the CSR for one bending magnet. The CSR emitted in the magnet goes out of the magnet and propagates in the drift space. Considering the effect of the CSR in the drift space, we integrated the longitudinal electric field not only in the bending magnet, but also from the exit of the magnet to infinity. The results were calculated for several different bunch lengths: $\sigma_s = 3$, 4, 5, and 6 mm).

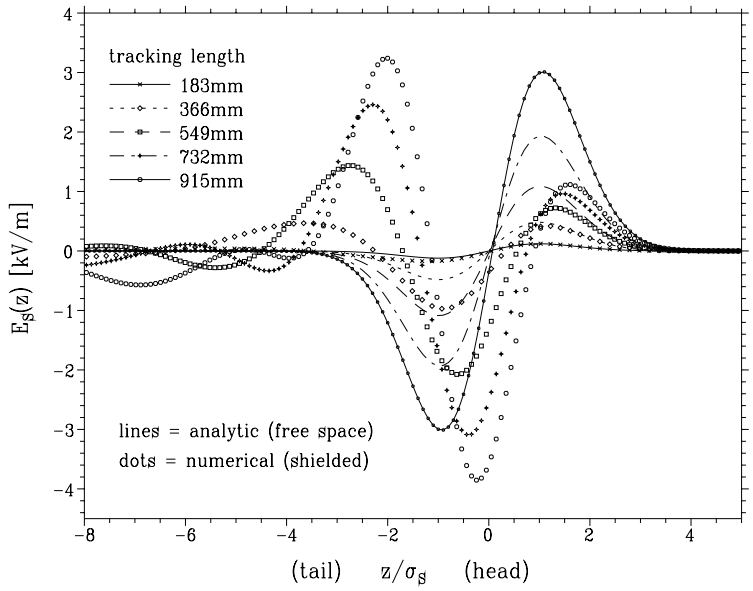

Figure 7.8: Longitudinal electric field, E_s, in a bending magnet of the KEKB LER. The different symbols show the tracking length, the same as in Fig. 7.7. The lines show the analytic solutions of transient state in free space. The different lines denote the tracking length from the entrance of the magnet: 183 mm (solid line), 366 mm (dotted line), 549 mm (dashed line), 732 mm(dash-dotted line), and 915 mm (solid-dotted line). The parameters are the same as in Fig. 7.7.

The energy change is larger for a shorter bunch. We find that the energy change for a bunch of 3 mm length is about ten-times larger than that of a 6 mm bunch in the region around the center of the bunch. Since the CSR includes higher frequency components for a shorter bunch, the CSR of the short bunch is less shielded by the chamber.

The energy change for various chamber sizes is shown in Fig. 7.10. The bunch length is 3 mm. One finds that the CSR is suppressed by the smaller chamber.

7.5.6 Conclusion

We have shown that the CSR can be calculated by using a mesh with a moderate amount of computing time. The most important point is the paraxial approximation, which enables the use of a mesh size larger than the relevant wave length. We compared the simulation results with the existing analytic formulas and found excellent agreements. Although we only calculated simple cases for which an analytic formula is available, the method is very flexible and can be extended to more general cases, such as:

- finite transverse beam size;
- chamber cross section other than rectangular;
- chamber size changing gradually;
- finite beam energy (but still large γ); and
- changing beam profile (but not due to the CSR itself).

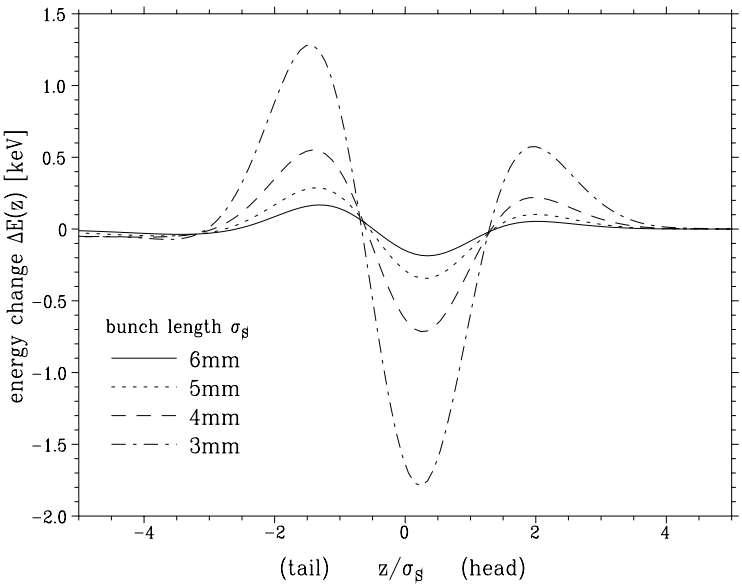

Figure 7.9: Energy change, ΔE, by CSR for one bending magnet. The different lines represent different bunch lengths: σ_s = 6 mm (solid line), 5 mm (dotted line), 4 mm (dashed line), and 3 mm (dash-dotted line). The transverse beam size is zero. The half height of the chamber is r = 47 mm. The length of the magnet is 0.915 m, bending radius is ρ = 16.3 m. The number of particles in a bunch is $N = 3.3 \times 10^{10}$.

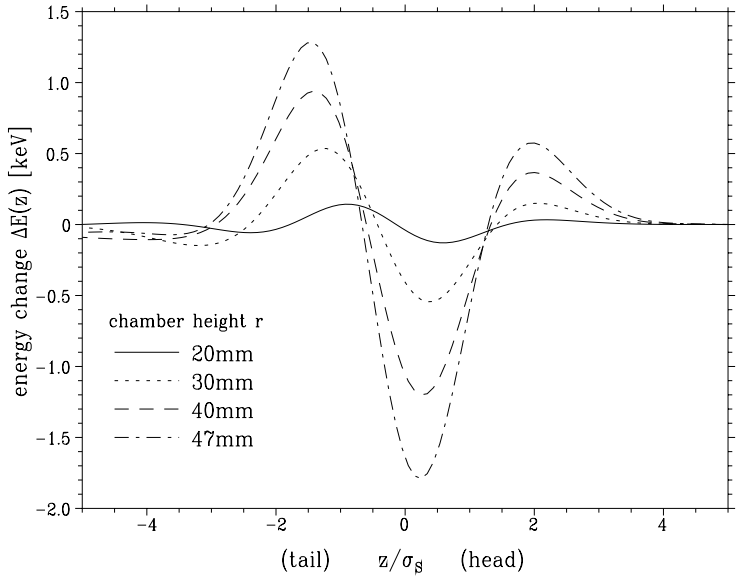

Figure 7.10: Energy change, ΔE, by CSR for one bending magnet. The bunch length is σ_s =3mm. The different lines represent different half-heights of the chamber cross section: r = 20 mm (solid line), 30 mm (dotted line), 40 mm (dashed line), 47 mm (dash-dotted line). The other parameters are the same as in Fig. 7.9.

It should also be possible to include the finite resistivity of the chamber wall by imposing a resistive boundary condition. We have only calculated the energy change due to E_s, but it is also possible to compute the transverse force. This issue will be discussed elsewhere. Another issue to be discussed is the range of the validity of the paraxial approximation. We have applied this method to the KEKB LER. We have shown that the CSR in the bending magnet is strongly shielded by the vacuum chamber. It has been determined that the CSR is still in a transient state. Therefore, the existing analytic formulas can not be applied to the KEKB LER. In the case of a bunch of 3 mm length, the CSR is reduced less by the chamber. The reason is that the CSR has higher frequency wave components.

7.5.7 Appendix A : Impedance Formula for Shielding by Parallel Plates

An exact impedance formula for a particle on a circular orbit between a pair of two parallel plates has been given by Warnock [8]. In actual applications the relevant wavelength, $1/k$, is much smaller than the orbit curvature radius, ρ. The condition that the circumference be an integer multiple of the wavelength is therefore unimportant. In such a case, one can obtain a simplified formula of the longitudinal impedance per unit orbit length:

$$Z(k) = \frac{2\pi}{h}\left(\frac{2}{k\rho}\right)^{1/3} Z_0 \sum_{p=0}^{\infty} F_0(\beta_p), \tag{7.51}$$

$$F_0(\beta) \equiv \mathrm{Ai}'(\beta^2)[\mathrm{Ai}'(\beta^2) - i\mathrm{Bi}'(\beta^2)] \tag{7.52}$$

$$+ \beta^2 \mathrm{Ai}(\beta^2)[\mathrm{Ai}(\beta^2) - i\mathrm{Bi}(\beta^2)], \tag{7.53}$$

$$\beta_p \equiv (2p+1)\frac{\pi}{h}\left(\frac{\rho}{2k^2}\right)^{1/3}, \tag{7.54}$$

where Z_0 is the impedance of a vacuum, and $\mathrm{Ai}(z)$ and $\mathrm{Bi}(z)$ are Airy functions defined by the solutions of a differential equation,

$$\frac{d^2 f(z)}{dz^2} - z f(z) = 0, \tag{7.55}$$

with values at fixed points:

$$\mathrm{Ai}(0) = \frac{1}{3^{2/3}\Gamma(2/3)}, \quad \mathrm{Bi}(0) = \frac{1}{3^{1/6}\Gamma(2/3)}. \tag{7.56}$$

The above formula can also be obtained in a simpler manner from the stationary solution of Eq (7.23) with the boundary condition that the wave propagates in the $\pm x$ direction at $x \to \pm\infty$.

The asymptotic form of $F_0(\beta)$ for $\beta \to \infty$ (strong shielding) is given by

$$\Re F_0(\beta) = \frac{\beta}{2\pi} e^{-4\beta^3/3}\left(1 + \frac{1}{24\beta^3} + \frac{1}{1152\beta^6} + O(\beta^{-9})\right), \tag{7.57}$$

$$\Im F_0(\beta) = -\frac{3}{16\pi\beta^5}\left(1 + \frac{105}{32}\frac{1}{\beta^6} + O(\beta^{-12})\right). \tag{7.58}$$

Therefore, the asymptotic form of $Z(k)$ for $k \to 0$ is given by

$$Z(k) = \frac{\pi Z_0}{kh^2}\left[e^{-2\pi^3\rho/3k^2h^3} - \frac{3i}{2}C_5\left(\frac{k^2h^3}{\pi^3\rho}\right)^2\right] \tag{7.59}$$

$$C_5 = \sum_{p=0}^{\infty}\frac{1}{(2p+1)^n} = 1.004524. \tag{7.60}$$

The other limit $k \to \infty$ (no shielding) is

$$Z(k) = \frac{Z_0}{4\pi}\frac{2\Gamma(2/3)}{3^{1/3}}\frac{(ik+0)^{1/3}}{\rho^{2/3}}. \tag{7.61}$$

Formula (7.51) was used in section 7.5.4 for a comparison with theories.

Bibliography

[1] V. Danilov et al.,Phys. Rev. ST-AB,4, 120101 (2001)

[2] L. F. Wang et al., Phys. Rev. ST-AB,5, 124402 (2002) and L. F. Wang, "User's Guode for CLOUDLAND", KEK Internal 2003-2.

[3] K. Ohmi and F. Zimmermann, Phys. Rev. Lett.,85, 3821 (2000)

[4] K. Ohmi, "RECENT DEVELOPMENTS IN DESIGNS FOR e+e- COLLIDERS", Proceedings of PAC2003.

[5] Ya. S. Derbenev, E. L. Saldin, V. D. Shiltsev, EPAC'96 1347.

[6] H. H. Braun, R. Corsini, L. Groening, F . Zhou, A. Kabel, T. O. Raubenheimer, R. Li, T. Limberg, Phys.Rev.ST-AB,**3**,124402 (2000).

[7] R. Hajima, Proc.ICAP'98 LTU16.

[8] R. L. Warnock, SLAC-PUB-5375 (1990).

[9] Ya. S. Derbenev, V. D. Shiltsev, SLAC-PUB-7181(1996).

[10] E. L. Saldin, E. A. Schneidmiller, M. V. Yurkov, Nucl.Inst.Meth.A398,373(1997), TESLA-FEL 96-14.

[11] M. Borland, Phys.Rev.ST-AB,**4**,070701 (2001).

[12] P. Emma, F.-J. Decker, P. Krejcik, C. L. O'Connell, M. Woodley, H. Schlarb, F. Stulle, Proc.EPAC 2002, 1479.

[13] R. Li, World scientific (22 May 2000).

[14] M. Dohlus, A. Kabel, T. Limberg, Nucl.Instr.Meth. A445 (2000) 338-342.

[15] G. V. Stupakov, I. A. Kotelnikov, Phys.Rev.ST-AB,**6**,034401 (2003).

[16] E. L. Saldin, E. A. Schneidmiller, M. V. Yurkov, PAC'97 1658.

[17] R. Li, C. L. Bohn, J. J. Bisognano, PAC'97 1641.

[18] A. Kabel, M. Dohlus, T. Limberg, SLAC-PUB-8559.

[19] A. Kabel, International Symposium on New Visions in Laser-Beam interactions Tokyo,Japan,1999-10-2.

[20] T. Limberg, A. Kabel, M. Dohlus, Zeuthen 2003,ICFA Beam Dynamics mini workshop.

[21] R. L. Warnock, P. Morton, Part.Accel.**25**, 113-151.

[22] W. H. Press, S. A. Teukolsky, W. T. Vetterling, B. P. Flannery, Cambridge University Press (1992).

Chapter 8

RF System

8.1 Overview

8.1.1 Base plan

The KEKB RF system has been designed to handle electron and positron beam currents of 1.1 A and 2.6 A, respectively. The large circulating beam currents make it imperative to keep the higher-order mode (HOM) impedance of the RF cavities as low as possible to avoid uncontrollable coupled-bunch instabilities (CBI). Serious problems common to B-factories are the excitation of fast growing longitudinal CBI by the accelerating mode of significantly detuned cavities, and phase modulations along a bunch train caused by transient beam loading due to a bunch gap. In order to overcome these difficulties, two types of innovative HOM-damped cavities with large stored energy have been developed. One is the normal-conducting Accelerator Resonantly coupled with Energy Storage (ARES) [1] and the other is a single-cell superconducting cavity (SCC) [2]. An increase in the stored energy per cavity decreases the detuning of the cavity, which makes it possible to reduce the growth rate of the CBI due to the accelerating mode. It also reduces the effects of bunch-gap transients.

For the design of the SuperKEKB RF system, a much higher beam current and a shorter bunch length compared with those of KEKB must be taken into account. The design beam current, 9.4 A in LER and 4.1 A in HER, is about four times as high as that of KEKB. The design bunch length of 3 mm is about half the operating bunch length of KEKB. As a base plan for the RF system, one scheme to be considered is adopting the same RF frequency as KEKB and using the existing RF system as much as possible, with improvements as necessary to meet the requirements for SuperKEKB. An alternative scheme would be to choose a different RF frequency and develop a completely new RF system. One advantage of a higher RF frequency, for example, is that the number of bunches can be increased and the HOM power reduced at a given total beam current.

Our strategy is to investigate first the possibility of the same RF frequency scheme. If this scheme is feasible, the construction cost is greatly reduced compared with a totally new system. Another advantage is that the technical uncertainties would be relatively small since much technology and operational experience have been accumulated at KEKB. The existing RF system has been operating successfully at KEKB up to about 2 A in the LER and 1.1 A in the HER. Its excellent performance shows potential for operating beyond the design beam current of KEKB [3]. We have investigated the possible problems

when it is used at the design parameters of SuperKEKB as well as necessary improvements and measures to solve them. As described in detail below in this chapter, we believe that there are realistic solutions and it is possible to improve the existing RF system to meet the requirements of SuperKEKB. Consequently, we have decided to adopt the same RF frequency as KEKB and to construct the RF system based on the existing RF system with necessary improvements and measures.

Table 8.1 gives the RF-related machine parameters and the design RF parameters. The types of cavities are the same as those in KEKB: the ARES cavities alone are used in the LER where the beam-loading is heavier, whereas a combination of the ARES and SCC is used in the HER. They are operated with a suitable relative phase-angle to assign higher cavity voltage to the SCC and heavier beam loading/voltage to the ARES, similarly to KEKB.

		SuperKEKB		
		LER	**HER**	
Beam current	I_b	9.4	4.1	A
Energy loss/turn	U_0	1.2	3.5	MeV
Loss factor	k_{total}	40	50	V/pC
Bunch length	σ_z	3	3	mm
Radiation loss power	$P_{b,rad}$	11.3	14.3	MW
Parasitic loss power	$P_{b,para}$	7.1	1.7	MW
Total beam power	$P_{b,total}$	18.4	16.0	MW
Total RF voltage	$V_{c,total}$	14.0	23.0	MV
RF frequency	f_{RF}	508.887		MHz
Revolution freq.	f_{rev}	99.4		kHz
Type of cavities		ARES	ARES+SCC	
No. of cavities		28	16+12	
Voltage/cav.	V_c	0.5	0.5/1.3	MV
Beam power/cav.	P_b	650	650/460	kW
Wall loss/cav.	P_c	233	150/-	kW
Detuning frequency	Δf_a	45	31/74	kHz
No. of cav./klystron		1	1/1	
No. of klystrons		28	16+12	
Klystron power	P_{kly}	930	850/480	kW
Total AC power		40	23+10	MW

Table 8.1: RF parameters for SuperKEKB.

According to recent beam-beam simulations, the crab crossing scheme is expected to significantly increase the luminosity. It has been adopted as a baseline design of SuperKEKB to achieve a luminosity of several times 10^{35} $\mathrm{cm}^{-2}\mathrm{s}^{-1}$. A key issue is to develop a crab cavity which can be used with a high current beam of 9.4 A. We have been developing a crab cavity, which is described in section 8.5.

8.1.2 High beam current and measures

The design RF parameters imply various improvements and measures for the much higher beam current of SuperKEKB. The most important issues are discussed below.

Instability due to large detuning of the accelerating mode

In electron storage rings, the resonant frequency of the accelerating mode should be detuned downward with respect to the RF frequency f_{RF} in order to compensate for the reactive component of the beam loading. The optimum detuning frequency Δf_a to minimize the input RF power is given by,

$$\Delta f_a = -\frac{I_b \sin\phi_s}{2V_c} \times \frac{R}{Q_0} \times f_{RF} = -\frac{P_b \tan\phi_s}{4\pi U}, \tag{8.1}$$

where ϕ_s is the synchronous phase, R the shunt impedance, Q_0 the unloaded Q value, and U the stored energy. In B- and Super-B factories, due to the high beam current and a low revolution frequency f_{rev} corresponding to a large circumference of the ring, the operation of conventional normal-conducting cavities would require a Δf_a several times the revolution frequency. As a result, a longitudinal coupled-bunch instability can be excited strongly with a growth time on the order of 100 μs. One of the key issues for the B and Super-B factory RF system is how to avoid this instability.

In the case of KEKB, the remedy is to use the innovative normal-conducting ARES cavities and the SC cavities. The large stored energy of these cavities reduces the amount of detuning Δf_a by an order of magnitude, compared with conventional normal-conducting cavities. The growth rate of the -1 mode is then reduced to a level of $(10\ \mathrm{ms})^{-1}$. Although it is still faster than the radiation damping time of 23 ms and the instability was observed at a beam current of higher than 1 A in LER, it has been suppressed by a -1 mode damping feedback system.

In SuperKEKB with the existing ARES and/or SCC, however, Δf_a would amount to about 70 kHz which is close to the f_{rev} of 99.4 kHz, and the growth time of the -1 mode is about 0.3 ms in LER and 1 ms in HER, much faster than the radiation damping time of 30 ms. In order to solve this problem, two measures will be taken. First, the ARES cavities for LER will be modified to further increase the stored energy. This is done by changing the ratio of stored energy in the storage cavity to that in the accelerating cavity. The cost to pay for it is an increase of the wall dissipation power at the storage cavity. Changing the ratio from the current value of 9:1 to 15:1 gives a reasonable balance between them. With this change the detuning frequency is reduced from 65 kHz to 45 kHz and the growth rate of the -1 mode is reduced to $(1.6\ \mathrm{ms})^{-1}$. Details will be described in Section 8.2. This modification will not be used on the HER-ARES cavities since the majority of the driving impedance in the HER is attributed to the SCC.

Second, the growth time for the -1 mode, 1.6 ms in the LER and 1 ms in the HER, is still faster than the radiation damping time by a factor of 20. A powerful feedback system for damping the -1 mode is required. In addition, the -2 mode also needs to be suppressed. The existing -1 mode damping system at KEKB consists of a single-side-band converter and a comb filter. The effectiveness of the damper has been confirmed experimentally and it has been operating successfully to suppress the instability in the LER [4]. For SuperKEKB, the impedance reduction of about 26 dB is required. Further study to test the performance limit of the existing damper and R&D to improve the performance, if

necessary, will continue. The implement of the -2 mode damper can be done by simply adding a -2 mode filter in parallel to the -1 mode filter.

Parasitic mode damping

Higher-order-modes (HOM) are well damped in both the ARES and SCC and no CBI caused by the HOM of cavities has been observed at KEKB. However, the requirements for the HOM dampers are much more severe at SuperKEKB. The damping property should be discussed from two viewpoints: the growth time of the CBI and the generated HOM power that should be absorbed by the HOM dampers.

First, the growth time of the CBI due to HOM of cavities as well as other parasitic modes is summarized in Table 8.2. For the HOM, only the fastest growing mode is listed for each type of cavities. The growth time is much faster than that of KEKB due to the higher beam current and the larger number of cavities. In addition to the HOM, instabilities can be excited also by an imbalance of the impedance at the 0 and π modes of the ARES due to the large detuning of the accelerating cavity (see Section 8.2). For the longitudinal modes in the LER, the growth time of the fastest HOM and the $0/\pi$ modes are shorter than the radiation damping time of 30 ms. Although the 0 and π modes are related to the accelerating mode, their frequencies are 4 MHz away from f_{RF}, which is outside the bandwidth of the klystrons. Therefore, a longitudinal bunch-by-bunch feedback system, which is not used at KEKB, is needed to suppress them. The required damping time is 4 ms. As described above, the instability of the -1 and -2 modes related to the fundamental mode will be suppressed by a feedback system with comb filters in the RF control system. For the transverse modes, the fastest growth time is about 4 ms and it can be suppressed by the present transverse bunch-by-bunch feedback system in KEKB, which has a damping time of less than 1 ms.

Secondly, due to the higher beam current and the shorter bunch length, the HOM power generated in the cavity region is much larger than that of KEKB. Upgrading of the HOM dampers of the ARES and SCC is of critical importance. It is also desirable to reduce the HOM power as much as possible by reducing the loss factor around the cavity region. Plans for improving the HOM dampers as well as reducing the loss factor will be discussed in detail in Sections 8.2 and 8.3.

Strengthening of RF power

The high current beam needs a large amount of RF power to compensate for the energy loss $P_{b,total}$ due to radiation and parasitic losses. The losses are 18.4 MW in the LER and 16 MW in the HER, about four times as high as those of KEKB. On the other hand, the required RF voltage is relatively low. Furthermore, the number of cavities should be kept as small as possible from the viewpoint of reducing the total impedance in the ring. To meet these requirements, the RF parameters in Table 8.1 are planned based on the following changes:

- In KEKB, one klystron drives two ARES cavities. This will be changed to one klystron/ARES configuration so that much higher power can be fed to each ARES cavity by the same klystrons.

- In KEKB, the input power to each ARES or SC cavity is about 300∼350 kW. This will be increased by a factor of about two. Since the existing input couplers have

Item	Freq.	**LER**		**HER**		**Cure**
	(MHz)	No. cav	Growth	No. cav	Growth	
(Longitudinal modes)						
ARES-HOM	1850	28	5 ms	16	47 ms	B-B
SCC-HOM	1020			12	49 ms	no need
Crab-HOM and LFM	655	2	41 ms	2	214 ms	no need
ARES-0/π modes	504	28	4 ms	16	29 ms	B-B
Fundamental -1 mode	508.79	28	1.6 ms	16+12	1 ms	RF
Fundamental -2 mode	508.69	28	20 ms	16+12	21 ms	RF
(Transverse modes)						
ARES-HOM	633	28	4 ms	16	33 ms	B-B
SCC-HOM	688/705			12	12 ms	B-B
Crab-HOM	773	2	4 ms	2	12 ms	B-B

Only the fastest mode is listed in each item.
B-B means bunch-by-bunch feedback system.
RF means feedbacks in RF control system.
SC version of new crab cavity is assumed (see Section 8.5).
LFM is the lower frequency mode of the crab cavity.

Table 8.2: Growth time of coupled-bunch instability due to RF cavities.

been tested up to about 900 kW in bench tests, they have the potential to be used at this power level.

- The total number of klystrons will be more than doubled.

The required number of RF cavities N_{cav} is determined by the power delivered by each cavity P_b and the loss factor as follows:

$$N_{cav} = \frac{U_0 I_b + T_b k_{others} I_b^2}{P_b - T_b k_{cav} I_b^2}, \tag{8.2}$$

where k_{cav} is the loss factor per cavity, k_{others} the total loss factor in the ring except the cavities, and T_b the bunch spacing. Using the loss factor k_{cav} of 0.67 V/pC for the ARES at σ_z=3 mm, the necessary number of ARES cavities in the LER is shown in Fig. 8.1.

Although the maximum output power of the klystrons is 1.2 MW, it is desired to avoid operating the klystrons at a power level close to the saturation region for stable control of cavities and klystrons in the presence of heavy beam-loading. In addition, operation at less than 1 MW gives a reasonable margin for the existing power supplies for the klystrons and various high power components. Consequently, in Table 8.1 the operating power of the klystrons is set to 930 kW, which gives P_b of 650 kW. Then N_{cav}=28 if k_{others} is assumed to be 21 V/pC. A much larger k_{others} would require a larger number of cavities, N_{cav}, which increases construction cost and electricity rates. Thus the k_{others} should be as small as possible, particularly in the LER. The estimated total loss factor is discussed elsewhere.

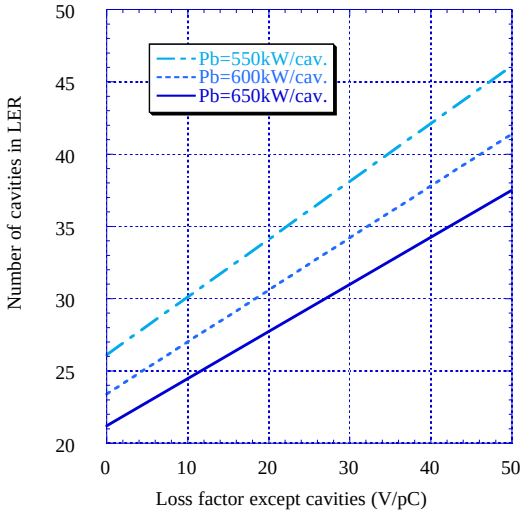

Figure 8.1: Required number of cavities as a function of the loss factor excluding the cavities.

Bunch-Gap Transient

A part of the ring is reserved as an abort gap where no bunch is filled to allow for a rise time of the beam abort kicker. The abort gap also works as an ion-clearing or photo-electron clearing gap in the electron or positron ring, respectively. The gap length of KEKB is about 0.5 μsec, which is 5% of the ring circumference. The bunch gap, however, modulates the phase of the accelerating voltage and the longitudinal position of the bunches, since the beam-loading effect is different between the bunch train and the gap. A large phase modulation can affect the RF system such as modulating the RF power and phase and deteriorating the performance of the feedback loops. In addition, the luminosity can be reduced by having different phase modulations between the two rings.

In order to avoid these harmful effects, the phase modulation should be kept below several degrees. The high stored energy of the ARES and SCC is beneficial to reduce the phase modulation, since it is inversely proportional to the stored energy. Even so, the gap length should be further reduced to less than 0.2 μsec for SuperKEKB. A faster rise time of the abort kicker is required.

8.1.3 Construction

Table 8.3 shows the number of existing RF units at KEKB and the required number for SuperKEKB. Each unit consists of a klystron, one (SuperKEKB) or two (KEKB) ARES cavities or an SCC, high power components and low-level control system. In order to accommodate the increased number of RF units, the buildings at D4, D7, D8 and D10 need to be extended. The total area to be added is estimated to be 1500 m^2.

It is expected that the earliest possibility for beam commissioning is in 2008 and the stored beam current will be increased in stages. To meet the commissioning schedule and the luminosity upgrade phases, the construction of the RF system is planned as shown in Fig. 8.2. By the time of commissioning, 14 RF units will be added to the existing 24 RF units, which can support more than half of the design beam current. The remaining 18 RF units will be added after the commissioning in several phases to increase the beam

		KEKB		SuperKEKB	
		LER	HER	LER	HER
Oho	D4		3		14
	D5		3	8	2
Fuji	D7	5		10	
	D8	5		10	
Nikko	D10		4		6
	D11		4		6
Total		24		56	

Table 8.3: Number of RF units.

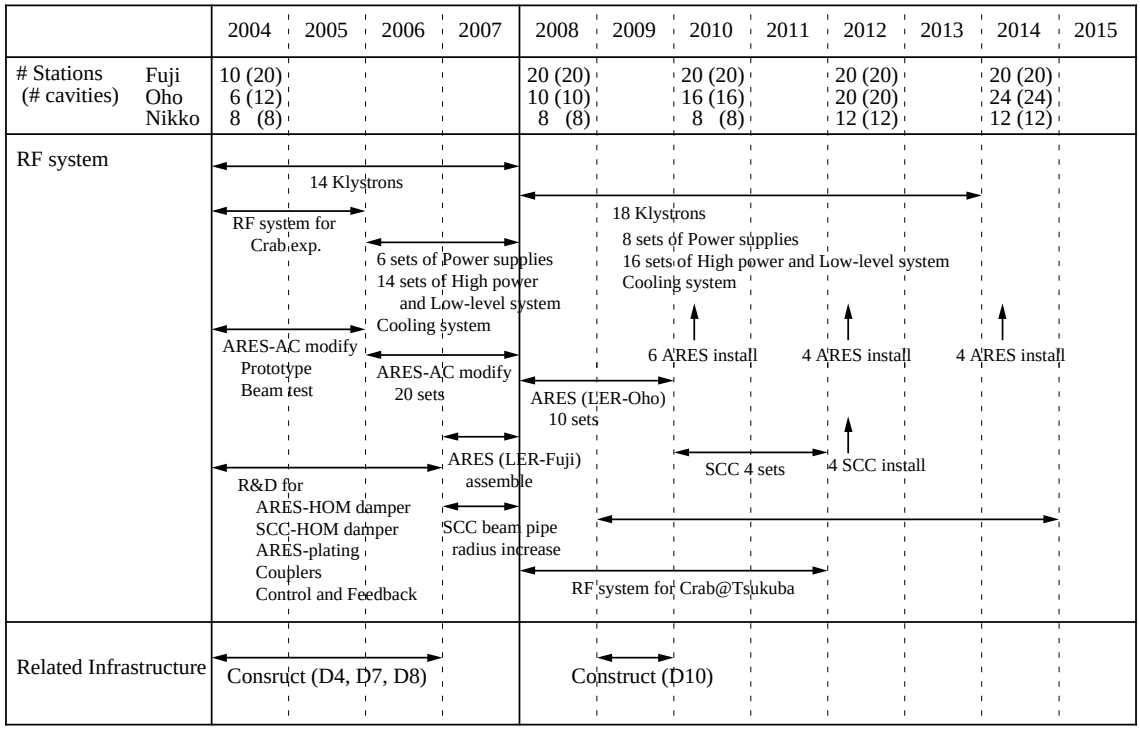

Figure 8.2: Schedule for construction of SuperKEKB RF system.

current. The total cost for the RF system is estimated to be 11.1 billion yen. It does not include the cost for related infrastructures such as buildings, electricity and cooling system.

8.2 ARES cavity system

8.2.1 Introduction

The ARES cavity was developed as a means to minimize the coupled-bunch instability due to large detuning of the accelerating mode. It is based on a three-cavity system stabilized with a $\pi/2$-mode operation [1], where a HOM-damped accelerating cavity is coupled with a large cylindrical high-Q energy storage cavity via a coupling cavity between. The ARES cavities have been successfully operated to store high-current beams stably at KEKB. Together with the current operational performance of the ARES cavity system, including accessory devices such as the input coupler, we discuss its expansion potential for the SuperKEKB project of boosting the luminosity frontiers beyond 10^{35} cm^{-2}s^{-1}. Figure 8.3

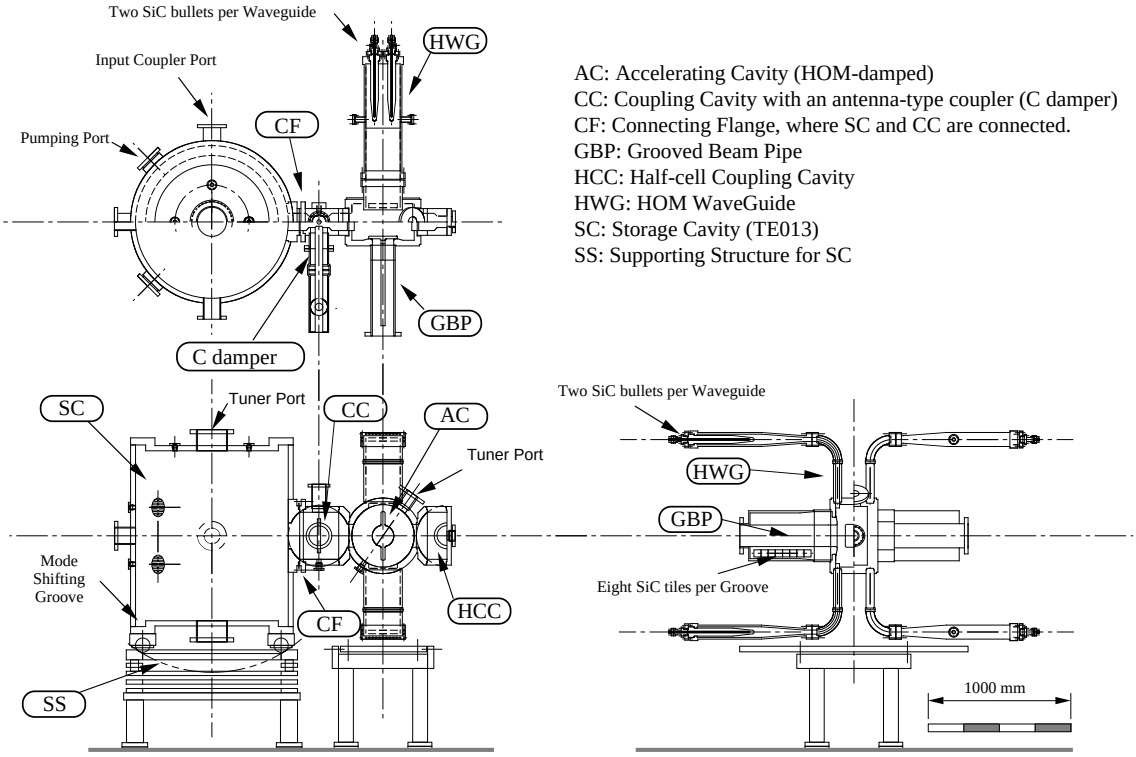

Figure 8.3: Front, side and top views of the ARES cavity for KEKB.

shows the front, side and top views of the ARES cavity for KEKB. Its design is based on a high-power conceptual demonstrator ARES96 [5] with a cylindrical energy storage cavity operated in the TE013 mode. The accelerating mode is the $\pi/2$ resonant mode of the three-cavity system. According to an equivalent circuit model [1], the stored energy ratio for the $\pi/2$ mode is given by

$$U_s/U_a = k_a^2/k_s^2 \tag{8.3}$$

where U_a is the stored energy in the accelerating cavity, U_s the energy in the storage cavity, k_a the coupling factor between the accelerating and coupling cavities, and k_s the coupling factor between the storage and coupling cavities. The energy ratio for the $\pi/2$ mode can be kept almost constant in the presence of detuning by Δf_a for the accelerating cavity loaded with beam. Therefore, the detuning for the $\pi/2$ mode will be reduced as

$$\Delta f_{\pi/2} = \frac{\Delta f_a}{1 + U_s/U_a} \tag{8.4}$$

Actually, the design ratio $U_s/U_a = 9$ for the KEKB ARES cavity gives $\Delta f_{\pi/2}$ = -20 kHz, small enough compared with the revolution frequency so that the growth rate of the most severe -1 mode of the CBI can be reduced to a level of τ=$\sim$10 ms where an RF feedback system [4] can damp it.

In KEKB, 20 ARES cavities have been successfully operated to store positron beams of up to 1.8 A in the LER, while 12 ARES cavities in combination with 8 super conducting cavities are used to store electron beams of up to 1.1 A in the HER. Many problems have been overcome one-by-one to achieve the present status [6]. Roughly, the problems can be divided into two categories: infancy problems especially with accessory devices being used in long term operation, and cavity problems attributed to quality control issues usually associated with the stringent cost goals in production phase.

Judging from the operational performance so far, we will probably be able to manage with the current version of the ARES cavity for the SuperKEKB HER at 4.1 A, 1.6 times the design beam current of 2.6 A for the KEKB LER. On the other hand, we need to upgrade the ARES cavity to operate the SuperKEKB LER at 9.4 A.

8.2.2 Fundamental mode issues

A beam current of 9.4 A will be supported by 28 ARES cavities at SuperKEKB, whereas 2.6 A is designed to be supported by 20 ARES cavities at KEKB. With the heavier beam loading of 9.4 A, the accelerating cavity itself needs to be further detuned by Δf_a = -200 kHz to -710 kHz. Consequently, the amount of detuning for the $\pi/2$ mode will become large, comparable with the revolution frequency, if the current energy ratio $U_s/U_a = 9$ is unchanged. Therefore, the first upgrade item should be to increase the energy ratio further. Fortunately, the ARES cavity system can be mechanically separated into two cavity parts: the storage cavity and the accelerating cavity part with the coupling cavity brazed. We are planning to remodel the accelerating cavity part together with the HOM loads, whereas the storage cavity will be reused.

Table 8.4 presents the RF parameters for three cases with $U_s/U_a = 9$, 15 and 18. As the energy ratio is increased, the unloaded Q value Q_0 increases, while the input coupling factor beta decreases as $1 + P_{beam}/P_c$. According to a computer simulation study, we need to increase the height of the rectangular aperture between the accelerating and coupling cavities from 160 mm to 175 mm for $U_s/U_a = 15$, and to 182 mm for $U_s/U_a = 18$, where the aperture width is fixed at 120 mm. Increasing the aperture height up to 185 mm is probably acceptable without significant changes to the cavity fabrication.

Figure 8.4 shows the real part of the coupling impedance of the $\pi/2$ mode, calculated for each case. As the energy ratio is increased, the amount of detuning decreases to less than one half of the revolution frequency, and the resonance also becomes somewhat

U_s/U_a	9	15	18	Unit
Coupling slot size (width×height)	120×160	120×175	120×182	mm^2
Beam current		9.4 (2.6)		A
Number of cavities		28 (20)		
f_{RF}		508.887		MHz
Harmonic number		5120		
Cavity voltage		0.5		MV/cav
Unloaded Q	1.11	1.27	1.32	$\times 10^5$
$(R/Q)_{\pi/2}$	15	9.4	7.9	Ω/cav
Input β	5.4	4.1	3.8	
P_c	150	210	240	kW/cav
Detuning frequency $\Delta f_{\pi/2}$	-72	-45	-38	kHz

Numbers in () for KEKB LER

Table 8.4: RF parameters of ARES cavity for SuperKEKB LER.

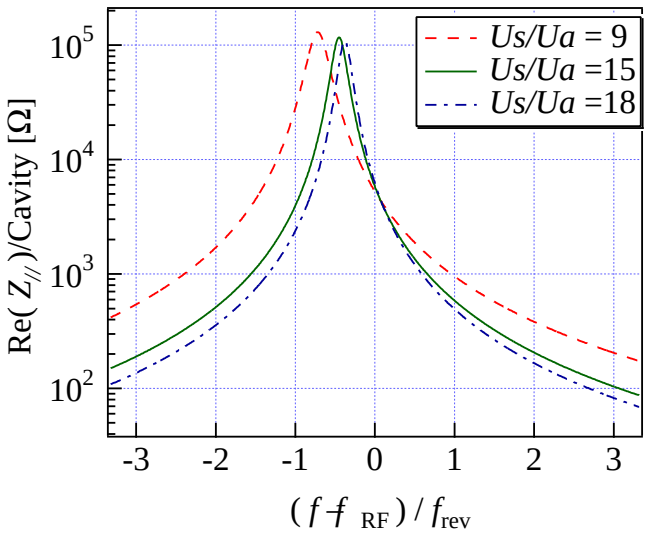

Figure 8.4: The coupling impedance of the $\pi/2$ mode loaded with 9.4 A for $U_s/U_a = 9$, 15, and 18.

sharper. That is because the loaded Q value, $Q_L = Q_0/(1+\beta)$, increases as U_s/U_a increases.

Figure 8.5 shows the growth rates calculated for the -1, -2, and -3 modes of the CBI driven by the $\pi/2$ mode, plotted as a function of the energy ratio U_s/U_a. By increasing

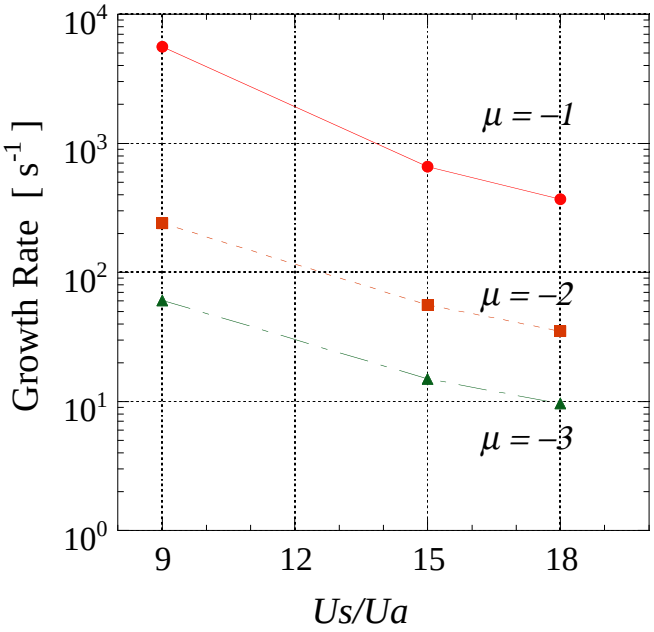

Figure 8.5: Growth rates of the CBI modes of μ = -1, -2, and -3 due to the $\pi/2$ mode, plotted as a function of U_s/U_a.

the energy ratio from 9 to 15, the growth rate of the -1 mode can be reduced by one order of magnitude, down to a manageable level of $\tau = 1.5$ ms. Balancing the relaxation in the growth rate and the increase in the cavity power P_c, an energy ratio U_s/U_a around 15 is favorable.

Another issue concerns the parasitic 0 and π modes brought about by the coupled-cavity scheme. Both parasitic modes can be damped with an antenna-type coupler attached to the center of the coupling cavity, whereas the $\pi/2$ mode does not couple to the coupler because of its field distribution with the electric-short boundary condition at the vertical mid-plane of the coupling cavity. Furthermore, the 0 and π modes are located almost symmetrically with respect to the $\pi/2$ mode to be tuned into the vicinity of the RF frequency. Therefore, the impedance contributions from the damped 0 and π modes can be counterbalanced between the excitation and damping terms for the CBI. However, the field distributions of the 0 and π modes are subject to the first order term of the tuning errors. For example, when the accelerating cavity is detuned by Δf_a, the first order perturbation term is proportional to $\Delta f_a/(f_\pi - f_0)$. Therefore, the delicate counterbalancing may deteriorate at heavier beam loading.

Figure 8.6 shows the coupling impedance of the 0 and π modes calculated for three cases: $U_s/U_a = 9$ with 2.6 A, $U_s/U_a = 9$ with 9.4 A, and $U_s/U_a = 15$ with 9.4 A. The impedance imbalance with respect to the RF frequency is also shown, where excitation is positive and damping is negative, and the fastest growth time is indicated for each case. This calculation was carried out as follows: The perturbation due to Δf_a was taken

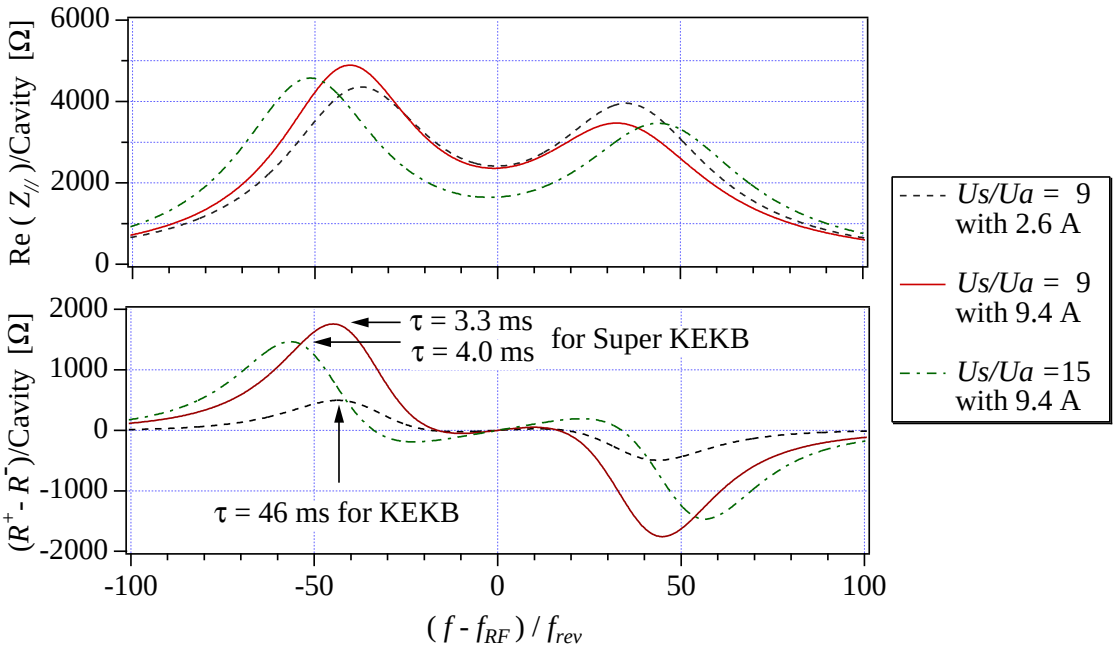

Figure 8.6: The coupling impedance (top) of the 0 and π modes, and the imbalance (bottom) with respect to the RF frequency.

into account up to the first order, and the external Q value of the coupling cavity to the antenna coupler was assumed to be 50 (the same as for KEKB), which gives Q_L =100 for the unperturbed 0 and π modes with $U_a = U_c$. As the accelerating cavity is detuned downward, the field distribution changes as $U_a > U_c$ for the 0 mode, whereas $U_a < U_c$ for the π mode, where the energy imbalance is proportional to $\Delta f_a/(f_\pi - f_0)$. For KEKB, the impedance imbalance is at an allowable level below 500 Ω/cavity, so that the CBI is expected to be suppressed well, and actually has not been observed so far. For SuperKEKB, the growth time will become 3.3 ms when $U_s/U_a = 9$. As U_s/U_a is increased to 15, the growth time will ease a little to 4 ms. That is because $\Delta f_a/(f_\pi - f_0)$ roughly reduces as k_a^{-1}, i.e. $(U_s/U_a)^{-1/2}$. In any case, some bunch-by-bunch longitudinal feedback system will be needed to suppress the CBI due to the 0 and π modes.

8.2.3 HOM load issues

The HOM-damped structure for the ARES cavity system was carefully designed to be smoothly embedded into the whole scheme without any structural or electromagnetic incompatibility. The toughest problem was an unavoidable boundary condition: two large rectangular coupling apertures at both sides of the accelerating cavity. One aperture is open to the coupling cavity, and the other to a half-cell coupling cavity for the $\pi/2$-mode termination in order to restore mirror symmetry for the accelerating field with respect to the vertical mid plane. The HOM-damped structure based on ARES96 [5] consists of four rectangular HOM waveguides (WGs) attached to the upper and lower sides of the accelerating cavity and two Grooved Beam Pipes [7] (GBPs) at both end plates, as shown in Figure 8.7, together with close-up views of the WG and GBP HOM loads [8].

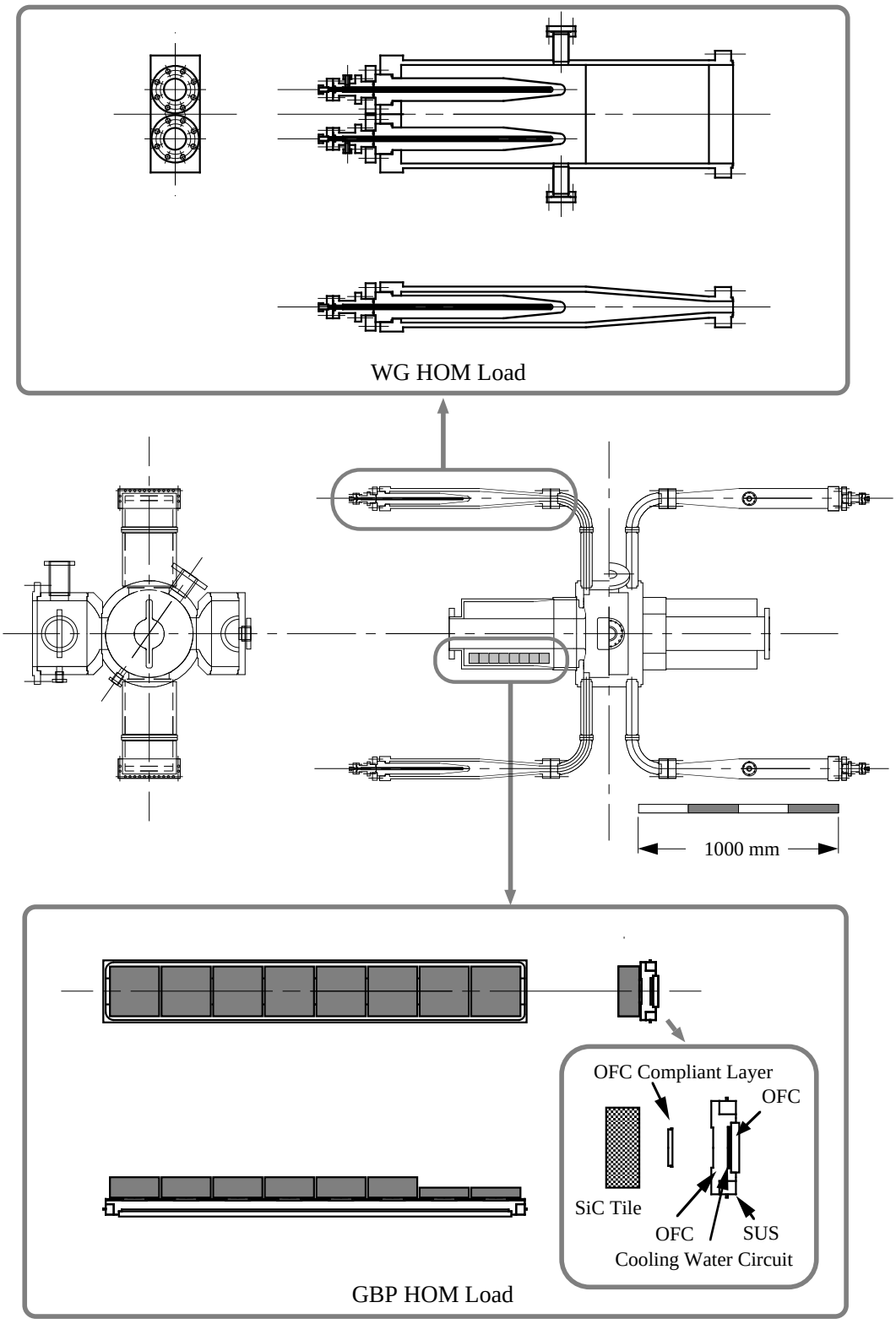

Figure 8.7: Front and side views of the HOM-damped accelerating cavity part of the ARES cavity system, together with close-up views of the WG and GBP HOM loads.

The monopole and vertically polarized dipole HOMs are guided out through the HOM WGs. The extracted HOM power is guided via an E-bend in the horizontal direction and finally dissipated in two bullet-shaped SiC ceramic absorbers which are directly water-cooled. The power capacity of the HOM absorber has been verified up to 3.3 kW per bullet (26.4 kW per cavity) at a test bench with an L-band CW klystron. But this limit was only due to the maximum power stably supplied from the klystron.

The horizontally polarized dipole HOMs are guided out through the twofold GBPs with upper and lower grooves. In each groove, eight SiC tiles are arranged in a line to absorb the extracted HOM power. Each SiC tile is brazed to a water-cooled copper plate with a copper compliant layer between. The GBP HOM load was also tested, with the same klystron, up to 0.5 kW per groove (2.0 kW per cavity) without any significant vacuum pressure rise observed.

Figure 8.8 shows the WG and GBP HOM load powers per cavity plotted as a function of the KEKB LER beam current (1224 bunches with 4-bucket spacing), together with the sum of these, i.e. the total HOM power dissipation per cavity. These data are

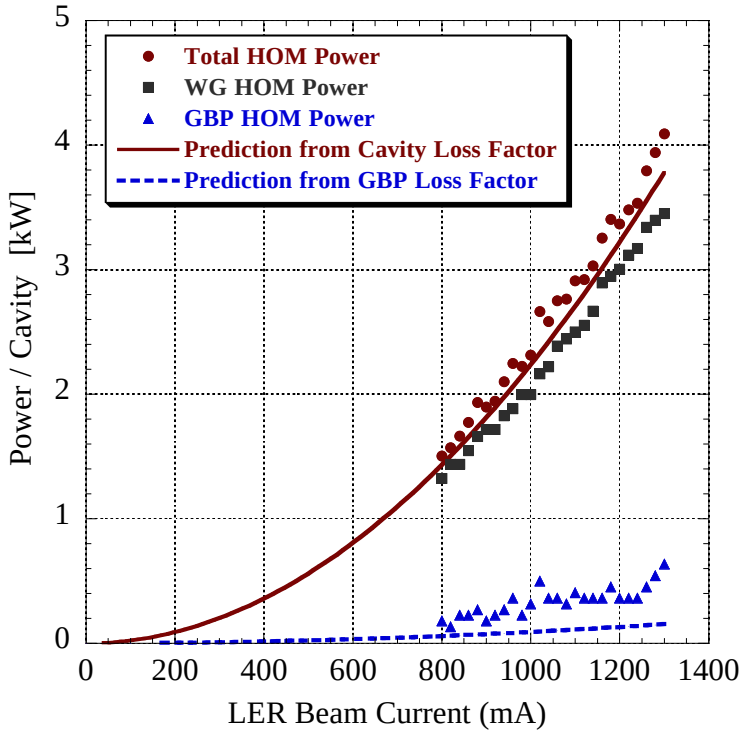

Figure 8.8: HOM load powers per cavity measured in the KEKB LER, compared with theoretical predictions.

based on calorimetric measurements for the WG and GBP loads at the downstream side with respect to the beam direction, and obtained by simply doubling the measured data owing to the mirror symmetry with respect to the beam direction (see the side view in Figure 8.7). Furthermore, the total HOM power and the GBP HOM power are compared with theoretical predictions shown by the solid and dashed curves, respectively. These two predictions are based on the loss factors computed with 3D-MAFIA for following two cases: the whole damped structure (AC + 2GBP); and the two GBPs only (2GBP), where

the bunch length $\sigma_z = 7$ mm was assumed in accordance with other measurements. Figure 8.9 shows the computed loss factors plotted as a function of the bunch length, together with simulation results computed with 2D-ABCI assuming a simplified axially symmetric accelerating cell with circular beam pipes (AC + 2CBP) instead of the GBPs. Considering

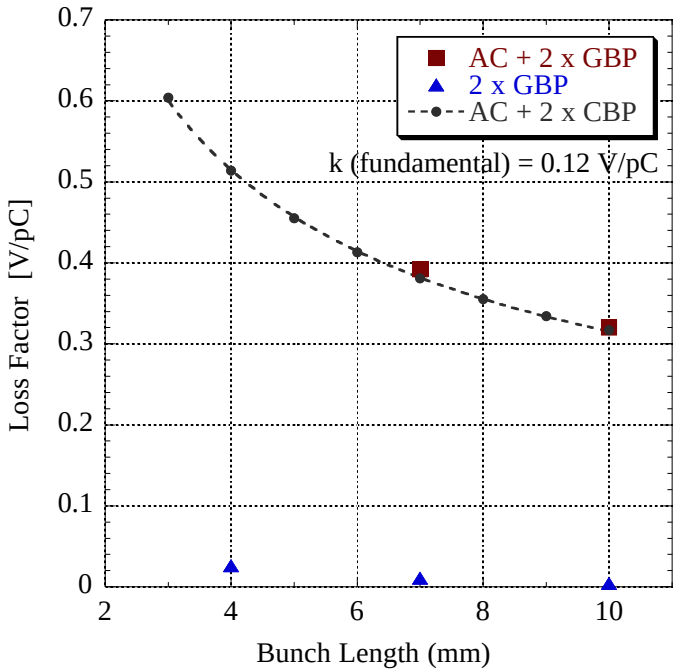

Figure 8.9: Loss factors computed for the whole damped structure and the two GBPs only are plotted as a function of bunch length, together with those for a simplified axially symmetric structure with circular beam pipes.

the errors in the calorimetric measurements, estimated as 10% for the WG load and 13% for the GBP load, the total HOM power data agrees well with the theoretical prediction. On the other hand, the excess of the measured GBP power over the prediction might be due to the mirror asymmetry of the accelerating cavity with respect to the vertical mid plane including the beam axis (see the front view in Figure 1). That is because the half-cell coupling cavity can restore mirror symmetry for the fundamental mode only.

According to the HOM power measurements and the loss factor computations, the WG and GBP HOM powers per cavity have been estimated as ∼80 kW and ∼20 kW, respectively, for a beam current of 9.4 A (5000 bunches with σ_z=3 mm). Therefore, we will need to upgrade both of the WG and GBP loads, for example: to increase the number of absorbers per WG load, depending on the results of the high power testing to be resumed soon; to replace the current GBP with a winged chamber loaded with directly water-cooled SiC absorbers as shown in Figure 8.10. Actually, this kind of chamber has already been developed in collaboration between the KEKB vacuum and ARES cavity groups, and several chambers have been installed to absorb the HOM power at the mask chamber sections in KEKB [9].

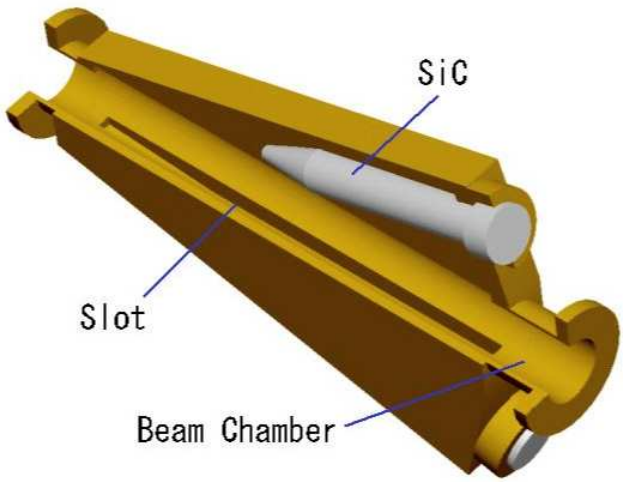

Figure 8.10: Winged chamber [9] loaded with directly water-cooled bullet-shaped SiC absorbers.

8.2.4 Coupler issues

The input coupler is an important accessory device through which the RF power is to be fed into the ARES cavity system, and also has a ceramic window to serve to separate vacuum and atmosphere. Figure 8.11 shows a schematic drawing of the input coupler [10] developed for the ARES cavity. The RF power coming through the rectangular waveguide

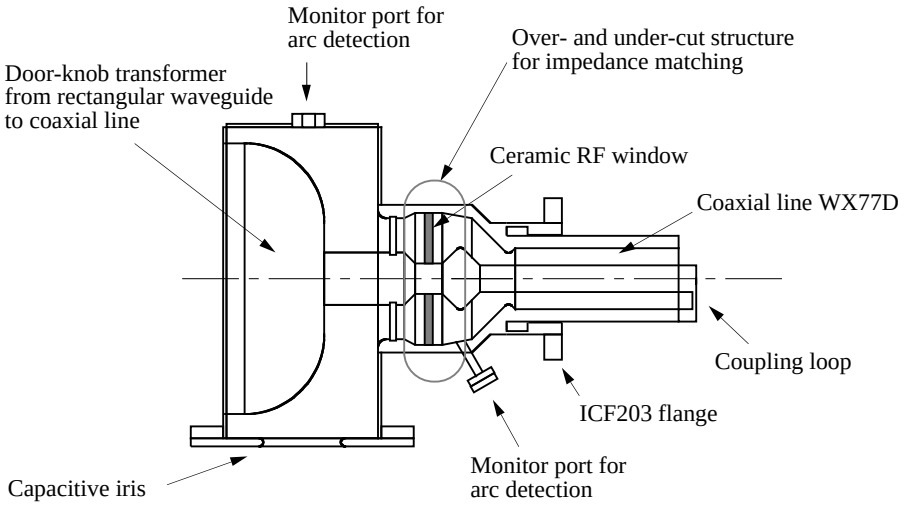

Figure 8.11: A schematic drawing of the input coupler for the ARES cavity.

WR1500 is transferred, via a doorknob transition with a capacitive iris at the entrance, to the coaxial line WX152D with a disk-type ceramic window where the coaxial line is over- and under-cut for impedance matching. Further, the coaxial line is tapered and reduced to a straight section of WX77D, and finally terminated with a magnetic coupling

loop. When driving the ARES cavity system, the input coupler is to be attached to one of the three circular ports at the middle level of the cylindrical side of the storage cavity. The design power capability of the input coupler is 400 kW at maximum for KEKB, and needs to be increased to 800 kW for SuperKEKB.

In advance of the coupler production for KEKB, prototype couplers had been tested up to 950 kW at a test stand with a through combination of two couplers as shown in Figure 8.12, where the two coupling loops were facing and electromagnetically coupled with each other in a two-port cylindrical vacuum chamber. The RF power went through

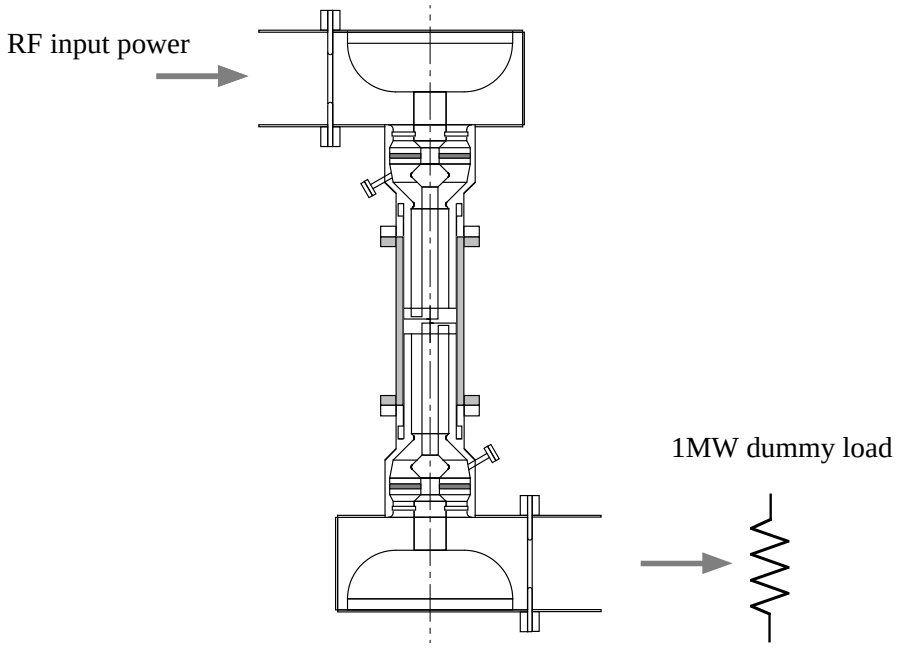

Figure 8.12: Through-combination of two couplers for high-power test.

those two couplers and dissipated in a 1-MW water load of the rectangular waveguide type WR1500. This result might allow us to claim that the current input coupler has been qualified for SuperKEKB. However, this statement can not be fully supported because the through-combination setup fails to simulate the actual operating condition for the input coupler attached to the ARES cavity system. As stated before, the ARES cavity has a large amount of electromagnetic stored energy and becomes a reactive load for the input coupler when the optimum coupling condition is not realized. Thus, the actual operating condition is much more sever than that for the coupler under high-power test with a matched resistive load.

In order to ensure the stable performance of the input coupler to feed an RF power of 800 kW into the ARES cavity system, we need another high-power test setup, where the actual operating condition for the input coupler can be reproduced as exactly as possible. Recently, we have started the first phase of the input coupler R&D [11] for SuperKEKB. The primary target is to make a prototype coupler for SuperKEKB by improving the reliability of the input couplers currently used at KEKB. Actually, our immediate plan is to suppress multipactoring discharge at the straight coaxial line section (WX77D), which a few out of 32 couplers in KEKB have been suffering from. Figure 8.13 schematically shows the setup for the first phase of the R&D. One of the storage cavities in reserve

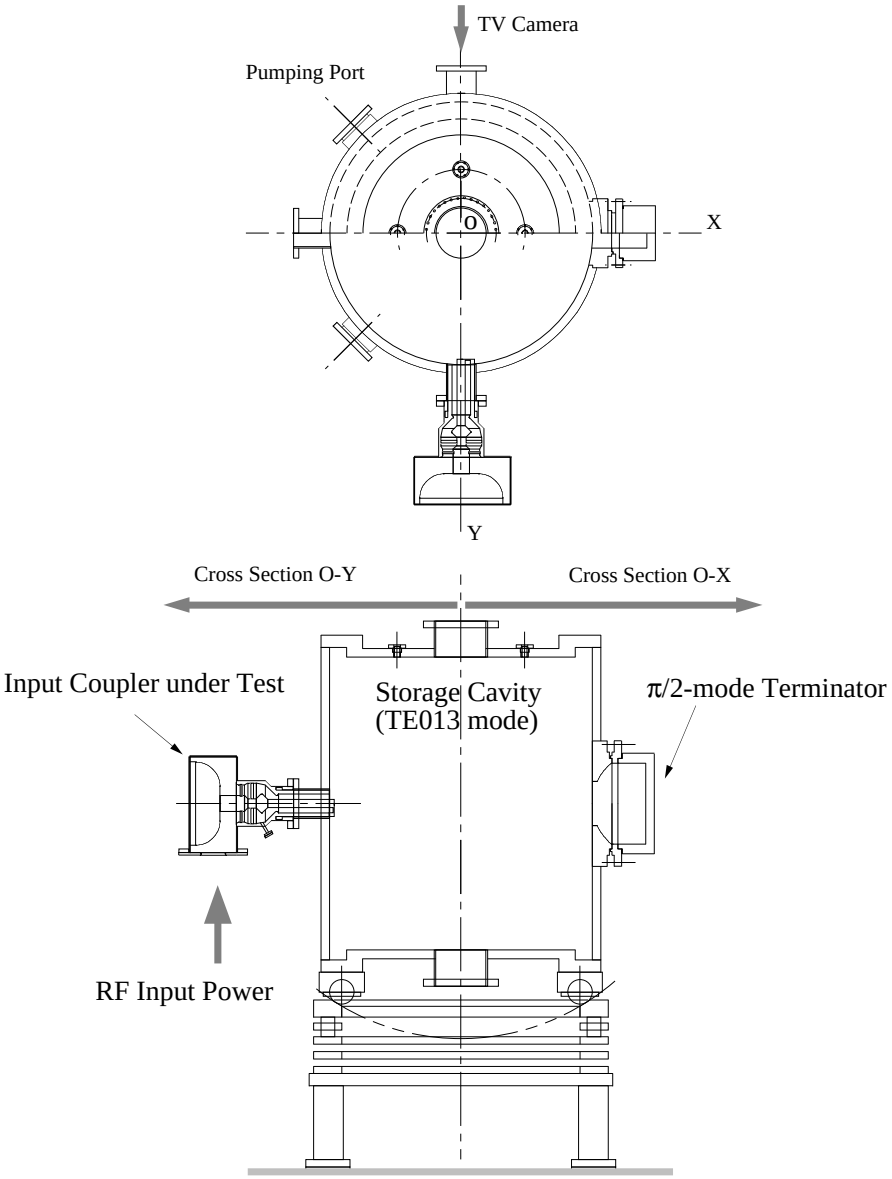

Figure 8.13: Setup with use of a storage cavity for high-power testing of the input coupler.

for KEKB is used, and a box-shaped structure for the $\pi/2$-mode termination is attached to the rectangular flange, to which the coupling cavity is to be connected for the full setup of the ARES cavity. The $\pi/2$-mode terminator is a water-cooled copper box with a rectangular stainless steel flange, originally developed for high-power testing of the storage cavity itself. The input coupler is attached to one of the three driving ports with a coupling factor (β) of about 3, nearly the same as that for driving the ARES cavity in KEKB. This setup has the following advantages. The first is that the input coupler can be tested under the same condition as for driving the ARES cavity system. The second is that the storage cavity itself is almost free from multipactoring discharge since it is operated in the TE013 mode. Up to now, three KEKB input couplers have been tested with this setup. The conditioning was carried out automatically with use of a computer, keeping the vacuum pressure below a specified level. The couplers have been conditioned up to 500 kW at maximum, which is enough for KEKB use. However, this limit was due to an enormous wall power dissipation of over 300 kW for the storage cavity, more than three times the design wall power of 90 kW, although the flow rate of cooling water was increased from 150 ℓ/min (design) to 300 ℓ/min. During the conditioning, the coaxial line part was monitored with a TV camera attached to the port opposite the coupler. In two of the three couplers, multipactoring discharge was observed inside the coaxial line, as shown in Figure 8.14, in the range of RF input power from 150 to 190 kW. The

Figure 8.14: Multipactoring discharge in bright blue inside the coaxial line of the input coupler, observed with a TV camera from the opposite side of the driving port. The silhouette of the coupling loop can be seen at 10 o'clock.

discharge was accompanied by a vacuum pressure rise and temperature rise of the cooling water for the inner and outer conductors of the coaxial line part. The heat load to the outer conductor due to the discharge was found to be significantly larger than that to the inner conductor. Fortunately, the multipactoring finally disappeared after careful pattern conditioning in that power range for both couplers. According to a computer simulation study on multipactoring and the temperature data of the cooling water, the observed discharge phenomenon can be considered to be single-surface multipactoring on the outer conductor surface [11]. At present, we are planning to apply TiN-coating to the outer conductor surface as well as to the ceramic RF window in order to reduce the secondary electron yield coefficient.

As stated above, the current setup with use of a storage cavity has a disadvantage that the cavity wall power dissipation limits the RF input power below 500 kW. For the next R&D phase, it will be indispensable to carry out high-power testing over 800 kW under the same condition as will be seen at SuperKEKB. Figure 8.15 schematically shows

a solution to this requirement, where another coupler is attached to the storage cavity and the extracted RF power is dissipated in a dummy load.

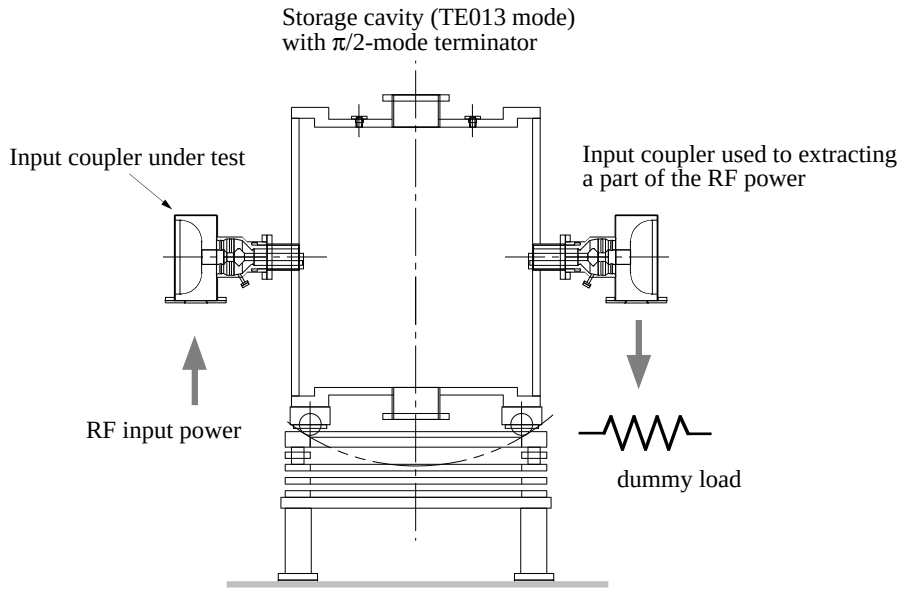

Figure 8.15: Setup with use of a storage cavity for high-power testing over 800 kW, where another coupler is attached and the extracted RF power is dissipated in a dummy load.

Another important accessory device is a coaxial-type antenna coupler [12], which is called a C-damper for short. The C-damper is to be installed on the central circular port of the coupling cavity in order to damp the parasitic 0 and π modes. As shown in Figure 8.16, the coupler is a coaxial line (WX120D) complex, which consists of a cross-stub support and a disk-type ceramic RF window, where the coaxial line is over- and under-cut for impedance matching. The extracted RF power is guided through a tapered coaxial line (WX120D-WX77D) and a directional coupler (WX77D), and finally to a water-cooled dummy load (40-kW CW). The RF window, similar to that for the KEKB input coupler, is expected to have enough power capability, over 100 kW. Therefore, the current C-damper will be used in SuperKEKB although the dummy load should be upgraded.

8.2.5 Summary

We have investigated the growth potential (or the critical limits) of the ARES cavity system including its accessory devices for use in the SuperKEKB LER at a beam current of 9.4 A.

By increasing the stored energy ratio U_s/U_a from 9 to 15, the severest -1 mode of the longitudinal CBI due to the $\pi/2$ mode can be eased by one order of magnitude down to a level of τ =1.5 ms, where an RF feedback system can to damp it. The growth time of the CBI due to the impedance imbalance between the parasitic 0 and π modes has been estimated to be $\tau = 4$ ms, faster than that for KEKB by one order of magnitude. However, this growth time may be comparable with those expected for other HOM-driven CBI modes. A bunch-by-bunch longitudinal feedback system will be needed.

As for the HOM loads, we will need to upgrade the power capabilities of the WG and GBP loads up to $\sim$80 kW and $\sim$20 kW per cavity, respectively. The grooved beam

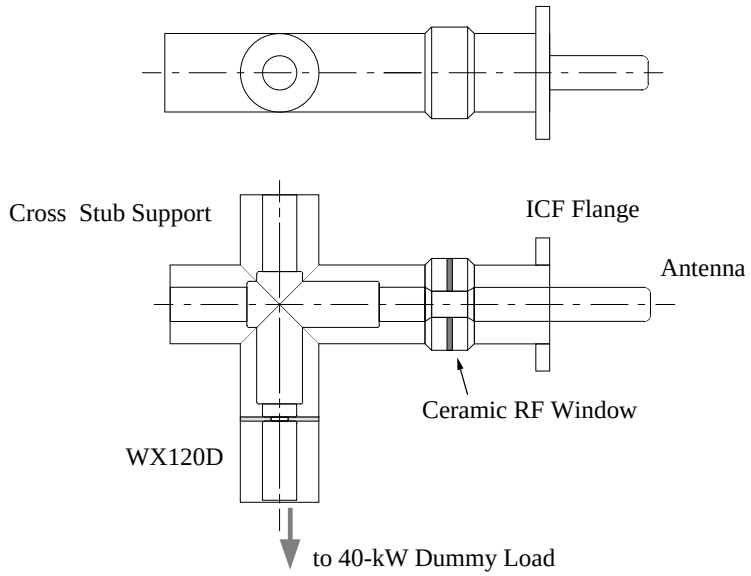

Figure 8.16: A schematic drawing of C-damper (a coaxial-type antenna coupler) attached to the coupling cavity in order to damp the parasitic 0 and π modes.

pipe may need to be upgraded to a winged chamber loaded with directly water-cooled SiC absorbers. Our immediate action should be to resume high-power testing for the HOM-loads, hopefully with a new L-band klystron supplying more than 10 kW.

The first phase of the R&D for the input coupler feeding RF power more than 800 kW into the ARES cavity is being carried out with a new high-power test setup with use of the storage cavity as load. Our immediate target is to improve the reliability and production yield of the KEKB couplers by suppressing the multipactoring discharge inside the coaxial line section by TiN coating.

8.3 Superconducting cavity

8.3.1 Introduction

The development of the SC damped cavity for KEKB began in 1991, aiming at achieving a sufficiently low higher order mode (HOM) impedance to avoid CBI and the high power handling capability required for an ampere-class beam intensity of KEKB. Optimization of cavity shape, HOM damping scheme, and an input coupler of several hundred kW were the main items of R&D for the SC damped cavity system.

The SC damped cavity is based on the single mode cavity proposed by T. Weiland [13], where the HOM modes in the cavity propagate out through the large beam apertures along the beam axis and are absorbed by dampers located in the beam pipes. Although this cavity shape has the disadvantage of a rather low R/Q as compared with normal-conducting cavities, the high Q of the SC cavity can still maintain the high shunt impedance R of 10^{11} Ω. The design of the cell shape was completed in 1992. A single cell cavity has a beam aperture of 220ϕ to achieve an external Q of 100 for monopole modes, and a 300ϕ cylindrical wave guide is attached on one side to extract the lowest dipole modes of TE11 and TM11 [14]. On the other hand, the direct connections of such large apertures to the

beam ducts can give rise to a large loss factor for a short bunch length. In order to reduce the loss factor, a beam-duct diameter of 150 mm is adopted at the RF sections and long tapers are used to connect the cavities and the ducts.

Each SC module has IB-004 ferrite absorbers of 300ϕ on one side and 220ϕ on the other side bonded on the inner surface of copper beam pipes by the Hot Isostatic Press (HIP) method, where sintering and bonding are done simultaneously [15]. The size and location of these absorbers as well as the connecting tapers were carefully optimized both by simulation codes and by measurements. The input coupler is a coaxial antenna type using a 152ϕ ceramic disk, which can transfer a traveling RF of 800 kW [16]. The inner and the outer conductors are cooled by water and He gas vapor, respectively. Penetration of the coupler tip into the beam pipe is chosen to be 12 mm to obtain an external Q of $5\times\ 10^4$.

Construction of the first four SC cavities started at the end of 1996 and was completed in 1998. The existing cryogenics that were used in KEK-TRISTAN, such as a 6.5 kW refrigerator system and the main He transfer line, have been reused. In the summer of 2000, another four cavities were added. Since their commissioning, the cavities have been operating successfully [17]. The maximum current of the HER exceeded the design current of 1.1 A with a four-bucket bunch spacing and a bunch length of 7 mm.

8.3.2 KEKB SC cavity

Cavity

A cross sectional view of the KEKB SC cavity is shown in Fig. 8.17, and the cavity parameters of the accelerating mode are summarized in Table 8.5.

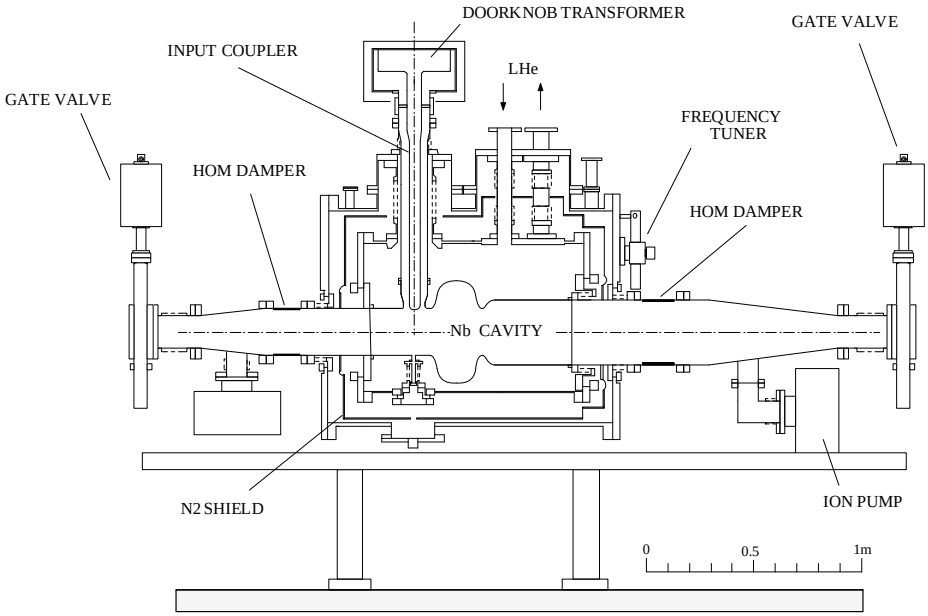

Figure 8.17: Superconducting cavity for KEKB.

Frequency	508.8	MHz
Gap length	243	mm
Diameter of aperture	220	mm
R/Q	93	Ω
Geometrical factor	251	Ω
Esp/Eacc	1.84	
Hsp/Eacc	40.3	Gauss/(MV/m)

Table 8.5: Cavity parameters of the KEKB superconducting cavity.

The cavity is made of 2.5 mm thickness Nb sheet RRR 200, formed by the spinning method. The process of surface treatment using electro-polishing was almost the same as that of TRISTAN cavities. To obtain a carbon free surface so as to suppress discharging, hydrogen peroxide rinsing was replaced by ozonized-ultrapure-water rinsing(OUR). The OUR treatment effectively removes the carbon contamination from the electro-polished Nb surface. Cold tests of the KEKB cavities showed sufficiently high Q values and a maximum accelerating field of 18.7 MV/m at 4.2 K. An air-exposure test of an OUR rinsed test cavity did not show any degradation of cavity performance, so all the cavities were rinsed with OUR and exposed to air for two days during full assembly into the cryostat. In the test of the fully assembled modules, the accelerating field of all cavities reached 10 MV/m after CW processing and by pulse aging, in which pulsed power of 5% duty cycle was added to the CW power level of just below the quench level.

One of the most troublesome issues of the SC cavity is RF trips due to discharging in the cavity and the input coupler region. From the experience of TRISTAN operation, the discharging was caused by a large amount of condensed gas on the cold surface. In the beam test in the Accumulation Ring (AR) in 1996, the prototype cavity frequently tripped from the arcing interlock of the input coupler, which was due to the poor vacuum pressure of the beam ducts and a large amount of gas which penetrated into the cavity. The trip rate was reduced by an improvement to the vacuum pumping system of the beam ducts and by the OUR-treatment of the beam duct surface. Therefore, at KEKB, NEG pumps are distributed every 60 cm in the beam pipes to protect the cavities against gas coming from the beam ducts.

The accelerating field in the cavities was measured using a vertical cryostat. The results were greater than 15 MV/m as shown in Fig. 8.18. Although the accelerating field decreased to 10∼12 MV/m after full assembling, it still exceeds the necessary operating field of 6∼8 MV/m.

HOM damper

Fig. 8.19 shows the HOM dampers made of IB-004 ferrite using the HIP method. The maximum power of 11.7 kW and 14.8 kW were given successfully to the 220 mm diameter and the 300 mm diameter dampers at a test stand using coaxial line with a 508 MHz klystron. In the high current beam operation at KEKB, a maximum HOM power of 12 kW per cavity can be absorbed by the HOM dampers without any damage.

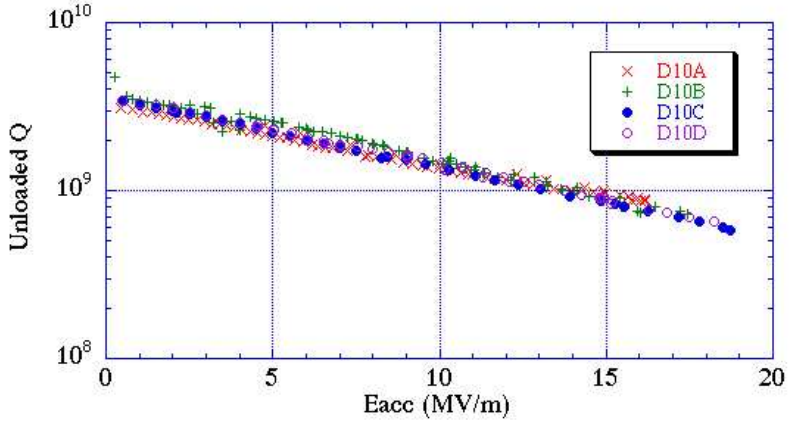

Figure 8.18: Vertical measurement.

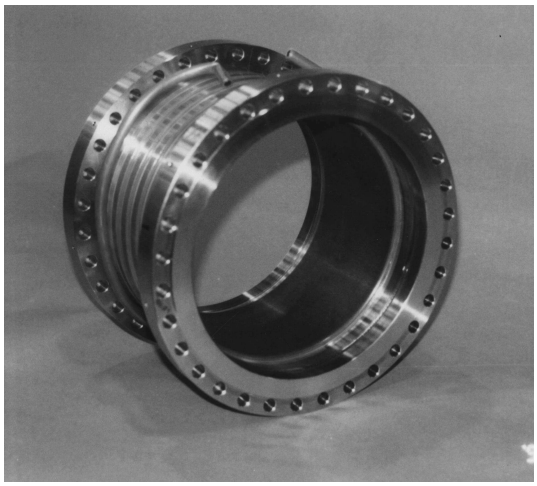

Figure 8.19: HOM damper.

Input coupler

Figure 8.20 shows a drawing of the input coupler. The gap length of 4 mm in the choke structure was used in order to reduce the field strength at the ceramic disk. For stable operation of the input coupler, the inner conductor is cooled by room temperature water. The calculated heat transfer by radiation is 0.6 W for the electro-polished mirror-like Cu surface. This heat transfer of 0.6 W is sufficiently small compared with the total loss of the cavity and has shown no trouble during operation so far even at the power level of 500 kW. The water flow rate of 1.5 l/minutes has enough cooling capacity for up to 1 MW. The ceramic window of the coupler is the same as that of 1 MW klystrons, which has shown a long lifetime of more than 50000 hours. However, the KEKB couplers need more diagnostics for precise RF processing and an interlock system for operation under bad vacuum condition compared to the klystrons. For this purpose, three monitoring ports surround the ceramic window to monitor vacuum pressure, electron and discharge light(arc sensor) for protection and diagnosis.

The KEKB couplers were conditioned to 800 kW with traveling wave and 300 kW with totally reflected standing wave, by changing the phase up to a half wave length. At the AR beam test, we developed a biased-type doorknob transition aiming at suppressing

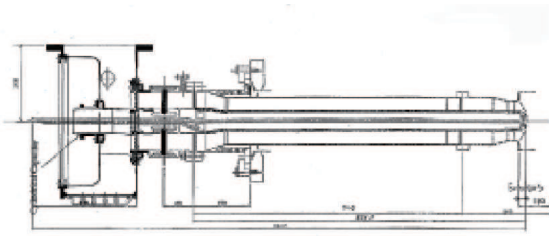

Figure 8.20: Input coupler.

multipactoring of the input coupler. The inner conductor and the doorknob were electrically isolated by two layers of polyimide (similar to Kapton) films with a thickness of 0.125 mm, which created a capacitance of 1300 pF. The prototype could supply power of up to 300 kW of both traveling and standing wave without any problem, even for the RF changing a phase by a half wave length. The bias-type door-knob transitions for KEKB cavities has been tested up to 500 kW in the transmission condition and 300 kW in the full reflection condition.

Operation status in KEKB

Four SC cavities were installed at D11 in 1998 and another four SC cavities were added in D10 in 2000. Fig. 8.21 shows the lineup of SC cavities in the D11 site. Table 8.6

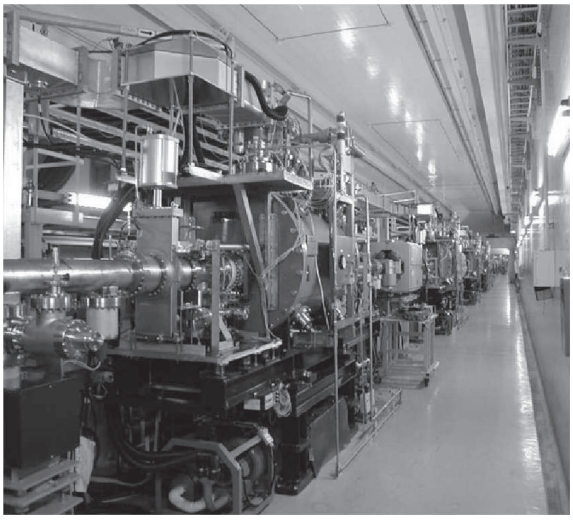

Figure 8.21: The SC cavities installed in the D-11 straight section.

summarizes the figures achieved by the SC cavities. Most of the cavities have been conditioned to 2.5 MV (10 MV/m). The operating voltage is typically 1.2∼1.4 MV per cavity, slightly less than the design value of 1.5 MV. The reason is to have a longer bunch length compared with the design value so as to reduce HOM heating in various vacuum components. In order to demonstrate the performance at higher operating voltage with a high current beam, one cavity (D11-B) has been operated at 2.0 MV for a month. The result was satisfactory.

Figure 8.22 shows the input and reflected power of the D11-A cavity as a function of

	Design	Achieved
Number of SC cavities	8	8
Beam current	1.1 A in 5000 bunches (2.2 nC/bunch)	1.2 A in 1284 bunches (9.4 nC/bunch) 0.78 A in 790 bunches (9.9 nC/bunch)
Bunch length	4 mm	6∼8 mm
RF voltage without beam	-	>2.5 MV/cavity
RF voltage with beam	1.5 MV/cavity	1.2∼2.0 MV/cavity
Q value	1×10^9 at 2 MV	$1\sim2\times10^9$ at 2 MV $0.3\sim 1\times10^9$ at 2.5 MV
Max. power transferred to beam	>250 kW/cavity	370∼380 kW/cavity
HOM power	5 kW/cavity at 1.1A	12 kW/cavity at 1.2A

Table 8.6: Summary of figures obtained in operation.

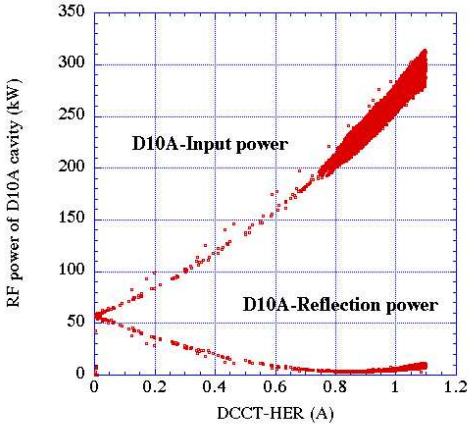

Figure 8.22: Input and reflected power of the D11A cavity.

the beam intensity. The input coupling is close to the optimum value at 0.7∼1.1 A, where the machine is typically operated for physics running. Thus most of the input power is transferred to the beam efficiently. The maximum power transferred to beam is 380 kW, much higher than the design value. This mark was reached before the D10 cavities were added, when larger power per cavity was needed.

In the physics run operation, four-bucket bunch spacing is chosen to avoid the beam blow-up in LER due to the photo-electron cloud and to optimize the luminosity. Due to the number of bunches being lower than the design by a factor of four, the HOM power is much higher than the design value at the same total beam current, even with a longer bunch length of 6∼8 mm. Too much HOM power would raise the surface temperature of the ferrite absorbers and considerably increase out-gassing. Figure 8.23 shows the HOM power of the D11-A cavity measured during physics run operation. The HOM power exceeds 10 kW per cavity, more than twice the design value.

No beam instability due to SC cavities has been observed for the beam up to 1.1 A so far. The rate of beam aborts due to trips of SC cavities is typically several times per

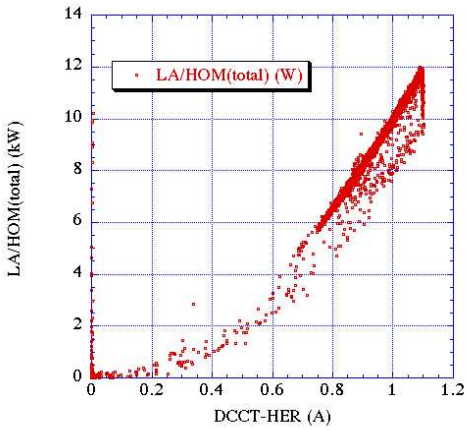

Figure 8.23: The result of the HOM power test.

month. In summary, the SC cavities for KEKB have shown excellent performance.

8.3.3 Issues for SuperKEKB

Based on the performance of the SC cavities at KEKB, we do not find any serious problems with the SC cavity itself from the viewpoints of the accelerating field, HOM impedance, and long-term stability. Key issues for the much higher beam current of 4.1 A in the SuperKEKB HER are related to the important accessory devices such as the HOM damper and the input coupler, as discussed below.

- The tapers connecting the cavity and the beam ducts significantly contribute to the loss factor around the cavity region. At σ_z=3 mm the loss factor would be 2.5 V/pC, if the same beam pipe diameter of 150 mm as KEKB is used. By using a larger beam pipe of 220ϕ, the loss factor will be reduced to 1.8 V/pC. Then the expected power load to the HOM absorbers is 50 kW per cavity at 4.1 A. Large aperture gate valves should also be developed for the larger beam ducts.

- The HOM damper is the most difficult issues for the SC system of SuperKEKB. We have started to test the limitation of handling power with the present dampers. If it does not meet the requirements, a new damper design may be needed, such as using a reduced thickness of ferrite or choosing another material.

- The input coupler for the SuperKEKB SC cavity is almost the same design as that of KEKB cavities. At a test bench, the couplers have been tested up to 800 kW with a through traveling wave condition. They have been stably operated with a high current beam of 1.1 A in KEKB at an input power of 300 kW. To check the performance at the power level of about 500 kW required for SuperKEKB, we will test the existing couplers by increasing the power level gradually in KEKB. It can be done by changing the phase of one cavity with respect to the others so that higher beam-loading is imposed on it.

8.4 High-power and low-level issues

8.4.1 High-power and low-level components

In each RF unit, the high-power RF system for the generation and distribution of power consists of a 1.2 MW klystron, its power supply, a 1 MW circulator, a 1.2 MW water load, WR-1500 waveguide components, cooling system, etc. Various improvements and modifications have been performed on the klystrons to obtain upgraded characteristic and greater stability [18] [19]. The klystron power supplies have been improved to eliminate any false firing of the crowbar circuit, which had been a long-standing problem in TRISTAN operation. Most of the high-power components of KEKB will be reused in SuperKEKB, which greatly reduces construction cost. Since the operating RF power in SuperKEKB will be close to 1 MW, higher than the current operation level of 700 kW in KEKB, it is planned to check and improve the performance, such as operating the power supplies at a higher voltage and more effective cooling of the high-power components.

The low-level control system consists of the reference line to distribute the RF signal along the ring [20], the tuning control system and feedback loops to control the accelerating field [21], protection system for the cavities and other hardware components [22]. Most of the low-level system for SuperKEKB can be made similar to those at KEKB, although some of analog parts may be replaced with digital ones. One of the key issues is the -1 mode damping system for curing the strong CBI due to the accelerating mode, which is described below.

8.4.2 The -1 mode damping system

During the operation of KEKB, instability due to the large detuning of the accelerating mode has not been observed in the HER up to a beam current of 1.2 A. In the LER, however, the -1 mode instability occurred at 1 A, a much lower current than was expected. One reason is that the operating RF voltage is lower than the design value. Another possible reason is that the feedback loop in the RF system for the zero-mode stabilization may affect the -1 mode impedance. In order to increase the beam current, it was decided to implement the -1 mode damping system in the LER, which we had developed as a backup scheme for the ARES [4].

For SuperKEKB, with the ARES cavities modified in order to increase the stored energy, the calculated growth rate in the LER is shown in Fig. 8.24 as a function of the beam current. Although the growth time is eased from 0.3 ms to 1.6 ms by the modification of the ARES, it is still shorter than the radiation damping time of 30 ms by a factor of 20. Furthermore, the growth time in the HER is as fast as 1 ms, since it is mainly determined by the SCC. Therefore, the instability must be cured by a feedback system specific to the -1 mode. Further study to check the performance limit of the existing damper a nd the R&D to improve the performance, if necessary, will be continued. The implementation of the -2 mode damper can be done by simply adding a -2 mode filter in parallel to the -1 mode filter. The existing damping system and the operation status at KEKB are described below.

System Description

Figure 8.25 shows the block diagram of the -1 mode damping system. A beam signal from

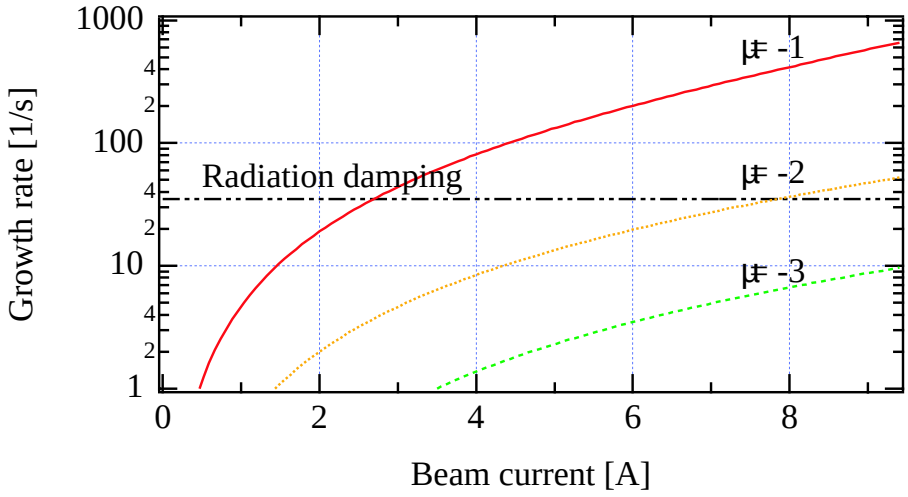

Figure 8.24: Calculated growth rate of the coupled-bunch instabilities due to the accelerating mode for the case of $U_s/U_a = 15$ in SuperKEKB.

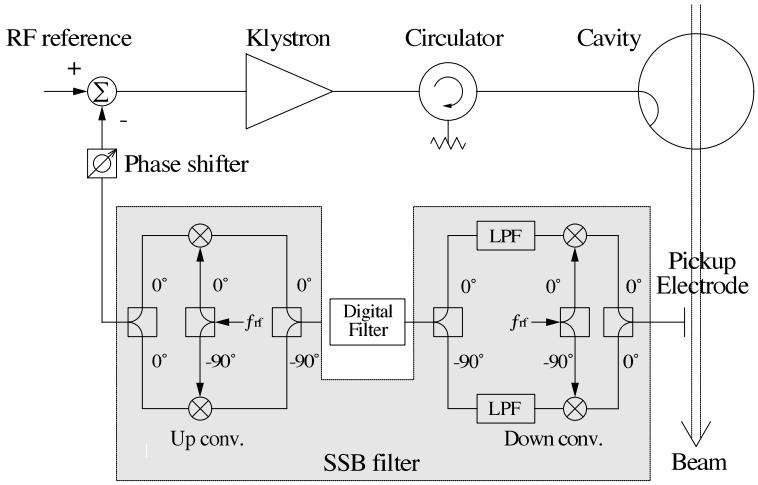

Figure 8.25: Block diagram of the -1 mode damping system.

a pickup electrode is down-converted to the baseband frequency, then filtered to pick up the -1 mode signal using a digital filter. After being up-converted to the RF frequency and adjusted in phase, it is fed back into the RF signal path to the cavity. The feedback is carried out only on the lower side of the RF frequency peak by using a single-sideband (SSB) filter that cuts the signal on the upper side of the RF frequency peak. The advantage of the SSB method is that the impedance at the upper side of the RF frequency peak that contributes to damp the -1 mode is not affected by the feedback. Figure 8.26 shows the measured transfer function of the SSB filter. It is seen that the filter rejects the signal on the upper side of the RF frequency peak. We have developed a new digital filter and replaced the analog one [23]. Fig. 8.27 shows the measured transfer function of the digital filter. In order to adjust the center frequency of the filter to the synchrotron upper sideband, the frequency offset relative to the revolution frequency (99.4 kHz) can be changed from 0 to -3 kHz by a 20 Hz step.

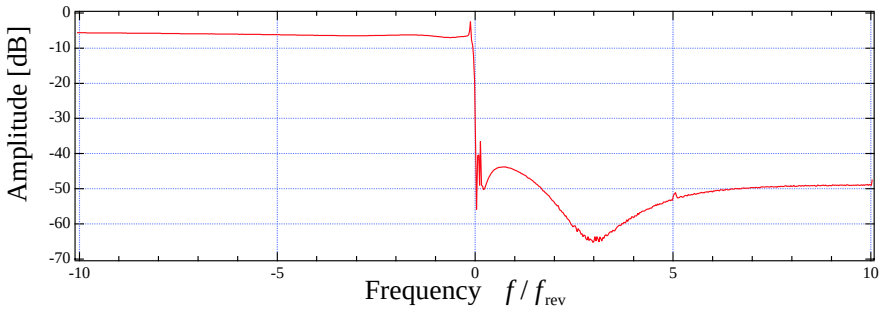

Figure 8.26: Measured transfer function of the SSB filter.

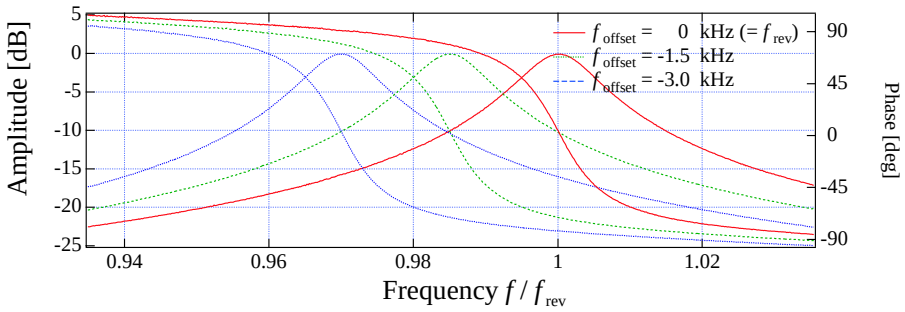

Figure 8.27: Measured transfer function of the digital filter.

Operation of the -1 mode damper

A preliminary test of the -1 mode damper was carried out in the LER in December 2001. The instability was excited by intentionally detuning two ARES cavities by -60 kHz. The -1 mode damper was implemented in one of eight RF stations. Fig. 8.28 shows the

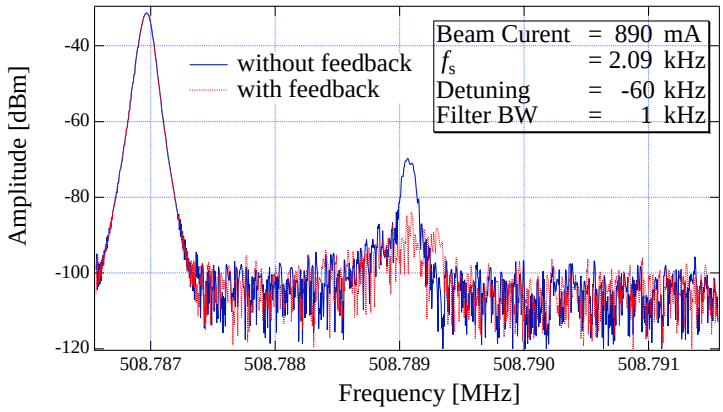

Figure 8.28: Measured spectrum of the -1 mode with and without the feedback in LER.

measured spectrum of the -1 mode with and without the feedback. The amplitude of the -1 mode upper synchrotron sideband decreased by 15 dB when the feedback loop was closed. Fig. 8.29 shows the change of the measured amplitude of the -1 mode oscillation when the feedback is switched off. The amplitude rapidly increases until the beam is finally lost. Thus the effectiveness of the damper was demonstrated.

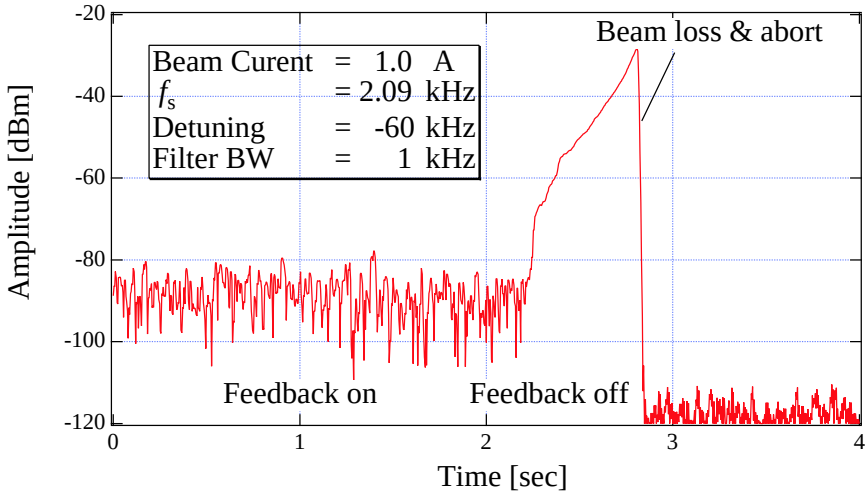

Figure 8.29: The change of the amplitude of the -1 mode oscillation when the feedback is switched off.

After this experiment, the -1 mode damper was incorporated into the RF system and has been operating stably. Fig. 8.30 shows the effect of the feedback during a beam

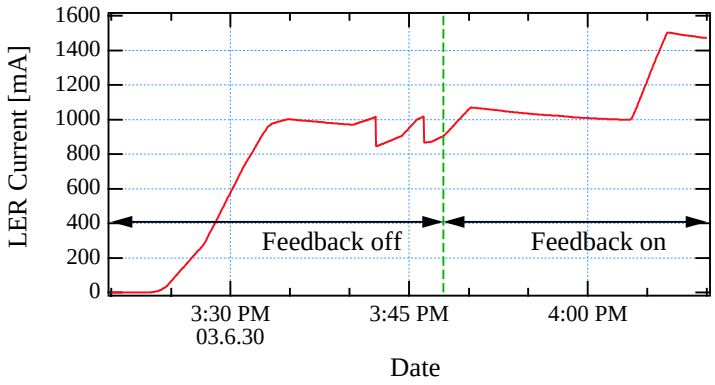

Figure 8.30: LER beam injection with and without the feedback.

injection. When the feedback is off, the beam current is saturated at 1 A and beam loss even occurs. After the feedback is switched on, the beam current could be increased. Fig. 8.31(a) and (b) show the measured spectrum of the -1 mode without and with the feedback. When the feedback is off at 1 A, the amplitude at the upper synchrotron sideband of the -1 mode is about the same as that of the revolution harmonic frequency (Fig. 8.31(a)). Thus a strong oscillation is excited. With the feedback on, the oscillation is sufficiently damped (Fig. 8.31(b)) and the beam current can be increased up to 1.86 A. This means that the feedback damping time is shorter than 8.5 ms.

The present limitation of the beam current in LER is not caused by the -1 mode instability. The beam current is rather determined by optimizing the luminosity.

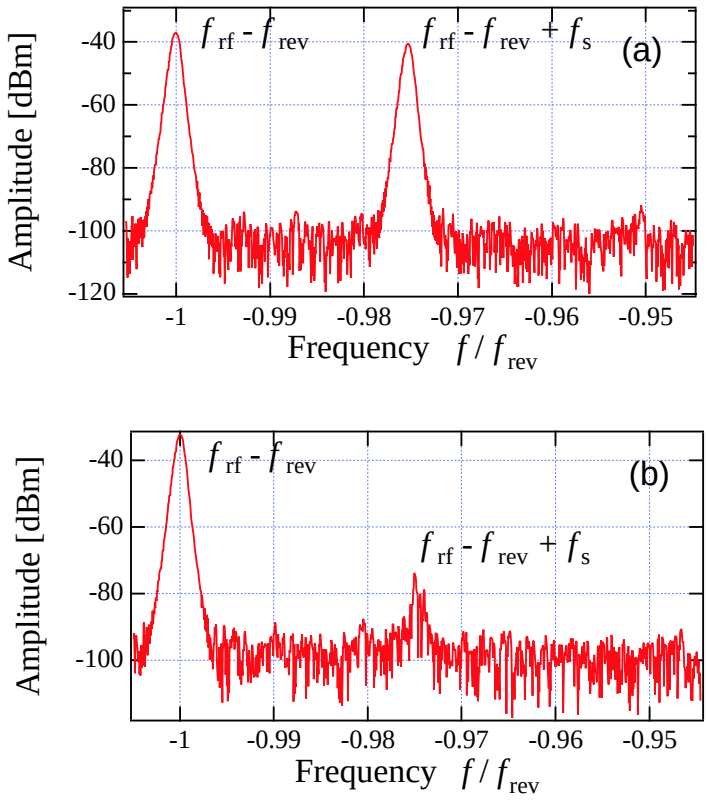

Figure 8.31: Measured spectrum of the -1 mode in LER (a) at 1.0 A without feedback, and (b) at 1.8 A with feedback.

8.5 Crab RF system

8.5.1 Introduction

Luminosity boost by crab crossing

The finite-angle crossing scheme adopted in KEKB does not require any separation dipole magnets and makes the interaction region much simpler than in the head-on collision scheme. Another advantage is that bunches are separated quickly after the collision so that parasitic collision is not a concern, even when every bucket is filled with bunches. In the crab crossing scheme [24], the beams collide head-on in the center-of-mass frame (Fig. 8.32). It eliminates harmful beam-beam effects that can arise from the finite-angle crossing scheme, while it keeps the advantages of the finite-angle crossing. Nevertheless, the non-crabbing finite angle crossing was adopted in KEKB and the design luminosity has been achieved with this scheme. The crab crossing scheme was considered to be a fall-back option in case some unexpected problems are encountered with the finite-angle crossing scheme.

A recent beam-beam simulation showed, however, that head-on collision can drastically increase the beam-beam tune shift limit that results in a significant luminosity increase of several times [25]. The effect is much greater than what had been previously expected. Consequently, the crab crossing scheme has been adopted as the baseline design for SuperKEKB. Parameters for the crab crossing are shown in Table 8.7.

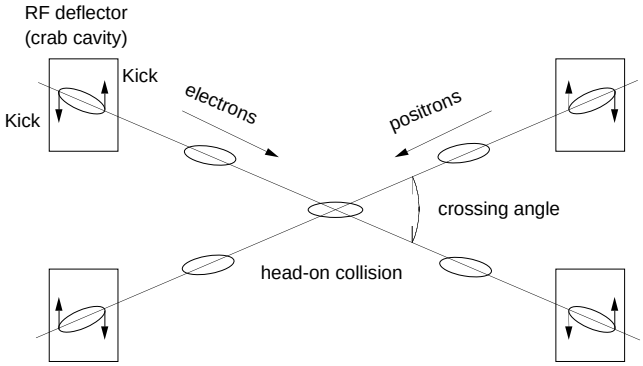

Figure 8.32: Schematic view of the crab crossing scheme.

	LER	**HER**
Beam energy (GeV)	3.5	8.0
Beam current (A)	9.4	4.1
RF frequency (MHz)	508.887	
Crossing angle (mrad)	$\pm$ 15	
β_x^* (m)	0.2	0.2
$\beta_{x,crab}$ (m)	100$\sim$200	300$\sim$400
Required kick (MV)	1.10$\sim$0.78	1.45$\sim$1.26

Table 8.7: Parameters for the crab crossing in SuperKEKB.

Parasitic modes

In order to generate t transverse kick needed for the crab crossing, crab cavities will be used. Because of the high beam current, it must be a damped structure like the accelerating cavities. Since the operating mode of the crab cavity (crabbing mode) is not the lowest frequency mode, there is a lower frequency monopole parasitic mode (LFM) corresponding to the accelerating mode of the accelerating cavities. It has a high longitudinal coupling impedance and can give rise to a strong CBI. It is impossible to damp this mode with a conventional damping scheme using waveguide dampers or wide beam pipes. In addition, there are several transverse parasitic modes whose frequency can be lower than, or close to, the crabbing mode. One is the unwanted polarization of the crabbing mode (UWC): when the crab cavity is operated with the horizontal polarization of the TM110 mode, the UWC is the vertical polarization of this mode. The others are some of TE-like modes. Thus the crab cavity requires special measures to cure these modes in addition to other parasitic modes.

8.5.2 Present crab cavity

A superconducting crab cavity for B-factories was proposed in 1992. It has an innovating damping scheme using a coaxial beam pipe damper attached to an extremely polarized cell named a squashed cell [26]. A schematic drawing is shown in Fig. 8.33. All monopole and dipole parasitic modes are damped, including the LFM and the UWC as well as the lowest frequency TE-like modes, while the crabbing mode is kept at a high Q value. The

damping property was confirmed by calculation and measurement. A superconducting crab cavity based on this design was made to test high-field performance: first, a one-third scale cavity [27] and later, a full-scale cavity [28]. In both cases, sufficiently high kick voltage was obtained. Thus this cavity has satisfactory properties for B-factories with a beam current of 1∼2 A. It is planned to test the crab cavity with a high current beam in KEKB in 2005. The purpose is to investigate experimentally the beam-beam effect of the crab crossing and the performance of the crab cavity.

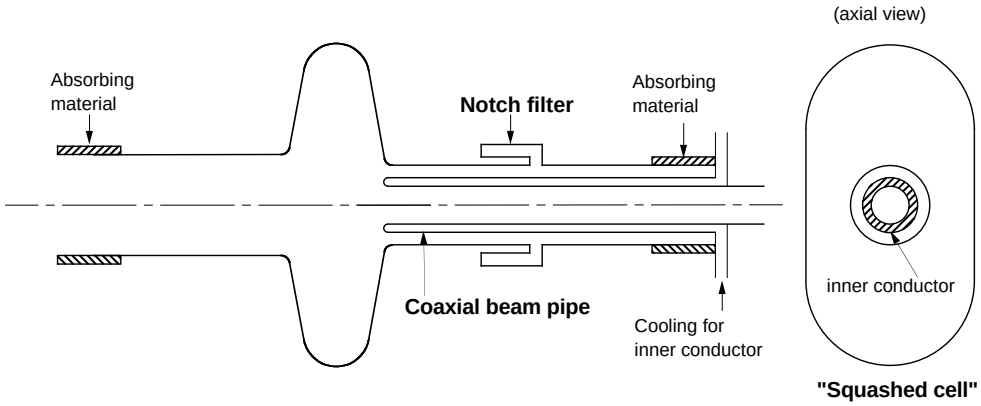

Figure 8.33: Superconducting crab cavity with a squashed cell and a coaxial beam pipe.

Since this cavity was designed for a beam of 1∼2 A, it is not necessarily optimized for a 10 A beam in SuperKEKB LER. First, the HOM power that would need to be absorbed by the dampers amounts to more than 200 kW at 9.4 A in LER. On the other hand, similar types of dampers used in the SCC of KEKB have been operated up to only about 12 kW so far. This big gap makes us hesitant to claim that it be overcome by the time the crab cavity would be needed in SuperKEKB. This would be a common problem with the SC accelerating cavities, if they were used in the LER. Second, much more reduction of the HOM impedance may be required for a 10 A beam, particularly for the transverse modes in the same direction as the crabbing kick (horizontal in our case). It should be noted that the growth rate of the transverse instability driven by one crab cavity can be comparable to that of about ten accelerating cavities, even if the HOM impedance is about the same. The reason is that a large beta-function at the crab cavity, $\beta_{x,crab}$, is chosen to reduce the required kick voltage, whereas the growth rate is proportional to $\beta_{x,crab}$.

8.5.3 New crab cavity for 10 A beam

We have designed a new crab cavity, which can be used with a 10 A class beam current [29]. The motivation is to ease the problem of the parasitic mode power and to obtain much heavier damping of parasitic modes. The design concept of the new crab cavity is as follows.

- The squashed cell shape similar as the original cavity is adopted. The frequencies of any parasitic modes except the LFM are made sufficiently higher than the crabbing mode.
- Waveguide dampers are attached to the squashed cell. All parasitic modes except the LFM can be guided out via the waveguides.

- In order to damp the LFM, coaxial couplers are attached, similar as the original cavity. The difference is that the coaxial couplers are located off-axis of the cell and thus not used as the coaxial beam pipe.

A schematic drawing of the new crab cavity is shown in Fig. 8.34. Four cross-shaped waveguide dampers are attached in both the $x > 0$ and $x < 0$ regions on both sides of the end plates ($z = +z_c$ and $z = -z_c$). Two coaxial dampers are attached on the upper and lower sides of the cell. This scheme allows for a wide beam pipe compared to the coaxial

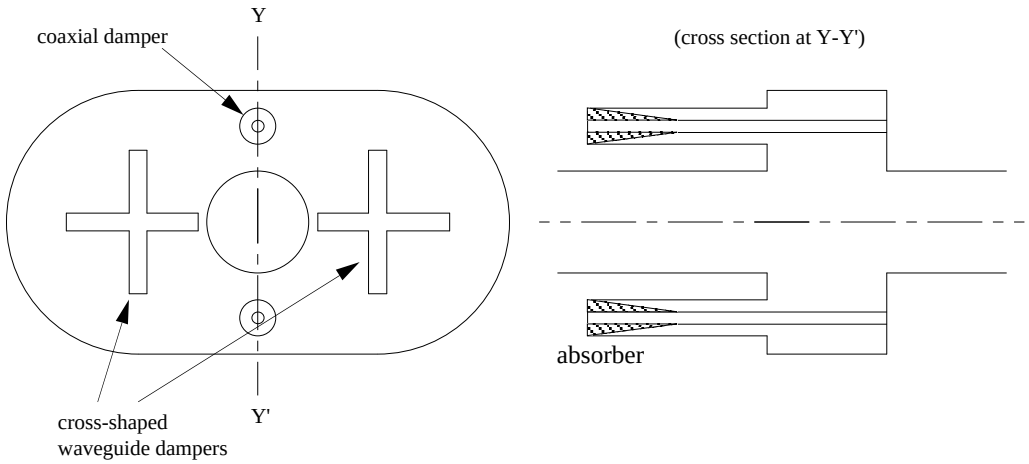

Figure 8.34: Schematic drawing of the new crab cavity. (left) The cross-shaped waveguide dampers and coaxial dampers are attached at the squashed cell. (right) Cross section of the coaxial damper at the cut plane of Y-$Y^{'}$.

beam pipe of the original cavity, which reduces the loss factor. In addition, the absorbers are not exposed to the beam. Furthermore, the generated parasitic mode power is divided into the waveguide dampers and coaxial dampers, which results in easing the load to each damper. Much heavier damping of parasitic modes is also expected.

Optimization of the cell and dampers has been carried out using MAFIA. The longitudinal and transverse coupling impedances were also calculated. In the following, we show the RF properties with the optimized design. The impedance of the crabbing mode is sufficiently high: the R/Q value is 60 Ω/m and the intrinsic Q-value for copper is 3.6×10^4. If it is made as a superconducting cavity (SC), a kick voltage of about 1.5 MV can be obtained, considering the performance of existing SC cavities such as the KEKB cavities. If it is made as a normal-conducting cavity (NC), a kick voltage of 0.4 MV per cavity is obtained at a conservative value of wall dissipation power of 70 kW.

The highest value of the transverse coupling impedance of parasitic modes and the highest value of the product of longitudinal impedance and frequency are summarized in Table 8.8, together with those of the original cavity. The horizontal transverse impedance is reduced by a factor of six and the longitudinal one by a factor of three compared with the original cavity. The loss factor of the cell is reduced by 23%. It could be further reduced, if necessary, by choosing a much wider beam pipe radius at the cost of decreasing the R/Q value of the crabbing mode. Note that the loss factor of the absorber on the widely opened beam pipe of the original cavity is not included in the table, which causes additional loss.

	Original	New	Unit
Z_T (horizontal)	25	4.4	kΩ/m
Z_T (vertical)		10.1	kΩ/m
$Z_{//}$ × Freq. [GHz]	2050	760	Ω
k_{loss} at σ_z=3 mm	0.73†	0.56	V/pC

† The loss factor due to the absorber is not included.

Table 8.8: Highest value of coupling impedance and loss factor.

The growth time and the parasitic power in the SuperKEKB LER and HER are summarized in Table 8.9 and Table 8.10, respectively. Here three cases are compared: the original SC cavity, the SC version of new cavity, and the NC version of new cavity. The number of crab cavities in the list shows the total number including both sides of the collision point.

	Original	New		Unit
	(SC)	(SC)	(NC)	
Number of cavities	1×2	1×2	2×2	
Horizontal growth time	0.9	4.0	2.5	ms
Longitudinal growth time	20	41	27	ms
Parasitic power /cavity	214	97		kW

Table 8.9: Comparison of crab cavities for SuperKEKB (LER).

	Original	New		Unit
	(SC)	(SC)	(NC)	
Number of cavities	1×2	1×2	3×2	
Horizontal growth time	2.6	12	5	ms
Longitudinal growth time	106	214	96	ms
Parasitic power /cavity	44	20		kW

Table 8.10: Comparison of crab cavities for SuperKEKB (HER).

The new cavity has advantages in terms of a heavier damping of parasitic modes and less parasitic power. In the case of the LER, the horizontal growth time is 2.5 ms (NC) or 5.4 ms (SC), which can be sufficiently suppressed with the present bunch-by-bunch feedback system. On the other hand, the growth time of 0.9 ms for the original cavity is marginal for the feedback. The parasitic mode power in the new cavity is less than half that of the original cavity. Furthermore, most of the power is divided into the coaxial dampers and the vertical waveguide dampers, so that the load to each damper is further reduced. Thus the new cavity is a promising candidate for the LER. The longitudinal growth time is slightly faster than the radiation damping time of 30 ms for the original cavity and the new NC cases. A longitudinal bunch-by-bunch feedback system is then needed, although the required damping time is not very short. In the case of the HER,

we can also manage to use the original cavity, provided that the absorbers of the dampers allow a parasitic mode power of 44 kW.

In summary, we have shown that the new crab cavity has heavy damping of all parasitic modes, reduced parasitic mode power for the dampers, as well as a high kick voltage. It meets the requirements for high-current accelerators with a beam current of 10 A and is a promising candidate for SuperKEKB.

Bibliography

[1] Y. Yamazaki and T. Kageyama, "A Three-Cavity System which Suppresses the Coupled-Bunch Instability Associated with the Accelerating Mode", Part. Accel. 44 p. 107, 1994.

[2] T. Furuya et al. Proc. 9th Workshop on RF Superconductivity, p. 31, 1999.

[3] K. Akai et al. "RF systems for the KEK B-Factory", Nuclear Instruments and Methods A, 499, p. 45 (2003).

[4] S. Yoshimoto et al., "The -1 mode damping system for KEKB", Proc. the 14th Symposium of Accelerator Science and Technology, p. 323, Tsukuba, 2003.

[5] T. Kageyama et al., "Development of High-Power ARES Cavities", Proc. PAC97, Vancouver, 1997

[6] T. Kageyama et al., "Operation of ARES Cavities for KEKB", Proc. the 13th Symposium of Accelerator Science and Technology, p. 223, Osaka, 2001.

[7] T. Kageyama, "Grooved Beam Pipe for Damping Dipole Modes in RF Cavities", Proc. the 8th Symposium on Accelerator Science and Technology, p. 116, 1991.

[8] Y. Takeuchi et al., "HOM Absorber for the ARES Cavity", Proc. PAC97, Vancouver, 1997

[9] Y. Suetsugu et al., "Development of Winged HOM Damper for Movable Mask in KEKB", Proc. PAC2003, Portland, 2003.

[10] F. Naito et al., "The Input Coupler for the KEKB ARES Cavity", Proc. APAC98, Tsukuba, 1998.

[11] T. Abe et al., "Study of multipactoring phenomena in RF coaxial-line input couplers", in Japanese language, Proc. the 14th Symposium of Accelerator Science and Technology, p. 320, Tsukuba, 2003.

[12] F. Naito et al., "Coupling Cavity Damper for the ARES Cavity", Proc. PAC97,Vancouver, 1997.

[13] T. Weiland, DESY 83-073, 1983.

[14] T. Takahashi et al. Proc. 9th Symp. Accel. Science and Technology, KEK, 1993, p. 327.

[15] T. Tajima, Thesis, KEK Report 2000-10, September 2000.

[16] S. Mitsunobu et al. Proc. 7th Workshop on RF Superconductivity, p. 735, 1995.

[17] T. Furuya et al. "Commissioning of the SC Cavities for KEKB", Proc. e+e- Factories, p. 55, KEK, 1999.

[18] S. Isagawa, et al. Proceedings of the First Asian Particle Accelerator Conf. 1998, p. 773.

[19] S. Isagawa, "Operation of the UHF CW Klystron at the World's Highest Power Level", Proc. 14th Symp. on Accelerators Sience and Technology, 2003, Tsukuba, Japan, p. 341.

[20] K. Ebihara et al. "RF Reference Line for KEKB", Proc. 12th Symp. on Accelerators Sience and Technology, 1999, Japan.

[21] K. Akai et al. "The low-Level RF System for KEKB", Proc. 6th EPAC, 1998, p. 1749.

[22] K. Akai et al. "Protection of Hardware Components with High-Current Beam against RF Trips in KEKB", EPAC2002, p. 2112, Paris, 2002.

[23] E. Ezura, et al. "RF Feedback for KEKB", Proc. International Workshop on Collective Effects and Impedance for B-factories, p. 437, Tsukuba, Japan, June, 1995.

[24] K. Oide and K. Yokoya, "The Crab-Crossing Scheme for Storage-Ring Colliders", Phy. Rev. A40, 315, 1989.

[25] K. Ohmi, M. Tawada and K. Oide, "Study of Beam-Beam Interactions with/without Crossing Angle", Proc. PAC 2003.

[26] K. Akai et al. "Crab Cavity for the B-Factories", Proc. B factories, p. 181, SLAC-400, 1992.

[27] K. Akai, et al. "Development of Crab Cavity for CESR-B" Proc. PAC'93, p. 769, Washington D. C. 1993.

[28] K. Hosoyama et al. "Superconducting Crab Cavity for KEKB", Proc. 1st Asian Part. Accel. Conf. , p. 828, 1998.

[29] K. Akai and Y. Morita, "Crab Cavity for High-Current Accelerators", submitted to Phys. Rev. ST Accel. Beams.

Chapter 9

Vacuum System

9.1 Overview

The design of the vacuum system is being carried out based on experience obtained so far, while also introducing some novel concepts at the same time [1, 2, 3]. Some R&D had essentially begun in 2001, and several trial models of vacuum elements have been installed in the present KEKB rings. Described here are the basic vacuum system design for arc sections of the rings, some R&D results obtained so far, and a brief discussion of the wiggler section. A design for the Interaction Region (IR) will be presented elsewhere in the future. In designing the vacuum system, the alignment and structures of the magnets in the ring are assumed to be retained basically as they presently are.

Typical layouts of the beam chambers in the arc sections of the LER and the HER are shown in Figs. 9.1 (a) and (b), respectively. The beam chambers in the arc section are roughly divided into three types: bend chambers (B-chambers), quadrupole chambers (Q-chambers), and straight chamber (S-chambers). The B-chamber is used for a bending magnet and has the same curvature as the corresponding bending magnet. The Q-chamber is used at a quadrupole and sextupole magnets, has electrodes for a beam-position monitor (BPM) and is fixed to a quadrupole magnet. The S-chamber is for drift spaces between the magnets. Each beam chamber is connected by flanges with a set of bellows at either end of the chamber. Consequently, there are two flange connections and two sets of bellows between one pair of quadrupole magnets. The two-bellows configuration described above is preferred because it simplifies the installation and alignment procedures. If the impedance of the bellows needs to be reduced, we can omit one of those bellows. Photon masks to protect them from SR are located just upstream of the flanges and bellows.

The first major issue for the vacuum system is intense synchrotron radiation (SR) arising from large beam currents. Some important parameters related to the vacuum system and the SR are listed in Table 9.1, where an ante-chamber structure is assumed for the beam chamber, as described later. The line power density of the SR in the LER is 27.8 kW m^{-1}, which is twice as high as that in the present KEKB [1, 2, 3]. The maximum power density, however, remains 38.7 W mm^{-2} which is almost the same as the present one because of the larger outer aperture of the ante-chamber structure. In the HER, on the other hand, the line power density of SR becomes 21.6 kW m^{-1}, which is four times higher than that of the present KEKB, and the maximum power density is 35 W mm^{-2}. The maximum power density in the HER is higher by a factor of 2.4 than that of the present one, but is almost the same as that of the LER.

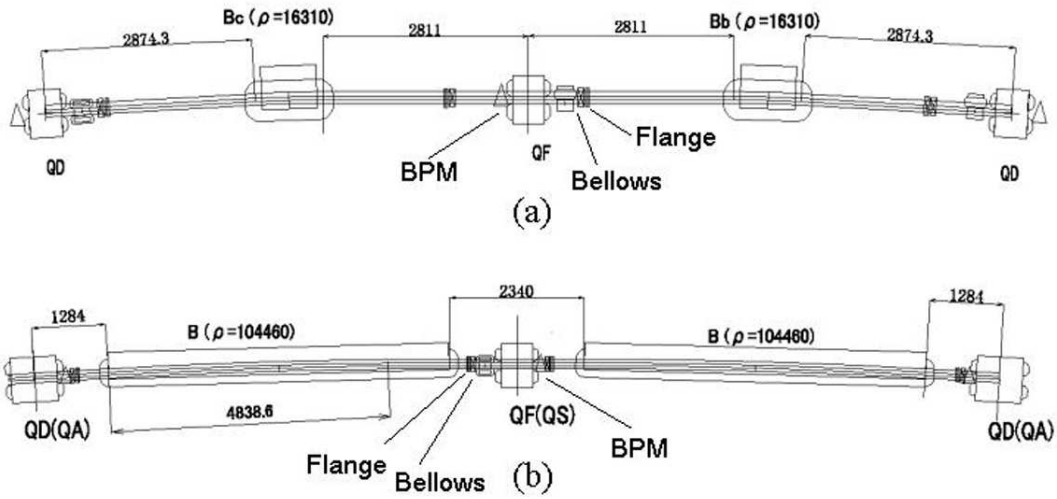

Figure 9.1: Layout of the beam chamber at an arc section. (a) LER and (b) HER.

	LER	HER	Unit
Energy	3.5	8.0	GeV
Beam current	9.4	4.1	A
Bunch length	3		mm
Circumference	3016		m
Number of bunches	5018 (2% abort gap)		
Bending radius	16.31	104.46	m
Bending angle	56.1		mrad
Half aperture	112		mm
Total SR power	7.65[*1]	14.21	MW
Max. line power density of SR	27.77	21.63	kW m^{-1}
Max. power density of SR	38.73	35.00	W mm^{-2}
Critical energy of SR	5.84	10.88	keV
Ave. photon density	1.21×10^{19}	1.20×10^{19}	photons m^{-1} s^{-1}
Ave. gas load	4.56×10^{-8}	4.54×10^{-8}	Pa m^3 s^{-1} m^{-1}

[*1] without wigglers

Table 9.1: Parameters related to the vacuum system.

The average line photon density is about 1.2×10^{19} photons $m^{-1}s^{-1}$ for both rings, which is four times larger than that of KEKB. The gas load is about 4.6×10^{-8} Pa $m^3s{-}1m^{-1}$ assuming a photon-desorption coefficient, η, of 1×10^{-6} molecules $photon^{-1}$.

Another issue is higher order modes (HOM) due to the large bunch current and the short bunch length. The HOM power, P_{HOM}, can be estimated by

$$P_{HOM} = T_0 \cdot \kappa(\sigma_z) \cdot \frac{I^2}{n_b}, \tag{9.1}$$

where T_0 is the revolution time, which is about 10 μsec at KEKB/SuperKEKB, κ is the loss factor, I is the beam current, and n_b is the number of bunches. The loss factor, κ, is a function of the bunch length, σ_z. The loss factors of various vacuum components need to be minimized to keep the HOM power losses as low as possible and to avoid excess heating. The main loss factors and their corresponding HOM powers are summarized in Table 9.2. The largest impedance source is a movable mask that protects the Belle/SuperBelle detector from particle background. The resistive wall and bellows impedances are the next largest sources. HOM absorbers will be installed near large impedance sources.

	κ[*1] (V/C)	Number of items	Total κ (V/C)	HOM power[*2] (kW)
Resistive wall[*3]	4.1×10^{9}	2200 m	8.9×10^{12}	1780
Pumping holes	8.8×10^{5}	2200 m	1.9×10^{9}	0.38
Flange	1×10^{8}	800	8×10^{10}	16
Bellows	4×10^{9}	800	3.2×10^{12}	640
Photon mask	1×10^{4}	800	8×10^{6}	0.0016
Gate valve	3×10^{9}	16	4.8×10^{10}	9.6
Movable mask[*4]	1×10^{12}	16	1.6×10^{13}	3200
Taper	3×10^{9}	72	2.2×10^{11}	44
BPM	N/A	400	N/A	N/A
IR chamber	N/A	1	N/A	N/A
Total			$30\sim40\times10^{12}$	6∼8 MW

[*1] $\sigma_z = 3$ mm
[*2] n_b=5000, f_0=1×10^5 Hz, I_b=10 A
[*3] Copper chamber with a radius of 25 mm
[*4] 8 horizontal and 8 vertical masks

Table 9.2: Loss factor and HOM power.

9.2 Design of vacuum system

9.2.1 Beam chamber

The beam chamber for the arc sections has an ante-chamber structure. The ante-chamber consists of a beam channel and an SR channel. A long, narrow slot connects those channels to each other. A schematic view of the ante-chamber for the LER is shown in Fig. 9.2. The beam goes through the beam channel and the SR passes through the SR channel and

hits the side wall of the SR channel. Pumps are equipped on the upper and lower sides of the SR channel. The pump channels are connected through many holes with typical diameters of 4 mm. A strip-type non-evaporable getter (NEG) is used as the main pump. A cooling channel is provided on the outside of the side wall of the SR channel, since that is where the SR hits. A photon stop scheme will not be used, except in certain places, because an extremely intense SR power load is concentrated on the photon stops.

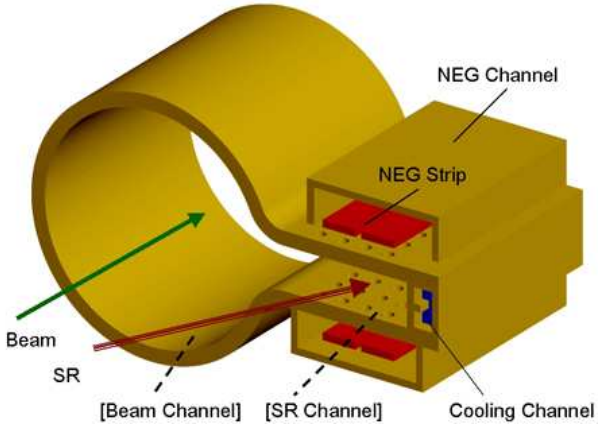

Figure 9.2: Schematic view of ante-chamber in LER.

One advantage of the ante-chamber is that the power density of the SR can be reduced. Since the incident point of SR on the side wall is far from the emitting point, as a result of the larger outer aperture, the incident SR power density is diluted. In the LER, the irradiated points are outside of the bending magnets. The ante-chamber, therefore, increases both the horizontal and vertical spreads of the SR. The maximum power density at the side wall of the ante-chamber is 38.7 W mm^{-2}, compared with 134 W mm^{-2} in the present single-beam chamber of KEKB. On the other hand, the first irradiated point is inside the bending magnets in the HER. Thus, the maximum power density is almost the same as that of the single beam chamber at KEKB. The power density, however, is decreased as the vertical spread of the SR increases.

The ante-chamber also has the advantage of a small beam impedance. Since the pumping channels are located in the SR channel, the pumping slots (holes) have little affect on the beam. The loss factor of the pumping holes is estimated to be 8.8×10^5 V C^{-1} per meter for a 3 mm bunch length, for 780 holes of 4 mm diameter. For a reference, the loss factor of the present pumping port with a grid-type RF shield is about 5.8×10^7 V C^{-1}. Photon masks to shield the flanges and bellows from SR at the downstream sides of the channel are placed on the side wall of the SR channel. A photon mask with a height of 30 mm has a loss factor of 1×10^5 V C^{-1} in the LER.

Electron-cloud instability will be a serious issue for the positron ring. The electron cloud is initially created by photoelectrons emitted from the inner chamber surface irradiated by SR. The ante-chamber structure also helps to minimize the effects of the photoelectrons. The emission points of the photoelectrons are far from the beam orbit and the attractive electric field induced by the beam is very weak there. It has been estimated from a simulation that the electric field at the side wall of the SR channel is five orders of magnitude smaller than that on the inner wall in the beam channel. Figures 9.3 (a) and (b) show the photoelectron density calculated for a circular beam chamber and

for an ante-chamber, respectively, where the photoelectrons are emitted in the horizontal plane from the side wall and secondary electrons from the surface are not considered. The electron density in the vicinity of the beam orbit is found to be reduced by one order of magnitude by using the ante-chamber. Furthermore, when applying a solenoid field to reduce the photoelectron effects, the magnetic field strength needed is smaller with the ante-chamber than in the case of the circular beam chamber. A saw-tooth structure, rough surface and/or special coating on the side wall of the SR channel will also reduce the photoelectron yield as well as the reflection of SR, as described later.

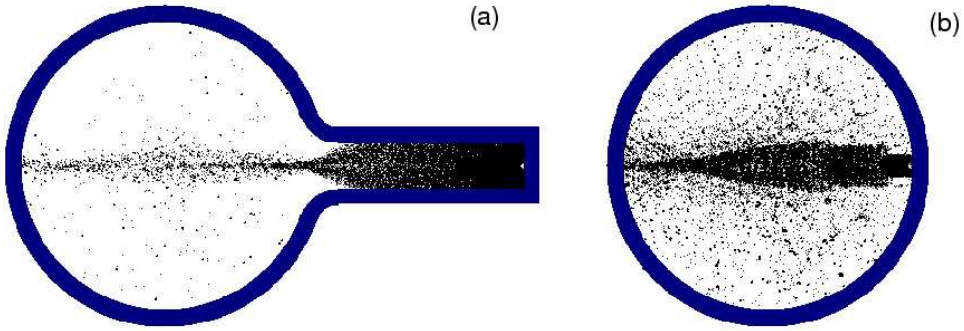

Figure 9.3: Simulation of photoelectrons in the (a) ante-chamber and (b) circular chamber.

Material

Common materials for a beam chamber are stainless steel, copper and aluminum. Due to the high heat load from intense SR, the use of stainless steel for parts exposed to SR will be excluded. Oxygen free copper (OFC) should be the most suitable material for a beam chamber owing to its high thermal strength, high electrical conductivity and relatively low photoelectron yield. Experience with copper beam chambers has been accumulated at KEKB, including welding and cleaning procedures [2, 3, 4]. Aluminum may be another candidate. Manufacturing and welding are easier than copper, but the thermal properties are inferior. We also had experience with aluminum beam chambers in the TRISTAN rings [5, 6] as well as in KEKB. Considering accidental irradiation of SR, however, copper beam chambers are highly preferable. If aluminum is used for the beam chamber for the positron ring, furthermore, some coating, such as TiN, will be indispensable to lower the secondary electron yield [7]. Aluminum will be used only for special and complex chambers in the straight sections.

Structure

Typical cross sections of the beam chambers for the LER and HER are shown in Fig. 9.4 and Fig. 9.5, respectively. The positions of the chambers in magnets for the LER and HER are also shown in Fig. 9.6. The beam channel for the LER has a circular shape with a diameter of 90 mm. A race-track shape is used for the HER; the width and height are 98 mm and 50 mm, respectively. The thickness of the beam chamber is 6 mm for both rings. A larger aperture gives a higher conductivity and is preferred from the point of view of gas evacuation. The resistive wall impedance will also decrease as the distance between a beam and the inner wall is decreased. However, the size of the beam chamber

is restricted by the aperture of the magnets. Furthermore, the sextupole magnets need to be able to move over a range of ±2.5 mm in the horizontal and vertical directions, as required from optics corrections. Therefore, it is necessary to maintain a clearance of at least 4 mm for the beam chamber in the sextupole magnets. Since the height of the SR channel is set to be 7 mm for both rings, as discussed below, grooves with a depth of 3 mm would be carved into the SR channel where the clearance is tightest to provide clearance between the chamber and the sextupole magnet. Solenoid winding in the quadrupole and sextupole magnets is not considered at present.

The height of the pumping channel for the HER is limited by the vertical aperture of the bending magnets, as shown in Fig. 9.6 (d). A height of at least 15 mm will be needed to install a strip-type NEG (Non-Evaporable Getter) pump. For other sections, there is no limitation on the height of the pumping channels. In order to activate the NEG pump, ports with feed-throughs are necessary to supply a high current (about 50 A at 50 V), as shown in Fig. 9.4 (d) and Fig. 9.5 (d). The ports for ion pumps or rough pumps are also located at the bottom of the pump channels, as drawn in Fig. 9.4 (c) and Fig. 9.5 (c).

The temperature distribution, deformation, and stress due to the SR, including atmospheric pressure, were calculated for a copper beam chamber using the ANSYS 6.0 code. The calculation was two dimensional. Heat convection to the atmosphere and to cooling water was included. The results are presented in Fig. 9.7. The maximum temperature and the thermal stress are expected to be about 160°C and 260 MPa, respectively, for the LER. The stress leads to a local strain of about 0.22%. The temperature is below the annealing temperature of about 250°C for 40% c.w. in Fig. 9.8 (a) [8]. The von Mises stress is about 2/3 of the yield strength of drawn copper. The chamber can withstand close to 10^5 cycles with this stress, as shown in Fig. 9.8 (b). It had been found that even annealed copper can still withstand 10^4 cycles of a 0.5% deformation at 150°C [1]. The vertical deformation is about 0.1 mm at most and presents no problem, except at the beam-position monitor section. That section, however, will be fabricated in a block, as in the present KEKB, or specially supported.

SR channel

The height of the SR channel is 7 mm in the present design. A lower height SR channel is better from the viewpoint of reducing the photoelectron effect in the positron ring. Furthermore, the low height of the SR channel can relieve the clearance problem in the sextupole magnets and the bending magnets. Actually, a half height of 7 mm for the SR channel is sufficient to absorb the SR if the beam follows the design orbit. The vertical spread of the SR is 0.146 mrad for the LER and 0.0639 mrad for the HER. The vertical half width of the SR becomes about 7 mm due to the spread 50 m downstream of a bending magnet in the LER and 110 m downstream in the HER, which is sufficiently larger than the maximum distance between adjacent bending magnets, 25 m. However, the beam orbit usually has some vertical deviation from the design orbit because of machine errors. There is a possibility that the SR hits the beam channel instead of the SR channel when the beam orbit has vertical deviations. We calculate the irradiation positions and the power densities of SR at the beam channels based on data from the present KEKB.

Figure 9.9 shows the distributions of the vertical deviations and the angles of the beam orbit in the bending magnets measured in the KEKB LER and HER [9]. For the worst case in the LER, the SR is emitted from a point 3 mm above/below the design orbit with

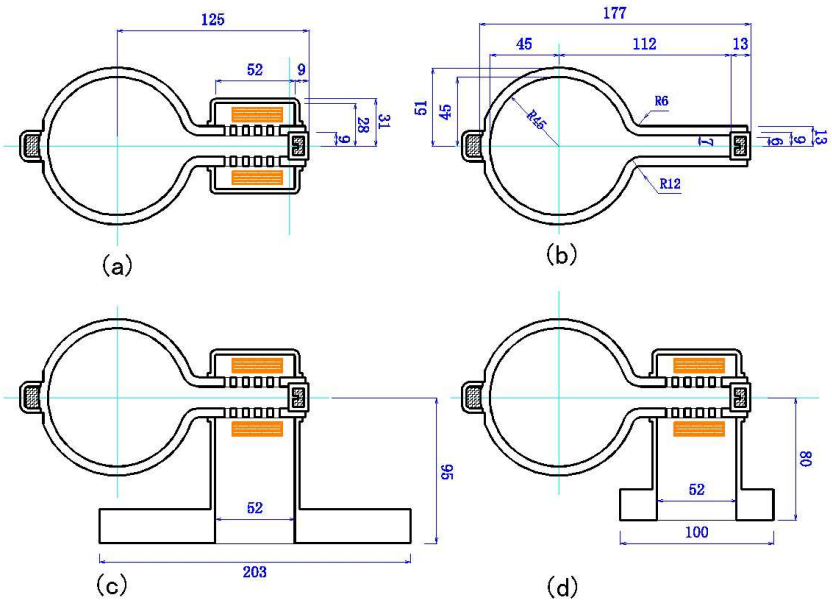

Figure 9.4: Cross section of the beam chamber for the LER. The beam chamber is used for (a) bending magnets and normal sections, and (b) quadrupole and sextupole magnets. (c) Port of rough-pump and ion pump. (d) High current feedthrough for NEG pump.

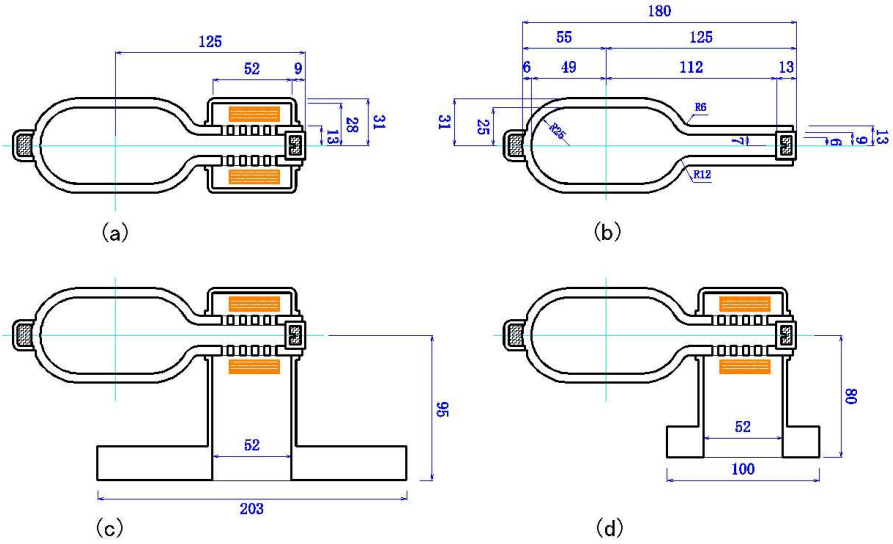

Figure 9.5: Cross section of the beam chamber for the HER. The beam chamber is used for (a) bending magnets and normal sections, and (b) quadrupole and sextupole magnets. (c) Port of rough-pump and ion pump. (d) High current feedthrough for NEG pump.

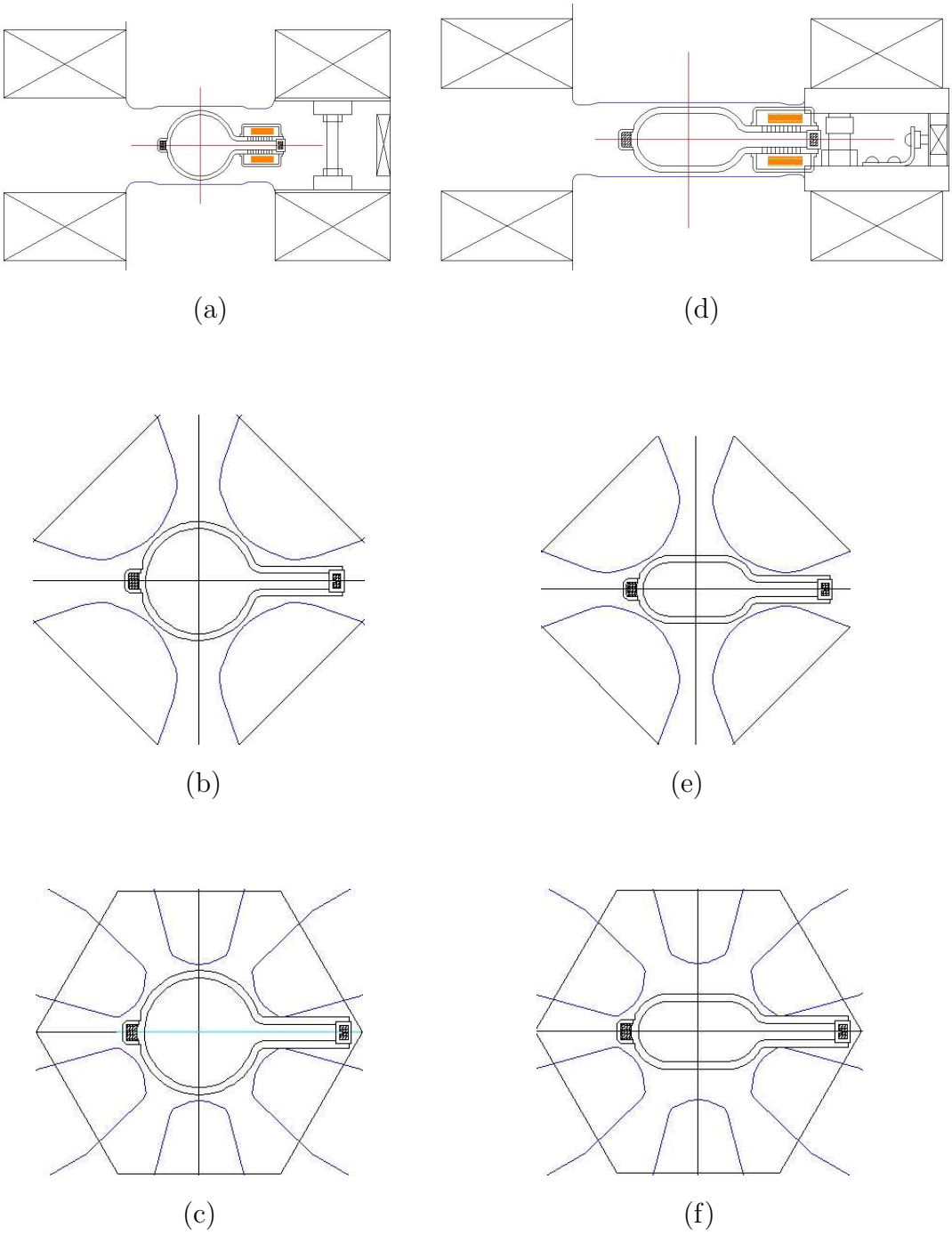

Figure 9.6: Vacuum chamber in magnet at the LER (left) and HER (right).

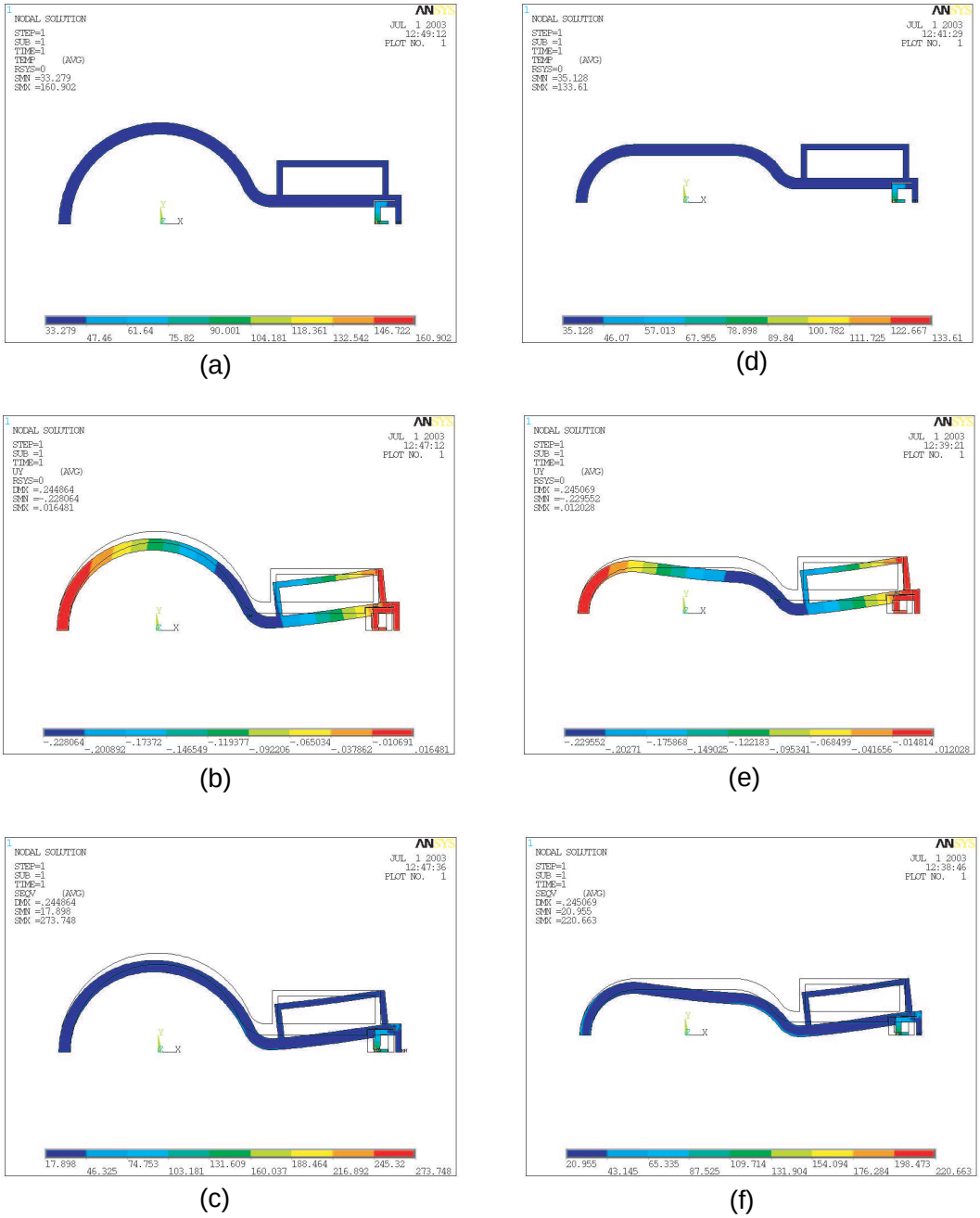

Figure 9.7: Simulation (2-dimensional) of the temperature distortion, deformation, and Von Mises stress due to SR. Cross section of the beam chamber for the LER (left) and HER (right). The flow rate is about 10 l min^{-1}. The temperature of the atmosphere and cooling water is 25 °C. Young modulus, Poisson ratio, thermal expansion rate of copper are 1.18× 10^5 Pa mm^{-2}, 0.33, and 1.77×10^{-5} K^{-1}.

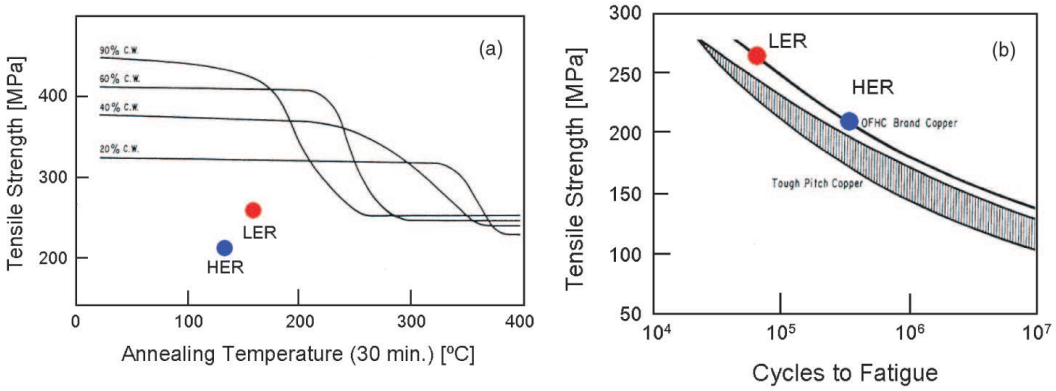

Figure 9.8: Tensile strength as a function of (a) annealing temperature and (b) cycles to fatigue for pure copper.

an angle of 0.3 mrad. SR with a vertical spread then hits the beam channel at about 9 m downstream from the bending magnet. The linear power density becomes 0.76 W mm^{-1} at the beam channel. In the case of the HER, on the other hand, the maximum deviation and angle are 2 mm and 0.2 mrad, respectively, from Fig. 9.9. The SR hits the beam channel about 19 m downstream of a bending magnet and the power density is about 0.36 W mm^{-1}. Thus, the distance from the bending magnet to the irradiated point is shorter than the longest distance between adjacent bending magnets (25 m). This means that the half height of 7 mm of the SR channel is not enough. Note here that orbit measurements of the vertical deviations in the present KEKB include local orbit bumps at sextupole magnets to correct the optics. The vertical deviations, therefore, could be reduced in SuperKEKB where sextupole movers are used instead of local bumps. The reduction rate, however, is not clear at present. The half height of 7 mm of the SR channel, which is the maximum considering the aperture of the magnets, therefore, is a safe and reasonable value at present.

The maximum temperature rise due to the SR is estimated to be about 50°C in the LER and about 40°C in the HER, respectively. Although the heating due to SR will not be serious, it is necessary to accommodate the thermal expansion of the beam chambers. Extra cooling channels may be installed on the side of the pump channels, or on the top or inner side of the beam channel, if necessary.

9.2.2 Pumping scheme

Pressure requirement

Assuming that the beam chamber has a sufficient physical aperture, the beam lifetime is mainly limited by Bremsstrahlung processes. The lifetime determined by this process needs to be much longer than the luminosity lifetime (about 1 hour), and sufficiently long to be compatible with the injection scheme. The lifetime, τ, is related to the average pressure, P, as

$$P \cdot \tau = 5.6 \times 10^{-6} \quad \text{[Pa Hours]}, \tag{9.2}$$

where a residual gas of CO and an RF bucket height of 0.01 are assumed [1]. For example, to achieve a beam lifetime of 10 hours, a pressure of about 5×10^{-7} Pa is required.

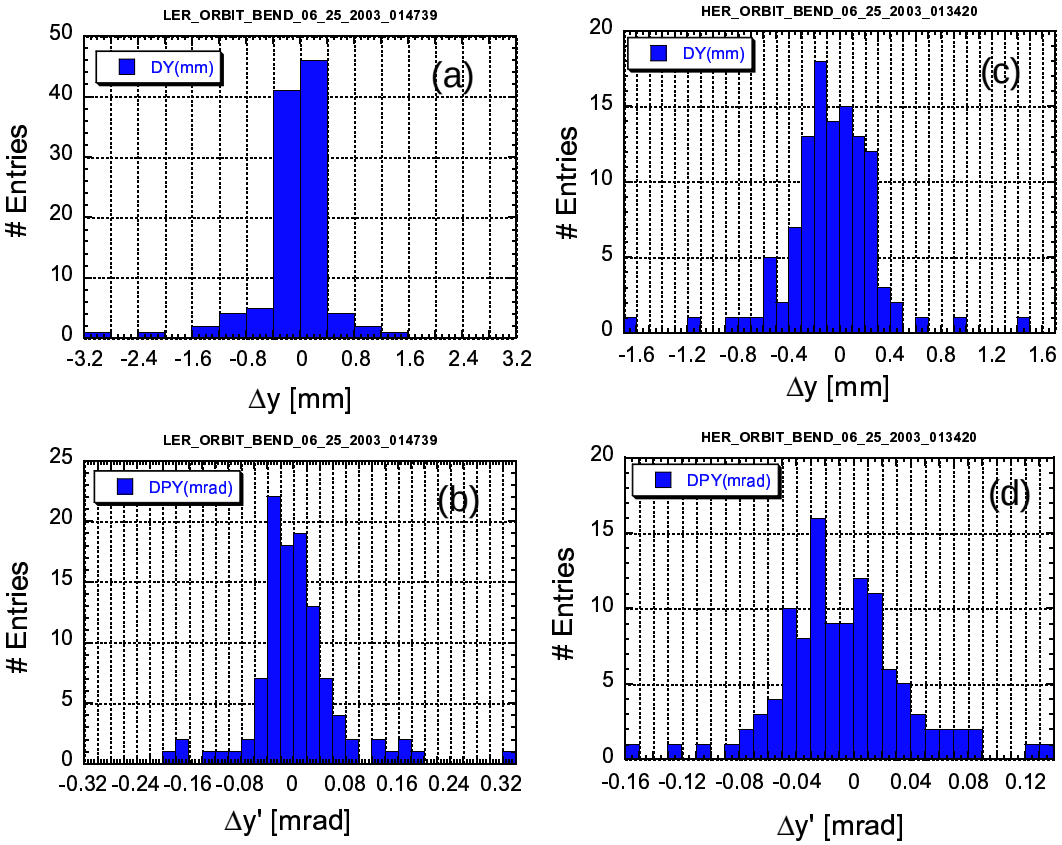

Figure 9.9: Vertical deviations and angles of the beam orbit in the bending magnets at the KEKB LER (left) and HER (right).

Another important issue is the beam background in the physics detector. Although a precise estimation has not yet been made, a pressure of less than 1×10^{-7} Pa will be required around the interaction region [2, 3]. From experience at KEKB, the pressure just upstream of the detector is more critical than that in the arc sections. In the arc sections, a movable mask system can reduce the detector background.

The next concern is ion-trapping phenomena (ion instabilities) in the electron ring. From experience at KEKB, an ion-trapping phenomenon sometimes occurs when the pressure in a local region becomes on the order of 10^{-6} Pa. This phenomenon strongly depends on the bunch fill pattern. The instability is suppressed by the bunch-by-bunch feedback system, since the growth time is larger than 1 msec at present. It is, therefore, difficult to specify exactly how low the pressure must be to prevent ion trapping. We assume that the necessary pressure is on the order of 10^{-7} Pa on average and 10^{-6} Pa locally.

Consequently, a target average pressure with the design beam currents is about 5×10^{-7} Pa at the arc sections for both rings. If this average pressure can be realized, any fast ion instability in the electron ring would also be suppressed by the bunch-by-bunch feedback system [10].

Pumps

To achieve an average pressure of 5×10^{-7} Pa, a linear pumping speed of about 0.1 m^3 s^{-1} m^{-1} is required, assuming a photo-desorption coefficient, η, of 1×10^{-6} molecules $photon^{-1}$ (see Table 9.1). The decrease of η in the case of KEKB (HER) is presented in Fig. 9.10 [11]. The value of 1×10^{-6} molecules $photon^{-1}$ can be achieved for a copper beam chamber at a photon dose of about 1×10^{25} photons m^{-1}. An η of about 5×10^{-7} molecules $photon^{-1}$ might be a reasonable value in the design stage at present, but an η of 1×10^{-6} molecules $photon^{-1}$ is taken for the design of the vacuum system in this chapter.

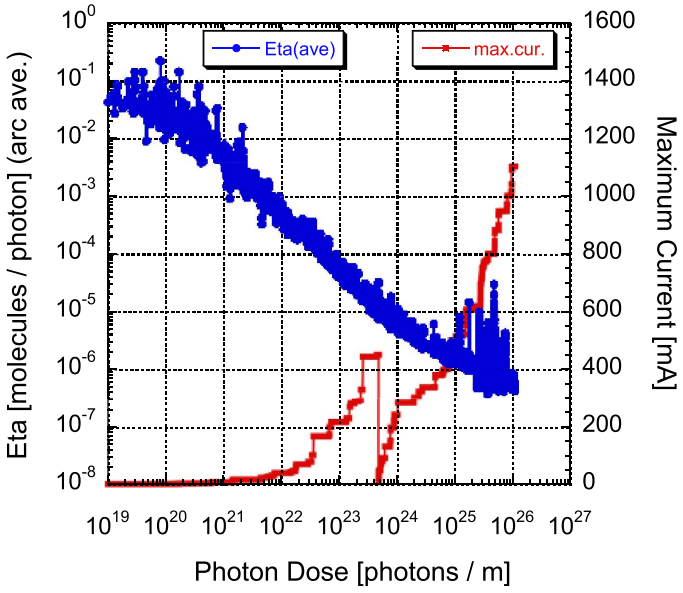

Figure 9.10: Photo-desorption coefficient as a function of photon dose at the present KEKB HER.

To evacuate the long, narrow beam chambers effectively, a distributed pumping scheme will be adopted. The main pump is a strip-type NEG, ST707 (SAES GETTERS Co. Ltd.). The strip has a width of 30 mm and NEG material is coated on both sides, as shown in Fig. 9.11 (a). The pumping speeds of the NEG strip for CO and H_2 are about 2.5 and 6.0 $m^3\ s^{-1}\ m^{-2}$, respectively, just after activation (about 450 °C) [12]. The pumping speed decreases as the NEG absorbs gas. In the following, the effective pumping speed is estimated for the case of 2.0 (1.25) $m^3\ s^{-1}\ m^{-2}$ (half of the maximum pumping speed), assuming CO only.

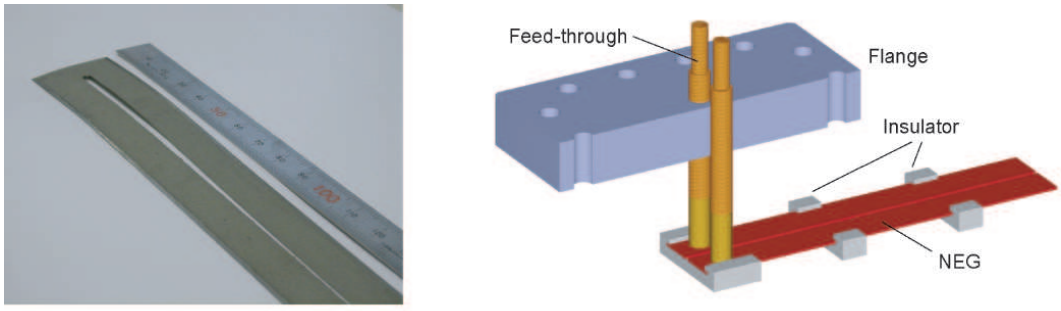

Figure 9.11: (a) NEG strip (width of 30 mm) with a narrow slit. (b) Schematic view of a high-current feedthrough for NEG.

For a strip of width 30 mm, the line pumping speed is 0.12 (0.075) $m^3\ s^{-1}\ m^{-1}$. The pumping holes between the SR channel and the pumping channel have a diameter of 4 mm, and a thickness of 6 mm. There are 625 holes per meter. The resulting conductance of the pump channel per unit length is 0.36 $m^3\ s^{-1}\ m^{-1}$, assuming a Clausing's coefficient (transmission probability) of 0.4 [13]. The effective pumping speed for one pump channel is 0.09 (0.062) $m^3\ s^{-1}\ m^{-1}$. The effective pumping speed for two pump channels, therefore, is about 0.18 (0.12) $m^3\ s^{-1}\ m^{-1}$, which is greater than 0.1 $m^3\ s^{-1}\ m^{-1}$. However, the pumping channel cannot be installed inside the quadrupole and sextupole magnets, due to the limited space between the magnets and the joints of the beam chambers. Rough estimations of effective pumping speeds for a half cell are presented in Figs. 9.12 (a) and (b) for the LER and the HER, respectively. There are two lumped pumps (0.1 $m^3\ s^{-1}$) between pairs of quadrupole and sextupole magnets. For the LER, an average pumping speed of about 0.09 $m^3\ s^{-1}\ m^{-1}$ can be obtained even for the case of a low pumping speed (1.25 $m^3\ s^{-1}\ m^{-2}$), since the magnets are relatively short and the wide spaces are available for pumps. For the HER, given the length of the quadrupole and sextupole magnets, the effective pumping speed is reduced, about 0.07 $m^3\ s^{-1}\ m^{-1}$ for the case of the lower pumping speed. Just after activation, the linear effective pumping speed is about 0.1 $m^3\ s^{-1}\ m^{-1}$. A more refined pump arrangement may be necessary, or additional lumped pumps will be installed between adjacent magnets. For reference, assuming an η of 5×10^{-7} molecules $photon^{-1}$ as obtained at KEKB (see Fig. 9.10), the pumping speeds described above will be sufficient.

Ports for flanges with a high-current feed-through to activate (heat) the NEG strips are attached to pump channels at regular intervals as shown in Figs. 9.4 (d) and 9.5 (d). The flange will be of a special rectangular shape. To decrease the number of ports, the input and output feed-through are on the same flange. The NEG strip, therefore, will be

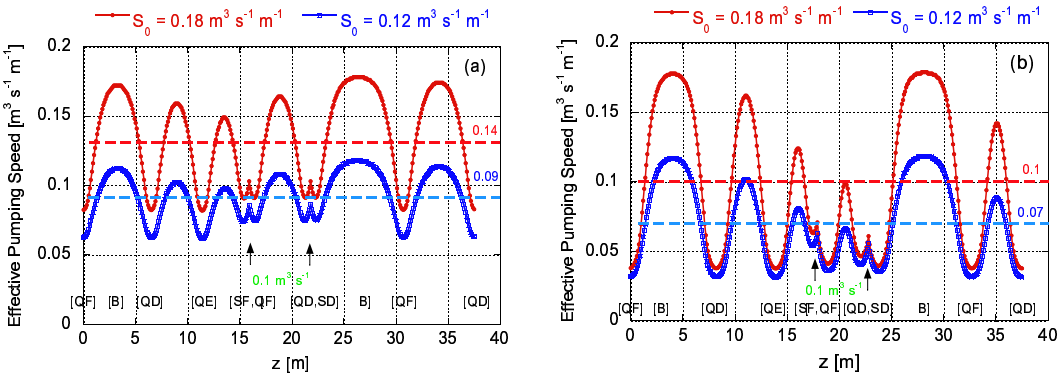

Figure 9.12: Effective pumping speed for a half cell of (a) LER and (b) HER.

divided in two along the strip and connected at the end, as shown in Fig. 9.11 (a). The schematic configuration near a feed-through is shown in Fig. 9.11 (b). The NEG strip is insulated electrically from the beam chambers by small ceramics blocks about every 100 mm. To evacuate non-active gases and to assist evacuation at relatively high-pressure regimes, just after exposure to air, for example, sputter ion pumps are provided. The ion pumps will be located every 10 m or so, as in the present KEKB [2, 3]. There are also pumping ports at pump channels as shown in Fig. 9.4 (c) and Fig. 9.5 (c). The flange will be a standard ICF-203 conflat flange. The pumps should maintain a sufficient pumping speed even at a pressure of 10^{-7} Pa. The rough-pumping scheme is based on that of the present KEKB [2, 3]. The pump system consists of a turbo-molecular pump and a dry pump. The system is completely oil free.

9.2.3 Flange and bellows

A Helico-flex gasket has been working well at KEKB as an RF-bridge between flanges [2, 3]. For SuperKEKB, however, the impedance of the flange (loss factor of about 1 Vn C^{-1} [14]) will be serious due to the small bunch length. The parasitic power loss becomes about 200 W for a 10 A beam current. The number of flange connections should be reduced as much as possible. The flanges and RF bridges between flanges are shown in Fig. 9.13 (a). The RF-bridge between flanges is a loop of copper with the same cross section as the corresponding beam chamber. The vacuum seal will be provided by a circular Helico-flex gasket outside. When the Helico-flex gasket is compressed, the inner RF-bridge is mated to both flanges. The material and the hardness for the RF-bridge require further consideration. Another possibility is an MO flange [15, 16]. This flange has been developed for wave-guide connections in the C-band RF-system. The flange has a square edge to maintain a smooth current flow across a copper gasket and as well as vacuum tightness for an ultra-high vacuum. Adaptation to a more complicated cross section might be possible.

Stainless steel is being considered as a material for the flanges. Another possible candidate is a copper alloy with a higher thermal strength than pure copper, Zr alloy. Welding to a pure copper beam chamber presents no problem.

Bellows are installed between adjacent beam chambers [17, 18] to ease beam chamber installation and to absorb any thermal deformation. Since the beam current is large and the bunch length is short in the SuperKEKB, a heating of bellows due to HOM, especially

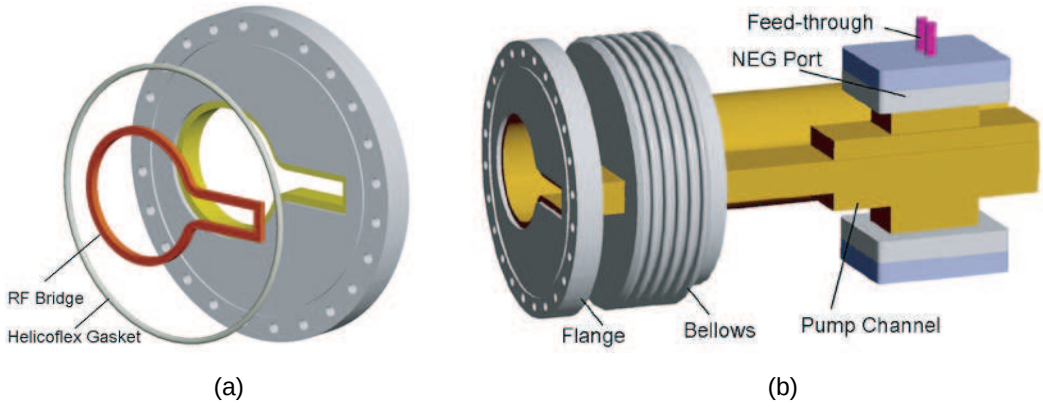

Figure 9.13: Flange and joint in LER.

TE-mode-like HOM, will become a serious problem. The TE-mode-like HOM is excited in any region where a bunched beam passes off-center, or the cross section of the beam chamber is asymmetric. Heating of the bellows caused by HOM has already been observed in the present KEKB [11, 19]. Even the impedance of a radial bump (1mm height and 20 mm axial length) at an RF-shield structure (loss factor of $\sim$10 V nC^{-1} at a bunch length of 3 mm, see Fig. 9.30.) would be large enough to be serious. The parasitic power loss for one set of bellows would be about 2 kW for a 10 A beam current in that case.

Removing the bellows and connecting adjacent chambers directly and welding in situ might be one strategy [20]. The question then is how to absorb the thermal expansion of the beam chamber during operation. If the temperature of the beam chamber is well controlled, the thermal stress might be tolerable. A position feedback system for the beam position monitor (BPM) will be indispensable at a quadruple chamber. The remaining critical problems are how to absorb any alignment and manufacturing errors in the beam chambers, and how exactly to fit a welding plane in situ.

The present design for SuperKEKB employs bellows. The bellows are equipped with an improved or new RF-shield structure that has a higher thermal strength and a lower impedance than that used before. The improved structure will replace the present one, with a shield finger that is thicker and coated with silver or gold. The length of the finger is short so as to avoid coupling with the TE-mode-like HOM. The main material of the bellows is pure copper or copper alloy. Another candidate for a new RF-shield structure is a comb-type RF shield that is different from the finger-type [21, 22, 23]. The R&D on the comb-type RF-shield is under way. To reduce the number of flange connections, one side of the bellows is welded to the beam chamber. The configuration of the flange and bellows is shown in Fig. 9.13 (b).

9.2.4 Taper

In a straight section where the SR is weak, beam chambers are simple pipes like those in KEKB. Therefore, tapers are required at the transitions between the arc sections and the straight sections to connect an ante-chamber to a single-pipe chamber. Special components at the arc sections, such as gate valves or movable masks, also need tapers at both ends. The loss factors for tapers with several lengths were calculated, and are shown in Fig. 9.14. For a taper with a length over 200 mm, the loss factor is about 3 V nC^{-1} at

a bunch length of 3 mm. Since the number of tapers is not very large, tapers at the SR channel will have little effect on the total impedance. The possibility of a trapped mode being excited between adjacent tapers and the SR power density on the side wall of a taper section should be studied.

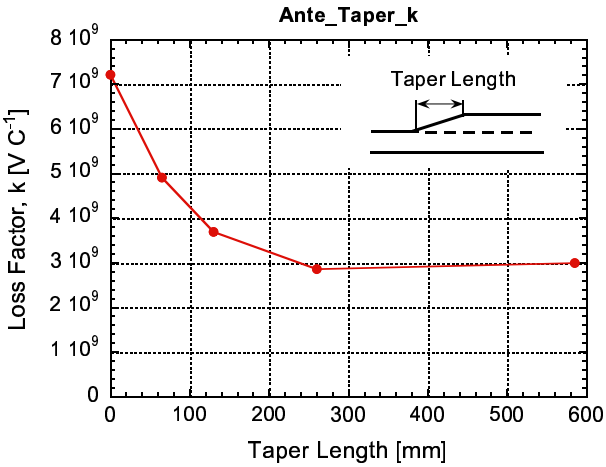

Figure 9.14: Loss factor as a function of taper length.

9.2.5 Gate valve

Gate valves are indispensable for a safe vacuum system. A gate valve should have an RF-shield structure inside like that used for the bellows. The VAT Series-47 type (VAT CO. Ltd.) has been used at KEKB and has worked well [2, 3]. The cross section has been specialized to fit that of the present beam chamber. However, since the gate valve RF shields are of the finger type, it is difficult to match the ante-chamber cross section. Another possibility is to make taper sections upstream and downstream of the gate valve. Heating of gate valves due to HOM has been observed at KEKB. The loss factor of a gate valve is estimated to be about 3 V nC^{-1} for a bunch length of 3 mm [19]. An improvement of the RF shield structure together with an increase in the cooling capacity will be required. One other option is to use a new type of RF shield, such as a comb-type RF shield.

9.2.6 HOM damper

At SuperKEKB, the stored beam currents are so high and the bunch length is so short that intense HOM can be generated in various vacuum components. For a component with a loss factor of 10 V nC^{-1}, for example, the parasitic power loss reaches 2 kW for a 10 A beam. The intense HOM leads to excess heating or an abnormal discharge in the affected components. A reduced-HOM design, that is, a design with long tapers where the cross section changes and with no big gaps, for example, should be widely adopted for the vacuum components. For some vacuum components, however, HOM absorbers (dampers) will be indispensable in SuperKEKB. HOM dampers have been utilized successfully in the accelerating cavities of KEKB [24]. The fundamental techniques have been developed through R&D efforts. Special HOM dampers for the movable masks have been installed

and work well. HOM dampers will be also important components in the interaction region (IR).

9.2.7 Movable masks

To protect the physics detector from damage due to spent particles and to reduce the background noise, a movable mask (collimator) system will be installed in each ring. The first issue of the movable mask is the HOM generated at the mask head, where the bunched beam passes extremely off-center through the beam chamber. A chamber-type movable mask, which has a trapped-mode-free structure, has been installed at KEKB and is working well [25, 26, 27]. A similar movable mask will be employed at SuperKEKB. The configuration and outside appearance of the chamber-type movable mask are shown in Fig. 9.15. Figure 9.16 shows the calculated loss factors for the HER vertical and horizontal movable masks as a function of the bunch length. At a bunch length of 3 mm, the loss factor reaches about 1 V pC^{-1}, which corresponds to a parasitic power loss of 200 kW for a 10 A beam current. The loss factor for the LER movable mask is almost the same as that of the HER. HOM dampers will have to be included with the movable mask as shown in Fig. 9.17. Another approach is to improve the present structure or develop new design for the movable mask in order to reduce impedance. An investigation of this possibility is also under way at present. One other problem is the development of grooves on the mask head, which have already been experienced at KEKB [25, 26]. The grooves on the mask head are now understood to be the result of the impact of an abnormally steered beam. An effective way to avoid the production of grooves is to use a light material as the mask head, such as carbon or beryllium, with a thickness of about one radiation length. Figure 9.18 is the calculated temperature rises for several materials along a beam path when a 1 A electron beam with a radius of 1.5 mm is incident on the material. Promising candidates are carbon and beryllium. A safe and rapid beam abort system using a beam orbit and/or a beam-loss monitor can also help to minimize any damage to the mask heads.

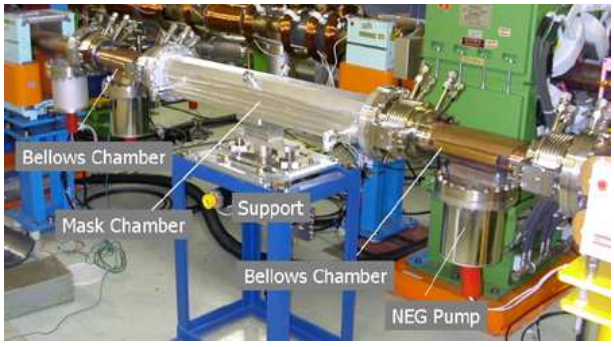

Figure 9.15: Mask chamber (vertical) in the present KEKB HER.

9.2.8 Solenoid and surface coating

The ante-chamber structure is expected to be effective for reducing photoelectron clouds in the beam channel of the positron ring. However, to suppress electrons more thoroughly,

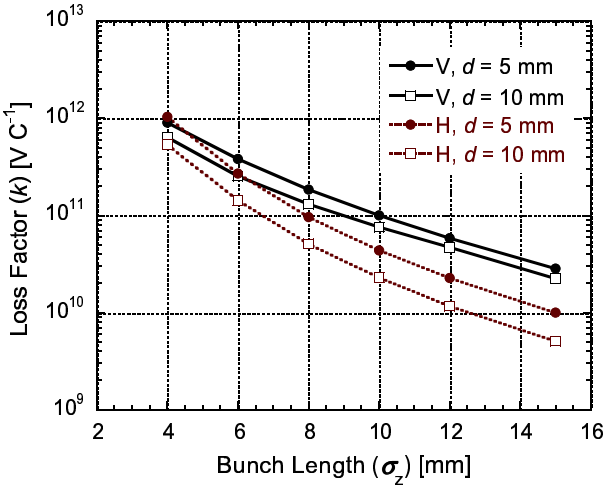

Figure 9.16: Loss factor as a function of bunch length.

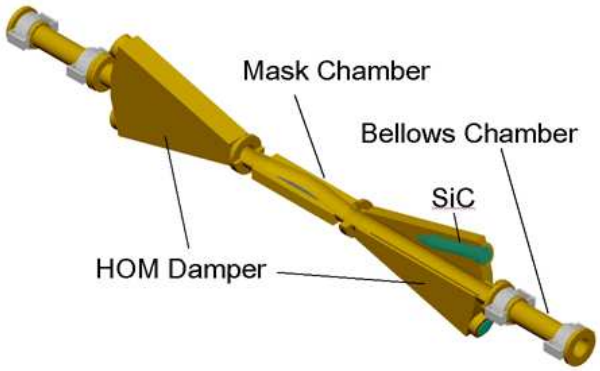

Figure 9.17: HOM damper with a movable mask.

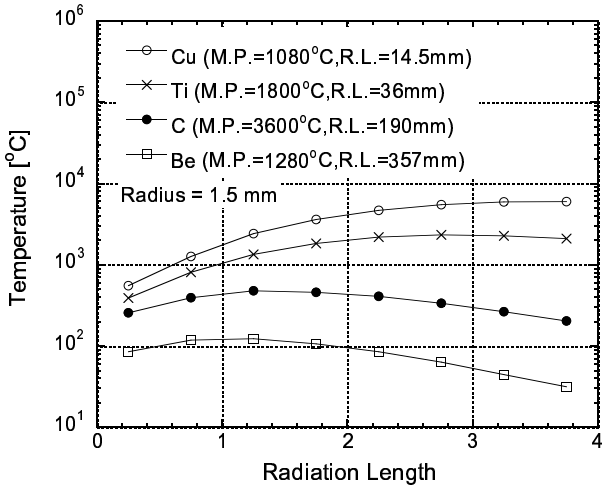

Figure 9.18: Temperature as a function of radiation length. The electron beam current is 1 A. The EGS4 simulation code was used in the calculation for copper, titanium, carbon, and beryllium.

the application of an external magnetic field via solenoids or permanent magnets is considered. Solenoid magnets have been working successfully at KEKB [28]. Figure 9.19 shows the photoelectron distribution in an ante-chamber under the same conditions as in Fig. 9.3 (a), except for an added axial magnetic field of 0.5 mT. The photoelectrons are completely removed by applying a solenoid field of only 0.5 mT. The external magnetic field is effective, since the electric field accompanying the beam is weak in the SR channel. Note here that the above discussion does not include secondary electrons, which are a cause of multipactoring [29, 30]. Some reflected or scattered SR irradiated on an inner wall of a beam channel will emit photoelectrons. Those photoelectrons will be accelerated by successive bunches and will emit secondary electrons when they hit the inner wall at high energy. That process leads to multipactoring if the secondary electron yield is large.

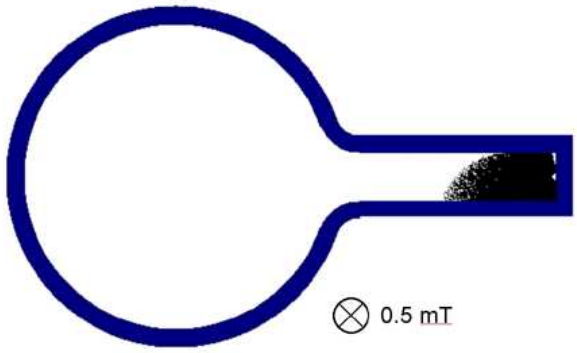

Figure 9.19: Photoelectron distribution in LER ante-chamber with a solenoid magnetic field of 0.5 mT.

A solenoid field is also very effective for preventing multipactoring and reducing the electron density around a beam [28]. However, the field strength needs to be greater than 0.5 mT. Since the present design of the ante-chamber has no pumping port in the beam channel, a more uniform solenoid field can be formed compared to the case at the present KEKB. The solenoid will be wound around the beam chamber before installation in the ring. One layer of a solenoid coil using electrical wire with a diameter of about 3 mm is sufficient. Arranging permanent magnets around a beam chamber is also a way to apply external magnetic fields. Permanent magnets can be applied to the quadrupole and sextupole magnets where the winding of solenoid wire is difficult due to the narrow clearance at the SR channel. The permanent magnet is suitable for narrow spaces and for BPM sections.

Another way to suppress secondary electron emission is to coat the inner surface with some material having a low secondary electron yield. If the thickness of the coating is thin (about 1 μm), it will have no effect on the resistive wall instability. A TiN coating has been used in the LER beam chamber of PEP-II [7]. However, the results from PEP-II indicate that the secondary electron yield from TiN is almost the same as that of cleaned copper. Another candidate is a coating of NEG compound [31]. The coated NEG was also found to have a low photo-desorption coefficient. One problem is that an activation of the NEG (i.e. baking up to 180 °C at least) is necessary to obtain a low secondary electron yield. After saturation, the secondary electron yield returns to the initial value. Furthermore, the thermal expansion of a copper beam chamber with, for example, a length

of 6 m is about 20 mm for a temperature rise of 200 °C. A common problem of coating will be exfoliation from the inner wall, i.e., the stability of the coating. Thus, quality control of the coating is another key point. Further investigation into the roughness and conductivity is necessary before applying it to a real beam channel.

9.2.9 Wiggler section

For the LER at SuperKEKB, a wiggler section is located in the Nikko straight section to reduce the damping time. The effective length and bending radius of the wiggler magnets are 346.2 mm and 15.48 m, respectively. Four bending magnets make up one bump orbit. The gaps between the magnets are 0.1538 m, 0.2538 m, and 0.5732 m (see Fig. 9.20). Line densities of the SR at the outside and inside of the beam chamber are shown in Fig. 9.21 (a) for the cases of outer half aperture of 47 mm and a 9.4 A beam. The power was calculated for three bumps, as shown in Fig. 9.20. The power density goes up to about 60 W mm^{-2} (the height of the SR is assumed to be 0.7 mm). In that case, the temperature and thermal stress go up to about 230 °C and 400 MPa, respectively. The temperature is almost equal to the annealing temperature and the thermal stress exceeds the tensile strength. The aperture at the wiggler section should be as wide as in the arc section. Figure 9.21 (b) is the calculated power density for the case of a half outer aperture of 112 mm, which is the same as in the arc section. The power density is reduced to about half of what it was in the former case. A possible cross section of the beam chamber in the wiggler section is shown in Fig. 9.22. The SR channels are on both sides of the beam channel. The SR channel has pump channels on both sides to evacuate the beam channel. For the wide aperture, however, the present wiggler magnets will need to be modified due to their narrow widths. The cooling system around the wiggler section also needs to be improved to absorb the localized intense SR power.

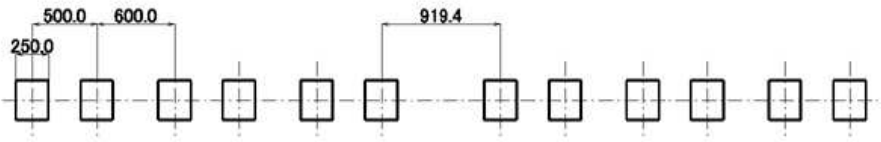

Figure 9.20: Layout of wiggler magnets.

9.2.10 Cooling system

At SuperKEKB, the cooling power should be improved since the total SR power increases by a factor of four. The SR power of the LER is 7.7 MW without wigglers, and that of the HER is 14.2 MW. The SR power from the wiggler section (LER) is 4.4 MW. The total SR power is then about 26 MW. When the dissipated power from HOM all over the ring is considered, the power absorbed by the beam chambers is increased (about 6 MW per ring). On the other hand, the present cooling capacity is about 8 MW in total for the vacuum system, which is almost the same as the total SR power expected from the design parameters of KEKB. An increase of the cooling capacity is indispensable for SuperKEKB. For a reference, the total flow rate is presently about 6000 l min^{-1}. The

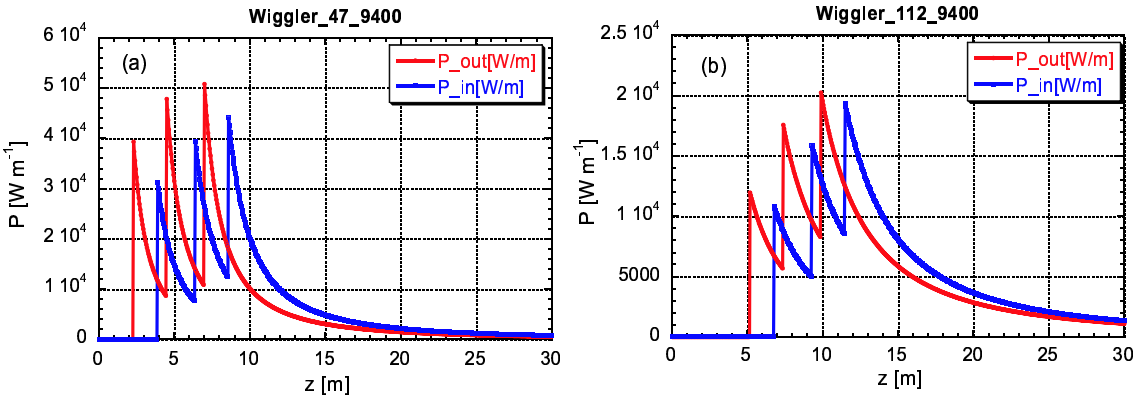

Figure 9.21: Calculated SR power line densities for (a) single beam chamber and (b) ante-chamber.

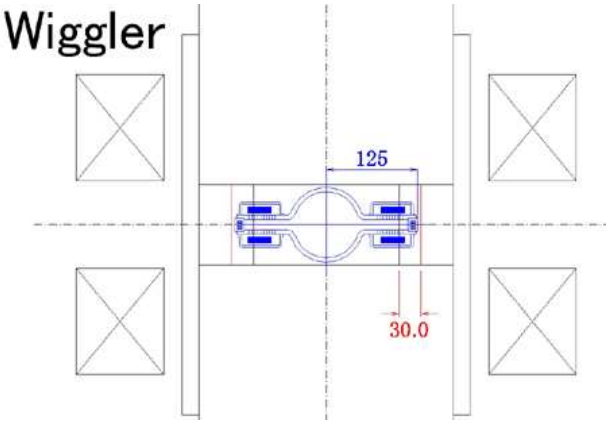

Figure 9.22: Cross section of the ante-chamber in a wiggler magnet.

average increase of temperature is estimated to be about 60°C ($2.6\times10^7/70/6000$). More concretely, one cooling loop has a length of about 10 m in the present KEKB tunnel. The typical flow rate is about 20 l min^{-1} and one loop cools both the LER and the HER. The flow rate used for one ring is about 10 l min^{-1}. At SuperKEKB, the average dissipated SR power per 10 m of the HER is about 65 kW ($14.2\times10^3/220$). The temperature rise for one loop would reaches 93°C ($65\times10^3/70/10$). The flow rate must be increased as well as the cooling capacity. The length of one cooling loop in the tunnel or the layout of the loop should also be optimized.

9.2.11 Controls and monitoring system

The design of the control and monitoring system follows that of the present system [32]. Vacuum gauges are cold cathode gauges (CCG), as in the present KEKB. The vacuum gauge is installed on top of the ion pumps and positioned about every 10 m. The compressed air system will also be reused to actuate the gate valves. Highly reliable alarm and interlock systems are required. Many components, such as photon stops, bellows, gate valves and so on, can easily overheat from the intense SR or from HOMs if the cooling system fails. The flow rates of the cooling water and the temperatures of the vacuum components must be monitored. Through an accident or misoperation, a mis-steered beam can easily damage the vacuum chambers and movable masks; a rapid and safe beam-abort system is required.

9.2.12 Vacuum scrubbing

Here, we try to estimate the time needed to achieve the target pressure of 5×10^{-7} Pa. Figure 9.23 shows a simulation of the vacuum scrubbing of the LER. The assumptions are as follows:

1. NEG pumps are activated when the pumping speed falls to 0.02 m^3 s^{-1} m^{-1}.
2. The beam current is increased by 9.4/500 A when the lifetime exceeds 5 hours.
3. η decreases as in Fig. 9.10.

In the figure, the pressure, P, the photo-desorption coefficient, η, and the beam current, I, are plotted as a function of the beam dose. The maximum beam current of 9.4 A will be achieved in 5 kA·hours if the commissioning proceeds satisfactorily. The steps seen in the pressure line correspond to the timings of NEG activation. The number of activation cycles is greater than 20 and the lifetime of the NEG strip may be a concern.

9.3 R&D status

9.3.1 Ante-chamber

A prototype ante-chamber made of oxygen free copper, as shown in Fig. 9.24, was installed in the KEKB LER from 2001 to 2003. No severe problems were found during operation up to a stored current of 1.4 A, although a resonant-like heating and also pressure bursts were sometimes observed for a particular bunch fill pattern. A photon stop was irradiated by

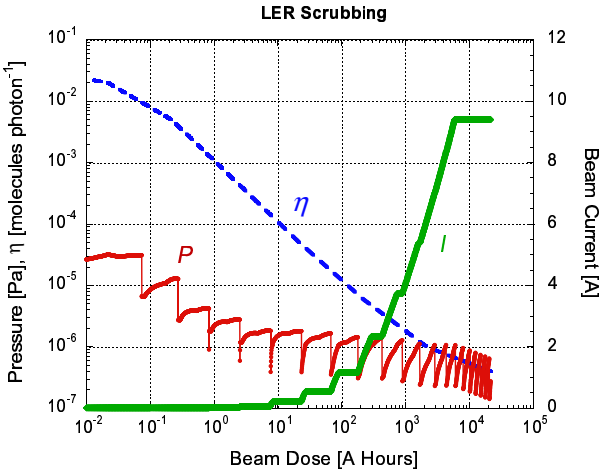

Figure 9.23: Simulation of vacuum scrubbing. Pressure, photo-desorption coefficient, beam current as a function of beam dose for LER.

SR in this proto-type. A positive (+100 V) grid just beneath the photon stop attracted the photoelectrons emitted from the stop. The number of electrons in the beam channel near the photon-stop was measured by a photoelectron monitor [33]. The number of electrons in the beam channel was found to decrease to about 1/7 of that in the single copper beam chamber, as shown in Fig. 9.25 [21]. The reduction of photoelectrons in the beam channel by using an ante-chamber structure was confirmed. A solenoid field was also effective in reducing the photoelectrons in the beam channel. The photoelectrons further decreased by 1/2 upon applying a solenoid field of about 5 mT, as shown in Fig. 9.25. A bellows with the cross section of an ante-chamber was manufactured without any problem.

Figure 9.24: Prototype ante-chamber (1st trial model).

After about two years of operation, it was found that the photoelectron grid had undergone extreme heating. Some insulators had melted, which explained some pressure bursts. We believe that the photon-stop structure traps a HOM. In addition, several RF shield fingers at the SR channel of the bellows were heated and welded at the sliding contact point. The bellows had been installed near a taper region where the beam chamber changes from ante-chamber type to single-chamber type We believe that the heating of the fingers is due to HOM at the taper.

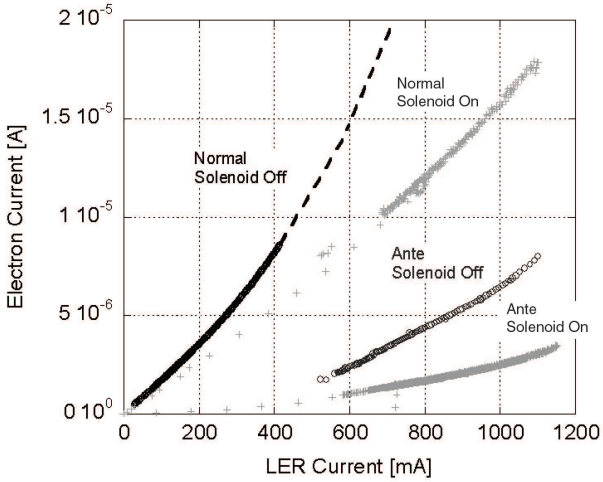

Figure 9.25: Measurement of the photoelectron yield as a function of LER beam current.

A second trial model of the ante-chamber, using the latest design, is now being manufactured and will be installed in the KEKB LER in 2004. In this design, the SR hits the side wall of the SR channel instead of a photon stop. A saw-tooth structure or a rough surface is etched into the surface of the side wall to reduce photoelectron emission and reflection of the SR.

Two manufacturing methods are being tested. One is to use a stamp (press) to form an ante-chamber structure. A test piece after pressing is shown in Fig. 9.26 (a). The piece is pressed from a copper (OFC) plate (6 mm thick). Two pressed pieces are electron beam welded together with a cooling channel to form one beam chamber. A key issue of this method is the accuracy of the pressing. The other method is to use a cold-drawn OFC pipe with an ante-chamber cross section. The drawing method can reduce the number of weld points and the cost as a result of mass production. The drawing test has just started and a sample piece of drawn pipe is shown in Fig. 9.26 (b).

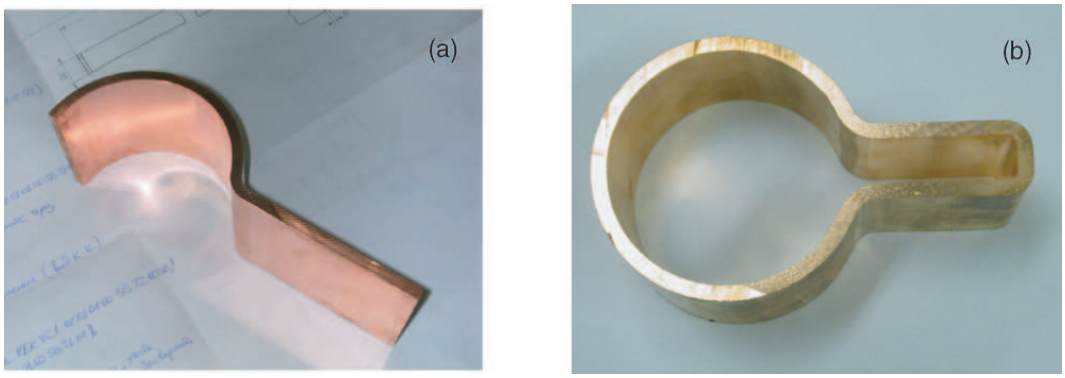

Figure 9.26: (a) Stamped plate and (b) drawn ante-chamber.

9.3.2 HOM damper

Heating of the pump elements due to HOMs generated at the masks had been observed [25, 34]. In order to reduce the HOMs, a winged HOM damper has been designed and a

trial model has been installed near the movable masks in the LER at KEKB. The damper has delta-type wings, with two SiC rods (ϕ55 mm $\times$ 400 mm) installed inside each wing as shown in Fig. 9.27. This design is based on a grooved beam pipe scheme that has been successfully used in the KEKB ARES cavity system [24]. These SiC ceramic rods had been originally developed as a HOM absorber for that system [35]. Typical real and imaginary parts of the relative dielectric constant are 21 and 5, respectively, at 1 GHz. The SiC rod is cooled directly by water flowing inside at a rate of 4 l min^{-1}. The SiC rod was tested up to an input power of about 3.7 kW using 1296 MHz microwaves. The capacity for one SiC rod is, however, expected to be about 10 kW from a thermal calculation. A calculation using the HFSS simulation code was used to optimize the whole structure. The angle between the axis of the SiC rod and the beam is 15°. The total length and width of the damper are 1200 mm and 505 mm, respectively. The loss factor is estimated to be less than 10 V nC^{-1} for a bunch length of 6 mm. The wing and beam chamber are connected via a long slot (20 mm wide $\times$ 707 mm long). TE modes in a wide frequency range can be absorbed efficiently.

Figure 9.27: SiC rod in a winged HOM damper.

A view of the winged HOM damper together with an LER horizontal-type mask is presented in Fig. 9.28. Two pairs of HOM damper were installed near the horizontal movable mask before the autumn run in 2002 [34]. The wings have been oriented vertically to absorb the horizontally polarized HOM excited by the horizontal mask. The absorbed power per damper was about 5 kW at about a 1.5 A beam current. The total excited HOM power from the horizontal masks is estimated to be about 20 kW. The absorbed power, therefore, is about 25% of the total HOM power. A pressure rise due to heating of the pump elements disappeared and heating of the bellows near masks was also suppressed. A HOM damper with the same structure will be used in SuperKEKB. The efficiency and capacity of the HOM damper, however, should be improved. The HOM power of the movable mask will reach 200 kW. Development of a powerful HOM damper will be an important issue for SuperKEKB.

9.3.3 Bellows

Recently, a comb-type RF shield structure for the bellows has been proposed [36, 22, 23]. An inside view of the comb-type RF-shield for a circular beam chamber is shown in

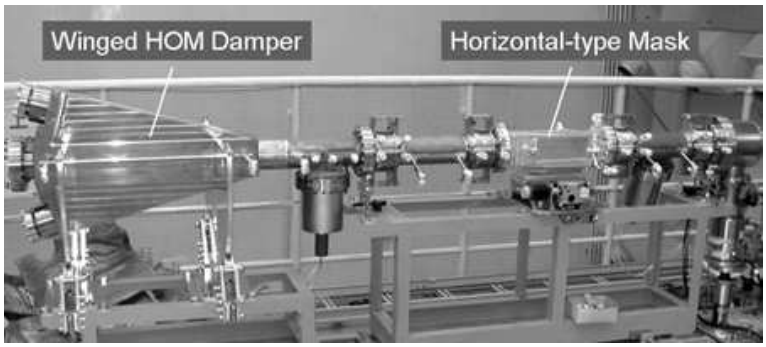

Figure 9.28: HOM absorber and a movable mask (horizontal).

Fig. 9.29 (a). The RF shield consists of thin, interlocking comb-teeth. In the trial model, the length (a), width (t), and radial thickness of the comb teeth are 10 mm, 1 mm, and 10 mm, respectively. The gap between adjacent teeth (c) is 2 mm and, therefore, the gap between nested teeth is 0.5 mm. In the nominal position, the total length of the RF-shield structure (b) is 15 mm. For a circular beam duct with an inner diameter of 94 mm, the number of teeth is about 100. The combs are made from pure copper and are easily machined. In principle, high-frequency wall currents accompanying the bunched beam will flow via capacitance between the nested teeth. To ensure the flow of DC current and to block penetration of the HOM from inside to outside, small fingers (back fingers) are installed along the outer edge between the nested teeth. The back fingers are made of silver coated Inconel alloy with a thickness of 0.1 mm and width of 5 mm. The contact force is set to be about 0.6 N per a finger in the trial model. Advantages of the comb-type RF-shield are as follows:

1. High thermal strength.

2. Low impedance. Dependence of loss factors on bunch lengths are shown in Fig. 9.30. The loss factor of the comb-type is smaller than that of finger-type by a factor of 3 or 4.

3. Small leakage of a TE mode-like HOM to outside.

4. No sliding contact on the inner surface.

5. Applicable to various cross sections of the beam chamber.

On the other hand, The axial stroke of the RF-shield is structurally limited. For the trial model described above, the usable strokes are ± 3 mm (expansion) and -4 mm (contraction), which are much smaller than that of a conventional finger-type, ± 10 mm typically. Although bending at the RF-shield of 20 mrad is possible, it depends on the size of the teeth.

Experiments on the bellows with the comb-type RF-shield started in 2003. The bench tests, that is, an abrasion test in a vacuum and a heating test transmitting 508 MHz microwaves up to 400 kW, gave promising results. Two prototype bellows with a comb-type RF shield, as shown in Fig. 9.29 (b), were installed in the KEKB LER in 2003. A back-up RF shield, which doubles as a movement guide, is attached just outside of the

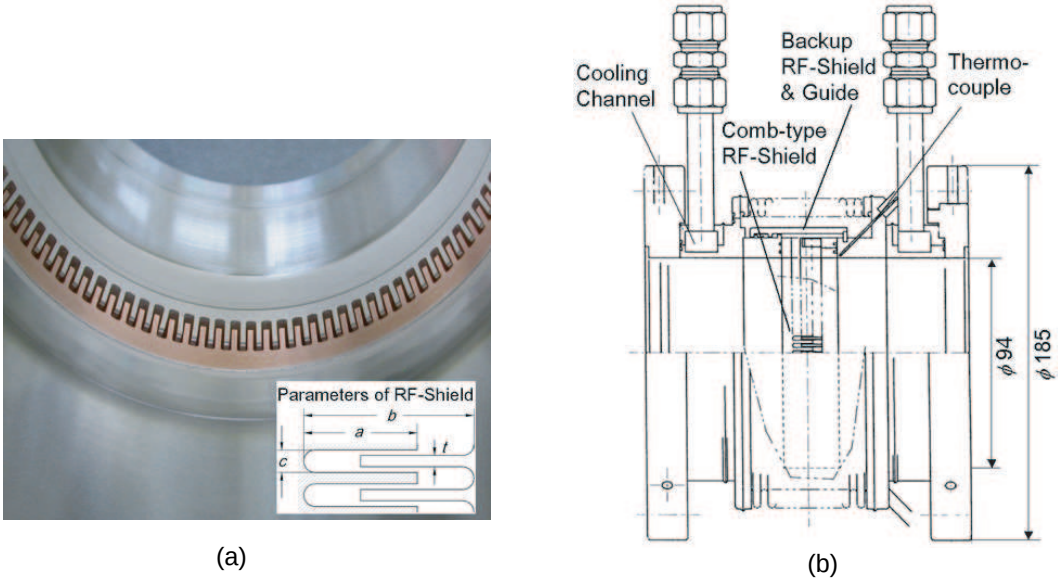

Figure 9.29: (a) Comb-type RF shield. (b) Prototype of bellows chamber with a comb-type RF shield.

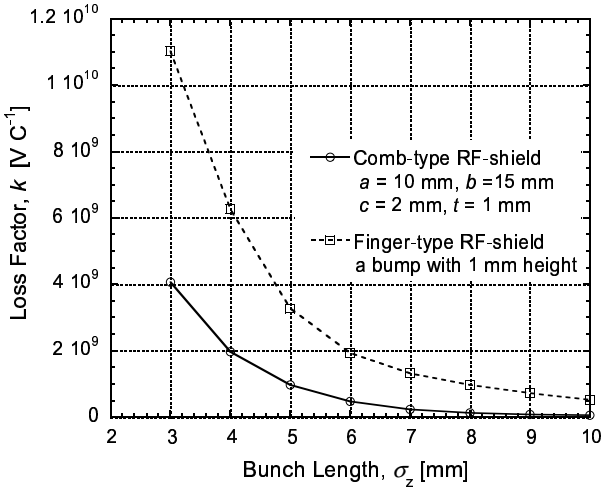

Figure 9.30: Loss factor as a function of bunch length for comb-type and finger-type RF shields.

comb-type RF-shield. The comb is copper but the outer shield is stainless-steel. Temperatures near the RF shield can be measured with two embedded thermo-couples. The bellows were installed just downstream of movable masks, where TE-mode like HOMs are relatively intense compared with other locations. The temperatures at the corrugations of the bellows with a conventional finger-type shield and with a comb-type RF shield during typical operations are presented in Fig. 9.31 (a), where the bunch spacing is about 4 buckets and the number of bunches is 1284. The temperature of the corrugation for the bellows with a comb-type RF shield is much lower than that of the finger type. Thus, the leakage of the HOM through the RF shield is very small when compared with the finger-type. Figure 9.31 (b) shows the temperature of the comb. The temperature at a beam current of 1500 mA is about 50°C, which means that the comb-type RF shield can be used for higher-beam-current operations, for example at 4 A, even with the same number of bunches ($25\times2.7^2+25=207$ °C). If the stainless steel in the cooling channel is changed to copper, the bellows can be used at even larger beam currents. R&D will continue on using the comb-type RF-shield with bellows having a smaller diameter or a race-track cross section.

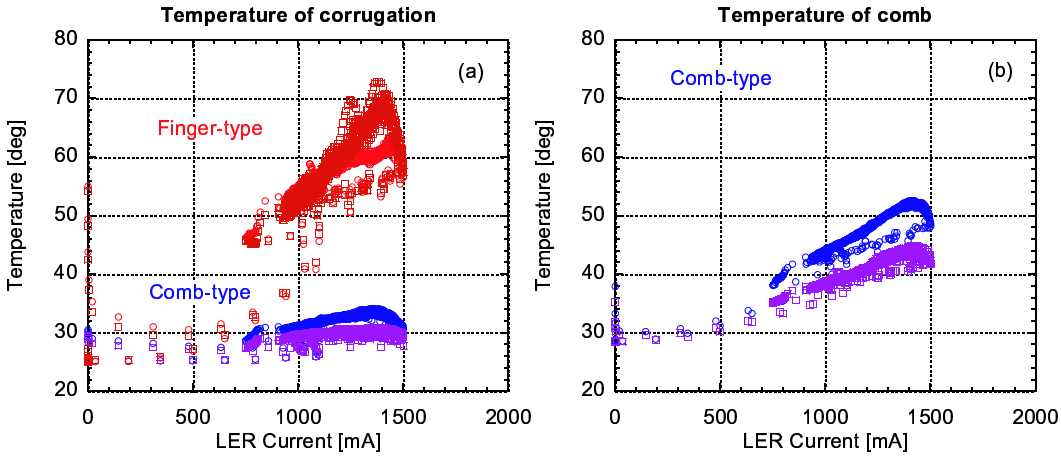

Figure 9.31: (a) Temperature at corrugations of the bellows with the conventional finger-type and with the comb-type RF shield as a function of the beam current. (b) Temperature of combs of comb-type RF shield as a function of the beam current. The bunch spacing is 3.77 buckets and the total number of bunches is 1280.

The comb-type RF-shield structure can also be used for the gate valves. No mechanical restriction is found in that case, where the stroke is small and no bending or tilting is necessary.

Bibliography

[1] K.Kanazawa, Y.Suetsugu and Y.Hori, "Vacuum System for the KEK B-Factory", KEK Report 90-24 (Accelerator Design of the KEK B-Factory), p.117 (1990).

[2] K.Kanazawa, S.Kato, Y.Suetsugu, H.Hisamatsu, M.Shimamoto, M.Sato and M.Shirai, " KEKB Vacuum System", Appl. Surface Sci. 169-170, p.715 (2001).

[3] K.Kanazawa, S.Kato, Y.Suetsugu, H.Hisamatsu, M.Shimamoto and M.Shirai, "The Vacuum System of KEKB", N.I.M.-P.R. A 499, p.66 (2003).

[4] K.Kanazawa, S.Kato, Y.Suetsugu, H.Hisamatsu, M.Shimamoto, M.Sato and M.Shirai, "Construction of KEKB vacuum system: installation of vacuum chambers", App.Surface Sci., Vol.169-170, pp.720 (2001).

[5] H.Ishimaru, T.Momose, K.Narushima, H.Mizuno, K.Kanazawa, H.Watanabe and M.Shimamoto, "All aluminum alloy ultrahigh vacuum system for a 30 GeV electron-positron collider", J.V.S.T. A4(3), p.1762 (1986).

[6] K.Kanazawa, Y.Suetsugu and H.Hisamatsu, "Vacuum Characteristics of TRISTAN Ring", Proc. 7th Symp. Acc. Sci. & Technol., Osaka, December 12-14, p.118 (1989).

[7] K.Kennedy, B.Harteneck, G.Millos, M.Benapfl, F.King and R.Kirby, "TiN Coating of the PEP-II Low-Energy Ring Aluminum Arc Vacuum Chamber", PAC'97, Vancouber, B.C., May 12-16, p.3568 (1997).

[8] AMAX Copper Inc.,"A Survey of Properties & Applications: OFHC", p.19-22 (1974).

[9] H.Koiso, private communication.

[10] H.Fukuma, private communication.

[11] Y.Suetsugu, K.Kanazawa, S.Kato, H.Hisamatsu, M.Shimamoto and M.Shirai, "Present Status of the KEKB Vacuum System", J.V.S.T-A21(4), p.1436 (2003).

[12] SAES Getters, "Technical Description of St707 Strip Type St707/CTAM/30D" (1984).

[13] J.M.Lafferty,"Foundations of Vacuum Science and Technology", John Wiley & Sons, Inc., New York, p.89 (1998).

[14] K.Akai, private communication.

[15] H.Matsumoto and M.Ohtsuka, "DEVELOPMENT OF THE VACUUM FLANGE FOR THE HIGH POWER RF APPLICATIONS", Proceedings of the 24th Linear Accelerator Meeting in Japan, July 7-9, Sapporo, pp.271-273 (1999).

[16] K.Kakiara, T.Ohgoe, M.Ikeda, T.Kamitani, S.Yamaguchi, T.Sugimura and S.Ohsawa, Proceedings of the 28th Linear Accelerator Meeting in Japan, July 30-August 1, Tokai, pp.294-296 (2003).

[17] Y.Suetsugu, K.Ohshima and K.Kanazawa, "Design Studies on a Vacuum Bellows Assembly with Radio Frequency Shield for the KEK B Factory", Rev. Sci. Instrum, 67, p.2796 (1996).

[18] Y.Suetsugu, K.Kanazawa and K.Ohshima, "Bellows Design and Testing for KEKB", Vacuum, 47, p.629 (1996).

[19] K.Akai et al., N.I.M.-P.R. A 499, p.191 (2003).

[20] J.T.Seeman, "High Luminosity B-Factory", PAC'01, Chicago, June 18-22, p.305 (2001).

[21] Y.Suetsugu, "Basic Design and R&D Items of Vacuum System for Higher Luminosity B-Factory", KEK Proceedings 2002-17, p.7 (2002).

[22] Y.Suetsugu, M.Shirai and K.Shibata, "Possibility of a Comb-type RF Shield Structure for High-Current Accelerators", PRST-AB, ID.103201 (2003).

[23] Y.Suetsugu, M.Shirai and K.Shibata, "COMB-TYPE RF-SHIELD FOR HIGH CURRENT ACCELERATORS", Proc. of 14th Symp. on Acc. Sci. Technol., Tsukuba, 11-13 November, pp.37-39 (2003).

[24] T.Kageyama, K.Akai, N.Akasaka, E.Ezura, H.Mizuno, F.Naito, H.Nakanishi, Y.Takeuchi, Y.Yamazaki and T.Kobayashi, "The ARES Cavity for The KEK B-Factory", EPAC'96, Sitges, June 10-14, p.2008 (1996).

[25] Y.Suetsugu, N.Akasaka, T.Kageyama, Y.Takeuchi, K.Kanazawa and K.Satoh, "Development of The Movable Mask Free from Trapped Mode for The KEKB", PAC'01, Chicago, June 18-22, p.2186 (2001).

[26] Y.Suetsugu, K.Shibata, T.Sanami, T.Kageyama and Y.Takeuchi, " Development of movable mask system to Cope with high beam current", Rev. Sci. Instrum, 74, p.3297 (2003).

[27] Y.Suetsugu, T.Kageyama, K.Shibata and T.Sanami, "Latest Movable Mask System for KEKB", to be published in N.I.M.-A (2003).

[28] H.Koiso, et al., "Present Status of the KEKB B-Factory", EPAC'02, Paris, June 3-7, p.341 (2002).

[29] O.Gröbner, "Beam Induced Multipactoring", LHC Project Report 127 (1997)

[30] Y.Suetsugu, "Observation and Simulation of the Nonlinear Dependence of Vacuum Pressured on the Positron Beam Current at the KEKB", PAC'01, Chicago, May June 18-22, p.2183 (2001).

[31] B.Henrist, N.Hilleret, C.Schererlein and M.Taborelli, "The Secondary Electron Yield of TiZr and TiZrV Non-Evaporable Getter Thin Film Coatings", App. Surface Sci., Vo. 172, pp.95 (2001).

[32] S.Kato, K.Kanazawa, Y.Suetsugu, H.Hisamatsu, M.Shimamoto, M.Sato, M.Shirai and M.Takagi, "Control of KEKB vacuum system", Appl. Surface Sci., 169-170, p.732 (2001).

[33] Y.Suetsugu, M.Tsuchiya, T.Nishidono, N.Kato, N.Satoh, S.Endo and T.Yokoyama, "Application of a Sawtooth Surface to Accelerator Beam Chambers with Low Electron Emission Rate", J.V.S.T.-A, 21, p.186 (2003).

[34] Y.Suetsugu, T.Kageyama, Y.Takeuchi and K.Shibata, "Development of Winged HOM Damper for Movable Mask in KEKB", PAC'03, Portland (OR), May 12-16, (2003).

[35] Y.Takeuchi, K.Akai, N.Akasaka, E.Ezura, T.Kageyama, H.Mizuno, F.Naito, H.Nakanishi, Y.Yamazaki and T.Kobayashi, "The SiC Absorber for the KEKB ARES Cavity", EPAC'96, Sitges, June 10-14, p.2020 (1996).

[36] Y.Suetsugu, K.Shibata and K.Kanazawa, "Conceptual Design of Vacuum System for Super KEKB", PAC'03, Portland (OR), May 12-16, (2003).

Chapter 10

Beam Instrumentation

10.1 Introduction

The planned beam currents for SuperKEKB are 9.4 A in the low energy ring (electrons) and 4.1 A in the high energy ring (positrons). In monitoring these high-current beams, we will encounter serious problems due to heating by beam-induced currents or due to the HOM components of the instrumentations installed in the ring. To overcome these heating problems, we are considering some modifications to the beam position detectors and kickers in the beam feedback systems.

The existing BPM system is usable for the precise COD measurement of the SuperKEKB rings. In addition, the development of the single-pass BPM system in the KEKB ring is progressing at present, and will be useful for injection tuning and optics diagnostics at SuperKEKB also.

The existing transverse beam feedback system is also sufficient to suppress the instabilities expected at the SuperKEKB rings. However, we will need to bring longitudinal beam feedback systems online for SuperKEKB, because unavoidable longitudinal instabilities from the RF cavities are expected due to strong HOM components and the incompleteness of the $0/\pi$ mode impedance cancellation as a result of heavy beam loading. To handle many kinds of instability, a high-speed digital filter board module (Gboard) is under development in a collaboration among KEK, SLAC and INFN. These will also be very useful for the investigation of instabilities with large memories incorporated.

For the synchrotron light monitors, the SR extraction system will be modified to decrease the power loss in the extraction mirror in the short wavelength region. This modification will also have the advantage of increasing the visible light intensity, which is required to improve the sensitivity of the individual bunch measurement by streak camera, gated camera, etc. In addition to these improvements, we are planning to construct another set of synchrotron light extraction and transport systems for each ring in order to compensate for the dynamic-beta effect in beam size measurements, since the beam size is, at present, observed at just one point in the ring; the estimated beam size at the collision point is affected by a very large dynamic-beta effect, which causes about a factor of 2 ambiguity, especially in the horizontal beam size measurement. Using two SR monitors for each ring, we can measure directly the beam-beam parameters in real time. We are expecting this type of the beam-beam parameter monitor to be very useful for the collision tuning to increase the luminosity. The preliminary design of the damping ring SR monitor required to monitor the damping process is also described.

10.2 Beam Position Monitors

10.2.1 BPM signal pickups

The performance of the existing BPM system of the KEKB rings is expected to be sufficiently good for the COD correction, optics correction and collision orbit feedback at Super-KEKB also, with some modification to the signal pickups to adjust the signal level for the design beam currents of 9.4 A at the LER and 4.1 A at the HER. In addition to the high beam current, the bunch length in each ring is planned to be 3 mm. These conditions require a reduction in the peak level of the beam bunch signal picked up by the button electrode in order to fit within the dynamic range of the existing front-end electronics. The expected output signal power of the pickup button electrode is summarized in Table 10.1. If the 12 mm diameter button electrode employed at the present KEKB ring were used at a beam current of 9.4 A, the expected signal power of 15.7 W would be too large for the front-end electronics; as a result, we plan to reduce the button size to 6 mm diameter. With this modification we expect a maximum signal power similar to that seen in the present KEKB at its maximum design current of 2.6 A.

	KEKB	SuperKEKB	Units
Beam current	2.6	9.4	A
Button	ϕ 12	ϕ 6	mm
Electrode output	0.798	1.17	W
Cable loss	0.789	1.16	W
Electronics input	0.009	0.009	W

Table 10.1: Signal power of BPM button electrodes of KEKB LER and SuperKEKB LER.

As for the signal component at the detection frequency (1.018 GHz) of the existing signal processing system, the detectable signal level decreases to a quarter of that seen at KEKB at the same beam current as shown in Table 10.2. We expect a signal level of 2.3 dBm at 9.4 A, which is an acceptable level for the present BPM front-end electronics.

	20 mA Beam	80 mA Beam
ϕ12 mm Button	-39.0 dBm (-49.0)	-27.0 dBm (-37.0)
ϕ6 mm Button	-51.1 dBm (-61.1)	-39.1 dBm (-49.1)

Table 10.2: Input signal power at 1.018GHz to the BPM front-end electronics transmitted by a 100 m (200 m) long signal cable.

For the special OCTPOS BPMs with 8 button electrodes installed at the front-end of the final-focus super-conducting quadrupole magnet, small button electrodes of 3 mm diameter (half of the present 6 mm) will be employed to handle a signal power corresponding to an equivalent beam current of 13.5A, since the positron and electron beams both pass by the BPMs in this section of beam-pipe.

10.2.2 Button Electrode Feedthroughs

N-type connectors are used with the feedthroughs of the BPM button electrodes in the KEKB ring in order to avoid problems due to loose connection of the central conductor of the connector. However, we have several tens of μm error in the orbit measurement sometimes caused by slight changes in contact pressure. To overcome such fluctuations, a special SMA connector with a male contact pin has been developed for the button electrode feedthrough. The button electrode with this special SMA connector, shown in Fig. 10.1, has been successfully used for the BPMs installed near the collision point in KEKB.

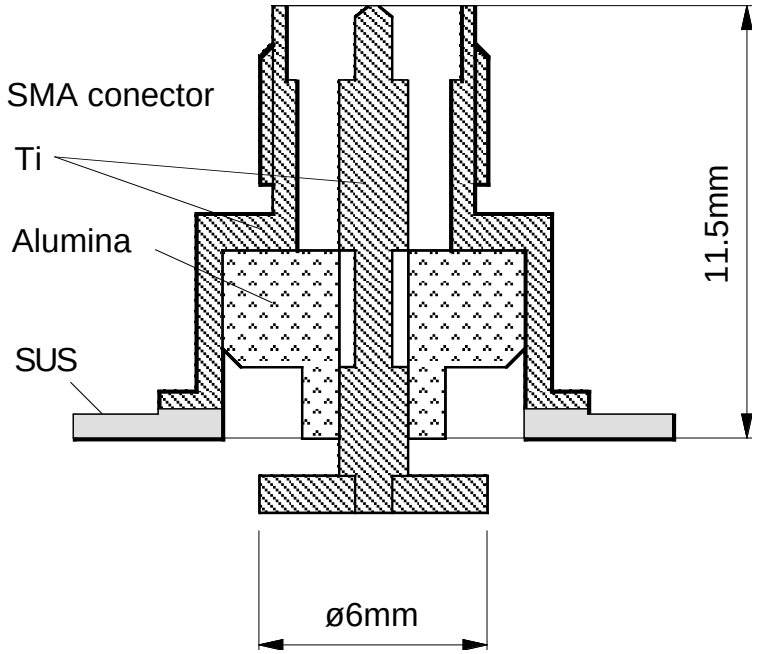

Figure 10.1: Feedthrough of the button electrode with a special SMA connector for KEKB.

In Super-KEKB the button electrode and special SMA will be mounted on the beam chamber via a connecting flange as shown in Fig. 10.2, instead of being welded directly on the chamber as at KEKB, for easy exchange in the event of problems. Each BPM signal pickup must be fixed firmly to a quadrupole magnet to avoid mechanical movement and vibration.

10.2.3 Electronics

The existing electronics system for the BPMs can also be used for Super-KEKB, with the addition of signal frequency converters to change the detection frequency to 508.9MHz in order to avoid HOM contamination to the signal due to the small cutoff frequency of the waveguide mode in the Super-KEKB ante-chamber.

10.2.4 Expected performance

The accuracy of COD measurement is expected to be same as at present. However, the minimum beam current to guarantee that accuracy will increase to 40 mA from the

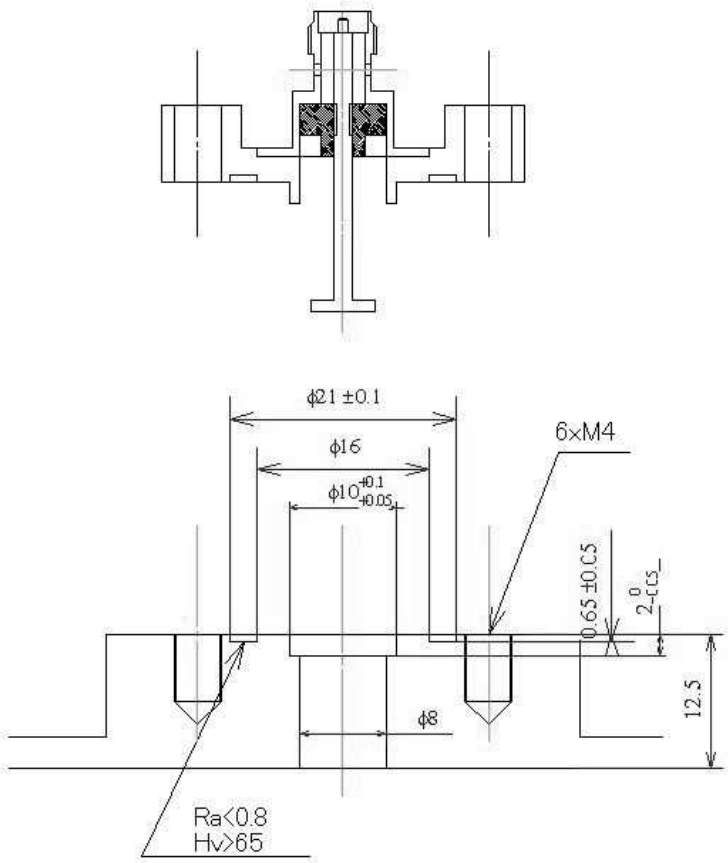

Figure 10.2: Button electrode of the Super-KEKB BPM signal pickup.

present current of 10 mA because of the reduction in size of the button electrode. In addition to the BPM system for the COD measurement, the installation of single-pass BPMs in the KEKB ring is in progress at present. In the Super-KEKB ring, 120 sets of single-pass BPMs will be installed. Using these BPMs we will be able to roughly correct the global COD for beam currents as low as 0.1 mA/bunch. In Table 10.3 we summarize the expected performance of the BPM systems at Super-KEKB.

	Averaging detection	Single-pass detection
Detection frequency	509/1018 MHz	250 MHz
Measurable beam current	> 40 mA	$0.1 - 30$ mA/bunch
Resolution	A few μm	$> 100\mu$m
Measuring time	4 sec	Turn by turn
Bunch number	Multi bunch/single bunch	Single bunch

Table 10.3: Expected performance of the BPM system for the COD measurement (averaging detection) and the single-pass BPM system (single-pass detection).

10.3 Bunch Feedback Systems

10.3.1 Design Considerations

The growth rates of the instabilities in the present KEKB rings have proven to be larger than initially estimated to be, even with a 4-RF-bucket-spacing filling pattern. In the KEKB LER, the growth rate of the horizontal instability at a beam current of 1.4 A easily exceeds 1/20 [1/turns]. The feedback systems are giving excellent performance to stabilize the instability up to the present beam current though the design damping time is around 100 turns. It is, however, obviously neither realistic nor safe to assume higher feedback-damping rates than the present ones for the transverse planes. Therefore, in the design of the bunch feedback systems for the SuperKEKB rings we concentrate our attention on the following items:

- Design durable components for high total beam current and high bunch current.
- Design low-level systems which have enough flexibility to meet the requirements coming from high beam loading.

We show the proposed design of the bunch feedback systems following the signal flow from beam signal pickups to signal processing systems, kickers and amplifiers.

We will prepare transverse feedback systems for both the HER and the LER, as in the present KEKB. As the estimated longitudinal growth rate of the instability from the cavity mode is larger or marginal than the radiation damping rate, we will also prepare longitudinal feedback systems for both the HER and the LER. The designed damping time for the transverse feedback system will be around 0.2 ms, the same as in the KEKB systems. For the longitudinal plane we expect around 1 ms.

10.3.2 Pickup electrode

We have been using SMA-type pickup electrodes for both the feedback detectors and the OCTPOS detectors (BPM pickups at the interaction point). For the octopos detector, we have changed the SMA interface to a special reverse-type (pin-type). They have shown excellent performance, especially in the OCTPOS detector; even with two beams of total current around 2.6 A passing with horizontal orbit offsets, no damage has been found. Figure 10.3 shows the simulated pickup response for a σ_L=3 mm bunch using MAFIA-T3. If we use ceramics with a lower dielectric constant in the feedthrough, for example $\epsilon_r \sim 4$ as compared to the present ϵ_r=9.8, TE-mode trapping modes would be reduced, and the response in the higher frequency region would be greatly improved, as shown in Fig. 10.4. Detailed R&D is necessary on a pickup electrode with lower ϵ_r.

The inner size of the pickup chamber will be almost the same as at present, that is, inner diameter of 64 mm. We can use the 2.5 GHz component with this chamber. The material of the chamber, cooling systems and the transition tapers from neighbor chambers will be modified in consideration of the higher beam currents.

10.3.3 Front-end circuit

Figure 10.5 shows the block diagram of the transverse feedback systems. The longitudinal front-end is similar, but using the sum signal to detect the bunch phase only. The front-

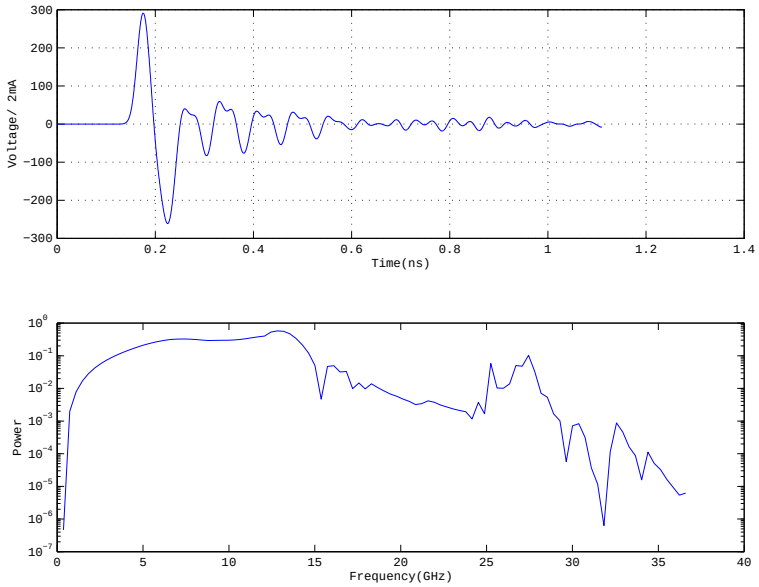

Figure 10.3: Simulated beam response of present pickup electrode for σ_L=3 mm bunch.

end circuit will be almost the same as the present circuit, except for a slightly increased detection frequency, from 2 GHz (=4×f_{RF}) to 2.5 GHz (=5×f_{RF}). Beam signals from the pickup electrodes are split four ways and recombined with delay cables to make a 2.5 GHz-FIR band pass filter, as shown in Fig. 10.6.

The lower figure of Fig. 10.6 shows the down-converted signal filtered by a 750 MHz low-pass-filter for several local-oscillator (LO: 2.5 GHz) phases. Sufficient flatness and good isolation from the next bucket are expected.

Presently we are tuning the LO phase and DC-offset manually by watching the waveform of the down-converted signal. For SuperKEKB, we will employ an intelligent automatic control system for these slow tunings.

10.3.4 Signal processing

We are now developing a general-purpose feedback signal processor as a single board module (Gboard) in collaboration with SLAC and INFN. Figure 10.7 shows the conceptural board layout of the Gboard. The specifications of the Gboard are as follows:

- Transverse bunch-by-bunch control at KEKB, PEP-II, DAΦNE and others.
- Longitudinal bunch-by-bunch control at KEKB, PEP-II, DAΦNE, etc.
- Transient-domain diagnostics features (e.g. instability growth/damping rate measurements).
- Fast bunch and beam instrumentation (e.g. bunch by bunch current monitor, tune monitor, gap transient/synchronous phase measurement).
- Support bunch spacings down to 0.66 ns with signal sampling at 1.5 GHz.

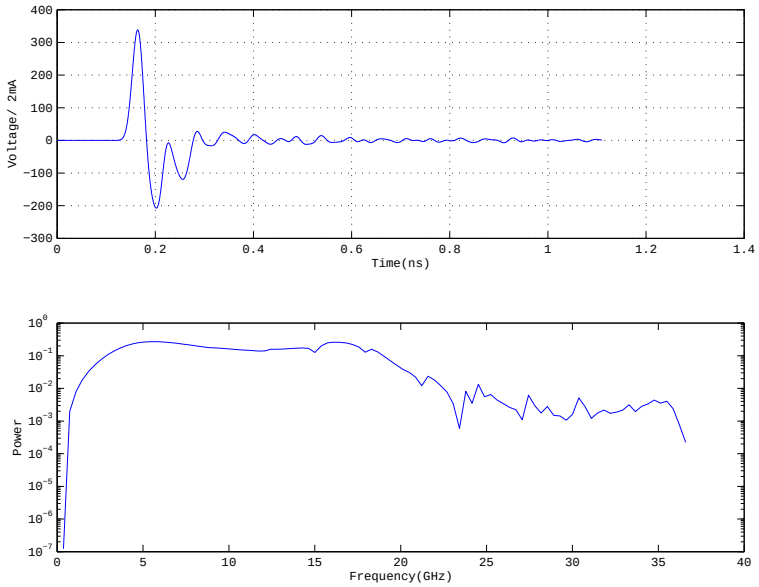

Figure 10.4: Simulated Beam response of pickup electrode with ceramic seal of $\epsilon_r = 4$.

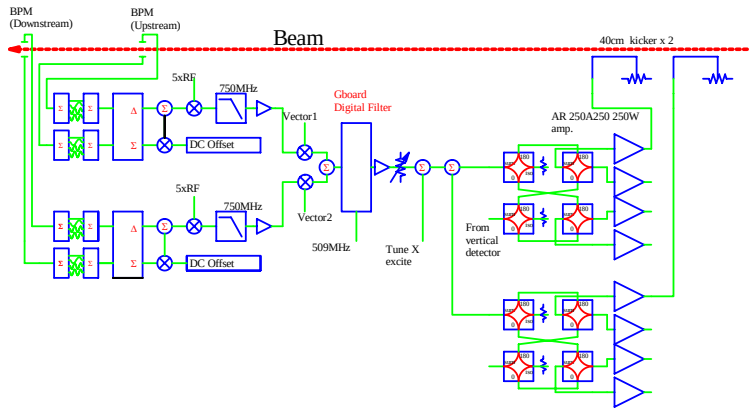

Figure 10.5: Block diagram of the transverse feedback systems.

The core functionality is general purpose, and re-configurable into a variety of signal processing and instrument functions - the reconfigurable Xilinx FPGAs define the exact algorithm.

We expect the following improvements with the Gboard:

- Good noise reduction compared to the present two-tap FIR filter;
- Wider frequency range for longitudinal feedback;
- Effective instability damping using a special digital-filter algorithm;
- Detailed understanding for the beam dynamics.

The backend electronics for the transverse feedback systems are almost the same as the present ones. To enlarge the feedback capture range, and to extend the stable feedback gain range, we may add a second transverse kicker system.

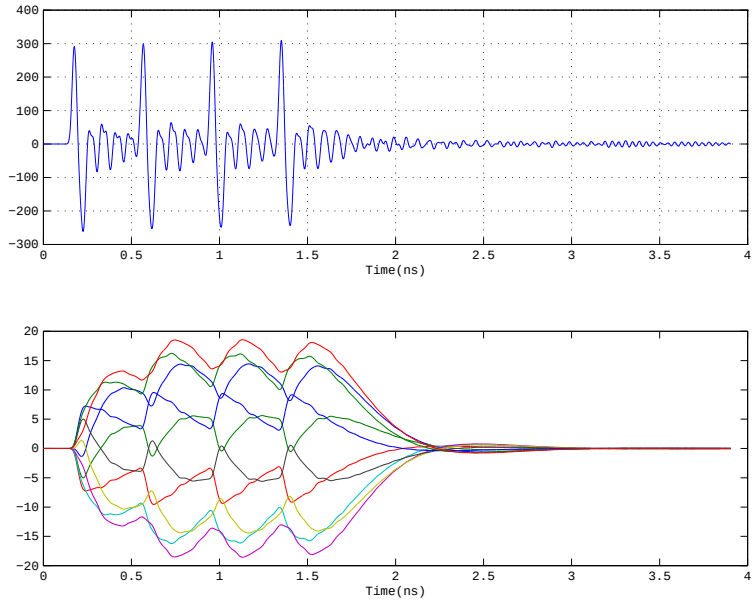

Figure 10.6: Beam signal after 2.5 GHz BPF (upper) and detected signal (lower).

For the longitudinal feedback system, we will use a QPSK modulation technique with a center frequency of 1145 MHz ($=2.25 \times f_{RF}$).

10.3.5 Power amplifiers and kickers

We have experienced some problems with the present transverse kickers and also high-power attenuators when increasing the beam current. Therefore, we need to design a much more reliable structure for the transverse kickers, and select durable attenuators. The estimated longitudinal loss factor using MAFIA-T3 for the present transverse kicker is 0.11 V/pC with a σ_L=7 mm bunch, which will get worse with a σ_L=3 mm bunch. Obviously the loss factor and estimated power loss at the transverse kicker are not acceptable even with the longitudinally flexible feedthrough design currently used to overcome the problem of electrode expansion due to temperature rise. For the transverse kicker for SuperKEKB, we will try several measures such as:

- Supports providing improved cooling for the kicker plates using beryllia.
- Very flexible longitudinal supports with good DC connection and a wideband response.
- Step back the radial plate position to the same level as the vacuum chamber around the kicker. Note that in this case we will have trapped modes inside the kicker and HOM dampers will be necessary.

Detailed designing is underway.

For the longitudinal kicker, we will use DAΦNE-type (low Q cavity) kickers. A design study done at PEP-II shows that it is possible to make the bandwidth of the kicker wide enough using a four-port structure (2 inputs and 2 outputs). However, because the beam power from the kicker is very large at SuperKEKB, we will conservatively use a eight-port structure. And, since we know even a very small deviation of VSWR of the feedthrough

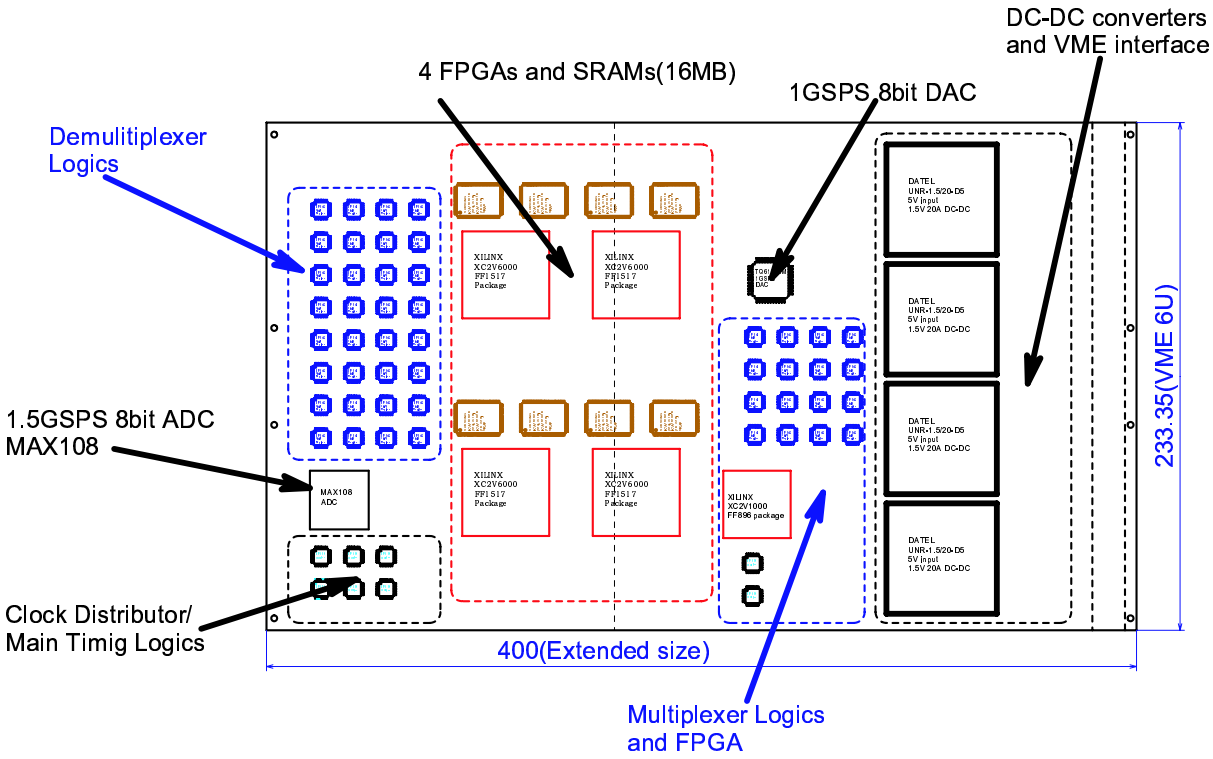

Figure 10.7: Board layout of the Gboard.

in the cavity range has a large effects on the frequency response, i.e. quality factor, we will need to use much better feedthroughs than the present ones.

We are using the best power amplifiers commercially available now. If the commercial situation does not change, we will continue to use the same or very similar amplifiers for SuperKEKB.

10.4 Synchrotron Radiation Monitors

10.4.1 HER and LER SR Monitors

The synchrotron radiation monitors are used for bunch-averaged beam-size measurement (via interferometers), and also for bunch-by-bunch diagnostics such as bunch length (streak-camera), gated camera (bunch profile), motion spectrum (photo-multiplier tube) and other measurements.

Heating

Three sources of heating of the extraction chamber have been observed: 1) wall-current heating in the beam duct inside the SR extraction chamber; 2) HOM heating in the spaces between the beam duct and the vacuum vessel surrounding it, and; 3) direct irradiation of SR power on the extraction mirror itself. We must evaluate the magnitudes of these effects with the current design.

The light-extraction chamber currently in use[1] at KEKB is shown in Figure 10.8. The chamber is located about 11 meters downstream of a weak (5-mrad) bending magnet.

A water-cooled beryllium mirror is mounted at a 45-degree angle in the outside wall of the beam pipe, with an extraction aperture located directly across from it. The beam pipe duct is made of copper. The beam-pipe temperature rise due to wall currents depends on the beam current, number of bunches and bunch length:

$$\Delta T \propto (I^2/N_{bunches})/\sigma_z^{3/2} \tag{10.1}$$

, where I is the total beam current, N the number of bunches, and σ_z the bunch length. For the current copper chamber, with a bunch length of 6 mm and a 4-bucket bunch spacing fill pattern, the temperature rise at 1.4 A of beam current is calculated to be 1.7 degrees, which agrees very well with the temperature rise as measured by a thermocouple mounted on the interior beam duct. Table 10.4 shows the calculated temperature rise for higher beam currents, shorter bunch lengths, and tighter bunch spacing.

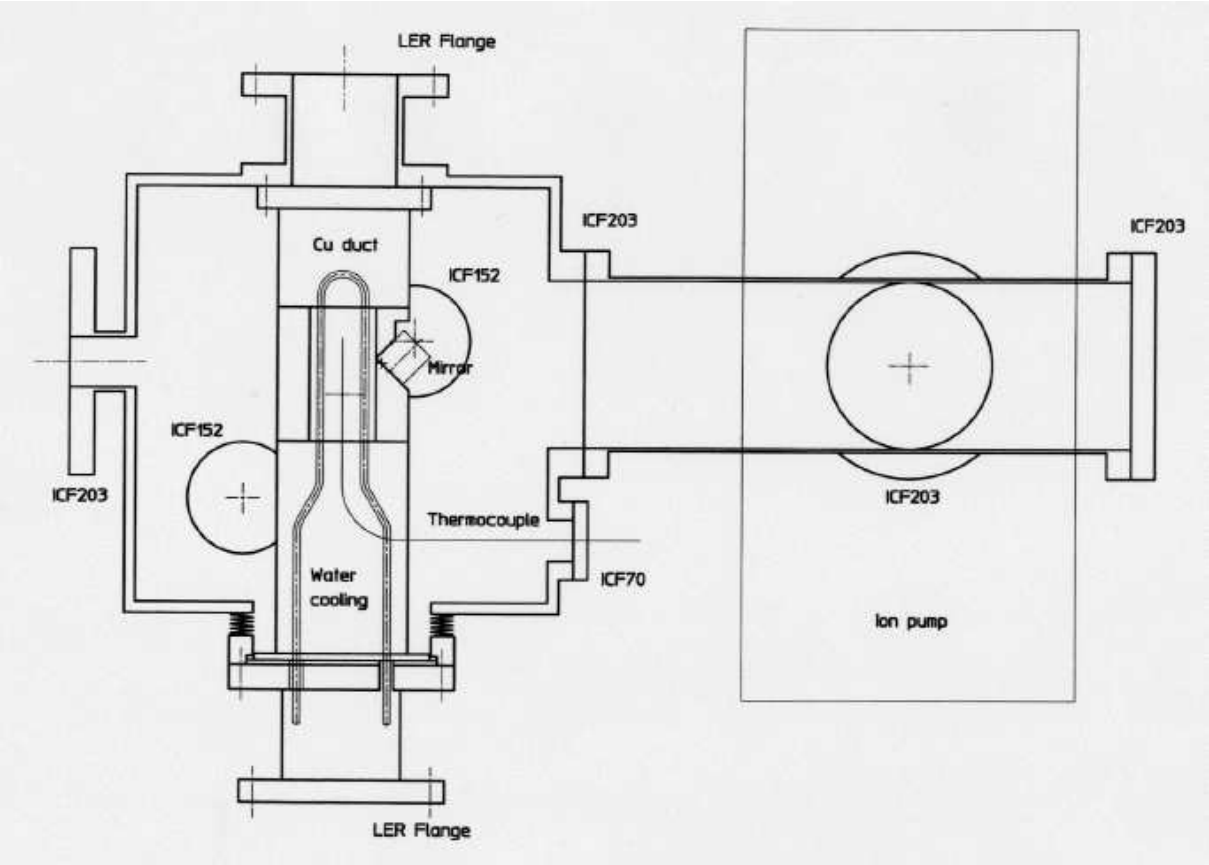

Figure 10.8: Current design of SRM extraction chamber (LER).

The most severe heating, 220 degrees, is seen at 4-bucket spacing and 3-mm bunch length. Increased water cooling will be needed.

The previous extraction chamber design, which had larger extraction apertures in the beam duct, showed symptoms of HOM leakage into the outer vacuum chamber, in the form of induced arcing between some thermocouple leads and the chamber surface. The extraction aperture has been reduced as much as possible, and no obvious signs of HOM leakage have been observed with the current chamber. MAFIA simulations suggest that about 100 W of leakage should be expected at a beam current of 2 A and a bunch spacing

Bunch Spacing (buckets)	σ_z (mm)	I (A)	ΔT (°C) [Calculated]	ΔT (°C) [Measured]
4	6	1.4	1.7	1.7
4	6	9.4	78	
4	3	9.4	220	
1	3	9.4	55	

Table 10.4: Beam-pipe heating with the current beam chamber design

of 4 RF buckets. At 9.4 A, with 1-bucket spacing, about 500 W are expected. However, this issue requires further study and measurement to see what happens at higher beam currents. It is possible that SiC absorbers may be needed in the space between the beam duct and the outer chamber wall; mounting flanges have been provided in the current chamber wall for this possibility.

Due to direct SR irradiation, the mirror itself also heats up and deforms, changing the apparent vertical beam size by about 6% between 500 and 1400 mA. This can to some extent be corrected for, but it is important to minimize the distortion that needs to be corrected. One way to do this is to increase the bending radius (and core length) of the source magnet. This raises the critical wavelength, λ_{crit}, lowering the total SR power, and reducing the heat load on the mirror and the resulting deformation. At the same time, it increases the light flux in the visible region ($\sim 500nm$), which is important for making low-current measurements. Figures 10.9 and 10.10 show the angular flux density and total SR power as functions of bending radius in both the HER and the LER.

Dynamic Beta Measurement

Dynamic beta effects due to beam-beam collisions have the effect of changing the beta functions and beam sizes around the rings. If we can measure this dynamic beta effect in real-time, the ability to observe the beam-beam parameters directly would make a powerful tool for collision tuning. In order to make these measurements, a second monitor would be needed in each ring, ideally at 90-degree betatron phase advance from the current locations. One set of candidate locations would be at other weak-bends in the ring, near arc-section entrances and exits. This would create relatively little disturbance to the machine lattice, but would require new optics huts and space for them above ground.

Another possibility, currently under study, is to locate the second sources in the arc sections, near the current locations. This has the advantage that the existing optical huts can be used, needing only new optical transfer lines to be extended out to the new locations. To minimize the disturbance to the lattice, a 3-bend local bump is contemplated, with the middle bend being the source bend. Figure 10.11 shows the location of the source point, using the current KEKB lattice. The light extraction mirror would be located just downstream of the source point for the first (current) interferometer. The optical path from source bend to optics hut would be increased from 40 m to 70 m, which could be accommodated with the current optical transfer tube diameter.

The first source point has a dispersion of essentially zero; this is not true of the new source point, which has a horizontal dispersion of 0.5 m, which would contribute about the same to the beam size as the emittance does. In order to measure β_1/β_2, it will be necessary to first measure the product of the horizontal dispersion at the second source

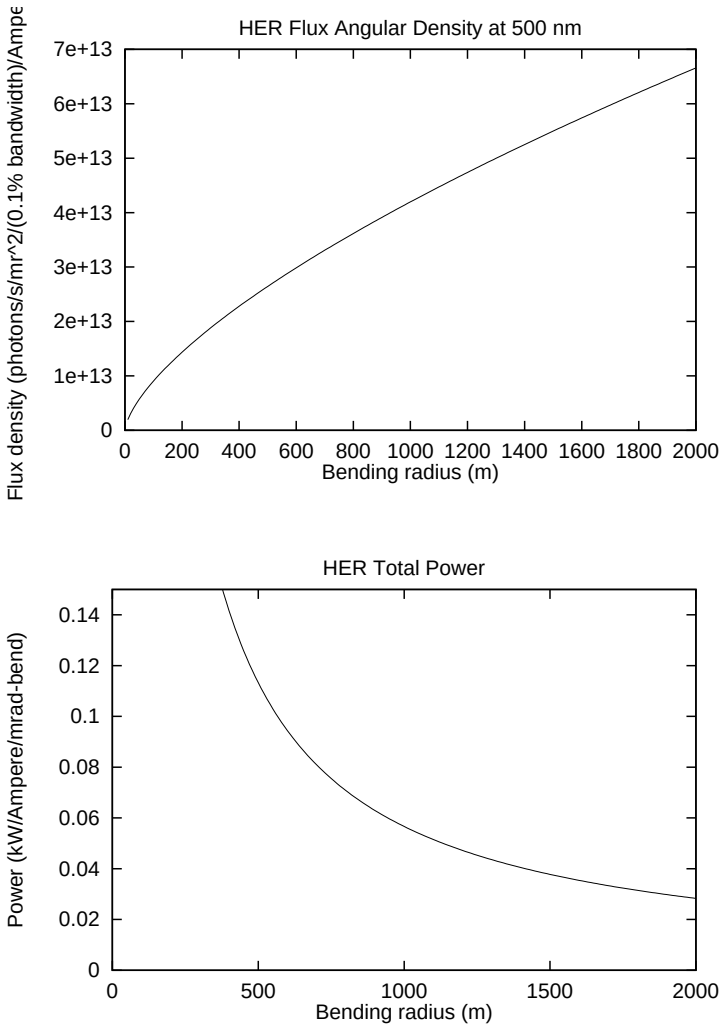

Figure 10.9: Visible light angular flux density and total SR power as functions of source bend radius in the HER.

point with the energy spread, $\eta_2 \frac{dE}{E}$ in single-beam mode, where

$$\left(\eta_2 \frac{dE}{E}\right)^2 = \sigma_2^2 - \frac{\beta_2}{\beta_1}\sigma_1^2 \tag{10.2}$$

for the undisturbed values of the beta functions. Then in colliding-beam mode, the dynamically-changed ratio of beta functions can be measured as:

$$r\prime = \frac{\sigma_1^2}{\sigma_2^2 - \left(\eta_2 \frac{dE}{E}\right)^2} = \frac{\beta_1}{\beta_2} \tag{10.3}$$

Besides measuring the beam-beam effect via the beta functions, the second monitor may also be useful for measuring the energy spread.

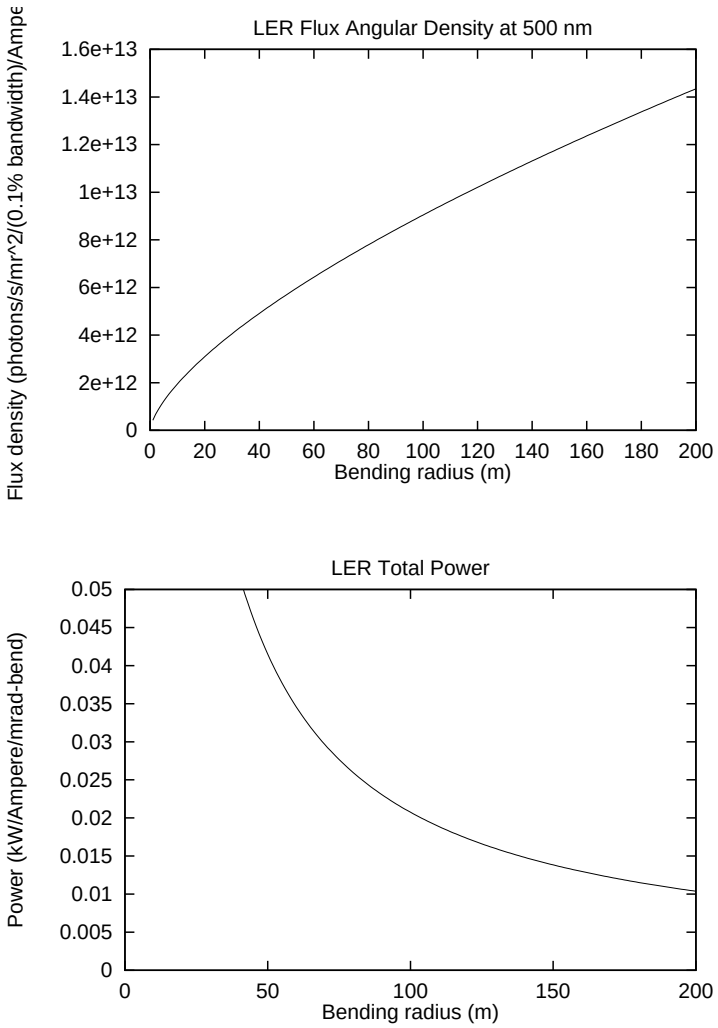

Figure 10.10: Visible light angular flux density and total SR power as functions of source bend radius in the LER.

10.4.2 Damping Ring SR Monitor

Source Characteristics

A synchrotron radiation monitor is the most effective way to monitor the emittance damping in the Damping Ring. Over the course of $\approx 90,000$ turns, the emittance is reduced by a factor of ≈ 100, and the beam size by a factor of ≈ 10. By imaging the beam with a gated camera, a single-turn transverse beam-size measurement can be made at any point in the damping process. Furthermore, since the full damping process takes ≈ 40 msec (for the damping time of ≈ 12 msec), then in order to inject into the Super-KEKB rings at 50 Hz a staggered injection scheme will be necessary. In this scheme, one or two bunches are injected into the damping ring at time t_0, and one or two more at time $T_0 + 20$ msec, with each bunch being extracted 40 msec after injection. So at any given time the ring will have 2 or 4 bunches circulating, at different stages of damping. At the maximum of 4 bunches, the bunches are separated by 109 nsec. A gated camera, with a gate width of less than 10 nanoseconds, will enable us to distinguish between individual bunches at

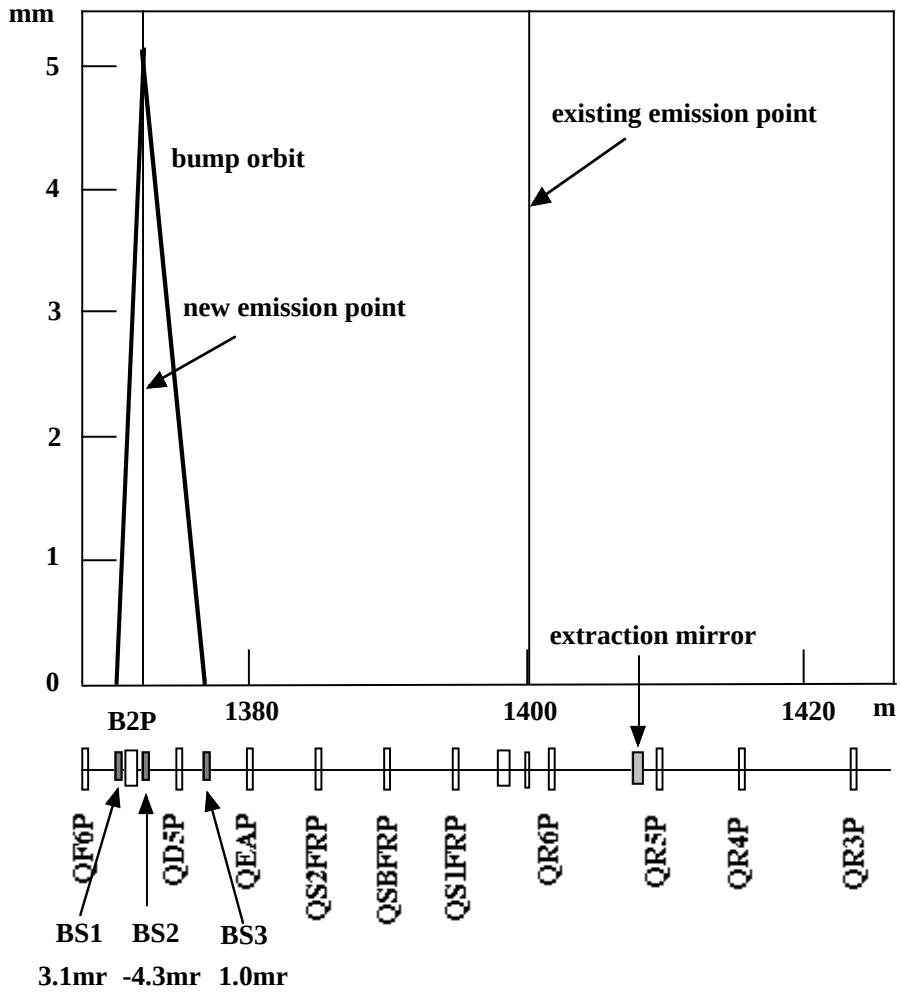

Figure 10.11: Proposed location of new SR source point.

each turn. For longitudinal phase-space measurements, a streak camera will be used.

We plan to use one of the bending magnets as the SR source point. The current design of the damping ring consists of alternating bends, with a field strength of $1.267T$. The forward bends have a core length of 0.7286 m, while the reverse bends have a length of 0.255 m. If the space between magnets permits, the extraction mirror could be located immediately downstream of a forward bend. Otherwise, we could use the final bend before the straight section, which is a reverse bend. The characteristics of the source are shown in Table 10.5, where the use of a forward bend is assumed.

The parameters above are unchanged for a reverse bend, except that the horizontal dispersion η_x is greater by a factor of two, which increases the horizontal beam size by 20%.

Extraction

The bending angle of the reverse bend is 81 mrad. The light fan of the emitted synchrotron radiation has a vertical half-width of

$$\Delta\Psi \approx (1/\gamma)(\lambda/\lambda_{crit}), \tag{10.4}$$

		Units
Beam Energy	1	GeV
Field Strength	1.267	T
Bending Radius ρ	2.6	m
Critical Wavelength λ_{crit}	1.36	nm
Critical Energy E_{crit}	0.84	keV
β_x	1.56	m
β_y	6.25	m
η_x	0.1	m
ϵ	$1.23 \times 10^{-6} \rightarrow 1.22 \times 10^{-8}$	m
$\Delta E/E$	$6 \times 10^{-3} \rightarrow 5.5 \times 10^{-4}$	
σ_x	$1500 \rightarrow 147$	μm
σ_y	$2800 \rightarrow 280$	μm
Damping time	11.95	msec

Table 10.5: Damping Ring SR Source Characteristics

which for visible light of 500 nm wavelength is 3.6 mrad. To extract the light, we will place a 25-mm diameter mirror immediately downstream of the end of the magnet, tilted upwards at a 45-degree angle to deflect the light vertically through a window mounted in the top of the extraction chamber. At this location it is located 0.51 m downstream from the center of the source bend, with the mirror center displaced 39.9 mm from the beam center. The angles subtended by the mirror relative to the center of the bend are 49 mrad in the horizontal axis and 34.7 mrad in the vertical direction.

The total power produced by the bend is

$$P[W] = 1270E^2[GeV]B^2[T]I[A]L[m], \tag{10.5}$$

where a beam current I of 10 mA maximum and core length L of 0.7286 m gives a total of 15 W generated (5 W in the case of a reverse bend). Of this, 3.1 W impinges on the mirror. For the mirror we are considering a Be or Al-coated SiC mirror with water temperature regulation, similar to the design used at the ATF, where SR power loads 10 times greater have presented no problem[3].

When using an imaging instrument like the gated camera, it is important that the imaging resolution be sufficient. To estimate the resolution, we assume an optical path-length from the source point to the focusing lens of 10 meters, with a 60 mm aperture. In this case, the point-spread function as expressed at the synchrotron radiation source point is shown in Fig. 10.12. This function, convolved with the beam distribution, would create an uncorrected apparent beamsize increase of $\approx 2\%$ in the smallest beam size (the horizontal beam size after full damping). Thus, as long as the usable mirror surface area is not much smaller than the available aperture, we can expect good resolution with the imaging camera system.

The above calculations were all made assuming a 40-cell configuration for the damping ring. The feasibility conclusions do not change notably for the cases of 30 or 50 cells.

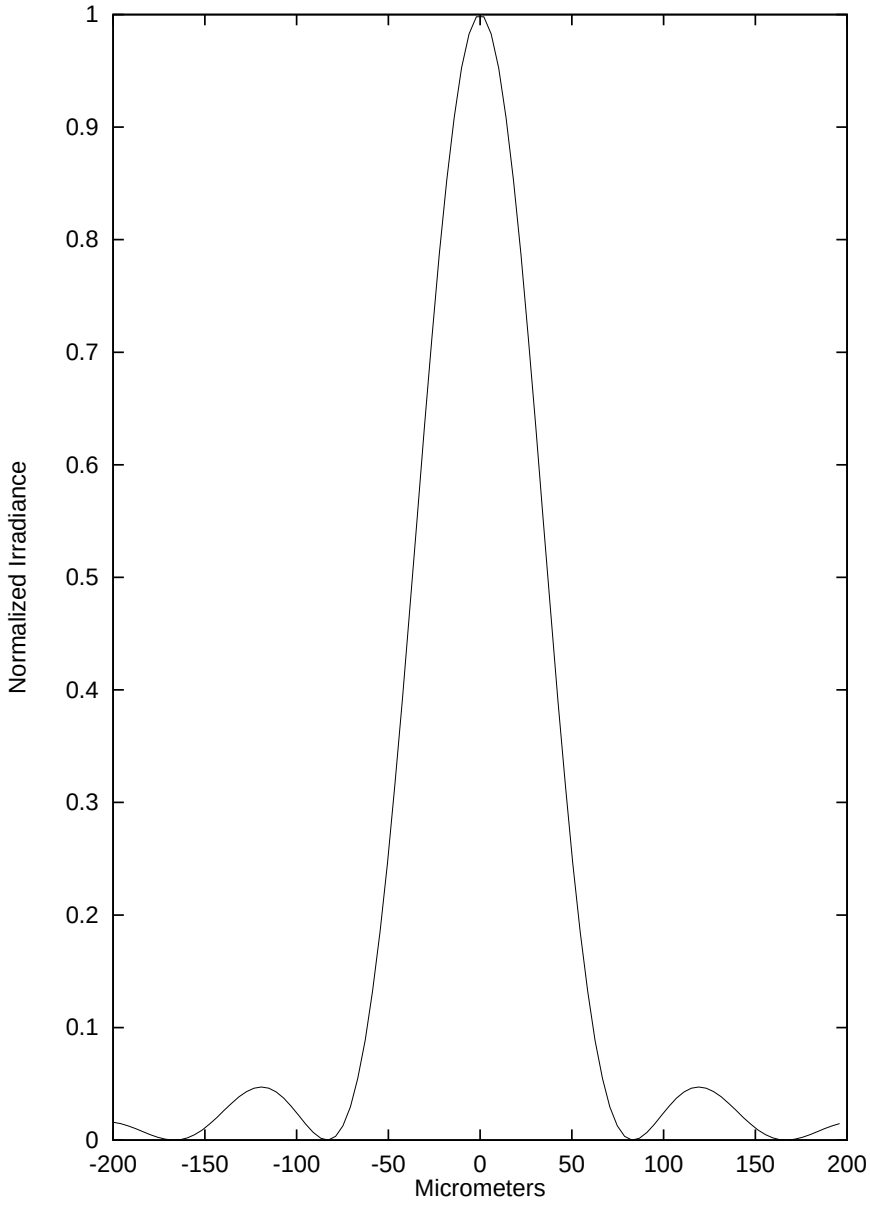

Figure 10.12: Point-spread function of damping-ring optical path, as expressed at the source point.

Bibliography

[1] J.W. Flanagan, S. Hiramatsu, H. Ikeda, K. Kanazawa and T. Mitsuhashi, "Improved SR Extraction Chamber for KEKB LER SR Monitor," Proceedings of PAC03, 2003.

[2] S. Hiramatsu, private memo.

[3] T. Naito, private communication.

Chapter 11

Injector Linac

11.1 Present Injector and its Upgrade

The present KEKB injector linac has been upgraded from the TRISTAN/PF 2.5-GeV electron/positron linac for full-energy injection to the KEKB storage rings (HER: 8.0-GeV electrons and LER: 3.5-GeV positrons) [1]. The linac has a J-shape, as shown in Fig. 11.1, to fully utilize the existing facilities, and because of constraints from the site boundary. The total length along the linac is 600 m. The linac is composed of 54 accelerator modules; 25 modules are placed before the positron generation target and 29 modules after it. Each module involves four 2m-long accelerating sections fed by a 50-MW class S-band (2856 MHz) klystron through a SLED-type RF pulse compressor. The klystron supplies, typically, 41 MW of output power in 4 μs duration. The RF pulse is compressed to have 3.4-times higher power in a 600 ns duration. The RF power from the compressor is divided equally into four accelerating sections to generate 21 MV/m of the accelerating field gradient. An accelerator module has an energy gain of 160 MeV. Thus, the maximum energy gain of the linac is 8.6 GeV. Electrons are accelerated to 8 GeV using

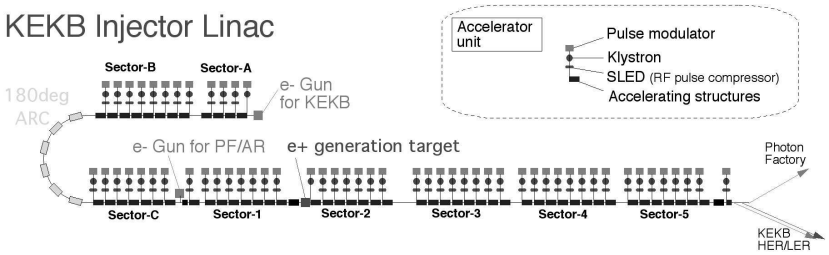

Figure 11.1: Laout of the present KEKB linac

the whole length of the linac for HER injection. For the positrons, the first half of the linac is used to accelerate high-intensity (10 nC/bunch) bunches of electrons to 4 GeV to irradiate a converter target to generate positrons. The positrons are captured by a strong solenoid field. The second half of the linac is used to accelerate the positrons to 3.5 GeV for LER injection. The linac can inject the beams at 50 Hz repetition. The beams are injected into the KEKB rings approximately 20 times per day. The linac also injects beam into the 2.5-GeV Photon Factory ring (once a day) and into the 6.5-GeV Accumulator

Ring (three times a day). These rings are used as synchrotron radiation facilities. The beam specifications of the linac are shown in Table 11.1. Before 2002, single-bunch beams

parameters	e^- (KEKB)	e^- (Primary)	e^+ (KEKB)	Unit
Beam Energy	8.0	4.0	3.5	GeV
Beam Intensity	1.0	10.	0.8	nC/pulse
Number of bunches	1	2	2	
Emittance	800.0	–	2500.0	$\times 10^{-6}$ m
Momentum spread (FWHM)	0.2	–	0.5	%
Injection rate	5.0	–	3.0	mA/s

Table 11.1: KEKB Injector Linac Beam characteristics

of positrons and electrons were used at KEKB. The injection rate of positrons was one third of that of electrons; in general, the positron intensity is lower than that of electrons because positrons are produced as secondary particles. Unfortunately, the positron stored current is a few times higher than that of electrons at KEKB. Most of the injection time is spent on the positrons. To reduce the injection time, two-bunch injection of positrons was considered [2]. From the constraints of the complicated frequency relationship between the linac and the storage rings, the bunch interval needs to be 96 ns. With this bunch spacing, the energy gain for each bunch differs due to the time dependence of the RF pulse from the pulse compressor and due to the beam loading effect. The energy difference between the two bunches is compensated by slightly adjusting the RF pulse timing. To effectively use this compensation method, the maximum number of bunches is two. This two-bunch injection has been successfully used for positrons since the autumn of 2002. The positron beam intensity per pulse and its injection rate have been doubled.

At SuperKEKB, which aims at more than a ten-times higher luminosity than KEKB, the stored current will be increased, as shown in Table 11.2. To ameliorate the electron-cloud instability in the positron storage ring, the ring energies of the electrons and positrons are switched from those of KEKB. The ratio of the stored currents should be the inverse of that of the beam energies for stable beam collision. As a result, the beam energy of the positrons is higher than that of the electrons, and the stored current of the electrons is higher than that of the positrons. In response to this large parameter change

parameters		**KEKB**	**SuperKEKB**
Beam Energy	(e^-)	8.0 GeV	3.5 GeV
	(e^+)	3.5 GeV	8.0 GeV
Stored current	(e^-)	1.1 A	9.4 A
	(e^+)	2.6 A	4.1 A

Table 11.2: KEKB and SuperKEKB beam parameters

of the storage rings, the injector linac is upgraded in the following ways. A schematic view of the upgraded linac is shown in Fig. 11.2.

- The beam intensities of the linac are increased proportionally to the increase of the stored currents. The positron intensity is doubled by introducing a stronger focusing field in the capture section, which is generated by a flux concentrator type

of solenoid. The electron intensity is increased five times by using two bunches of increased beam current from the pre-injector.

- For 8-GeV full energy injection of the positrons, in 24 accelerator modules out of 29 in the latter half of the linac, the accelerating sections and the RF sources are replaced by C-band types in order to double the accelerating field gradient.

- From the constraints on the design aperture of the collision point in the storage ring and of the smaller aperture in the C-band accelerating sections, the positron emittance is required to be small, comparable to that of the electrons. To achieve this, a positron damping ring is introduced in the middle of the linac.

- To achieve quick switching of the injection modes (electron↔positron), a pulse beam-kicker is installed before the positron generation target. In the positron mode, high-intenisty electrons go straight to the positron generation target. In the electron mode, low-intensity electrons are kicked out to the beam-transfer line for injection to the electron storage ring. The switching of the electron beam intensity can be done with independent grid pulsars installed at the electron gun. Thus, the injection modes can be switched for every beam pulse. This quick switching requires an upgrade in the beam-position monitor system to read out the position information at 50 Hz.

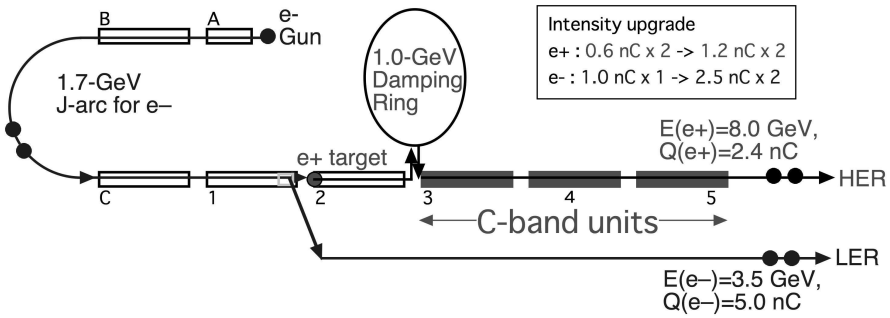

Figure 11.2: SuperKEKB injector linac

In the following sections, detailed descriptions of the intensity upgrade, the energy upgrade and the upgrade in the beam-position monitor system are given. The damping ring has many issues to be considered, and is described in a separate chapter.

11.2 Intensity upgrade

For SuperKEKB, the stored currents are substantially increased, as shown in Table 11.2 (1.6 times for positrons and 8.5 times for electrons). To illustrate the importance of the intensity upgrade, we show the dependence of the effective integrated luminosity upon the injection beam intensity. First, a typical operation KEKB in one day is shown in Fig. 11.3. The declining curves in the upper two columns show the stored currents in the LER and the HER and the declining curve in the lowest column shows the luminosity. The currents decrease due to electron-positron collisions, beam-gas collisions and other reasons. The luminosity also decreases as a consequence. Every 80 - 90 minutes, the

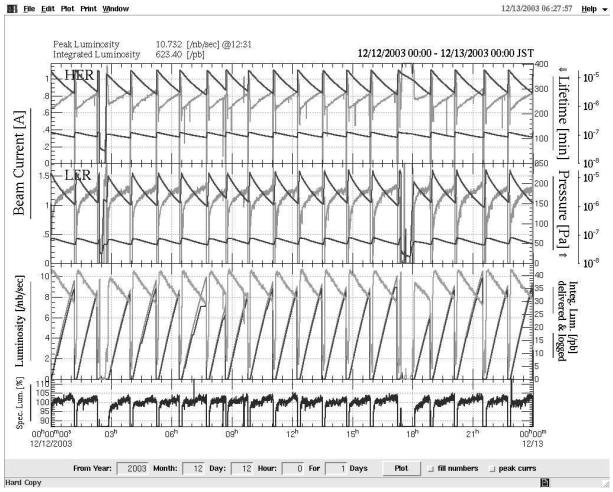

Figure 11.3: KEKB operation status

beams are refilled from the linac. This interval is determined to optimize the integrated luminosity. Besides routine refilling, in the case of beam aborts that occur suddenly due to beam instability, RF breakdown and other reasons, the beams are refilled from scratch. Such beam aborts occur 5 - 6 times a day; they can also be seen in Fig. 11.3. During the injection, the Belle detector does not take data in order to avoid severe beam background. The typical 10 minutes of dead time during a routine refilling injection includes times to: change the Belle status to injection mode, inject electrons, change the linac status from electron to positron-mode, inject positrons, and change the Belle status back to collision mode. The linac status change takes 30 seconds to move the converter target (into or out of the beam line) and to change the focusing and steering magnet strengths and the RF phases of the acceleration. In the case of beam aborts, it typically takes 20 minutes for refilling, and the dead time is longer. In the case of Fig. 11.3, the peak luminosity is 10.7 (/nb/s) and the integrated luminosity would be 927 (/pb) per day if the peak value could continue for 24 hours. In reality, because the integrated luminosity is 623 (/pb) per day, the efficiency is 67%. If we assume the present beam intensity of the linac at SuperKEKB, the efficiency would be degraded to be only 36%, even with no beam aborts. By increasing the intensity by 5 times for electrons and twice for positrons, the efficiency recovers to 61%.

Recently, as an attempt to maintain the peak luminosity for long times, operation with a continuously injected beam has been tested. In this mode of operation, the linac injects beam continuously at low repetition (5 - 10 Hz) to make up for the loss of stored current while the Belle detector continues taking data, except for a short dead time (4 ms) after every beam injection. Investigations into the effects on the detector and of the data quality are still underway, but the results seem to be promising. This continuous-injection mode will improve the luminosity efficiency by more than 20%. Even if this mode of operation is used at the SuperKEKB, an intensity upgrade of the linac is still important in order to minimize the beam repetition and the total dead time.

The present electron beam is a single bunch with a charge of 1 nC. For SuperKEKB, the electron beam from the gun will be two bunches of 2.5 nC each. At present, the intensity of the primary electron for positron production is two bunches of 10 nC each. Thus, there is no problem to generate a beam of the required intensity. However, the beam quality may be a problem because electrons from the linac are injected directly

into the storage ring. To reduce the emittance growth from short-range wake fields, two bunches of 2.5 nC are used instead of a single bunch of 5 nC. Here, the long-range wake field effect between two bunches is assumed to be negligible. In order to increase the positron intensity, the present pulse solenoid coil (2.3 Tesla) in the positron capture section is replaced by a stronger solenoid (7 Tesla) of the flux-concentrator type. This type of solenoid has been used at SLC for a long time, and has proven useful to improve the positron intensity. It is expected to increase the positron intensity by a factor of two with this upgrade of the capture section.

In the early stages of the upgrade consideration, it was planned to use two electron bunches from the first half of the linac: one for injection and the other for positron production. In this case, the C-band accelerator modules, described in the next section, accelerates a single bunch of positrons. However, it was found not to give the needed flexibility to choose injection buckets in the storage rings independently for the electrons and positrons. It is now planned to use both of the bunches for injection, or for positron production. Switching between electrons and positrons can be done pulse-by-pulse. This provides quasi-simultaneous injection of the positrons and the electrons. One problem with this scheme is that the energy gain of a C-band module is 5 percent lower in order to equalize the beam energies of the two bunches. It requires a higher output power from the RF source or some improvement in the RF pulse compression. It is still under investigation to find the best way to achieve sufficient energy gain in the C-band modules for both bunches.

11.3 Energy Upgrade

The biggest change in the linac for SuperKEKB is 8-GeV positron injection. The present maximum energy gain for the positrons is 4.8 GeV with the 29 accelerator modules in the latter half of the linac. The simplest scheme to achieve 8 GeV energy gain is to double the accelerating field gradient (21 $\rightarrow$ 42 MV/m). In order to achieve such a high gradient, we will adopt C-band accelerating sections that are operated at a twice higher frequency (2856 $\rightarrow$ 5712 MHz). It is a general strategy to use a higher frequency for a higher gradient, for example in the R & D for future linear colliders. Taking a single accelerating cavity for example, if the RF frequency is doubled, the dimension of the cavity is halved and the field gradient is doubled for the same RF input power. A problem in using this higher frequency is that most of the components are still in an R & D stage and the technology is not yet established for long-term operation. Fortunately for the C-band, a 50 MW klystron has already been developed [3] in the R & D work for the JLC [4]. So we decided to start R & D of the other C-band components to fulfill the design specification of the SuperKEKB injector linac. Considering the simple scale down of the present S-band module to the C-band, the dimension of the accelerating section is halved. So the total length of a module is also halved and we can install two C-band modules in the space of one S-band module. However, the size of the RF source (the klystron and its modulator) can not be simply half of the S-band. It is a major issue to make the RF source compact. A schematic view of the C-band accelerator module for SuperKEKB is shown in Fig. 11.4. The schematic shows the two C-band modules that replace an S-band module. Each C-band module involves two 2 m-long accelerating sections fed by a 50-MW class C-band klystron through a LIPS-type RF pulse compressor

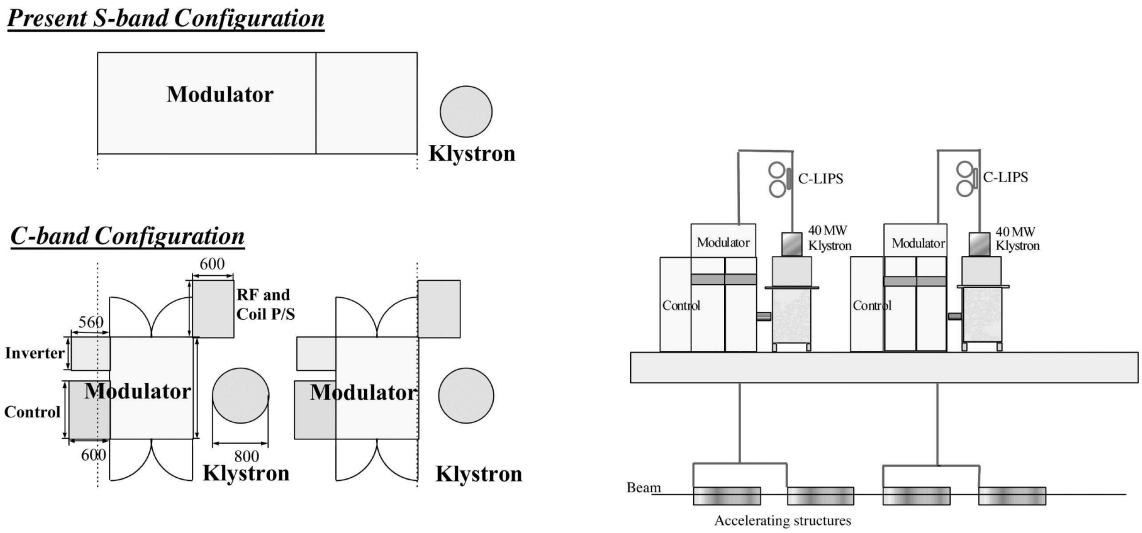

Figure 11.4: C-band accelerator module layout

[5]. The RF power from the klystron is assumed to be 40 MW over a 2 μs duration with a 20% power margin for stability and long-term operation. The RF pulse is compressed to have a 3.4-times higher power over a 400 ns duration. In place of the SLED-type pulse compressor used in the S-band, the LIPS-type of compressor is adopted because of the higher Q-factor to satisfy the required power multiple. The RF power from the compressor is divided equally into two accelerating sections to generate 42 MV/m of the accelerating field gradient. A C-band accelerator module has an energy gain of 160 MeV. A simple scaling down of the present S-band accelerating sections (four 2m-long sections in an accelerator module) gives four 1m-long sections using a quarter of the power from the RF source in each section. However, two 2m-long accelerating sections using half of the RF power in each section are adopted for more efficient use of the RF power in achieving the required accelerating field gradient.

In the following sections, the present status of the development of the RF source, the accelerating section and other components are described.

11.3.1 C-band RF System

Basic RF system concept

- Modulator:

  It is shown in the previous section that the energy upgrade using the C-band structure assumes that the average accelerator field gradient is 42 MV/m, which is achieved by combining a scaled-down version of the presently used S-band structure, a high Q RF pulse compressor (LIPS type) that has almost the same field multiplication factor as the currently used one, and a 50 MW klystron. If the commercially available C-band klystron of 50MW is adopted, the number of rf sources is required to be twice as many. Since the S-band klystron presently outputs a 4 μs pulse width, the output pulse width from the C-band klystron is chosen to be 2 μs from energy considerations. If the same power delivering scheme as in the S-band case is assumed, where the klystron rf power from one modulator is delivered to four 2 m-long accelerator guides, two C-band klystrons must be operated with the

existing modulator and it is required to increase the PFN (Pulse Forming Network) capacitors by 30% to generate the 2 μs rf pulse; this presents a difficulty in installing the required PFN in the present modulator cabinet. At the same time, we must reinforce the DC power supply section of the modulator.

Another possible scheme is one modulator having 2 PFN circuits, and each one supplies a pulse to a C-band 50MW klystron; however, this also needs a larger modulator cabinet; it is hard to fit all the modulators in the existing klystron gallery.

An alternative and promising scheme is realized by introducing an inverter DC power supply that charges the PFN directly. In this case, one modulator with an inverter DC power supply drives one C-band klystron and the total number of modulators is doubled. A DC inverter power supply of 32 kJ energy, which is the maximum energy available commercially, can be used to charge the PFN capacitors and to eliminate the rectifier, charging and de-Qing circuits of the existing modulator; it is possible in this way to reduce its size to one-third of the currently used modulator. Assuming a pulse width of 2 μs, existing PFN capacitors can be reused for the specified output pulse requirement with slight changes. For this design, in the C-band modulator two PFN circuits with 14 capacitors (14,6 or 15,5 nF) and 14 inductors (1.55 nH) each are placed in parallel to generate a pulse with a 2 μs pulse width, while the existing S-band modulator uses the same circuits with 20 sections having the same capacitors and inductors. Therefore, in this scheme, two modulators for the two klystrons are installed in the same space in the klystron gallery, as shown in Fig. 11.4. Since the C-band klystron produces 50 MW of output power at an applied voltage of about 350kV, which is slightly higher than the current operating voltage, it is necessary to rewind the existing pulse transformer from the step-up ratio of 13.5 to 15 to generate the 350 kV pulse, but it is possible to use the same core and the same oil tank, which works at up to 350 kV. Then, it is possible to utilize most of the components in the S-band modulators, like the PFN, capacitors, thyratrons, cabinets, pulse transformers and oil-tanks with or without slight modification. To install forty-eight C-band sub-modules, it is sifficient to manufacture only twenty-four new sub-modules, and another twenty-four sub-modules are obtained by modifying the existing ones; this leads to a reduction of the upgrade cost.

- RF System:

  For the rf system, it is a great cost advantage to employ the existing sub-booster (SB) driving system, since it can generate 80 kW pulsed power, which is sufficient to drive 8 high-power klystrons. The C-band SB klystron is usable with a slight retuning of the operation frequency of a commercially available C-band klystrons (for example, Mitsubishi PV-5101) used for weather satellites. In this case, it is possible to use the existing SB modulator, which supplies a 30kV voltage pulse to the SB klystron. Since most of the present low-power rf components can be reused, we achieve some cost reduction. An overall block diagram for the whole rf system is shown in Fig. 11.5. If, for example, dedicated use of the RF system for fast feedback is necessary in the beam-energy adjusting section, a traveling wave tube (TWT) type of amplifier can be used to drive a 50-MW klystron. Though TWT amplifiers are relatively expensive at present, we are considering the possibility of using them instead of the sub-booster system in the whole RF system, if a cost

reduction is realized in the future.

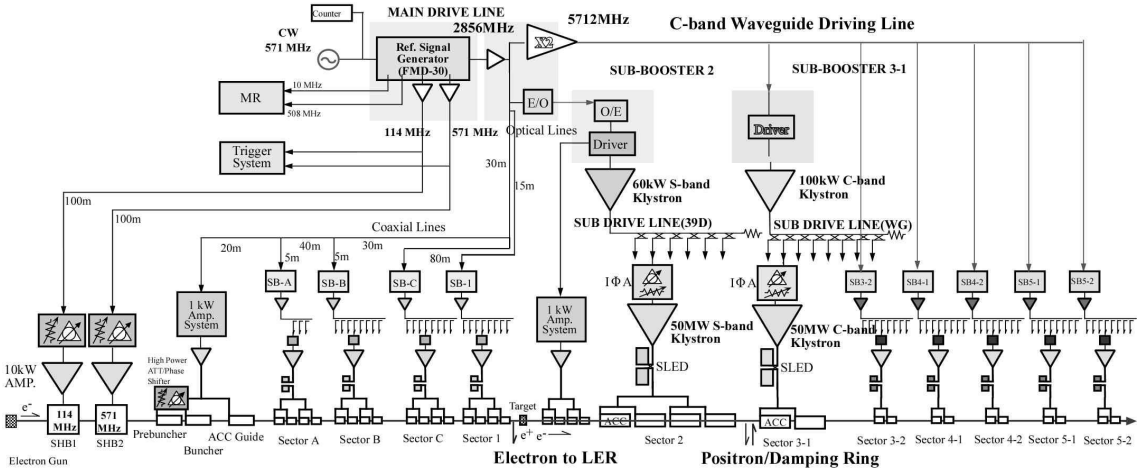

Figure 11.5: RF system diagram

R&D Development [6]

- Compact Modulator: A compact modulator is a key issue in being able to install the required number of the accelerator modules in the limited space of the existing klystron gallery. A proto-type modulator was manufactured using a dc inverter power supply, which charged the PFN with the same capacitors and inductors as mentioned above. We achieved the designed flattop RF pulse width of 2 μs and a characteristic PFN impedance of 5 ohms. A pulse transformer having a 1:15 step-up ratio provides a 350 kV pulse at maximum to the high-power klystron. Except for some problems caused by break-down of the IGBT, it has been stably operating for more than 1000 hours so far. In an investigation into the cause of this break down, it was observed that abnormal transient sequences occur with very low probability to make the IGBT load short when the thyratron has a missfire at irregular timing. Intense R&D for developing a more reliable circuit is underway.

- 50-MW klystron and driving system: Compared with what is needed to develop a new C-band RF signal generator, a simpler RF system was used in the test stand, which comprised a 2856-MHz signal generator, a frequency doubler, a pulse modulator, an 8W-transistor amplifier and as SB klystron. The SB klystron was manufactured by retuning a commercially available klystron for weather satellites. From the SB klystron, the output power was fed through a WR-5 waveguide to a Toshiba 50-MW klystron. The high-power klystron socket was used in the same manner as the S-band one, which can be used up to 350 kV.

- High-Power RF Window: It was necessary to use an RF window to separate the vacuum systems between the klystron and the accelerator guide. Although two windows were provided in the high power klystron, because of the simplicity of the vacuum system, we developed a high-power RF window, which was capable of being

used at the 50-MW power level. This was a mixed-mode window (TE_{11}+TM_{11}) proposed by Kazakov [7]. Using this window, the field decreases at the ceramic surface and on the edge, where brazing was done.

- RF dummy load: To absorb the output power from the accelerating section and the reflected RF pulse, an RF dummy load has been developed. The design is based on the S-band dummy load used for the KEKB linac [8]. SiC blocks of different heights are aligned in a wave guide to absorb the RF power uniformly. It works stably up to an input power of 21 MW.

- RF pulse compressor: We will adopt the CERN LIPS type of TE038-mode cavity for the C-band RF pulse compressor instead of the SLED type of TE015-mode cavity used in the KEKB linac. This is because the power multiplication factor is higher, due to its higher Q-value. The precise design is underway. Fine tuning of the cavity dimensions will be performed with a low-power model. The first high-power prototype will be fabricated and tested in 2004.

Figure 11.6: Klystron assembly and Modulator at KEKB linac 4-4 module

- High-power test at the test stand: A C-band test stand was built in the accelerator assembly hall next to the S-band klystron test hall at the KEKB linac. In this stand, a modulator test was performed in February 2003, and a C-band klystron test was conducted up to 42.5 kV of Es (PFN voltage) with a pulse repetition of 50 pps and a pulse width of 2 μs. An output power of 43 MW was measured with two water loads. Then, the klystron output characteristics were measured. We also adjusted the pulse flat top by changing the PFN inductance. Approximately 1.3% flatness was obtained. Another adjustment led to a flatness corresponding to a phase variation of 2.6 degrees. A resonant ring test of an RF window up to a forward traveling wave of 160 MW was performed in March, 2003, which confirmed

the high-power capability of a mixed-mode RF window. A high-power test of the SiC dummy load up to 43 MW was successfully conducted in June, 2003.

- Installation to the KEKB linac: After successful RF processing of the accelerating section at the test stand, an RF measurement was conducted to show that there was no damage by the processing. Details of the RF processing at the test stand are described in the next section. Then, during the summer shut-down period in 2003, the C-band system including the accelerating section, the 50 MW high-power klystron assembly and the associated driver system, was moved from the test stand to Accelerator Module 4-4 in the KEKB linac. The compact modulator was a new second prototype that had been manufactured, installed and tested in advance with a resistive load at Module 4-4. The RF source installed at Module 4-4 is shown in Fig. 11.6.

11.3.2 C-band accelerating section

Compared to the accelerating sections being developed for linear colliders, the structure for SuperKEKB can be much simpler. Since many bunches (more than 100) are accelerated in a short interval (1.4 ns for JLC) in the linear colliders, the wake field induced by a preceding bunch has a large influence on the following bunches. To prevent this effect, the structure of the accelerating section becomes rather complicated in order to let the wake field escape from the central part of the cavity. In contrast, the number of bunches is two at maximum, and the bunch interval is rather long (96 ns) for the SuperKEKB linac. We adopt a rather simple accelerating section which is a scaled-down version of the present S-band section (traveling-wave, disk-loaded structure, quasi constant gradient, $2\pi/3$ phase advance per cell). Shown in Table 11.3 are the characteristics of the S-band accelerating section used in the present KEKB linac, the C-band 1m long section (1-st prototype) and the C-band 2m long section. The layout of the 1-st prototype is shown in Fig. 11.7. The S-band accelerating section has five variants in which the cavity dimensions are slightly different. The purpose of this is to spread out the resonant frequencies of the wake field and minimize the influence to the beam. The first prototype is based on type A, which has the largest disk-iris aperture. The dimensions in the regular cavity cells are precisely half those of the S-band type A. The structure of the input and output coupler cells are similar to that of S-band. Each coupler has single port which couples the electromagnetic fields in the wave guides and in the cavities through a small and thin iris. The dimensions of the couplers are slightly different from the those for the S-band because the cross section of the industrial standard wave guide for C-band is not simply half that of the S-band. The redesign of the couplers has been done by numerical simulation as well as by iterative fabrication and measurement using a low-power model. The first prototype is a 1m long section, but that used at SuperKEKB will be 2 m long. This is because the combination of two 2 m-long sections, each using half of the power from a klystron, has a larger energy gain than the combination of four 1 m-long sections, each using one quarter of the power. In the case of using 2 m long sections, the input power to the coupler cavity is twice as high. Though the C-band 2 m long section has not yet been fabricated, the expected specification is listed in Table 11.3 In fabricating the first prototype of the C-band accelerating section, the technical knowledge accumulated in the design and the fabrication of the S-band sections is utilized. In particular, the electroplating method is

	S-band	C-band		
Parameters	KEKB	1-st prototype	2m-structure	Unit
total length	2.072	1.082	2.0	m
number of regular cells	54	54	108	
regular cell length (d)	35.0	17.5	17.5	mm
disk thickness (t)	5.0	2.5	2.5	mm
disk iris diameter (2a)	24.95 - 20.90	12.48 - 10.45	14.03 - 10.54	mm
cavity diameter (2b)	83.0 - 82.0	41.5 - 41.0	42.0 - 41.0	mm
group velocity (v_g/c)	1.4	1.9 - 1.0	2.8 - 1.0	%
shunt impedance	57	75 - 85	67 - 85	MΩ/m
Q factor	13700	9690	9700	
RF power in cells	30 - 15	34 - 15	59 - 15	MW
Field gradient	21	41.2 - 39.0	42.5 - 38.1	MW/m
Filling time	462	234	376	ns
Attenuation constant	0.302	0.434	0.696	

Table 11.3: Accelerating section characteristics

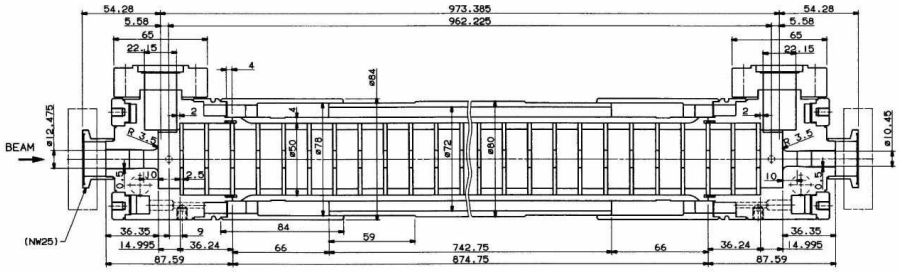

Figure 11.7: C-band 1m-long accelerating section (1-st prototype)

used for uniting the regular cells of the C-band section. Compared to the generally used brazing method, electroplating has some merits: there is no need to tune the resonant frequencies of each cell by deforming them, and copper formed by electroplating has a higher rigidity. On the other hand, the precision in fabricating the components of the cells needs to be higher and the frequency shift in the electroplating process should be carefully managed. The fabricated first prototype of the C-band accelerating section has been installed in a test stand and RF processing has been done. RF power (43 MW at maximum) from a klystron is fed into the single 1 m-long section. The accelerating field gradient at this power level is expected to be more than 40 MV/m. After 300 hours of RF processing, the accelerating section and the RF source were installed in the KEKB injector linac for a beam acceleration test (Fig. 11.8). The result of the test is shown in Fig. 11.9. The obtained energy gain is 41 MV/m for the klystron output power of 43 MW. This result agrees well with the expectation within measurement errors. However, frequent breakdown has been experienced, around ten times an hour. It is found that most breakdown occurs at the input coupler, from an analysis of the RF pulse shapes of the transmitted and reflected waves and of the vibration sensors that detect the breakdown locations. We suspect that the breakdowns occur in the region around the thin and sharp-edged iris in the coupler. We will pursue a modified coupler shape that has a smooth

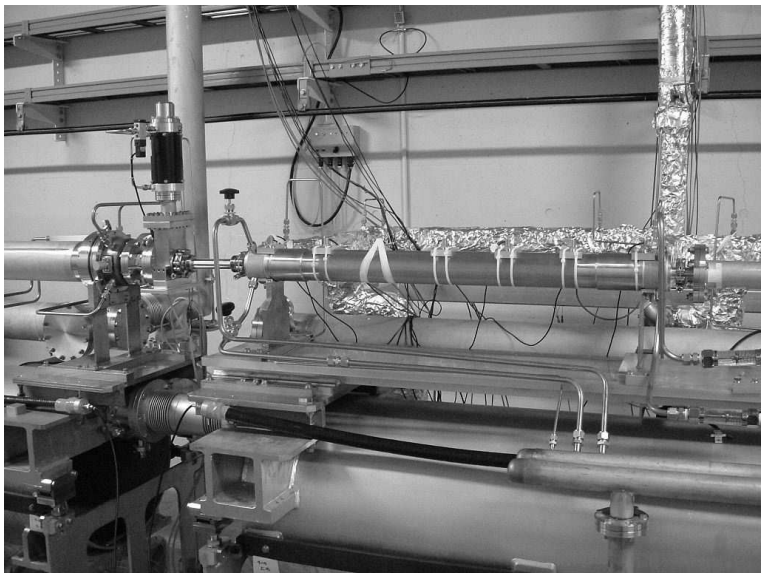

Figure 11.8: C-band 1m-long accelerating section installed in the KEKB linac

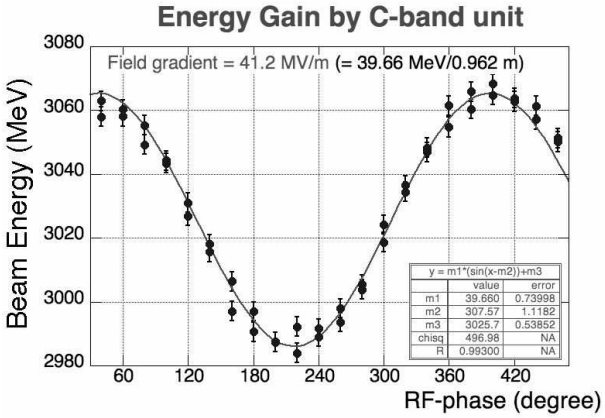

Figure 11.9: Measured energy gain

surface around the iris. Adopting a double-sided coupler instead of the present single-port coupler will also be helpful to reduce the frequency of breakdowns. A second prototype with the improved coupler structure will be fabricated and tested in 2004.

11.4 Upgrade in beam position monitors

The present beam position monitor (BPM) system uses strip-line type monitors and oscilloscopes to digitize the signals from them. The position resolution is 100 μm and the data read-out interval is 1 second. The advantages of the present system are:

- There are no active components other than the oscilloscopes. Thus, the system is relatively inexpensive. One oscilloscope covers 20 electrodes on average. Therefore, the maintenance tasks are minimized and the failure rate is very low.
- In the two-bunch injection scheme, where bunches are separated by only 96 ns, simultaneous read-out can be accomplished without any fast electronics.

- The calibration of the BPM's is straight forward. It requires mapping information in 2-dimensional 3rd-order polynomial functions, attenuation factors of cables and other passive components, and position offsets deduced from beam-based alignment.
- Since the signals from the four electrodes are read separately, information on the beam aspect ratio can be extracted easily.

For SuperKEKB, it is desirable to read out the beam-position information at every beam pulse. The reasons are:

- Fluctuations of the beam orbit and the measurement may degrade the beam stabilization algorithms. Such fluctuation should be tracked so as to improve the beam quality, including Fourier components faster than 1 Hz.
- Since continuous injection at low beam repetition will be carried routinely, beam pulses between injection beam pulses should be utilized to optimize the accelerator equipment and beams.
- The average over several beam pulses will help improve the position measurement resolution. This may improve the slow beam stabilization feedback loops.

The present data read-out interval is limited by the data-processing speed of the oscilloscopes that were available during KEKB construction. We are planning to replace the oscilloscopes with newer ones that can read out the data at 50 Hz.

In the case of quick switching of the injection modes for electron and for positrons, the electron beam charge in those pulses are very different. Since the dynamic range of the oscilloscope measurement may affect the position resolution, it may be desirable to employ a logarithmic amplifier. As an option for better position resolution, several techniques using such a sophisticated read-out circuit are being investigated. In this case, independent read-out for the two bunches in a beam pulse needs to be achieved and the maintenance cost may be greater.

Bibliography

[1] I. Abe et al., The KEKB injector linac, Nuclear Instruments and Methods in Phys. Res. A, Vol. 499, Issue 1, 21, February, pp.167-190, 2003.

[2] Y. Ogawa, et al. "Two-Bunch Operation of the KEKB Linac for Doubling the Positron Injection Rate to the KEKB Ring", presented at 2001 Asian Particle Accelerator Conference, September 2001, Beijing, China

[3] "Development of C-band 50 MW pulse klystron for e^+ e^- linear collider", By T. Shintake, N. Akasaka, H. Matsumoto, Y. Ohkubo, H. Yonezawa, KEK Preprint 97-47, Presented at 1997 Particle Accelerator Conference, Vancouver, BC, Canada, May 12-16, 1997

[4] http://c-band.kek.jp/

[5] A. Fiebig, et al. "Design Considerations, Construction and Performance of a SLED-type Radiofrequency Pulse Compressor using Very High Q Cylindrical Cavities", CERN/PS 87-45 (RF), March 1987, presented at 1987 Particle Accelerator Conference, March 1987, Washington D.C.

[6] S. Fukuda et al., R&D Status of the Linac Upgrade Plan Using a C-band System for SuperKEKB, Proc. of the14th Symposium on Accelerator Science and Technology, KEK, Tsukuba, Japan, November 11-13, pp.105-108, 2003.

[7] S. Y. Kazakov, A New Travelling-wave mixed-mode RF Window with a Low Electric Field in Ceramic-metal Brazing Area, KEK Preprint 98-120, 1998.

[8] H. Matsumoto et al., "Experience on the high-power SiC microwave dummy-load using SiC absorber", KEK Preprint 99-13, presented at the 1999 particle accelerator conference (PAC'99) Mar 29 - Apr 2, 1999, New York City, New York, U.S.A.

Chapter 12

Damping Ring

12.1 Introduction

In the present design of SuperKEKB, a damping ring (DR) is assumed only for the positron beam. The design parameters of the DR, however, should allow for the future possibility of an upgrade for the injector complex, in particular an electron damping ring. In the *adiabatic* construction scenario, sufficient acceptance must be provided for both the LER and the HER. By adopting a positron DR, the emittance of the positron beam would be much smaller than that of the electron beam. Thus, the required acceptance of the main ring is determined by the emittance of the electron beam. The normalized emittance of the electron beam is 3.13×10^{-4} in the present KEKB injector linac. The emittance of the positron beam extracted from the DR is less than 160 nm with an energy of 1 GeV. We consider the range of acceptable parameters and the extensibility of the machine. Since the acceptance of the main rings, especially around the IR, is determined by the emittance of the electron beam, the smaller emittance of the electron beam should relax the constraint for the IR aperture. A beam background to the physics detector originating from the halo of intense electron beams might arise during the continuous injection. The option of a electron DR would significantly improve the detector background. Thus, the electron DR should be considered as an upgrade option for SuperKEKB. In that case, the emittance of the DRs, in turn, will determine the apertures of the main rings.

When we consider the design of the positron DR, we also consider the option of an electron DR. The emittance of the DR is not given by external conditions and is determined through the lattice design itself as the smallest achievable value. The positron beam is extracted at the end of Sector-2 from the injector linac via the LTR line and injected to the DR. Since the energy spread of the positron beam is too large for injection to the DR, it is compressed prior to injection through an energy compression system (ECS). The ECS is incorporated into the LTR line. After 40 ms, which is two periods of the 50 Hz repetition injection rate, the damped beam is extracted and sent back to the Linac via the RTL line. The bunch length of the extracted beam is compressed by a bunch-length compression system(BCS), since it is too long to be accommodated by the C-band accelerating structures. The BCS is incorporated in the RTL line. A schematic layout of the whole system, LTR-DR-RTL, is shown in Fig. 12.1.

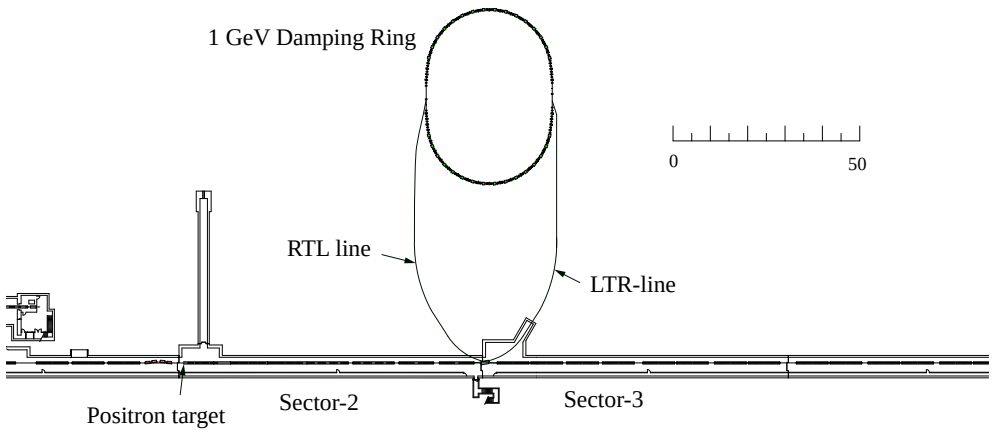

Figure 12.1: Layout of LTR-DR-RTL system. The ECS and the BCS systems are incorporated into the LTR and the RTL line, respectively.

12.2 Beam Parameters

12.2.1 ECS

Since the positron beam from the linac injector has a long tail in the energy profile, the energy acceptance of the DR is one of the most important issues from the viewpoint of the capture efficiency. The energy profile of the linac beam is shown in Fig. 12.2(a). The transmission efficiency as a function of energy acceptance is also shown in Fig. 12.2(b). In order to capture 95% of the particles, the energy acceptance must be ±4% without energy compression. It is difficult for the DR to achieve an energy acceptance of ±4%. Thus, we utilize an energy compression system (ECS) prior to the DR injection in order meet to the energy acceptance.

A simulation using EGS4 code has been performed for the positron beam from production through acceleration to 1 GeV with the S-band accelerating structure. The result is shown in Fig. 12.2(b). The dotted line shows the result from the simulation and the solid line shows that from a calculation with a simple model. The model is based on a two-dimensional Gaussian beam with a bunch length, σ_z, of 2.3 mm and an intrinsic energy spread, σ_ϵ, of 1.7×10^{-3}. Using this model, the energy compression factor is assumed to be 1/3. The simulation is well reproduced by the simple model.

The energy profile after the ECS was calculated as shown in Fig. 12.2(c). The transmission after the ECS is given in Fig. 12.2(d). This shows a significant improvement compared with that before the ECS. After the ECS, almost 100% of the particles are included within the energy band-width of ±1.5%.

12.2.2 Parameters of injected beam

In order to maximize the charge per pulse of the injected beam, we have adopted a two-bunch injection scheme. In this scheme, two bunches separated by 98 ns are accelerated in a single linac pulse. Parameters of the injected beam and the ECS are summarized in Table 12.1.

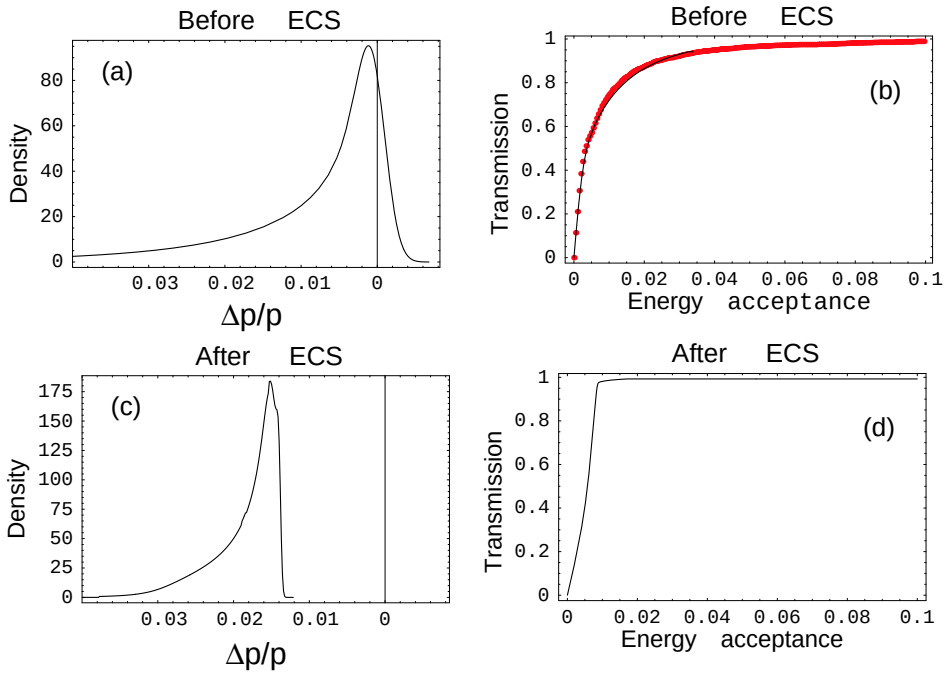

Figure 12.2: Energy profile and transmission before and after the ECS. The energy acceptance is defined as half the energy band-width.

	before ECS	after ECS	Unit
Energy	1.0		GeV
Emittance	1.225×10^{-6}		m
Energy spread†	1.30	0.406	%
Bunch length†	2.30	6.05	mm
Number of bunches per pulse	2		
Bunch spacing	98		ns
Bunch charge	2.56		nC
ECS cavity voltage	30.5		MV
ECS cavity frequency	2.856		GHz
R_{56} component	-0.486		m

†defined as extension that contains 95.5% divided by 4.

Table 12.1: Parameters of injected beam.

12.3 Design of Damping Ring

The dynamic aperture is a critical issue in designing a damping ring, since the injected beam has a large energy spread and a large transverse emittance. It is well known that a FODO cell has the good feature of a large dynamic aperture. A momentum aperture of several percent of the dynamic aperture can be realized. However, the momentum compaction factor tends to be large, resulting in a higher accelerating voltage. In order to overcome this situation, we adopt a variant of the FODO cell: FODO with alternating bends, which has a reverse bend for one of the two bends. A schematic view of the layout is shown in Fig. 12.3. Bending magnet B2 is the reverse bend, with a bending angle of -rθ ($1 > r \geq -1$), where θ is the bending angle of the normal bend B1. In the case of $r = -1$, it reduces to the normal FODO lattice. We assume that the bending radius is the same for both B1 and B2. Since the dispersion function is positive at B2, the momentum compaction factor is reduced. This type of cell preserves a good dynamic aperture and can attain a low positive/negative momentum compaction factor.

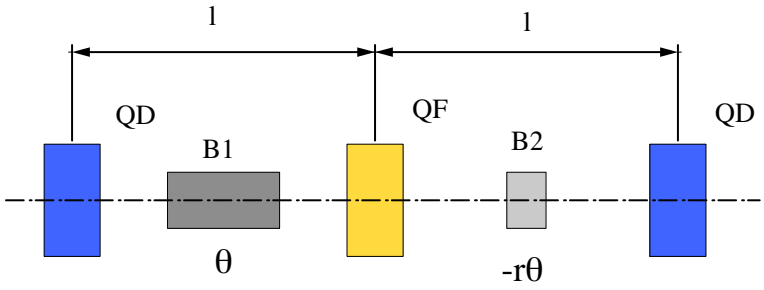

Figure 12.3: FODO cell with alternating bends. The B2 is a reverse bend and the bend angle is -rθ, where θ is the bend angle of the normal bend B1.

In a thin-lens model the momentum compaction factor α_p is written as

$$\alpha_p = G(r,\mu)\theta^2, \tag{12.1}$$

$$G(r,\mu) = \frac{(1+r^2)(3+\cos\mu) - 8r}{16\sin^2\frac{\mu}{2}}, \tag{12.2}$$

where μ is the phase advance per cell. An equal phase advance for both the horizontal and vertical planes is assumed. If r is greater than $2-\sqrt{3}$, there exists a combination of r and μ such that α_p=0. In Fig. 12.4 (a), the phase advance μ that satisfies $G(r,\mu) = 0$ is shown as a function of r. A remarkable feature is that for a fixed r, by adjusting the phase advance, a low positive or negative α_p can be achieved, as shown in Fig. 12.4 (b).

The emittance is given by following expressions in the thin-lens model:

$$\varepsilon_0 = 1.834\times10^{-7}F(r,\mu)\frac{\ell\theta^2}{\rho}E_0^2, \tag{12.3}$$

$$F(r,\mu) = \frac{3-4r+3r^2+(1-4r+r^2)\cos\mu - r\frac{1-|r|}{1+|r|}\left(3\sin\frac{\mu}{2}-\sin\frac{3\mu}{2}\right)}{\sin^2\frac{\mu}{2}\sin\mu}, \tag{12.4}$$

where ℓ is the half cell-length, ρ is the bending radius, and E_0 is the beam energy in GeV. Since we select μ and r such that $\alpha_p \approx 0$, then with r being expressed in terms of μ, Eq.

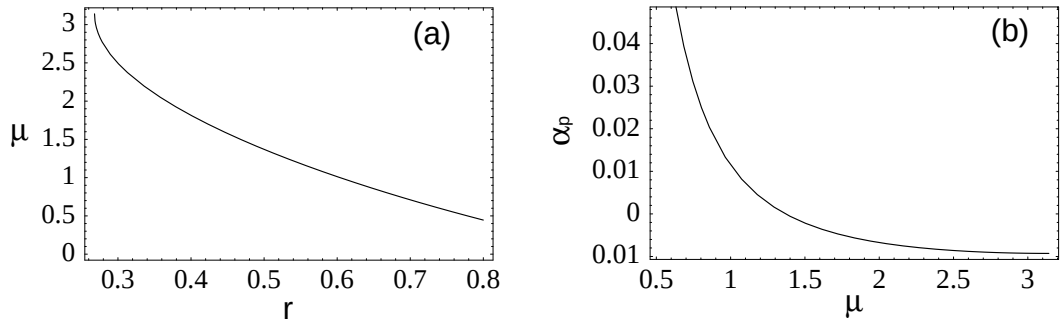

Figure 12.4: (a) Phase advance per cell that satisfies α_p=0 as a function of r. (b) The α_p as a function of phase advance for fixed $r = 0.5$ and $\theta = 0.314$.

(12.4) can be rewritten as

$$\varepsilon_0 = 1.834 \times 10^{-7} f(\mu) \frac{\ell\theta^2}{\rho} E_0^2. \tag{12.5}$$

The function $f(\mu)$, shown in Fig. 12.5, has its minimum at μ=2.1, which corresponds to r=0.35.

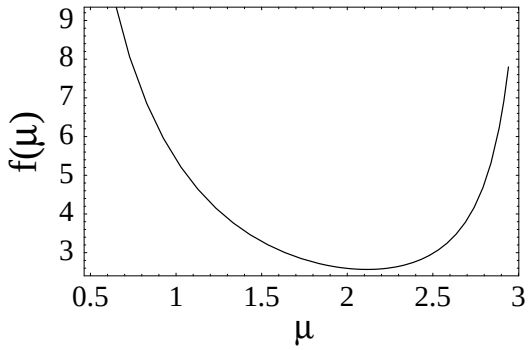

Figure 12.5: The function f(μ), taking its minimum at μ=2.1.

12.3.1 Parameters of Damping Ring

The parameters to be optimized are the damping time, τ, the phase advance, μ, and the number of cells, n. The horizontal damping time is given by

$$\tau = \frac{2E_0}{J_x U_0}\frac{C}{c} = \frac{2}{cJ_x C_q}\frac{\rho}{E_0^3}\left\{2\pi\rho + \frac{1-r}{1+|r|}(n\ell_1 + 2\ell_2)\right\}, \tag{12.6}$$

where C and U_0 are the circumference and the radiation loss per turn, J_x is the damping partition number, and c is the speed of light. We assume $J_x = 1$ in the design of the DR. The length $2\ell_1$ and $2\ell_2$ are, respectively, the cell length minus the length of the bends, and the length of the straight sections. The second term stems from the equations

$$U_0 = C_q \frac{1+|r|}{1-r}\frac{E_0^4}{\rho}, \tag{12.7}$$

$$C = \frac{1+|r|}{1-r} 2\pi\rho + n\ell_1 + 2\ell_2. \tag{12.8}$$

If ℓ_1, ℓ_2, and E_0 are fixed, the bending radius, ρ, is determined from Eq. (12.6), as a function of τ, r, and n: $\rho(\tau, r, n)$. Similarly θ and ℓ can be written as a function of r and n: $\theta = 2\pi/(1-r)n$, and $2\ell = \ell_1 + (1+|r|)\rho\theta$. Since the ratio r is a function of μ, provided that α_p=0, the emittance is thus a function of τ, μ, and n: $\varepsilon_0(\tau, \mu, n)$. The emittance at extraction, ε_{ext}, is

$$\varepsilon_{ext} = \varepsilon_0 + (\varepsilon_i - \varepsilon_0)\exp(-2T/\tau), \tag{12.9}$$

where ε_i is the emittance at injection and T is the beam circulation time, which is 40 ms. Two bunch-trains are accommodated in the ring. The dependence of the emittance at extraction on the parameters τ, μ, and n is shown in Fig. 12.6. It is found that the minimum emittance can be obtained for any n in the region around τ=12 ms and μ=2.3. The behavior of the emittance at extraction in the τ direction comes from $\rho(\tau, r, n)$ in Eq. (12.5) and the $\exp(-2T/\tau)$ term in Eq. (12.9), while in the μ direction, the function $f(\mu)$ dominates.

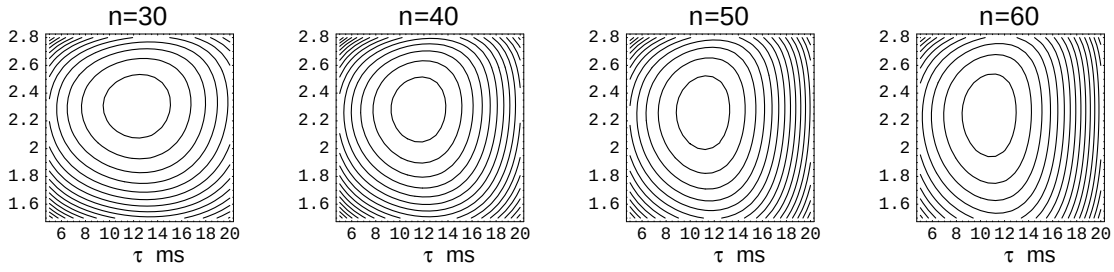

Figure 12.6: Contour plot of the emittance at the extraction in (τ,μ) plane for various number of cells n.

To determine the number of cells, we must take the field strength of the bend and the circumference into account. Figure 12.7 shows the dependence of the magnetic field and the circumference on the phase advance for the case with τ=12 ms. Since the kicker rise/fall time is planned to be 100 ns, the circumference needs to be greater than 120 m. Taking the optimum phase advance, μ, of around 2.3, the conditions on the circumference requires that the number of cells must be greater than 40. The magnetic field of the bend is then 1.3 T, which is attainable with sufficient margin.

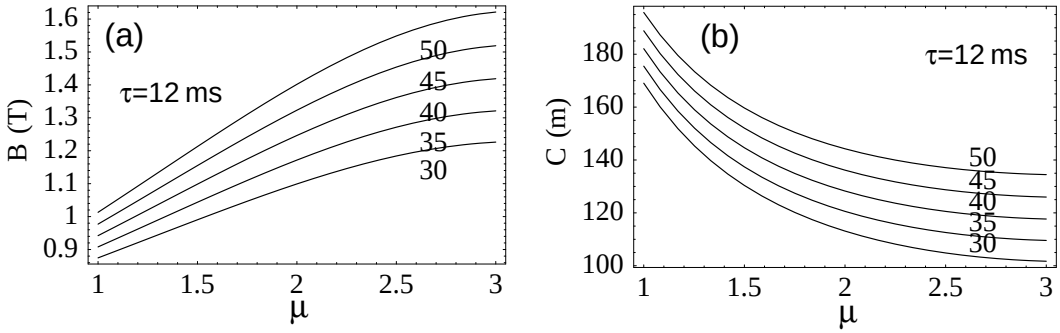

Figure 12.7: (a) Magnetic field. (b) Circumference. Number attached to each curve is the number of cells.

Consequently, we adopt the ratio $r = 0.35$, and $n = 40$ cells. The parameters of the DR are shown in Table 12.2. In the thick-lens model, the phase advance, μ, which makes

α_p zero is 2.6, while it is 2.1 in the thin-lens model. The emittance, on the other hand, has a flat minimum for μ from 1.9 to 2.5. From the view of the dynamic aperture, a smaller phase advance is preferable. We should avoid high-order resonances driven by sextupole magnets, which would be enhanced if μ is close to $2\pi/3 = 2.09$. We chose 1.93 as a compromise. The cavity voltage of 0.261 MV is still within the specification of the KEKB ARES cavity of 0.5 MV for a single cavity.

		Unit
Energy	1.0	GeV
Number of bunch trains	2	
Number of bunches/train	2	
Bunch spacing	98	ns
Bunch charge	2.56	nC
Repetition frequency	50	Hz
Circumference	131.3	m
Energy loss per turn	73	keV
Horizontal damping time	11.95	ms
Injected-beam emittance	1.23	μm
Equilibrium emittance	12.2	nm
Emittance at extraction	13.7	nm
Energy spread of injected beam	4.06×10^{-3}	
Bunch length of injected beam	6.05	mm
Energy spread	5.29×10^{-4}	
Bunch length	5.03	mm
Bend-angle ratio of reverse-bend	0.35	
Phase advance/cell	1.932	rad
Momentum compaction factor	0.0019	
Number of normal-cells	40	
Bend field	1.267	T
Quad field	16.3	Tm^{-1}
Sextupole filed	426	Tm^{-2}
Length of straight sections	2×6	m
Length of main bend	0.7286	m
Length of reverse bend	0.255	m
Length of quad	0.25	m
Length of sext	0.1	m
Minimum space between magnets	0.1	m
Cavity voltage for 1.5% bucket-height	0.261	MV
RF frequency	509	MHz

Table 12.2: Parameters of Damping Ring

Figure 12.8 shows the optical functions for the normal cell and that for the entire ring. The main bend is placed at the minimum of the dispersion function while the reverse bend is placed near to the maximum for the greatest effectiveness in reducing the momentum compaction factor. In the dispersion suppressor cells, 14 quadrupoles has been used in total as free variables during optics matching. Sextupoles are placed on both sides of the

reverse bend in the normal cells. Chromaticity correction is done by using two families of sextupole magnets.

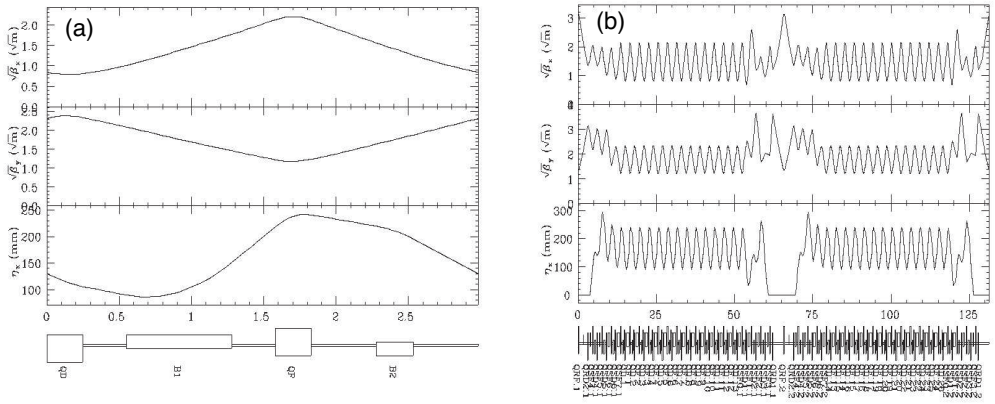

Figure 12.8: (a) Optics functions of normal cell. (b) Optics functions of entire ring.

12.3.2 Dynamic aperture

We performed a tracking simulation of the proposed ring, and confirmed that it has sufficient dynamic aperture, even with machine errors included. The results are shown in Fig. 12.9. The tunes are chosen to be (ν_x, ν_y)=(12.24, 4.26). The RF bucket height is 4%. The two solid lines show the largest initial amplitude of the particles, for each initial momentum deviation, that survived after 4000 turns. The thick line is for the case of the ideal machine, while the thin line shows an example that includes machine errors. The errors are assumed to obey a Gaussian distribution with tails truncated at 3σ: a strength error of 3×10^{-4} and 5×10^{-4} for the quadrupole and sextupole magnets, respectively, and random misalignments of 0.5 mm for the magnets in the horizontal and the vertical plane. The resultant orbit is corrected with dipole correctors. The rectangular region represents a maximum amplitude of 4.9 μm and an energy deviation of $\pm1.5\%$ for the injected beam.

The proposed ring has a wide operational tune space. Figure 12.10 shows the dependence of the dynamic aperture on the operational tune for the case with no errors. Figure 12.10 (a) shows the 'score' at each tune, which corresponds to the sum of the largest initial amplitude over each bin of energy deviation, or equivalently, the area under the line in Fig. 12.9 for each tune. The brighter region has a larger dynamic aperture. The highlighted area in Fig. 12.10 (b) shows the region of tune space where the dynamic aperture is larger than the extent of the injected beam. A strong third-order resonance has been seen in the horizontal plane, driven by sextupoles with a phase advance of 2.026, which is very close to $2\pi/3$=2.09.

12.4 Bunch Compression System

Since the bunch length at extraction, 5 mm, is too long to be accepted in the subsequent C-band accelerating structures, it is compressed to 1 mm through a BCS system, which

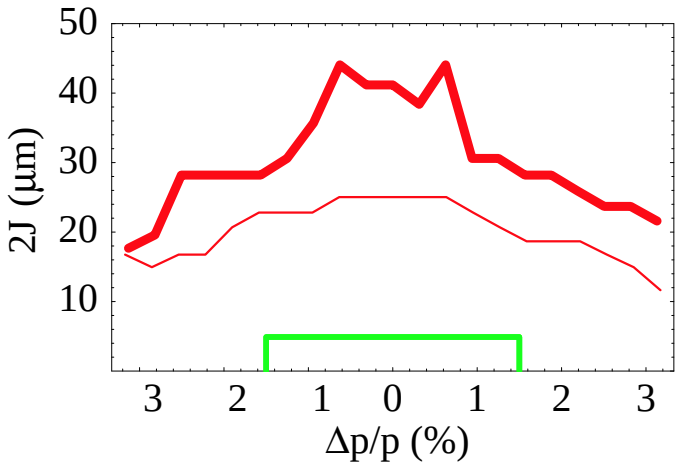

Figure 12.9: Dynamic aperture of the proposed ring. The thick line shows the largest initial amplitude of particles for each of energy deviation that survived after 4000 turns in the case of the ideal machine. The thin line shows the same, but includes machine errors, for just one random seed. The rectangular region shows the region that corresponds to the maximum amplitude and energy deviation of the injected beam.

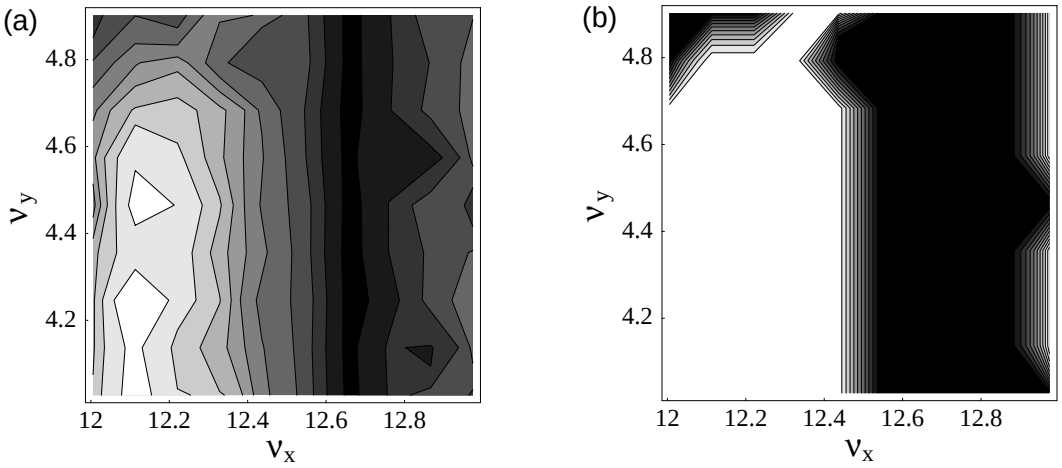

Figure 12.10: Tune survey results for the dynamic aperture. (a) Dynamic aperture for each tune. Brighter areas designate a larger aperture. (b) The highlighted area shows the tune space that has a larger dynamic aperture than the injected beam.

is incorporated into the RTL line. The basic parameters of the BCS system are given in Table 12.3.

	before BCS	after BCS	Unit
Emittance	13.7		nm
Energy spread	5.29×10^{-4}	4.99×10^{-3}	
Bunch length	5.03	0.59	mm
BCS cavity voltage	17.5		MV
BCS cavity frequency	2.856		GHz
R_{56} component	-0.95		m

Table 12.3: Parameters of BCS system

12.5 Conclusion

The design of the positron damping ring has been presented. The parameters are chosen assuming the future possibility of an electron damping ring. We adopt the FODO cell with alternating bends in the DR design. The proposed ring has the good feature that a very low positive or negative momentum compaction factor can be achieved by changing the phase advance of the normal cells. The RF voltage is 0.26 MV, and can be provided by a single ARES cavity. We have shown that the ring has a very wide dynamic aperture over a large region of tune space, and the momentum aperture is greater than 4%, which is limited by the RF bucket height.

Chapter 13

Facility

The power losses from the magnet system, SR, HOM, and the RF system are shown in Table 13.1. The power loss from the magnet system is ∼10 MW at maximum, which is the same for both KEKB and for SuperKEKB. The AC power for the RF system is 73 MW total. The total power loss at SuperKEKB is 83.2 MW, which is higher by a factor of 2.4 than that at KEKB. Since a total power consumption of up to 120 MW is allowed at the KEK site, there is no difficulty in principle to supply the required power. We have 3 substations, Nikko, AR(AR+Fuji), and Oho, which can supply electric power to each section of the SuperKEKB ring. For the injector linac, the electric power is supplied from the PF substation. Figure 13.1 shows the location of each substation at KEK. The Oho substation and the Nikko substation can supply 32 MW at maximum. The AR substation can supply 51.5 MW at maximum, because it covers the Fuji section and the PF-AR facility. However, the distribution of the power consumption to the RF system is 10 MW for Nikko, 28.6 MW for Fuji, and 34.4 MW for Oho at SuperKEKB, respectively. Therefore, the lack of electric power at Oho has to be covered by the PS substation which is locate near Oho and has a 56 MW capacity. We expect that the PS (Proton Synchrotron) will be shutdown when the SuperKEKB project starts.

	KEKB (design)		SuperKEKB	Unit
Magnet p.s.		3.84		MW
Magnet		6.35		MW
SR	8		26	MW
HOM	0.43		9	MW
RF system	16		38	MW
Total	34.6		83.2	MW

Table 13.1: Power losses for KEKB and SuperKEKB.

The cooling system must be upgraded for SuperKEKB. The cooling system is divided into four sections along the KEKB ring: Fuji, Nikko, Tsukuba, and Oho. Although the total cooling capacity is 84.73 MW in the present system, the location, water type, and flow rate that is required for each component should be taken into account. Klystron power loss, which is one of the largest sources of power loss, is estimated to be ∼32 MW. We utilize a VAPODINE system, which is a special cooling system for klystrons. The VAPODINE system is compact and can be put on the roof of the klystron buildings. In

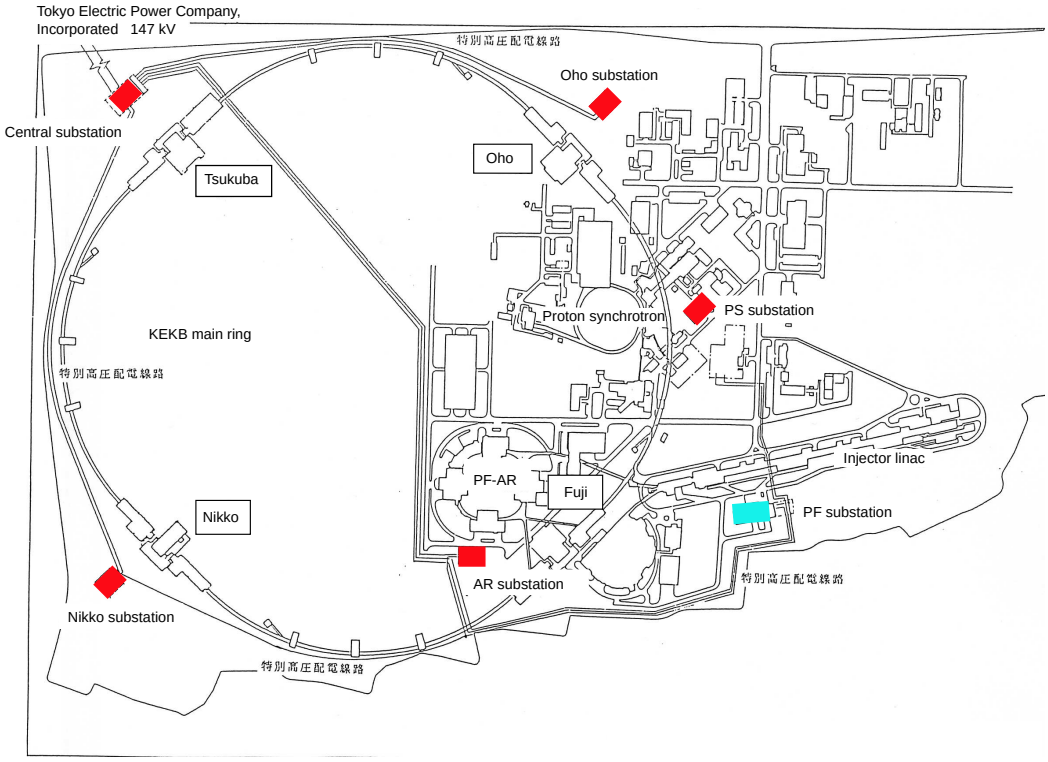

Figure 13.1: AC distribution system at KEK.

addition to the VAPODINE system, We consider 12 sections for SuperKEKB, adding 8 sections where cooling systems will be constructed. The cooling system for the vacuum system consists of an air cooled heat-exchanger, a chiller, and pumps. Figure 13.2 shows a schematic layout of the cooling system. We plan a flow rate of 2000 l/min, an incoming water temperature of 45 °C, and an outgoing water temperature of 24 °C. The cooling system for the magnet system, cavities, and dummy loads consists of air cooled heat-exchanger and pumps. Because there is no chiller, this conventional system is simple and reliable.

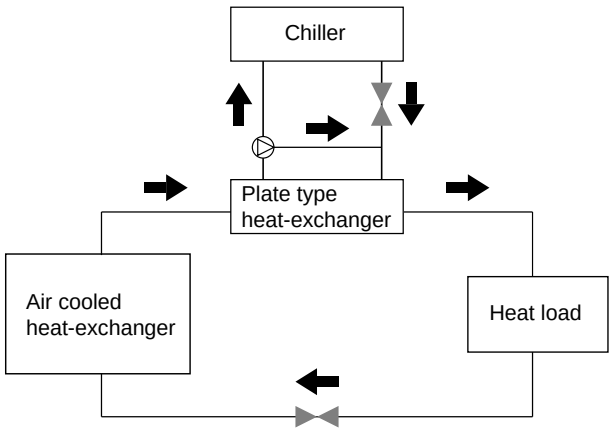

Figure 13.2: Cooling system for the vacuum system.

Chapter 14

Construction Scenario

The upgrade of KEKB to SuperKEKB is proposed in around 2007. The tentative schedule is shown in Tables 14.1, 14.2, 14.3, and 14.4. The R&D and production of various components will be done in the first four years in parallel with the physics experiment at KEKB. The installation will be done during a one year shutdown in 2007, and then the commissioning of SuperKEKB will begin.

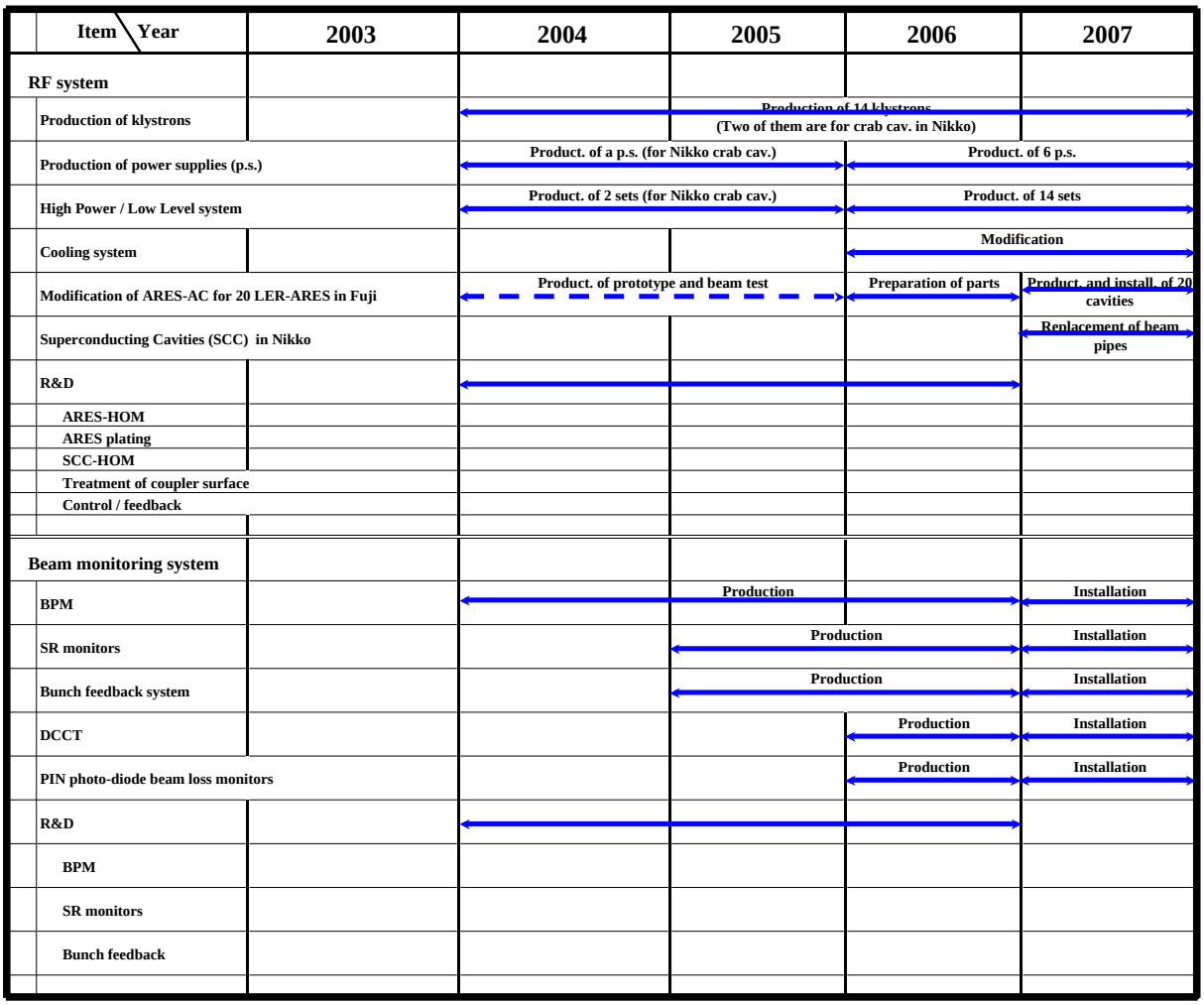

Figure 14.1: Construction schedule.

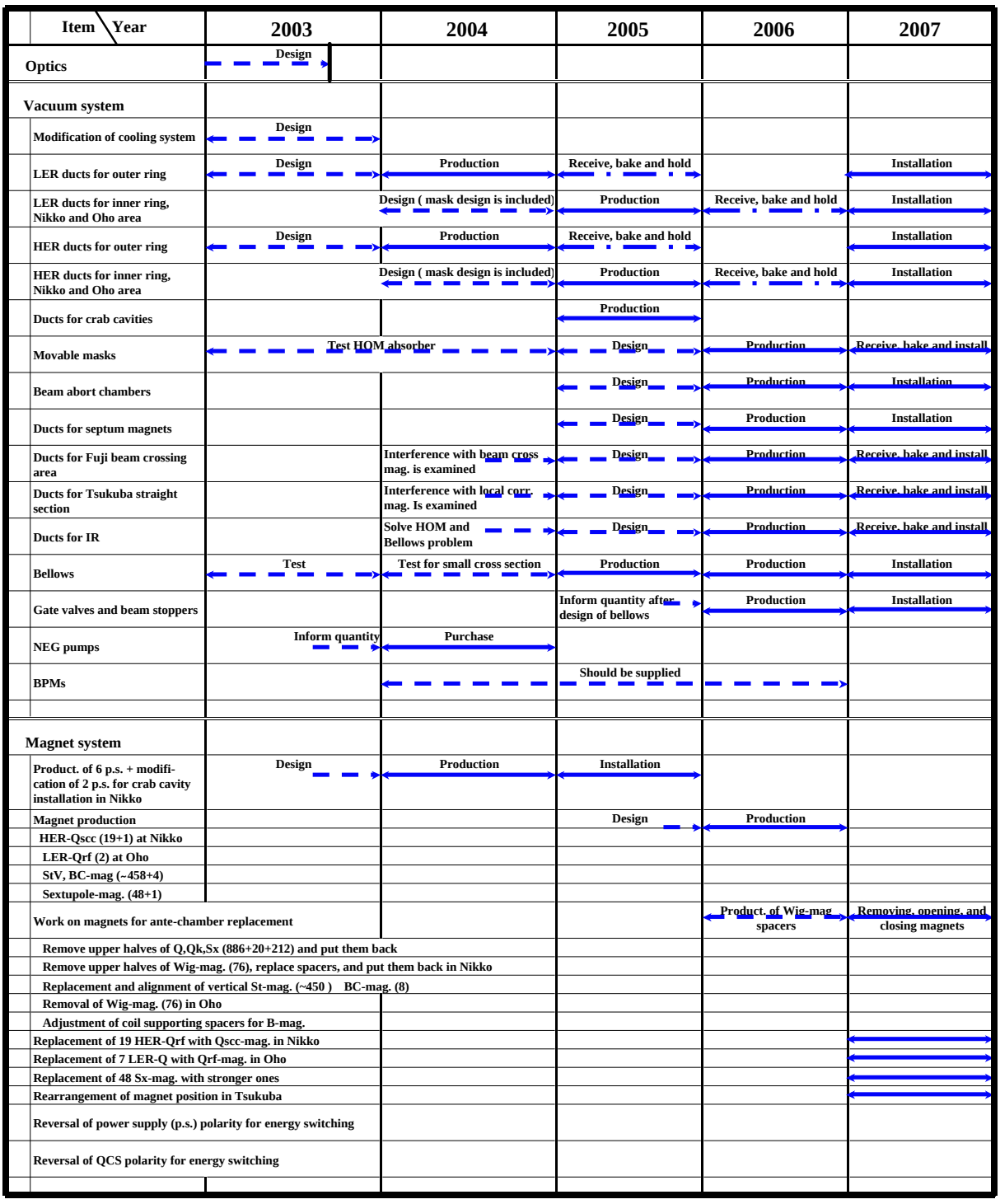

Figure 14.2: Construction schedule (cont'd).

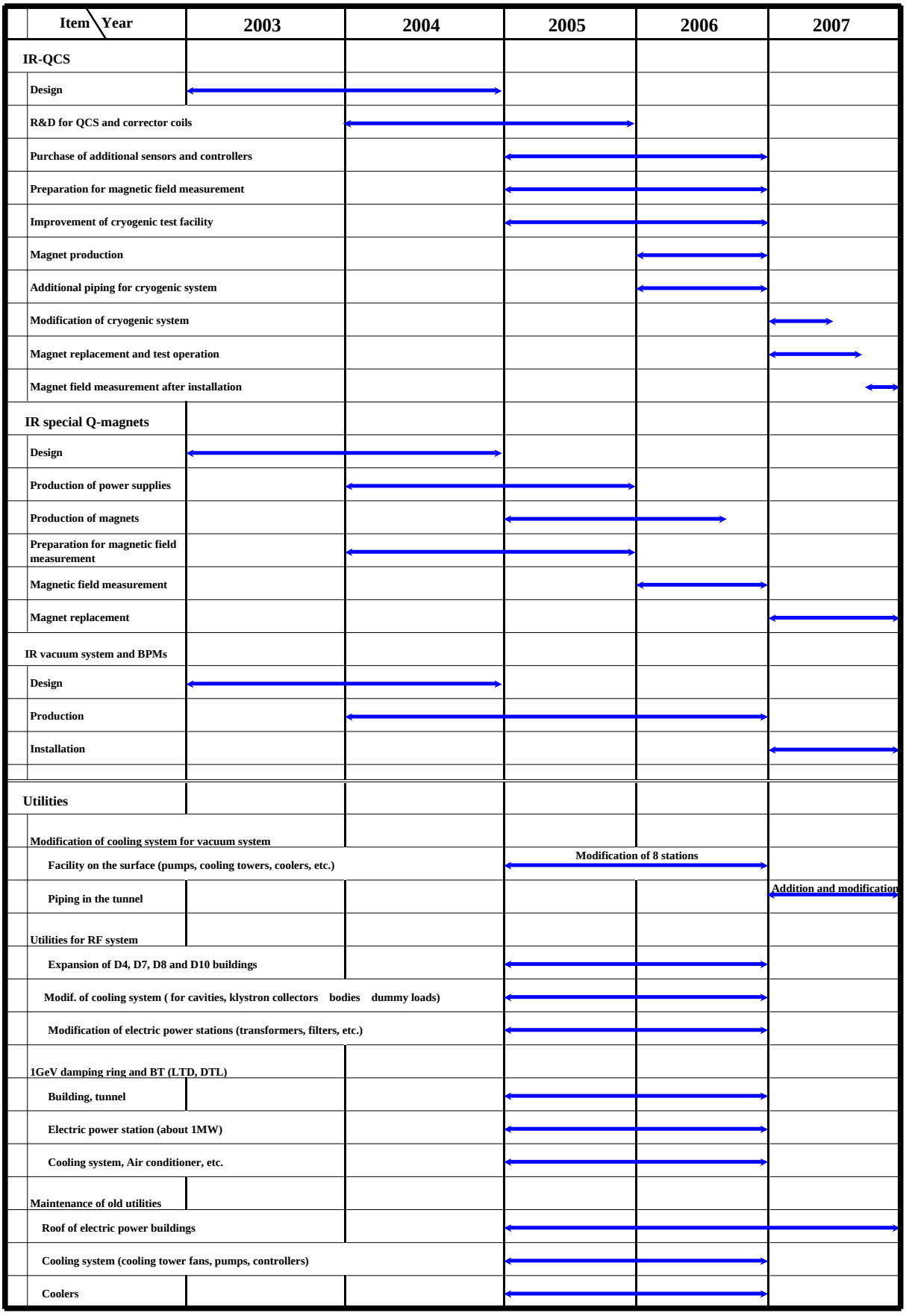

Figure 14.3: Construction schedule (cont'd).

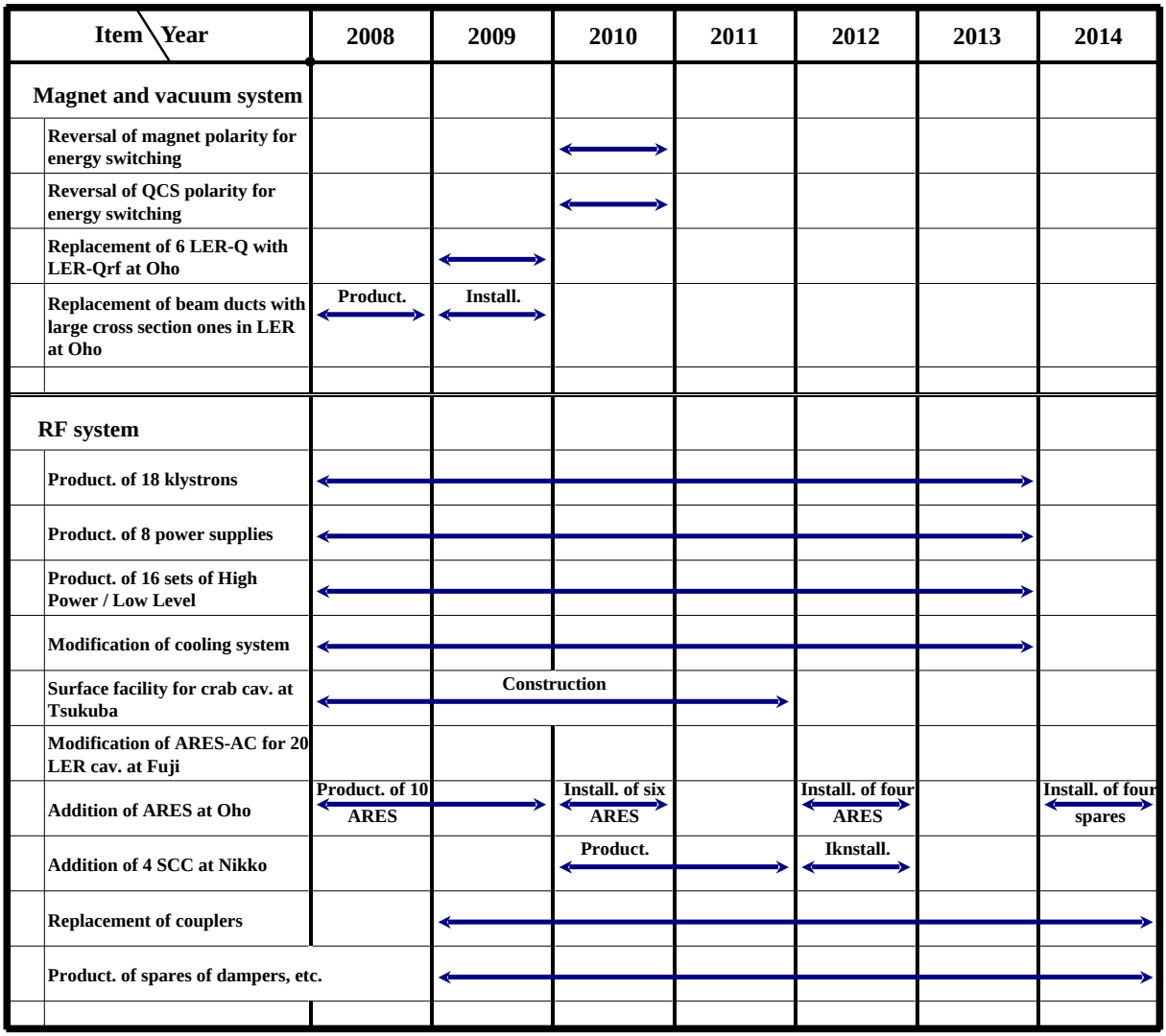

Figure 14.4: Construction schedule (cont'd).